A THERMODYNAMIC MODEL OF ADIABATIC MELTING OF THE MANTLE

Thesis by

Paul David Asimow

In Partial Fulfillment of the Requirements

for the Degree of

Doctor of Philosophy

California Institute of Technology

Pasadena, California

1997

(Submitted May 28, 1997)

Chapter 2 (pages B-1 to B-48) reprinted from

Geochimica et Cosmochimica Acta volume **59**,

P. D. Asimow, M. M. Hirschmann, M. S. Ghiorso, M. J. O'Hara, and E. M. Stolper,

"The effect of pressure-induced solid-solid phase transitions on decompression melting of the mantle," pages 4489-4506, © 1995,

with kind permission from Elsevier Science Ltd.,

The Boulevard, Langford Lane, Kidlington OX5 1GB, UK.

Chapter 3 (pages C-1 to C-47) reprinted from

Philosophical Transactions of the Royal Society of London volume **A355**,

P. D. Asimow, M. M. Hirschmann, and E. M. Stolper,

"An analysis of variations in isentropic melt productivity", pages 255-281, © 1997,

with kind permission from The Royal Society,

6 Carlton House Terrace, London SW1Y 5AG, UK.

Acknowledgment

I owe thanks to many people for helping to create this thesis and to prepare me as a person and a scientist for this work and for whatever lies ahead. Most importantly, Ed Stolper is a fabulous mentor and advisor. He has given me almost complete freedom to work on whatever excites me, but is nevertheless a fountain of ideas and good advice. He is tolerant of the bizarre work habits of graduate students (at least of my own). His intuition on scientific problems is remarkable; he often guesses the solution to an experimental or theoretical difficulty even though he clearly lacks sufficient information to know the answer. When, in his stubbornness, he refuses to take anything for granted, my initial reaction may be annoyance that he would question such obvious points. Usually it turns out that he was right, and the obvious points were either poorly stated or simply incorrect. His own private scientific method has greatly influenced my thought and this work: reduce every insight to its essential core, look for it in systems simple enough to understand completely, but always remember that simple systems can deceive. Thank you, Ed, for everything: for the hours of mind-numbing editing and redrafting of my manuscripts, for the free rein to explore new subjects, for magnanimity when these turn out to be dead ends, and for shielding me so far from most of the realities of funding.

I am deeply grateful to Marc Hirschmann for getting me started on thermodynamic modeling, for patient advice, for long days (and nights) of struggle with programming bugs or math problems or bad assumptions. I solved many problems along the way simply by going to talk to Marc about them. Sometimes he knew the answer, sometimes we found it together, and sometimes I found it myself once I had someone with whom to share the problem. I thank Marc especially for allowing me to take over projects and papers that were originally his, even when I took advantage of a student's lack of other responsibilities to get there first. Mark Ghiorso took a risk in letting me in to the MELTS source code, his masterpiece (another thank you to Marc Hirschmann for shepherding me into Mark's good graces). I hope I have repaid that trust in the valuable currency of fixed

bugs and improved code, or at least in intangibles like scientific results. None of this work would have been possible without Mark's indulgence, not to mention Mark and Richard Sack's decade or more of work developing the models and algorithms that I so blithely apply herein.

Although I regret not having any permeability measurements for him yet, I am grateful to Dave Stevenson for years of patient advice and funding support. The geodynamical side of me, represented in this work only by Chapter 4, owes a great deal to Dave's mentoring. I also want to thank Geoff Blake, my academic advisor, for quarterly signatures and checkups, and for chairing my committee and reading this tome. Mike Gurnis and Peter Wyllie also merit gratitude for serving on the committee despite busy schedules. Many other people at Caltech have helped me through my graduate career: Lee Silver on my first proposition; Andy Ingersoll on an obscure question concerning gravity-compensated enthalpy (or moist static energy depending who you ask); G. J. Wasserburg on an even more obscure issue of notation in Chapter 3; Sam Epstein and George Rossman simply for taking a benevolent interest; and Sally Newman, John Beckett, and Mike Baker for endless and generously offered help on matters practical and experimental, and for keeping this place running despite destructive rogue elements such as myself.

For Chapter 2, I thank my co-authors Marc Hirschmann, Mark Ghiorso, Mike O'Hara, and Ed Stolper. For Chapter 3, further thanks to Marc Hirschmann and Ed Stolper, co-authors on the published version of that work. For Chapter 4, thanks to Marc Spiegelman for in-depth discussions of the batch melting analogy and to Peter Kelemen for extended discussions of melt focusing and discordant dunites. For Chapter 5, thanks to Charlie Langmuir for providing the spreadsheet that implements his melting model.

I want to thank John Wood, my undergraduate thesis advisor, for telling me to go to Caltech; that was good advice; my brother Dan for encouraging me to take a geology class, or anything other than physics; J. B. Thompson for teaching that first geology class and addicting me to earth science; my parents Michael Asimow and Carol Gray for many

things — my father's example of academic life, my mother's love of science, for sending me to the best schools, for whatever unknown sacrifices and hardships they undertook to raise little old me; my son Lev for inspiration, and for being a good reason not to work all the time. And, last and deepest, my eternal gratitude to Jenny for loving me, for letting me love you, and for any dreams of your own that have been postponed or lost while I followed mine.

Abstract

Mid-ocean ridge basalts (MORB) are mixtures of melts produced over a range of pressure and temperature in a nearly adiabatic open system undergoing changes in composition as melting proceeds. Interpretation of the compositional variations observed in MORB and their correlation with geophysical aspects of the ridge therefore requires complex forward models to connect experimental observations of isothermal, isobaric batch melting of peridotite to natural compositions. Previous attempts to construct such models have relied on parameterizations of melt composition or partition coefficients and extent of melting in pressure-temperature space from experimental batch melting data. This thesis undertakes the examination of an alternative approach using thermodynamic models of silicate minerals and melts to predict equilibria under quite arbitrary constraints, including variable bulk composition and constant entropy. The liquids predicted from the thermodynamic models along polybaric paths can then be integrated to produce comprehensive forward models of MORB genesis.

Chapter 1 introduces the nature of the MORB modeling problem and the motivation of the thermodynamic approach in greater detail. Chapter 2 illustrates the thermodynamic approach by demonstrating that the effect of the garnet-spinel and spinel-plagioclase peridotite transitions, which retard or reverse isentropic melting, can be easily understood. Chapter 3 looks at the variables affecting isentropic melt productivity (i.e., the increment of additional melting per decrement of pressure at constant entropy). I find that this quantity is likely to increase during progressive melting, punctuated by drops where phases are exhausted from the residuum. Chapter 4 extends this approach to issues of melt transport in one dimension and steady state; I evaluate the magnitude of entropy production due to gravitational dissipation and thermal interactions with migrating fractional melts and examine the effect of focused melt flow. Finally, chapter 5 deals with the compositions and mean properties of MORB obtained by integrating the compositions and melt fractions predicted by our models. We compare our results to published models of MORB compositions and consider the implications. The algorithms and source code, including subsolidus capability, added to the MELTS package of Ghiorso and Sack for these calculations are included as appendices.

Table of Contents

List of Tables

List of Figures

Chapter 1. Introduction

Background and motivation

Over the past forty years it has become clear that the surfaces of terrestrial planets are dominated by basaltic magmatism (BVSP, 1981). On Earth, basaltic rocks underlie the entire ocean floor (Engel et al., 1965) and much of the continents [i.e., Archaean greenstone belts (Goodwin, 1977), continental and rift-related flood basalts (White and McKenzie, 1989; White and McKenzie, 1995), and continental arc terranes (Rudnick, 1995)]. Basalts are exposed on the lunar surface (Head, 1976; Papike et al., 1976) and over nearly the entire surface of Venus (Head et al., 1992). On Mars, basaltic flows and edifices are visible (Carr, 1975), much of the surface apparently consists of weathering products of basalt (Toulmin et al., 1977), and the shergottite meteorites are thought to be direct samples of basalt from Mars (McSween, 1994). There are also igneous meteorites presumed to represent basaltic magmatism on minor planets (Stolper et al., 1979). It is clear from the universal nature of basaltic magmatism that no special conditions are required for basalt formation and that its source is a common material, namely peridotite, the generic bulk silicate mantle composition shared to first order by all the terrestrial planets. But not all basalts are the same. There are coherent variations in major and trace element composition that reflect variations in source composition, conditions of melting and melt transport, and differentiation histories. In this thesis I focus primarily on terrestrial mid-ocean ridge basalt (MORB), the most voluminous type of basalt magma being erupted on Earth at present. Much of this work may also apply to other terrestrial and planetary basalt suites, but I begin with MORB for several reasons: (1) it is produced in the simplest environment of all terrestrial basalts, away from preexisting continental or oceanic crust and lithosphere; (2) there is a large quantity of observational data on MORB compositions and their correlation with physical variables of the mid-ocean ridge system; (3) there has been some success in compensating for the effects of differentiation on

MORB compositions, allowing study of mantle source processes; and (4) there are important and systematic covariations in chemical, isotopic, and physical parameters against which to test model predictions.

If each sample of basalt could be traced backwards through the differentiation process to a unique primary liquid composition that was in equilibrium with its mantle source at some unique pressure (P) and temperature (T), then basaltic magmatism would be entirely understood by now. The methods of experimental petrology would allow us to work out the conditions of formation and the mineral compositions in the source of a given primary liquid by seeking multiple saturation points. Similarly, for any putative source composition, the complete spectrum of possible liquids that might be derived from it could be observed by varying pressure and temperature in simple melting experiments.

There are, however, several ways in which the study of basalts is not so simple. First, it is nontrivial to identify primary liquids from a suite of differentiated basalts. For example, it is not necessarily true that every member of a suite shares a common primary liquid, and for multiply saturated compositions there is no way to uniquely trace the fractionation process backwards to a primary composition. Secondly, once a primary liquid is identified, it may be in fact a mixture of liquids equilibrated over a range of conditions, i.e., an aggregate primary liquid. Third, the sources for the range of primary liquids mixed to create an aggregate primary liquid may vary in composition, either as a result of preexisting heterogeneity in the mantle or as a result of the melting process itself if the liquids are mobile, e.g., during fractional fusion (an idealized end-member process in which melts are isolated instantaneously from the residue). Finally, the range of thermodynamic conditions (P, T) through which a mantle source will pass during the melting process and the melt productivity, $-(dF/dP)$, cannot be known *a priori* or measured directly in experiments.

The identification of primary basalt compositions occupied much of the attention of petrologists studying basaltic magmatism until the mid-1980's (BVSP, 1981). For

MORB, there were two prevailing schools of thought. One view held that the most magnesian observed MORB liquids were primary or only slightly fractionated basalts, which implies a depth of origin near 1 GPa (Frey et al., 1974; Langmuir et al., 1977; Presnall et al., 1979; Rhodes et al., 1979). The alternative view held that all MORBs were significantly fractionated from picritic primary magmas originating near 3 GPa (O'Hara, 1968; Stolper, 1980; Yoder, 1976). This debate was never resolved; rather its underlying assumption, that of a single primary magma with a well-defined last pressure of equilibration, collapsed. An evolving physical model of melting over a range of pressures (Ahern and Turcotte, 1979) and of melt segregation during melting (McKenzie, 1984; Waff and Bulau, 1979), together with evidence from trace elements of fractional melting (Johnson et al., 1990) and from short-lived radioisotope disequilibria of rapid extraction of liquids (Condomines et al., 1981; Newman et al., 1983) led to the understanding that primary MORBs are in fact aggregate liquids produced by mixing of melts extracted from a range of pressures. The power of polybaric melting models to explain variations in MORB chemistry and the correlation of chemical and physical aspects of the ridge system became clear with the landmark contribution of Klein and Langmuir (1987) and subsequent work (Brodholt and Batiza, 1989; Klein and Langmuir, 1989; Langmuir et al., 1992; Plank and Langmuir, 1992). Klein and Langmuir's insight depended on the idea of regional averaging, to account for imperfect mixing of the liquids which nominally make up the primary aggregate melt from a region, and on correction to a constant MgO content to account for low-pressure differentiation.

The fundamental observations of Klein and Langmuir (1987; 1989) and Langmuir et al. (1992) are reproduced in Figure 1 (figures redrawn from and original data sources listed in Langmuir et al., 1992). The concentrations of Na_2O and FeO* in MORB samples show three components of variation (Fig. 1a): the dominant control in each region is due to low-pressure fractional crystallization, which moves samples roughly parallel to the calculated liquid lines of descent shown. When the effects of fractionation

are eliminated by correcting along parallel or subparallel liquid lines of descent to 8.0% MgO (an arbitrary standard), or when only samples with 8.0 ± 0.25% MgO are considered, then on each local segment (e.g., Kane or FAMOUS/AMAR regions on the Mid-Atlantic Ridge) there remains a range of variability (shaded rectangles) inferred to represent variation in primary liquid compositions. Finally, when the fractionation-corrected compositions for all samples from a ridge segment (i.e., generally ~100 km regions) are averaged, there is variability among these regional averages (white circles). The regional averages for $Na_{8.0}$ and $Fe_{8.0}$ (i.e., Na_2O and FeO* corrected to 8.0% MgO to account for low-pressure fractionation) from worldwide ridge segments are negatively correlated (Fig. 1b); this is termed the "global trend" (Klein and Langmuir, 1987). Back-arc basins and hot-spot affected ridges also show a negative correlation of regional averages, offset from the trend for normal MORB. On slow-spreading ridges such as the Mid-Atlantic Ridge, however, the values of $Na_{8.0}$ and $Fe_{8.0}$ in fractionation-corrected but unaveraged individual samples from a single region are positively correlated (Fig. 1c); this aspect of variation, at high angle to the global trend, is labeled the "local trend" (Klein and Langmuir, 1989) or, more specifically, the "slow-spreading local trend" (Langmuir et al., 1992) since unaveraged samples from the fast-spreading East Pacific Rise show negative correlations.

The model derived by Langmuir and co-workers to explain these observations calls for long-wavelength temperature variations in the mantle, resulting in variations in the pressure at which the solidus is crossed and melting begins. Regions with low potential temperature (i.e., the temperature of the mantle beneath the onset of melting corrected to 1 bar along a metastable subsolidus adiabat, a monotonic function of entropy; see McKenzie and Bickle, 1988) start melting at relatively low pressure and reach relatively low extents of melting; regions with relatively high potential temperature begin melting at high pressure and reach relatively high extents of melting. This leads to a positive correlation in aggregate liquids between the mean extent of melting, the mean

pressure of melting, and the crustal thickness and hence an inverse correlation between Na_2O contents (interpreted as an indicator of extent of melting) and FeO contents (interpreted as an indicator of pressure) of regionally-averaged basalts corrected for fractionation and an inverse correlation between Na_2O and axial depth (which depends on both mantle temperature and crustal thickness). Models of this type have been constructed that quantitatively reproduce the global trend in $Na_{8.0}$ vs. $Fe_{8.0}$ (Langmuir et al., 1992).

Unmixed samples of liquid from this type of melting regime, however, would show the opposite sense of correlation in that within a local melting regime with a fixed potential temperature, the liquids extracted from the highest pressure are produced at the lowest extent of melting and the liquids extracted from the lowest pressures are produced at the highest extent of melting. It has proven difficult, however, to quantitatively model the local trend observations from either slow- or fast-spreading ridges with intracolumn variations of this type (Langmuir et al., 1992). The model assumes that conductive cooling from the surface does not penetrate deeply into the melting regime and that melting continues to a globally uniform shallow depth, perhaps the base of the crust. A competing viewpoint, advocated by Shen and Forsyth (1995) and Niu and Hékinian (1997a; 1997b), envisions large variations in the final pressure of melting caused by conductive cooling and relatively subdued variations in mantle temperature except perhaps at hotspots as well as a significant role for heterogeneity in mantle source compositions.

The interpretation of MORB chemistry when primary liquids are mixtures from an evolving source is significantly more difficult than the interpretation of one-stage partial melts equilibrated with residual minerals at a single P and T. Experimental constraints on partial melting of peridotite traditionally come in two forms. Batch melting experiments work with a constant total bulk composition and at fixed P and T. Such an experiment, ideally, yields the amounts and compositions of all the coexisting

phases, including a melt fraction (F) and a melt composition. Sandwich experiments, on the other hand, equilibrate basaltic liquid compositions at fixed P and T with suites of residual minerals to find multiple saturation points. These experiments show that a liquid is a possible mantle melt, but they do not control the bulk composition or yield a meaningful melt fraction. If we seek to use one or both types of experiments to interpret an aggregate primary liquid in terms of the ranges or mean values of P, T, F, and source composition from which it was produced, it is clearly necessary to combine the results of many such experiments. This idea has been pursued through the use of numerical parameterization of peridotite melting experiments by numerous authors (Kinzler, 1997; Kinzler and Grove, 1992a; Kinzler and Grove, 1992b; Klein and Langmuir, 1987; Langmuir et al., 1992; McKenzie and Bickle, 1988; McKenzie and Bickle, 1990; Niu and Batiza, 1991; Watson and McKenzie, 1991). These authors use a variety of datasets, independent variables, and fitted parameters; their results are broadly consistent (since they are mostly fit to the same data) and have contributed enormously to our understanding of MORB and other basaltic magmas.

The evolution of source composition and the thermodynamic path of upwelling mantle, however, constitute particular difficulties for the parameterization approach described above. Evidence of rapid melt extraction and highly depleted residues implies that melting approaches fractional fusion. Those parameterizations that simply fit liquid compositions as functions of P and T (Klein and Langmuir, 1987; McKenzie and Bickle, 1988; McKenzie and Bickle, 1990; Watson and McKenzie, 1991), with no consideration of the variation in source compositions among experiments or during fractional fusion, cannot account for the effects of fractional fusion on liquid composition. Other parameterizations that instead fit partition coefficients to batch melting data (Langmuir et al., 1992; Niu and Batiza, 1991) may account for the effects of fractional fusion to first order, but will be inaccurate to the extent that partition coefficients themselves vary with source composition, with solid mineral compositions, or with liquid components not

modeled. The approach of Kinzler and Grove (Kinzler, 1997; Kinzler and Grove, 1992a; Kinzler and Grove, 1992b) accounts in principle for the variation of source composition but depends on the assumption that the multiple saturation surfaces are linear in the chosen parameters. For calculation of aggregate MORB primary liquids, all these approaches are furthermore subject to two levels of additional uncertainty in that (1) the melt productivity and the *P-T* path are unknown even for batch melting as discussed in the following paragraph and (2) the effects of fractional fusion on productivity and *P-T* path are also unknown.

The size of upwelling regions beneath mid-ocean ridges and the typical rate of upwelling compared to the rate of thermal diffusion are such that to first approximation the upwelling is considered adiabatic and reversible (McKenzie, 1984; Verhoogen, 1965). Hence by the second law of thermodynamics, entropy (*S*) is a constant. *T*, on the other hand, is a dependent variable under these conditions. Worse, the *P-T* path of isentropic melting is dominated by the absorption of entropy of fusion on melting. Hence to find the *F-P-T* path followed by a parcel of mantle undergoing isentropic upwelling requires either a complete thermodynamic model which includes the entropy of all coexisting phases or a series of assumptions. Reasonable assumptions lead to roughly constant values for productivity of 1-2 %/kbar for batch melting (Hess, 1992; Klein and Langmuir, 1987; Langmuir et al., 1992; Turcotte and Ahern, 1978). The assumptions and methods used, however, are poorly suited to envisioning variations in the productivity, and indeed published estimates of its behavior during progressive decompression melting range from constant (Kinzler and Grove, 1992a; Klein and Langmuir, 1987; Niu and Batiza, 1991; Scott and Stevenson, 1989; Sparks and Parmentier, 1991; Turcotte and Ahern, 1978), to decreasing as melting proceeds (Langmuir et al., 1992; Longhi, 1992; McKenzie, 1984; McKenzie and Bickle, 1988; McKenzie and Bickle, 1990), to increasing as melting proceeds (Asimow et al., 1995a; Asimow et al., 1995b; Hirschmann et al., 1994), to complex and irregular (Iwamori et al., 1995; McKenzie, 1984; McKenzie and O'Nions,

1991; Miller et al., 1991). Until the work described in this thesis became available, the literature contained only first order guesses at the effect of fractional fusion on productivity (e.g., Langmuir et al., 1992).

Summary of this work

The subject of this thesis is an attempt to construct a forward model of adiabatic mantle melting that can account for variations in source composition during fractional melting and that includes a consistent entropy balance to account for thermodynamic constraints on the relationship between phase compositions, F, P, and T. More generally, I seek to avoid imposing any arbitrary functional forms on the variation of liquid composition, as any parameterized interpolation or extrapolation must do. My approach is to use thermodynamic models of minerals and silicate melts together with algorithms for seeking equilibrium by potential minimization. This method can in principle satisfy the above goals: no particular bulk composition is assumed in constructing the model; all thermodynamic variables are known simultaneously including entropy; and while activity-compositions relations of minerals and melts are fit to functional forms, these have far more theoretical justification than the fitting of more derived quantities like peridotite partial melt compositions. Throughout this work, I use the models and algorithms of the MELTS package by Ghiorso and Sack (Ghiorso, 1994; Ghiorso et al., 1994; Ghiorso and Sack, 1995; Sack and Ghiorso, 1989; Sack and Ghiorso, 1991b; Sack and Ghiorso, 1994a; Sack and Ghiorso, 1994b; Sack and Ghiorso, 1995). MELTS consists of activity-composition relations and equations of state for minerals, based on the self-consistent end-member mineral database of Berman (1988); endmember properties, a mixing model, and an equation of state for silicate melts; and algorithms for detecting phase saturation, minimizing thermodynamic potentials to find equilibrium, and detecting metastability and phase exsolution.

MELTS is intended as a general-purpose model for all silicate magmatic phenomena and is calibrated across a broad range of natural compositions from komatiite through evolved ultrapotassic liquids. Although in the course of this work I have discovered various shortcomings in the MELTS models for my purposes, I have refrained so far from attempting to improve or customize the model for peridotite melting. The suitability of MELTS for the purpose of modeling mantle melting at high pressure has been discussed in several papers published or in draft. Baker et al. (1995) and Hirschmann et al. (1994) demonstrated that trends of liquid composition against melt fraction or temperature from 1 GPa batch melting experiments matched well the corresponding trends from MELTS, although temperatures and several oxides (notably SiO_2 and MgO) show roughly constant offsets from the isobaric experimental values. Three manuscripts in preparation (Hirschmann et al., 1997b; Hirschmann et al., 1997c; Hirschmann et al., 1997a) comprehensively discuss the successes and failures of MELTS in reproducing isobaric melting data. I have confined myself in this thesis to discussion of polybaric and integrated melting calculations, which cannot be compared at this time to experiments but only to the predictions of other models based on parameterization of experiments or to actual basalt data from the field.

Although I have left the underlying models in their most general form, I have made several improvements to and customizations of the computational methods. The Appendices at the end of this thesis document the improvements and extensions I have made to the implementation of MELTS, mostly those needed to perform fractional melting calculations efficiently. In modeling perfect fractional fusion as a series of small increments, it is desirable to extract completely the melt phase at each increment, as even a small residual porosity can significantly change the behavior of the most incompatible elements. The original MELTS program, however, was intended only for magmatic processes and does not function without a liquid phase. Hence complete extraction of the liquid required starting over from a totally liquid initial guess, a very inefficient process

for computations near the solidus. Furthermore, these search processes are fraught with danger when a system crash lurks anytime the solidus is crossed. Hence I extended MELTS to function without a liquid, enabling fractional fusion calculations but at the same time enabling more general subsolidus modeling. Appendix 1 describes the algorithms needed for subsolidus calculations. Appendix 2 contains all the additional software I wrote to perform the calculations described in the body of the thesis.

Chapter 2, which has previously been published (Asimow et al., 1995a), demonstrates the unique perspective of a thermodynamic approach by examining the effect of phase transitions among the residual minerals during isentropic melting, notably the garnet peridotite to spinel peridotite transition and the spinel peridotite to plagioclase peridotite transition. Conventional petrologic wisdom held that these reactions led to extra melting beyond the usual 1-2 %/kbar (Presnall et al., 1979; Salters and Hart, 1989). However, both reactions have positive Clapeyron slope, and hence the lower pressure mineral assemblage has higher entropy. If the system is at constant total entropy, this means that melting must slow, stop, or even reverse during the phase transition. I prove this result in one-component and two-component systems and then show that MELTS predicts it for multicomponent peridotite. In the context of forward modeling of MORB petrogenesis, these effects are probably minor except for very cold mantle temperatures and issues related to the contribution of residual garnet and U-series disequilibria. However, chapter 2 provides a useful introduction to the methods used throughout the thesis and shows how they lead to insights that have been invisible to non-thermodynamic approaches.

Chapter 3, which is also previously published (Asimow et al., 1997), is a detailed discussion of the variations in isentropic melt productivity. This is the most important variable relating the geometry of the melting regime to the amount of melt produced. It is also one of the quantities that is hardest to infer from experimental data and hence poor knowledge of productivity is a major shortcoming (in my view) in all of the

aforementioned parameterizations of MORB melting. Again reasoning by analogy to suitable simple systems and phase diagrams, I show that the strongly increasing productivity predicted by MELTS for peridotite is the expected behavior for a broad class of petrologic systems (those where liquid is more compressible than solid and where during progressive melting the liquid and the solid become more alike in composition). An understanding of the origin and magnitude of the productivity variations predicted by MELTS is one essential ingredient in understanding how my predictions for aggregate primary MORB composition differ from other models.

Chapter 4 deals with some of the assumptions inherent in the isentropic fractional melting model by looking at sources of entropy production during melt migration and at some of the possible chemical interactions between migrating melts and upwelling mantle. There is a rich field of possible investigations in two-dimensional and three-dimensional time-dependent melt migration dynamics using MELTS to compute the amount and composition of phases as heat and matter are advected through the system, but at this stage I consider only one-dimensional steady-state results. It has previously been shown in the literature (Ribe, 1985; Richter, 1986; Spiegelman and Elliott, 1993) that for trace elements and for major elements in binary systems there is a close kinship between one-dimensional steady-state equilibrium porous flow and ordinary closed-system batch melting. I extend this result to major element equilibria in an arbitrary number of components, delineate the assumptions involved, and then use the kinship to simplify melt transport calculations.

Two types of one-dimensional steady-state calculations are performed, with different applications. One looks at focusing of melt into an equilibrium porous flow column, to simulate either a convergence of melt streamlines at the axis of a mid-ocean ridge (Spiegelman, 1996; Spiegelman and McKenzie, 1987) or, on a smaller scale, the concentration of melt flow into high-porosity channels by a fingering or shear instability (Aharonov et al., 1995; Kelemen et al., 1995a; Kelemen et al., 1995b; Stevenson, 1989).

This process, given a high enough melt flux, leads to the formation of dunite residues (Kelemen, 1990; Kelemen et al., 1992). Given the analogy to batch melting, an intuitive explanation for this behavior is proposed and the melt flux required is quantified. This approach is better than that of Kelemen for envisioning the evolution of residual composition and mineralogy as a function of pressure and melt flux, whereas Kelemen's assimilation calculations are better suited to examining the evolution of liquid compositions.

The second type of one-dimensional steady-state calculation performed in chapter 4 evaluates the energetic consequences of melt migration. McKenzie (1984) recognized that vertical motion of liquids leads to two source of entropy production: (1) liquids moving adiabatically will reach higher temperatures than the surrounding mantle so irreversible thermal equilibration between them will cool the liquid (possibly causing partial crystallization) and at the same time heat the mantle (and cause extra melting) and (2) separation of materials of different density in a gravity field liberates gravitational potential energy which in the inertia-less approximation is promptly dissipated by viscous flow in the liquid. I evaluate the magnitude of these two effects according to MELTS, with particular emphasis on the circumstances under which the liquid begins to crystallize and the thermal consequences of such crystallization. I still neglect perhaps the most important source of irreversible entropy production, namely dissipation due to shear and compaction of the solid residue, but proper evaluation of these effects calls for dynamical calculations accounting for the two-dimensional or three-dimensional flow field as well as the possibly complex viscosity structure of the solids (Hirth and Kohlstedt, 1996; Phipps Morgan, 1997).

Chapter 5 represents a first attempt to move beyond the basic issues of isentropic melt production considered so far and to construct a forward model of MORB genesis. One goal is to test the consequences of variations in solidus pressure (as envisioned by Klein and Langmuir, 1987) versus variations in final pressure of melting (as advocated by

Shen and Forsyth, 1995). Another contentious aspect of the debate about controls on MORB variability concerns the role of source heterogeneities. Langmuir et al. (1992) argue that heterogeneity does not control the global trend of Na-Fe covariation in regionally averaged compositions or the local trend in unaveraged compositions observed at slow-spreading ridges, but may explain the local trend on the fast-spreading East Pacific Rise. Shen and Forsyth (1995) maintain, based on K_2O/TiO_2 and $(Sm/Yb)_N$ arguments, that the global trend is mostly a manifestation of source heterogeneity. Niu and Hékinian (1997a; 1997b), while advocating a physical picture of ridge melting similar to that of Shen and Forsyth, dismiss the possibility that source heterogeneity controls major element trends such as CaO/Al_2O_3. Several issues related to the effect of source heterogeneity on isobaric melting trends according to MELTS are discussed in Hirschmann et al. (1997b). Chapter 5 extends this discussion to consider integrated polybaric melt compositions.

The melt compositions and melt fractions from adiabatic fractional melting calculations (and also batch melting calculations for comparison) are added together to simulate certain ideal melting regimes. I consider two end-member flows (illustrated schematically in Figure 2): simple plate-driven passive flow, in which case a melting region with essentially triangular cross section develops and off-axis streamlines turn horizontal and stop melting at depth; and buoyancy-driven active flow, in which case a rectangular cross section develops, and all streamlines that cross the solidus reach some shallow depth. The resulting primary liquid compositions and their mean pressures, mean extents of melting, and crustal thicknesses result from the convolution over the initial to final pressure range specified of melt productivity, the incremental melt compositions, and the mixing model representing the flow regime. In Figure 2, the small circles represent points from which melts are extracted to contribute to the primary aggregate liquid. In the case of batch melting, liquids are sampled only on the boundary of the melting regime; for fractional melting liquids are sampled throughout the interior

as well as on the boundary. Aggregate liquids compositions and weighted mean properties calculated at the points of melt extraction, i.e., mean pressure $\bar{P}$ and mean extent of melting F_V (Plank et al., 1995), from passive flow regimes can be obtained by integrating one-dimensional polybaric fractional melt compositions twice or batch melt compositions once. Aggregate liquids from active flow regimes are singly integrated fractional melts or, for batch melting, simply the melt composition present at the final depth of melting. The crustal thickness and the bulk extent of melting F_B, weighted by the residual melting column as it exits the melting regime, however, do not depend on whether melting is fractional or batch except to the extent that the productivity of melting is different in these two cases. Both the productivity and the incremental melt compositions predicted by MELTS are novel in many respects compared to previous forward models based on parameterization. Some of the novel aspects of melt compositions predicted by MELTS, particularly at low melt fraction, have been confirmed (or anticipated) by experimental work (Baker et al., 1995; Baker and Stolper, 1994; Kushiro, 1996) more recent than any of the parameterizations except Kinzler (1997). Hence a convergence between the results of the thermodynamic approach and the parameterization approach is likely in the future. I attempt to distinguish what aspects of the current MELTS forward model for aggregate primary MORB liquids are likely to be correct and which are likely to be artifacts of shortcomings of the model.

Taken together, these five chapters represent a unified body of work examining the current state of the art in thermodynamic modeling of adiabatic mantle melting at mid-ocean ridges. The consequences of entropy conservation for melt productivity (chapter 3) and the effect of phase transitions (chapter 2), as well as the magnitude of deviation from constant entropy due to melt migration (chapter 4), represent elementary constraints that all models of adiabatic melting ought to include. The particular model obtained with the current MELTS calibration (chapter 5) has several weaknesses but is the first to show the consequences of productivity variations, phase transitions, and novel

low melt fraction behavior. This is not the last word on MORB petrogenesis; there are clear areas for continued work on improving and extending the thermodynamic approach, for applying it to new types of calculations, and for using the insights gained to improve conventional direct parameterization methods.

Figure 1. Summary of observations concerning major element variations in mid-ocean ridge basalts. Figures are redrawn from Langmuir et al. (1992); data sources listed therein. (a) Raw data for Na_2O vs. MgO from two segments of the Mid-Atlantic Ridge, showing three components of variation: (1) control by fractional crystallization, parallel to the liquid lines of descent shown (Weaver and Langmuir, 1990), (2) local variability in compositions at constant MgO or corrected for fractionation to 8% MgO (shaded rectangles), and (3) differences between the averages of all samples from each region, corrected to 8% MgO (white circles). (b) The global trend in regional averages of fractionation-corrected quantities $Na_{8.0}$ and $Fe_{8.0}$. Filled squares are MORBs from normal ridge segments, diamonds are from back-arc basins, open squares are from hotspot-affected ridge segments, and crosses are from ridge segments immediately adjacent to hotspots. Fields show the range of normal MORB data and back-arc data. (c) Local trends in fractionation-corrected but unaveraged data from individual segments on slow-spreading ridges, shown superimposed on the global trend of normal MORBs (shaded field). Open squares, Atlantis II fracture zone (FZ) on the Southwest Indian Ridge; open circles, 26 °N to Atlantis FZ, Mid-Atlantic Ridge; filled squares, Atlantis FZ to Hayes FZ, Mid-Atlantic Ridge; filled triangles, Reykjanes Peninsula, Mid-Atlantic Ridge.

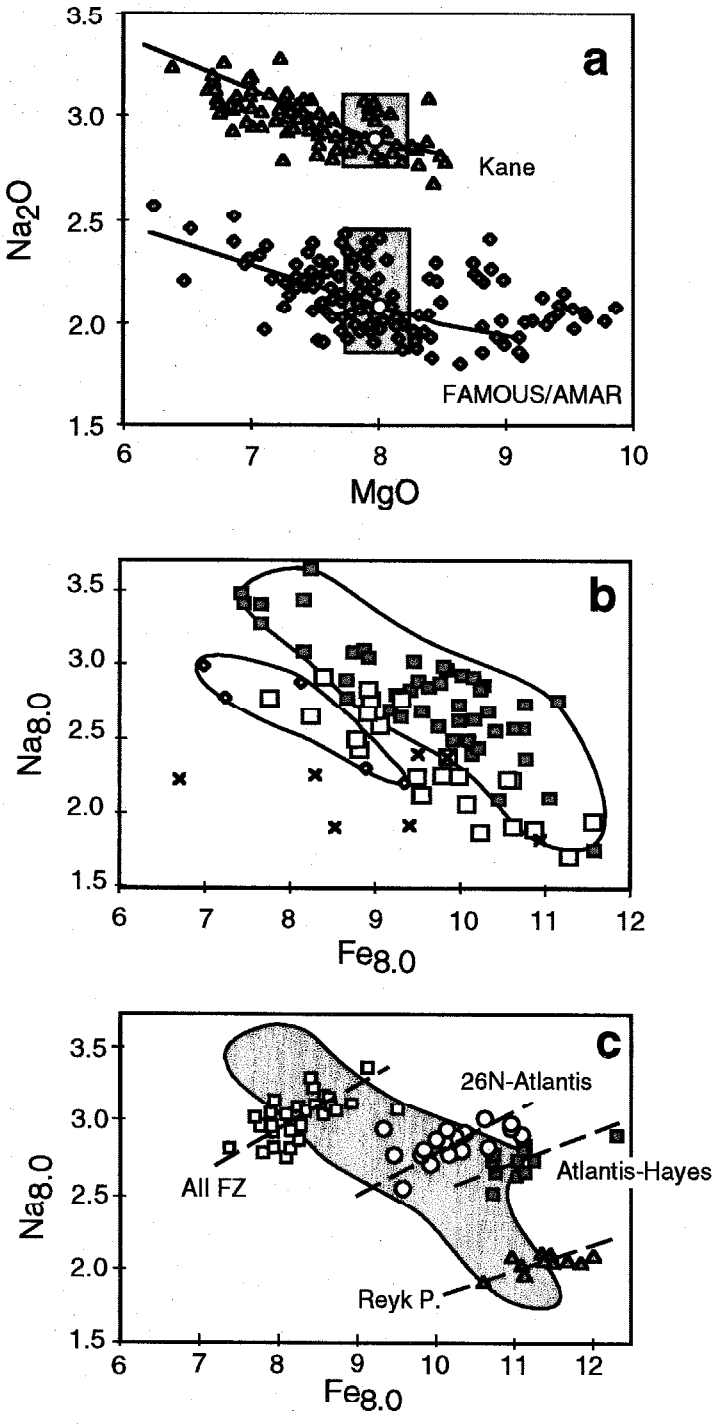

Chapter 1, Figure 1

Figure 2. Schematic illustration of end-member flow regimes and melt extraction models at mid-ocean ridges in two dimensions. The mantle is isothermal before melting begins (hence all streamlines intersect the solidus at the same depth). Passive flow (*left*) is driven by plate spreading without internal buoyancy, the result is corner flow with off-axis streamlines that turn at depth. Decompression melting continues only so long as material moves upwards, so the top of the melting regime is approximately triangular (the width of the triangle and the curvature of the upper edges can vary). Active flow (*right*) is dominated by the buoyancy of retained melt and depleted residue, resulting in secondary convection cells off-axis. In the extreme limit, all unclosed streamlines that cross the solidus are taken to reach a uniform shallow depth before turning aside. Points where increments of melt cease to be in equilibrium with the residue or are extracted into a rapid transport network are indicated by small open circles. Batch fusion (*top*) implies that liquids are sampled only from the points where streamlines exit the melting regime. Fractional fusion (*bottom*) implies that liquids are sampled instantaneously from throughout the melting regime. Z_c is the crustal thickness, which is less than or equal to Z_f, the final depth of melting (at pressure P_f), depending on the efficiency of conductive cooling from the surface (which can also flatten the top of passive-flow systems, not shown). Z_o is the initial depth of melting (at pressure P_o). The mean pressure $\bar{P}$ is the average pressure of last equilibration of the liquid, weighted by the flux of liquid from each pressure. The melt fraction axis on the right-hand side of each diagram is not to scale — the productivity $-(dF/dP)$ is not constant and differs for batch and fractional fusion — but in each regime the melt fraction increases upwards from 0 at the bottom to F_{max} at the top. F_V is a weighted mean of the extent of melting at which each increment of melt was extracted, whereas F_B is the bulk extent of melting of the whole system and can be measured along the boundary of the melting regime or in the residual mantle column that results (Plank et al., 1995). The crustal thickness is roughly proportional to the product of F_B and $(P_f - P_o)$.

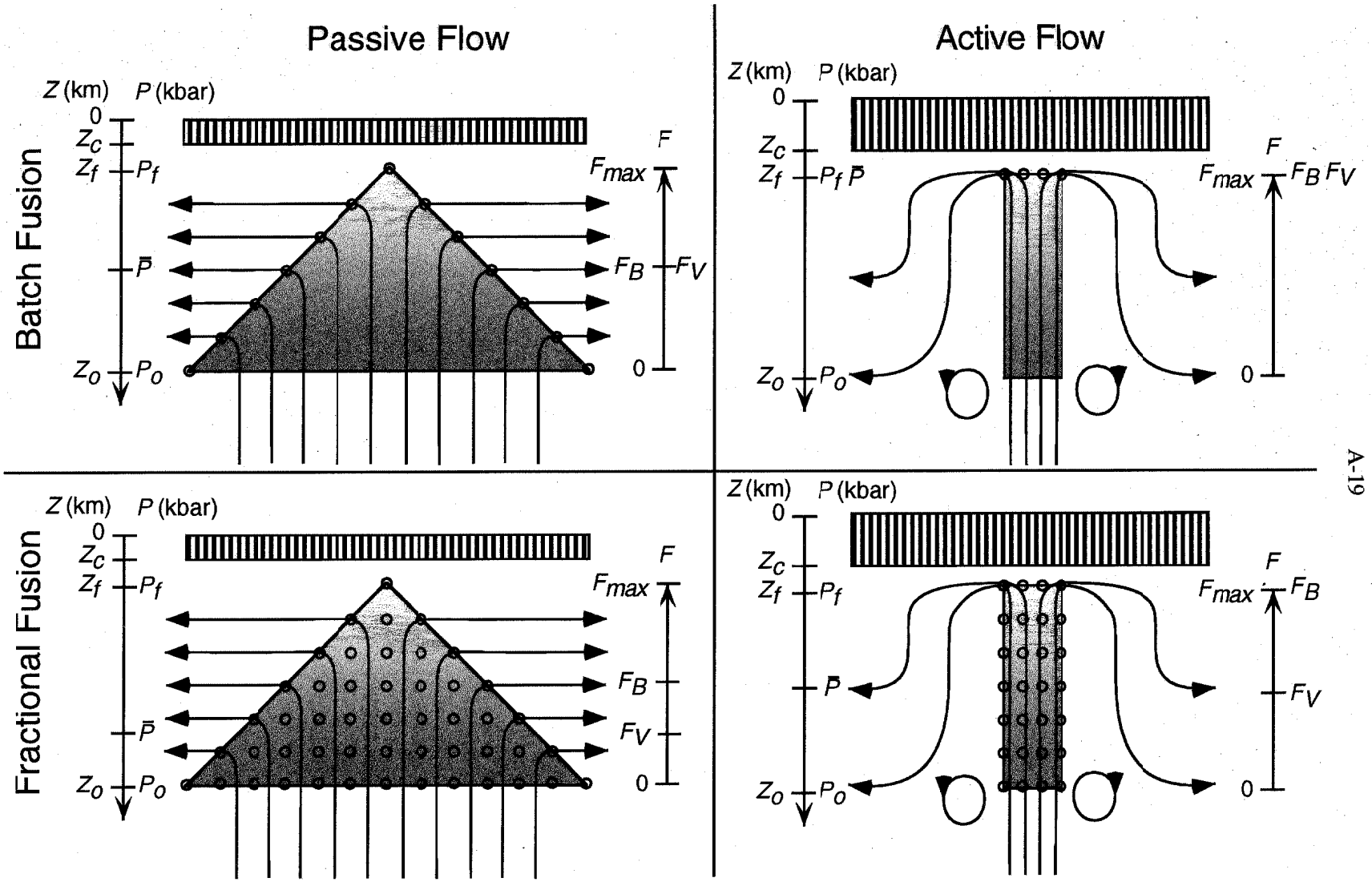

Chapter 1, Figure 2

Chapter 2. The effect of pressure-induced solid-solid phase transitions on decompression melting of the mantle

Abstract—Pressure-release melting of the earth's mantle is thought to be an isentropic process. The intersection of an isentropic melting path with a solid-state phase transition affecting the residual minerals must result in some change in melting rate unless the entropy of reaction of the phase transition is exactly zero. Furthermore, both phase transitions of primary interest for peridotite melting in the upper mantle (garnet-spinel peridotite and spinel-plagioclase peridotite) have positive Clapeyron slopes, and hence the lower-pressure assemblage has a higher molar entropy. Thus these phase transitions must retard isentropic, decompression melting or even lead to freezing. There cannot be enhanced melting accompanying such phase transitions, even if there is a "cusp" in the solidus.

Model calculations in simple one-component and two-component systems demonstrate the effect of solid-solid phase transformations on isentropic decompression melting. Conversion of low entropy solids to high entropy solids in the presence of liquid results in crystallization; the amount of crystallization depends on the relative molar entropies of the solid and liquid phases, on the modal abundance of the reacting solid phases, and on the proportion of liquid present when the reaction is initiated. The effect of solid-solid phase transitions on freezing is more pronounced for fractional fusion than for batch fusion in that melting ceases for a finite pressure interval at pressures below the invariant point where melt and the solids involved in the phase transition coexist.

Isentropic upwelling calculations for a model nine-component peridotite using a modified version of the MELTS potential minimization algorithm (Ghiorso et al., 1994; Ghiorso and Sack, 1995) verify that the simple-system behavior can be extended to multicomponent, mantle-like systems: melt production is suppressed during the

transformation from garnet-to-spinel peridotite and for batch melting there is freezing during the transformation from spinel-to-plagioclase peridotite; these effects are exaggerated during fractional fusion and barren zones are produced as in the simple systems. These results imply that melt production during upwelling may be highly non-uniform. Very slow melt production in the spinel-garnet transition region may enhance development of U-Th disequilibria. If significant contributions of melt from garnet peridotite are needed to account for the Lu-Hf systematics and REE patterns in MORB, melting must begin deep within the garnet stability zone. If plagioclase ever appears in the melting residue, this event is likely to end decompression melting despite further upwelling. Regions such as the garnet-spinel and spinel-plagioclase peridotite transitions may serve as nucleation sites for solitary waves in porous flow or regions of fracture formation and enhanced melt segregation.

Introduction

The rate at which melt is generated as peridotitic mantle ascends, the melt productivity, is one of the key parameters governing the dynamics and geochemistry of mantle melting. For example, melt productivity controls the maximum thickness of crust that can be generated at a given potential temperature by decompression melting beneath mid-ocean ridges and elsewhere (McKenzie and Bickle, 1988). Non-uniformities in productivity as a function of depth would lead to non-uniform contributions to melt chemistry from different depth ranges; this could strongly influence the major and trace element characteristics of mid-ocean ridge magmas, which are widely accepted to form from mixtures of melts generated by near-fractional fusion of ascending mantle over a significant depth range (Johnson et al., 1990; Langmuir et al., 1992). Since productivity and its pressure dependence strongly depend on source composition and the melting process (e.g., fractional vs. batch fusion), magma composition and quantity could depend in complex ways on these properties of source regions. Non-uniform melt productivity

with depth could also strongly influence the distributions of short-lived radioisotopes in magmas (Beattie, 1993a). Finally, heterogeneous melt production may have a critical impact on melt transport and segregation (Spiegelman, 1993a; Spiegelman, 1993b).

Despite its importance for understanding the production and composition of mantle-derived magmas, little is known about melt productivity. Because of the difficulty in simulating complex, polybaric melting by experiment, most estimates of melt productivity are based on simple thermodynamic energy balance considerations that yield approximately constant values of melt productivity during source ascent of 1-2 %/kbar (Hart, 1993; Hess, 1992; Langmuir et al., 1992; McKenzie and Bickle, 1988) These estimates do not, however, take into account quantitatively the many factors that can affect melt productivity. For example, Asimow et al. (1997) and Hirose and Kawamura (1994) have shown theoretically and experimentally that productivity is not constant and varies with degree of melting, and in particular is reduced during the early stages of fractional fusion. Other potentially important factors include the effects of bulk composition, complexities of the phase equilibria of natural peridotites (e.g., the influence of "cusps" on the solidus arising from solid-solid phase changes; Presnall *et al.*, 1979), differences in melt productivity during fractional vs. batch fusion (Hirose and Kawamura, 1994; Hirschmann et al., 1994; Langmuir et al., 1992), and variations with pressure related to the high compressibility of silicate melt relative to solids (Miller et al., 1991).

Solid-solid phase changes in mantle peridotite (e.g., garnet-to-spinel peridotite, spinel-to-plagioclase peridotite) lead to so-called "cusps" in the solidus and are frequently assumed to have a major influence on melt productivity. In particular, it has been stated that under conditions near a solidus cusp melting will be enhanced compared to that which occurs away from solid-solid phase transitions (Flower, 1981; Natland and Melson, 1980; Presnall, 1980; Presnall et al., 1979; Presnall and Hoover, 1987; Salters and Hart, 1989; Wyllie, 1988). Although the sign and magnitude of this effect require evaluation, it is simple to understand why solid-solid transitions must modify melt productivity. For

example, assume that *each increment* of decompression melting during ascent is isentropic, as vertical transport of the mantle under mid-ocean ridges and in plumes is rapid compared to heat conduction through solid mantle and because mantle melting takes place slowly enough that it can be considered reversible (note that melt separation is an irreversible process, so if melt segregation occurs then this assumption is only valid for each infinitesimal fraction of melt production). Near a cusp, the entropy balance includes a contribution from the entropy change of the solid-solid reaction in addition to the usual balance between entropy changes associated with melting and changes in temperature (T) and pressure (P). Maintenance of the adiabatic (isentropic) condition during solid-solid reactions will therefore affect the P-T path and the productivity of ascending mantle.

In this paper we evaluate the effects of solid-solid phase transitions on melt productivity during isentropic, pressure-release melting. We first develop the principles governing these effects with graphical constructions in one- and two-component systems. These constructions show clearly that solid-solid transitions with positive Clapeyron slopes (such as the plagioclase-spinel and spinel-garnet peridotite transitions) diminish rather than enhance melt productivity, and in fact, during batch melting, one- and two-component systems must freeze where the univariant curves intersect the solidus. For fractional fusion during upwelling, the decrease in melt productivity associated with such transitions is exaggerated relative to its effect during batch fusion, such that in the one- and two-component systems there is a pressure interval with no melt production associated with each solid-solid transition. To evaluate the quantitative importance of the insights gained from simple systems for the melting of complex natural peridotites, we perform thermodynamic calculations using the MELTS package (Ghiorso, 1994; Ghiorso et al., 1994; Ghiorso and Sack, 1995; Hirschmann et al., 1994), which combines a solution model for natural silicate liquids and activity-composition relations for many solid phases with algorithms for minimizing thermodynamic potential to find heterogeneous equilibrium. As suggested by simple system analysis, this modeling confirms that garnet-

spinel (gt-sp) and spinel-plagioclase (sp-pl) phase transitions are associated with reduced melting or even freezing. Finally, we discuss some possible implications of infertile (in the sense of low melt productivity) depth intervals associated with solid-solid phase transitions for several problems in mid-ocean ridge basalt (MORB) petrogenesis.

Simple systems

One-component systems

The independent thermodynamic variables during adiabatic upwelling of the mantle are pressure (P) and entropy (S), and the thermodynamic potential that reaches a minimum at equilibrium is the enthalpy. Thus, our evaluation of pressure-release melting will start with S-P diagrams for one component systems, as these give significant direct insights into the factors controlling melt productivity. Although P-T diagrams are not as useful for understanding isentropic, pressure-release melting, we also follow the paths of upwelling mantle on such plots because they are more familiar.

As our example of a solidus cusp for a one-component system in which the solid-solid phase transition has a positive Clapeyron slope, we consider SiO_2 in the vicinity of the invariant point where the phases quartz (Q), coesite (C), and liquid (L) coexist at equilibrium. The analysis will be perfectly general, but we find it easier to discuss real rather than hypothetical phases. Figure 1a is an S–P diagram for this system at pressures near the triple point. The pressure of the triple point is extrapolated from Boyd and England (1960). Note that quartz has a higher entropy and volume than coesite at all pressures (reflected in the positive Clapeyron slope of the quartz-coesite reaction); the liquid has higher entropy and volume than both solid phases. This diagram can be read like the familiar T-X diagrams in binary systems (i.e., regions with horizontal tie lines indicate the coexistence of two phases; in these fields the total entropy, the relative amounts of the two phases present, and the entropy of each phase at a given P are related geometrically by the lever rule). The slopes of the boundaries of the two phase regions are

related simply to thermodynamic quantities. For example, the slope of the liquid edge of the coesite + liquid two-phase region is given by

$$\left.\frac{dS_{liq}}{dP}\right|_{liq+coes} = \frac{Cp_{liq}}{T}\left.\frac{dT}{dP}\right|_{liq+coes} - V_{liq}\alpha_{liq} \qquad (1)$$

Two representative isotherms are also shown as dashed lines. Figure 1b shows a *P-T* diagram for the same system in the vicinity of the triple point.

An isentropic decompression path can be followed with a vertical line on a *S-P* diagram. The vertical line labeled A (heavy black dashed line) in Figure 1a illustrates a representative adiabat for batch melting. Consider progressive decompression along this adiabat. The system begins as coesite. At about 53 kbar, line A passes into the two-phase, coesite + liquid field, and melting begins. The amount of melt present at any pressure can be determined from the lever rule and to the degree that the coesite and liquid boundaries of the two-phase field are linear and parallel, the melt productivity (the increment of melt per pressure decrement) is approximately constant. For the example shown, the sample is about 40% liquid when it reaches the pressure of the triple point. From the lever rule, it is clear that when the pressure decreases from infinitesimally above the triple point to infinitesimally below it, the system must crystallize, such that it comprises quartz plus only ~20% liquid. Kinetic considerations aside, this freezing is accomplished at the unique pressure and temperature of the triple point. The system maintains constant entropy by balancing the increase in entropy required to convert coesite to quartz with a decrease in entropy resulting from the freezing of liquid to solid. Further decreases in pressure lead to continued melting with slowly increasing productivity (due to the curvature of the phase boundaries); the instantaneous productivity is initially lower than the productivity of isentropic coesite melting. The system will be completely molten at about 19 kbar (off the bottom of this figure), where line A crosses the boundary of the liquid field. Note that if quartz were prevented from forming and coesite continued to melt metastably at pressures lower than the triple point, melting would be complete at a higher pressure (~34 kbar) than that at which the system completes stable melting. Consequently, the pressure interval

required to achieve total melting is greater (and average melt productivity is lower) because of the coesite-quartz transition. Figure 1b illustrates this same isentropic path in *P-T* space.

Consider next the case of adiabat B (medium-weight black dashed line in Figures 1a and 1b). The system is initially colder than adiabat A, but still it begins melting in the coesite field. Rather than partially crystallizing at the triple point, however, it freezes completely to quartz + coesite. It then completes the coesite-quartz transition under subsolidus conditions, balancing the increase in entropy due to the phase change with a decrease in entropy due to significant cooling along the quartz + coesite univariant reaction. The system enters the quartz-only field after conversion of the coesite is complete, and then begins to melt again when it intersects the quartz + liquid two-phase field. Again, average melt productivity over the melting interval is significantly decreased by the intervention of the solid-solid phase transition.

The *S-P* diagram shown in Figure 1a is also useful for evaluating fractional fusion paths in which each increment of melting is accomplished isentropically, followed by extraction of the melt. Path C in Figure 1a describes such a process with a starting entropy for coesite similar to that for the batch fusion process illustrated by isentropic path A. The integrated melting process is not reversible or isentropic because melt leaves the system, carrying entropy with it, but we can still plot the entropy of the solid residue and model infinitesimal isentropic melting intervals. As coesite melts via this process, the entropy of the residue declines until the residual coesite reaches the *P* and *T* of the triple point and its entropy reaches that of coesite at the triple point. As pressure decreases below the triple point (43 kbar), no more melt is generated and the system converts isentropically from coesite to quartz, again cooling to balance the entropy increase due to the phase change. The system continues to decompress as quartz until it begins melting again at the intersection of the path with the quartz + liquid two-phase region at ~26 kbar. This example shows that melting ceases at the triple point during fractional fusion and that there is a finite pressure interval at pressures lower than the triple point over which the system

remains subsolidus before it once again begins to melt. All fractional paths of this type (i.e., that begin melting in the coesite field) will have the same melting gap of ~17 kbar. The *P-T* path corresponding to this process is labeled C in Figure 1b. While the residue is undergoing the quartz-coesite transition, its *P-T* path follows the quartz-coesite reaction and cools by ~100 K while decompressing only 1.5 kbar. This example shows that temperature gradients across transitions may become high enough that heat conduction will be significant. In this example, heat would flow upwards from the (hot) coesite field to the (cold) quartz field; this would spread out the effect of the transition asymmetrically, shutting off melting deeper than the triple point; this effect would, however, be unable to cause melting of quartz just shallower than the triple point.

Figures 1c and 1d demonstrate the effect of a solid-solid phase transition with a negative Clapeyron slope in a generic one-component system. Since the Clapeyron slope is negative, the high-pressure phase β must now have higher molar entropy than the low-pressure phase α. Path A demonstrates that an adiabat that begins melting as phase β undergoes an impulse of extra melting at the triple point followed by continued melting of phase α at lower productivity. Path B is subsolidus until the heat liberated by the phase transition leads to an increase in temperature along the α–β reaction to the triple point and it begins to melt at the cusp in the solidus. This behavior is only possible in a one-component system if the solid-solid reaction has a negative Clapeyron slope. Path C is a fractional melting path beginning at about the same entropy and pressure as path A. Along this path, β reacts to α+liquid at the triple point, at which point the entropy of the residue decreases from that of β to the (lower) entropy of α via extraction of the melt produced at the triple point. Melting of the low pressure phase α continues with further decompression, in contrast to the case of a solid-solid transition with a positive Clapeyron slope (Figures 1a,b) that has a barren zone over a pressure interval below the triple point.

Regardless of whether freezing (Figures 1a,b) or enhanced melting (Figures 1c,d) takes place at the triple point, the productivity of stable melting (batch or fractional)

averaged over the *entire* melting interval is lower than that for stable and metastable melting of the high-pressure phase starting at the same pressure. This decrease in average productivity, given roughly linear phase boundaries in the *S-P* planes shown in Figures 1a and 1c, is required from a consideration of the metastable extensions of the edges of the two-phase fields. Near the three phase coexistence, the curve for the liquid coexisting with the low-pressure phase must be steeper than that for the liquid coexisting with the high-pressure phase. Since the liquid is the same infinitesimally below and above the triple point, Cp_{liq}, V_{liq}, and α_{liq} are the same, and the change in slope of the liquid phase boundaries in *S-P* space reflects only the change in the Clapeyron slope in *T-P* space (see equation 1). The slopes of the solid edges of the two-phase fields reflect also the change in solid properties, but this is likely to be dominated by molar volume, which is larger for the low-pressure phase and thus contributes to the slope in the same sense as the change in Clapeyron slope. Although the curvature of the phase boundaries means that the instantaneous productivity of quartz melting increases away from the triple point, the difference in integrated productivity between metastable coesite melting and stable quartz melting is dominated by the inflection at the triple point. Hence, we can distinguish two effects of the phase transition in one-component systems: (1) There is a freezing or melting event at the triple point whose sign and magnitude depend on the entropy change and Clapeyron slope of the solid-state reaction, and (2) there is a change in average melt productivity, which is always lower for the low-pressure assemblage, whatever the entropy change of reaction.

The amount of freezing or melting that occurs on isentropic decompression through a triple point in a one-component system can be described precisely in terms of two variables. The first is the ratio $\Sigma \equiv \Delta S_{\alpha\beta}/\Delta S_{L\beta}$, where $\Delta S_{\alpha\beta} = S_\alpha - S_\beta$ (α is the low pressure solid phase and β is the high pressure phase) and $\Delta S_{L\beta} = S_L - S_\beta$ is the entropy of melting of the high-pressure phase. If $\Sigma > 0$, the solid-solid transition has a positive Clapeyron slope; if $\Sigma < 0$, the reaction has a negative *P-T* slope. The second variable is the

melt fraction present in equilibrium with the high-pressure phase as the system reaches the triple point, denoted $\phi_{L\beta}$. Σ is a function of material properties, whereas $\phi_{L\beta}$ depends on the starting conditions of the decompression (e.g., the potential temperature, McKenzie and Bickle, 1988) and the nature of the melting process (e.g., for perfect fractional melting, $\phi_{L\beta}$ is always zero). The entropy of the system before and after the transition is given by

$$S_{L\beta} = S_L - \phi_{L\beta}\Delta S_{L\beta} \quad (2)$$

$$S_{L\alpha} = S_L - \phi_{L\alpha}\Delta S_{L\alpha} \quad (3)$$

where $\phi_{L\alpha}$ is the melt fraction in equilibrium with the low-pressure phase at a pressure just below the triple point, and $\Delta S_{L\alpha} = S_L - S_\alpha$ is the entropy of melting of the low-pressure phase. For an isentropic process, $S_{L\beta} = S_{L\alpha}$, which leads to

$$\phi_{L\alpha} = \frac{\phi_{L\beta} - \Sigma}{1 - \Sigma} \quad (4)$$

Figure 2 shows $\phi_{L\beta}$ vs. $\phi_{L\alpha}$ for different values of Σ. If $\Sigma = 0$, the solid-solid phase transition is horizontal in *P-T* space (i.e., there is no entropy change associated with the solid-solid transition), and the melt fractions above and below the transition are equal. For any $\Sigma > 0$, $\phi_{L\alpha} < \phi_{L\beta}$, and furthermore if $\phi_{L\beta} < \Sigma$, then $\phi_{L\alpha} = 0$; i.e., the isentrope leaves the triple point along the subsolidus phase boundary rather than the low-pressure melting curve. If, on the other hand, $\Sigma < 0$, then $\phi_{L\alpha} > \phi_{L\beta}$ and an adiabat that intersects the solidus at the triple point will produce melt at the cusp up to melt fraction $\phi_{L\alpha} = \frac{\Sigma}{\Sigma\text{-}1}$. The quartz-coesite-liquid triple point discussed earlier has $\Sigma \sim 0.25$, although uncertainties in the thermodynamic parameters (e.g., thermal expansion of silica liquid) can lead to large errors in this value. Hence coesite rising along any isentrope that reaches the triple point with less than 25% melt will freeze completely; hotter isentropes will still have some liquid when the transition to quartz is complete.

Two-component systems

A simple graphical analysis is also possible in a two-component system and shows that the principles for a one component system can be generalized to higher order systems.

For discussion purposes we consider the region near the four-phase invariant point where jadeite (Jd), albite (Ab), quartz and liquid coexist in the system $NaAlSi_2O_6$-SiO_2 at about 33.5 kbar and 1385 °C. Figure 3a is a *P-T* projection in the vicinity of this invariant point (I_{Ab}) showing the associated univariant curves (Bell and Roseboom 1969). Figures 3b and 3c show *T-X* sections at pressures just above and below the invariant point. Jd + Q assemblages begin to melt at a eutectic at the pressure of Figure 3b. In contrast, Ab is stable at the solidus at the pressure of Figure 3c; it melts incongruently to Jd+L and Ab+Q melts eutectically. Figures 3d and 3e are *S-X* sections showing the same phase relations at the same two pressures. With decreasing pressure along the solidus, Ab first becomes stable at I_{Ab}. At the invariant point itself (not plotted), Ab is stable at a unique *S* and *X* which would plot inside the three-phase triangle Jd+L+Q, because the entropy of Ab must be less than that of liquid but greater than that of Jd + Q under these conditions (reflecting the positive Clapeyron slope of the Ab = Jd + Q reaction and its negative volume change). By contrast, if the solid-solid phase transition had a negative Clapeyron slope, the low-pressure phase would plot below the three-phase triangle formed by the liquid and the two high pressure solid phases; i.e., the four phases coexisting at the invariant point would form a quadrilateral in the *S-X* projection.

An isentropic batch melting process can be portrayed as a fixed point on *S-X* diagrams at successively lower pressures; the phase assemblages and proportions for different compositions and entropies can be readily determined as the two- and three-phase regions change position and orientation. Comparison of fixed points on the *S-X* diagrams shown in Figures 3d and 3e for pressures slightly above and below the intersection of the solidus with the Ab-Jd-Q transition allow evaluation of the effect of this solid-solid phase change on isentropic batch melting. Consider, for example, the *S-X* conditions represented by the stars in Figures 3d and 3e, leading to the *P-T* path marked by stars in Figure 3a. The topological change that accompanies the appearance of albite clearly requires an abrupt decrease in the amount of liquid at I_{Ab} (the position of a point in a three-phase triangle

gives the relative proportions of the three phases; the length of the perpendicular projection to the base opposite a phase divided by the corresponding altitude of the triangle is the fraction of that phase). This behavior is analogous to path A in the one-component system in Figure 1a. A more jadeite-rich initial composition starting at the same entropy (shown by asterisks in Figure 3) freezes completely at the invariant point; the corresponding *P-T* path is marked by asterisks in Figure 3e and leaves the solidus at the invariant point, moving down along the Ab+Jd+Q univariant curve until jadeite is consumed, and then crossing the divariant Ab+Q field until the solidus is intersected again at lower pressure. This behavior is analogous to path B in the one-component system in Figure 1a. The possible magnitude of the cooling effect and pressure interval affected can be estimated by considering an assemblage with the composition of albite that just begins batch melting in the Jd + Q field, at a pressure just above the invariant point. This system would freeze at the invariant point to Jd + Q with a trace of Ab. It would then cool by ~190 K while decompressing to 30 kbar along the Ab = Jd + Q univariant curve, at which point it would be pure albite and would leave the univariant curve. Along this isentrope, albite would not resume melting until about 5 kbar! If the composition varies slightly from albite, so that some quartz remains when jadeite is exhausted or some jadeite (which later converts to nepheline) remains when quartz is exhausted, then melting would resume in either case (with very low productivity) near 10 kbar.

We can also use *S-X* diagrams at successively lower pressures to evaluate the progress of fractional melting assuming infinitesimal isentropic melting increments. As an example, we consider a mixture of jadeite plus quartz with the same initial composition and entropy as the first batch isentrope described above (i.e., the star in Figure 3d). As the system moves down in pressure and intersects the solidus, an infinitesimal amount of melt is generated isentropically. The melt is then removed and the crystalline residue plots on the bottom edge of the Jd + Q + L three-phase triangle in *S-X* space. With continued decrements of pressure, the Jd + Q + L three-phase triangle moves downward in entropy,

more melt is generated in infinitesimal isentropic increments, and the residue always plots on the bottom edge of the Jd + Q + L triangle. The path of the residue is shown schematically by the curved polybaric arrow projected into Figure 3d; the curvature reflects movement of the eutectic liquid to lower SiO_2 and lower entropy as pressure decreases (Bell and Roseboom 1969). Because the residue from fractional fusion plots on the base of the Jd+L+Q triangle at a pressure infinitesimally above I_{Ab} (shaded circle in 3d), the topological change in *S-X* space that occurs at I_{Ab} requires that at an infinitesimally lower pressure such a residue must fall in the Jd+Ab+Q triangle; i.e., the residue remains solid through the transition at I_{Ab} and melting stops (shaded circle in 3e). The residue remains completely solid, first as Jd+Ab+Q and then as Ab+Q until the L+Ab+Q triangle has moved downwards sufficiently to reach the position of the residue at some lower pressure, at which point the Ab+Q begins to melt eutectically. The *P-T* path corresponding to this fractional fusion process is shown as the heavy, dashed sequence terminated by shaded circles in Figure 3a.

The magnitude of the freezing that takes place at the Jd-Ab-Q-L invariant point is illustrated in Figure 4. We consider only *S-X* combinations that plot inside the Jd-Q-L triangle at a pressure just above the invariant point. *S-X* combinations that plot in the Ab+Jd+Q triangle freeze completely. The lines in the Jd-Ab-L and Ab-Q-L triangles are contours showing the ratios of melt fractions infinitesimally above to those just below the transition. For example, a system with *S* and *X* that place it on the L-Q line will contain L and Q in the same proportions before and after the transition, whereas a system near the Ab-Q line will undergo nearly complete freezing. The ratio of melt fraction after to melt fraction before the transition is everywhere less than or equal to unity, reflecting the positive Clapeyron slope of the Ab-Jd-Q univariant curve. The examples shown in Figures 3 and 4 extend to two component systems the key principle deduced for one component systems: *a phase transition with a positive Clapeyron slope causes*

instantaneous freezing on batch adiabats at the invariant point, and creates a broad barren region along fractional melting paths.

Model Peridotite Calculations

The simple system exercises presented above demonstrate that the effects of phase transitions on melt production in upwelling mantle are sensitive to the stoichiometric details of both the melting and solid-solid reactions and to the entropies of these reactions. Analysis of the relationships between solid-solid phase transitions and melt production in the earth's mantle therefore requires a method for anticipating the detailed reaction stoichiometries of partially molten peridotite during upwelling as well as the entropies of the phases involved. In order to examine the degree to which our results from simple systems carry over to actual mantle melting, we present here the results of adiabatic batch and fractional melting calculations on eight- and nine-component model peridotite system using a modified version of the MELTS package (Ghiorso et al., 1994). MELTS combines: (1) a regular solution model for natural silicate liquids, calibrated with several thousand experimental statements of crystal-liquid equilibrium; (2) activity-composition relations for the relevant multicomponent solid phases, including cation ordering contributions; (3) a method for estimating phase saturation; (4) an algorithm for minimizing thermodynamic potentials to find equilibrium; and (5) an algorithm for examining solid phases for metastability and exsolution. Details of the solution models and algorithms have been published elsewhere (Ghiorso, 1994; Ghiorso and Sack, 1995; Hirschmann, 1991; Sack and Ghiorso, 1989; Sack and Ghiorso, 1991a; Sack and Ghiorso, 1991b; Sack and Ghiorso, 1994a; Sack and Ghiorso, 1994b; Sack and Ghiorso, 1995). The general character of the results of MELTS calculations of mantle melting are reported by Hirschmann *et al.* (1994); these calculations reproduce key aspects of the results of peridotite melting experiments (Baker et al., 1995; Baker and Stolper, 1994; Falloon et al., 1988; Hirose and Kawamura, 1994; Jaques and Green, 1980; Kinzler and Grove, 1992a),

giving us confidence in the insights we derive below from this analysis. Here we restrict our attention to the modeled effects of solid-solid phase transitions on decompression melting.

Although MELTS is equipped to consider 15 components, we chose to restrict our attention to the system SiO_2-TiO_2-Al_2O_3-Fe_2O_3-FeO-MgO-CaO-Na_2O±Cr_2O_3. Cr_2O_3 is problematic because the present version of the pyroxene solution model does not incorporate Cr_2O_3. The lack of Cr_2O_3-bearing pyroxene has the effect of overestimating the stability field of spinel (and therefore underestimating the stability fields of plagioclase and garnet) when Cr_2O_3 is present in the calculations (Webb and Wood, 1986). On the other hand, excluding Cr_2O_3 from all phases results in underestimates of the spinel stability field and produces unrealistically narrow transition regions. We therefore performed calculations both with and without Cr_2O_3. Neither provides an ideal prediction of the width, location, or stoichiometry of these mantle phase transitions, but these characteristics of the phase transitions in a model containing both Cr_2O_3-bearing spinel and Cr_2O_3-bearing pyroxenes probably lie between the two types of calculations shown here. Moreover, the effect of the phase transitions on melt production are quite similar in both sets of calculations. We excluded K_2O from the calculations because of its small abundance in upper mantle compositions and its strong incompatibility. During fractional melting, almost all K_2O would be removed during the first increment; during batch melting, the liquid K_2O concentration would be inconsequential except at very low melt fractions.

We used Hart and Zindler's (1986) estimate of the composition of fertile peridotite to set the initial bulk abundances of cations (Table 1). The proportions of Fe^{2+} and Fe^{3+} were chosen in the bulk composition to correspond to an fO_2 one log unit below the fayalite-magnetite-quartz buffer (QFM-1) at the pressure of initial melting (Kress and Carmichael, 1991). The calculations were done with a constant bulk oxygen content; i.e., oxygen fugacity was not externally buffered. We found, nevertheless, that the system

remained within one log unit of QFM-1 due to partial buffering by Fe^{3+}-bearing pyroxenes and spinel.

Given the bulk composition, we used two methods to calculate the equilibrium liquid-solid assemblage, including the composition and quantity of the liquid and of all solid phases (olivine, two pyroxenes, and garnet, spinel, or plagioclase). The first method used free energy minimization at a starting P and T above the solidus. Using the total entropy at this P and T as a reference, for batch melting calculations we moved to a lower P in constant pressure increments (which can be arbitrarily small) and searched for the T at which the equilibrium state had the same total entropy (within 10^{-8} J/K/g). This iterative procedure allowed us to approximate adiabatic paths. The second method minimized enthalpy at fixed entropy and P, thereby finding the adiabatic path directly. We compared the results; they were in all cases identical. Initial calculations considered the whole range of solid phases incorporated in the MELTS package (Ghiorso et al., 1994), but thousands of calculations with this peridotitic bulk composition (and its residue from fractional melting) indicated that in all cases only olivine, clino- and orthopyroxene, spinel, plagioclase, and/or garnet were predicted to be stable, so we saved computation time by turning off checks for other solid phases (melilite, nepheline, oxides, titanite, etc.) and exsolutions (high-Ca olivine, jadeitic pyroxene, etc.) that had never been encountered.

Both the above methods were extended to near-fractional melting calculations. First, we implemented a double search for the P and T where free energy minimization showed that the system was both on the reference adiabat and had a fixed incremental melt fraction (we have successfully performed the calculation with melt increments as low as 0.025%). In the second method, only a search in P along the adiabat determined by enthalpy minimization was needed to find the desired melt fraction. The melt was then removed from the system, taking some entropy with it. The entropy and composition of the residue were used as the reference for the next step. The near-fractional calculations were made much more efficient by a further modification of the MELTS algorithm that

allows subsolidus initial guesses, liquid-absent equilibrium calculations, and computation of the chemical affinity of the liquid with respect to subsolidus assemblages.

Typical results at the spinel-plagioclase and garnet-spinel peridotite transitions are shown in Figures 5 and 6, respectively. Figures 5a-d show results for the Cr_2O_3-absent composition; Figures 5e-h show corresponding results for the Cr_2O_3-bearing composition. Figure 5a shows P vs. T for a typical batch adiabat and a near-fractional melting path starting at the same P and T conditions; the paths diverge by no more than ~10 degrees, even after 10-15 kbar of decompression (Hirschmann et al., 1994). For both processes, the ascending peridotite achieves plagioclase saturation at ~6 kbar. These paths intersect the solidus at about 15 kbar; i.e., they would represent relatively cool mantle (e.g., the Cayman Trough, Klein and Langmuir, 1987). Only on such cool adiabats is the degree of melting small enough that plagioclase is still predicted to be stable in the residual assemblage at low pressure (i.e., on hotter adiabats, there is sufficient melting at greater depth that the constituent components of plagioclase are largely in the liquid by the time that the pressures at which plagioclase is nominally stable are reached). The appearance of plagioclase in the residue and the disappearance of spinel are shown as functions of pressure for the batch and fractional melting paths in Figure 5b. Figure 5c plots for the same melting paths, F, the total degree of melting experienced by the residue, vs. P. Productivity is equal to the slope of lines on this plot and is seen more clearly in the plot of dF/dP vs. P in Figure 5d.

The most striking feature of the calculations shown in Figure 5 is that when plagioclase appears, the system either undergoes freezing or ceases melting, in accord with the predictions based on our analysis of simple systems. During batch "melting" in this example, the amount of melt present decreases for nearly 500 bars, and does not regain its previous peak melt fraction for another 1 kbar (Figure 5c, solid curve). During fractional melting, melting stops at the appearance of feldspar and does not resume for 2 kbar. Note that the freezing along the batch adiabat causes observable heating of the adiabatic path in

Figure 5a. The upturn in productivity after the transition is, however, not related to the appearance of plagioclase. We demonstrated this by running this calculation with plagioclase suppressed (i.e., metastable melting of the spinel lherzolite assemblage; Figure 5d); even under these conditions we observed a similar steady increase in productivity, although without the gap resulting from the transition. The low productivity at low melt fraction (e.g. $P \sim 15$ kbar in Figure 5c) in this calculation is caused by rapid changes in melt composition (especially dilution of alkalis); once a large fraction of melt is present the liquid composition changes more slowly and this effect diminishes (Asimow et al., 1997; Hirschmann et al., 1997b; Hirschmann et al., 1997c; Hirschmann et al., 1997a). The metastable spinel lherzolite melting curve in Figure 5d also demonstrates that, at least in this case, stable melting of the plagioclase lherzolite at a given pressure below the transition is less fertile than metastable melting of the high-pressure mineral assemblage; this is consistent with the behavior observed in one-component systems and discussed above, where stable quartz melting is less fertile than metastable coesite melting in the stability field of quartz.

The Cr_2O_3-bearing calculations at the spinel-plagioclase transition are shown in Figures 5e-h. The appearance of plagioclase here occurs at ~5 kbar rather than 6 kbar, and spinel is always present. Nevertheless, during batch upwelling freezing is observed at the appearance of plagioclase (Figure 5g), and although the freezing is not as sudden as in the Cr_2O_3-absent case, it persists over a slightly wider interval (Figure 5h). The barren zone at the transition during fractional melting has roughly the same width in both compositions.

The calculated garnet-spinel peridotite transition (Figure 6) appears over a much wider range of potential temperature than the spinel-plagioclase peridotite transition; we show calculated paths that intersect the solidus at 28.5 kbar and 45 kbar in the Cr_2O_3-absent case (Figures 6a-d) and at 35 kbar and 50 kbar in the Cr_2O_3-bearing case (Figures 6e-h), with a batch and a fractional path for each. As was shown in Figure 5a for lower pressures, the *P-T* paths of batch and fractional processes are not greatly different (Figures

6a,e). Two potential temperatures are shown to demonstrate that the effects do not depend qualitatively on the amount of melt present or the extent of depletion of the residue at the transition. The location of the transition along each path is shown by the modal abundance of spinel and garnet, plotted in Figures 6b and 6f. Although the inflections in slope at the transition in P-T space (Figures 6a,e) and in the F vs. P plots (Figures 6c,f) are small, it is clear from plots of dF/dP vs. P in Figures 6d and 6h that the phase transition region represents a low-fertility zone. In the Cr_2O_3-absent case, where the transition from garnet to spinel peridotite is quite sharp, the transition interval produces virtually no melt, and the system may experience a very small amount of freezing. Fractional and batch paths produce similar results; the productivity gap is marginally wider along fractional paths. The metastable melting of garnet lherzolite in the stability field of spinel lherzolite is shown for the hotter batch melting path in Figure 6d; as described above in the one-component system and for the spinel-plagioclase transition, metastable melting of the high-pressure assemblage yields higher productivity than stable melting of the low-pressure assemblage. On the other hand, the colder batch adiabat in Figure 6d does not obey this rule. This shows that it may not be a general principle. In Cr_2O_3-bearing calculations, spinel is present throughout the pressure interval studied. The transition interval in each calculation therefore stretches from the solidus intersection to the exhaustion of garnet. In every Cr_2O_3-bearing case (hot, cold, batch, fractional), although melt is produced in the transition interval, there is a sudden increase in melt productivity (by up to a factor of two) at the exhaustion of garnet (Figure 6h).

The garnet-spinel transition has a more muted effect on the melting process than the spinel-plagioclase transition in part because the modal weight fraction of spinel being made is smaller in the higher pressure case than the weight fraction of plagioclase being made in the low-pressure case. Since aluminous phases are always being consumed by melting, it is the growth of the low-pressure (high-entropy) phase rather than the exhaustion of the high-pressure phase that leads to the extraordinary entropy sink at these transitions. Spinel

is richer in Al_2O_3 than garnet or plagioclase and hence its modal abundance in its stability field is smaller for the same bulk composition. Furthermore the solubility of Al_2O_3 in pyroxene is much smaller at the pressure and temperature of the spinel-plagioclase transition than at the pressure of the garnet-spinel transition near the solidus, which leaves more Al_2O_3 to be taken up by plagioclase when it appears than by spinel when it appears. The magnitude of the effects on melt productivity and the width of the transition both increase with the bulk Al_2O_3 concentration in the peridotite.

We emphasize that only certain aspects of these calculations should be interpreted as quantitative predictions about the mantle. The calculated pressures of phase boundaries involving spinel are very sensitive to variations in the concentration of Cr_2O_3. For example, if Cr_2O_3 is present in the calculations, the stability of spinel is overestimated because Cr-pyroxenes are not included in the pyroxene solution models. Consequently, spinel is a residual phase from 1 bar to at least 50 kbar and up to large extents of melting, and the garnet-spinel transition occurs over too large a range of pressure. If Cr_2O_3 is absent, on the other hand, then the stability field of spinel is underestimated. Neither choice at present yields reliable predictions of the pressures at which the solid-solid phase transitions are predicted to occur. We have shown, however, that both choices produce phase transitions with similar melt production behavior. The pressures at which plagioclase becomes stable in both the Cr_2O_3-bearing and Cr_2O_3-free cases are 2-4 kbar lower than experimental values (Hess, 1992); this is due to a systematic under-prediction in the silica activity that MELTS estimates for the coexistence of orthopyroxene and olivine at elevated pressures. In addition, the width of each solid-solid transition and the appearance of actual freezing at the garnet-spinel transition (as opposed to merely reduced productivity) are sensitive to Al_2O_3 content. The fertile mantle composition used in the calculations shown in Figures 5 and 6 has ~4% Al_2O_3. For this composition, the modal abundance of spinel is about 1% at the completion of the garnet-spinel transition, this transition is only 250 bars wide (in the Cr_2O_3-absent case), and dF/dP drops to zero in the transition interval

for a wide range of conditions but only becomes negative for a few tens of bars and only in a narrow range of potential temperatures. In contrast, with 8% Al_2O_3, the modal abundances of the aluminous phases are doubled, the garnet-spinel transition widens to 2 kbar (without Cr_2O_3) and freezing is clearly present (i.e., $dF/dP < 0$ near garnet-out). On the other hand, in our calculations every composition that allowed plagioclase to appear in the residue caused freezing at the spinel-plagioclase transition. The key point is that we know of no bulk composition or melting process for which there is enhanced melting at the sp-pl and gt-sp phase transitions, and every case we have examined leads instead to freezing or considerably decreased melt productivity.

The exact magnitude of the effect of solid-solid phase transitions on productivity is difficult to predict for mantle compositions because of uncertainty in thermodynamic parameters. Although MELTS makes internally consistent estimates of all these parameters that are compatible with available experimental data, the entropy of fusion of peridotite is uncertain (Langmuir et al., 1992), as are the entropies of individual solid phases at elevated temperatures and pressures (Berman, 1988). In addition, although the sign of the entropy change of each solid-solid phase transition is known from the Clapeyron slope, these reactions involve multiple phases with solid-solution and exchanges of several components among the participating phases; hence, the magnitude of the entropy change is poorly known. In the presence of melt, balancing the relative contributions of the entropy of the melting reaction against the entropy of the solid-solid reactions is yet more difficult, because partitioning of species among liquid and solids is variable. The flows of entropy among solid phases and the liquid in a sample Cr_2O_3-absent calculation are shown in Figure 7. For the hotter of the Cr_2O_3-absent batch adiabats across the garnet-spinel transition shown in Figure 6, Figure 7a shows the pressure derivative of the mass of each phase as a function of pressure; these values can be thought of as the sum of the stoichiometric coefficients of all the reactions occuring. In the phase transition region, the reaction (where phase compositions are all on a single-oxygen basis) is approximately 3gt

+ ol = 3opx + sp. Figure 7b shows the corresponding pressure derivatives of the entropy content of the phases. These figures demonstrate that the entropy flows among the solids dominate the phase transition region, overwhelming the gradual transfer of entropy into the liquid that characterizes ordinary adiabatic melting and thereby explaining why these solid-solid transitions might have dramatic effects on the progress of decompression melting. It is also clear from this figure that, for a given bulk composition and modal abundance of aluminous minerals, a thicker transition region will have smaller solid stoichiometric coefficients (per unit pressure) and hence a more muted effect on productivity. The most important point of this figure, however, is that the specific entropies of the solid phases are all similar, so the net entropy of reaction is a small number obtained by subtracting two large numbers (entropy of products and entropy of reactants); hence, as described above, its magnitude is sensitively dependent on details of the solids and their entropies.

Discussion

Melting at "cusps" on the solidus

Given the preceding exploration of the effects of solid-solid phase transitions on melting in simple and complex systems, it is now possible to examine the role of so-called "cusps" in melting of mantle peridotite. In this discussion, we use the word "cusp" in the context of multi-component systems to refer to a region of the solidus where two aluminous phases coexist in the residue, without implying that the solidus has a single sharp point where dT/dP is discontinuous. As first described by Presnall *et al.* (1979), cusps have been inferred to have two important roles in mantle melting: (1) because they are low temperature regions of the solidus, it has been suggested that melting is likely to begin at cusps; and (2) because of an envisioned thermal buffering effect, cusps were suggested to "stabilize" the geotherm so that pressure of melt generation remains fixed. The idea that there is extra melting at a cusp originated from this hypothesized thermal

buffering, which Presnall *et al.* (1979) proposed as part of a model in which MORBs are generated over a narrow pressure interval.

Melting in the MORB source region is now generally thought to be a polybaric process in which the initial depth of melting varies spatially and temporally (e.g., Klein and Langmuir, 1987; McKenzie and Bickle, 1988), but the idea of extra melting at cusps has persisted. For example, Salters and Hart (1989) argued that Hf isotope systematics require that 15–30% of melting in the MORB source region occurs with garnet in the residue. Such high proportions of melt generated at depths sufficient to stabilize garnet are difficult to reconcile with the maximum degrees of partial melting interpreted from major element data in MORB (e.g., Klein and Langmuir, 1987), so Salters and Hart suggested that a relatively large amount of melting may be generated at the cusp in the solidus related to the garnet-spinel transition.

Consideration of the energetic role of solid-solid phase transitions on adiabatic melt production indicates that there is no reason to expect that melting should begin at cusps or that cusps are the loci of enhanced melting. In contrast, cusps should be the sites of diminished melt production or freezing and there are no thermal buffering effects that will constrain a geotherm to remain at a cusp or generate extra melt there. In cases where the adiabatic gradient happens to intersect the peridotite solidus near a cusp, one of two things may happen, depending on the stoichiometries and entropy budgets of the solid solid and solid-liquid reactions. If these reactions have characteristics similar to that of the spinel-plagioclase transition as modeled by MELTS, then little or no melt will form at the cusp. The entropy required to convert spinel to plagioclase will cause the temperature to be deflected downwards from the solidus and the adiabat will remain sub-solidus until some pressure below the transition. Alternatively, if these reactions have characteristics closer to those of the garnet-spinel transition as modeled by MELTS, then a small amount of melt could form at the cusp, but significant melting will not commence until the pressure where garnet is completely consumed (i.e., a pressure lower than that of the cusp) is reached.

Most mantle adiabats will not intersect the peridotite solidus precisely at the cusp. In the view of Presnall *et al.* (1979), adiabats that intersect the solidus at some pressure above the spinel-plagioclase cusp may be expected to migrate down to the cusp, owing to the cooling effects of melt formation. More recent descriptions of mantle melting relate the pressure of initial melting to the potential temperature of the mantle below the melting region (e.g., McKenzie and Bickle, 1988). The adiabat will not migrate down to the cusp owing to melting reactions because new unmelted material will continue to upwell and begin to melt at the intersection between the solidus and that solid adiabat. Therefore, solid-solid phase transitions are likely to be encountered above the solidus, where some melt has already been formed (or in the case of fractional melting, from mantle that has already had some melt extracted).

Geochemical and geodynamic consequences of solid-solid phase transitions during MORB melting

Most petrologic models of adiabatic mantle upwelling under mid-ocean ridges assume constant or nearly constant productivity per increment of upwelling (Kinzler and Grove, 1992b; Klein and Langmuir, 1987; Langmuir et al., 1992; McKenzie and Bickle, 1988), although some allow productivity to vary independent of thermodynamic considerations (Brodie et al., 1994; McKenzie and O'Nions, 1991; White et al., 1992). If such assumptions are incorrect, estimates of the average degree of melting or the average depth of melting of MORB and of basalts from other environments (Albarède, 1992; Klein and Langmuir, 1987; Langmuir et al., 1992; McKenzie and Bickle, 1988) may require substantial revision. Both thermodynamic calculations (Hirschmann et al., 1994) and experiments (Hirose and Kawamura, 1994) indicate that productivity during fractional melting is indeed not constant, and in particular that productivity is substantially smaller during the first increments of melting than during later increments. The additional consideration developed in this paper that conversion of garnet to spinel peridotite and of spinel to plagioclase peridotite reduces or shuts off melting for intervals up to 10 km

(Nickel, 1986) suggests that the distribution of melt generation in the MORB source region is likely to be quite heterogeneous and that average degrees or depths of melting inferred from models that assume nearly constant melt productivities should be interpreted cautiously. In this section, we consider some geochemical and geodynamic consequences of these transitions. We emphasize the possible implications of a non-uniform distribution of melt productivity with depth for observed major and minor element compositions and isotopic compositions of MORBs, and we point out how low-productivity or barren zones associated with solid-solid transitions may have implications for several major problems in MORB petrogenesis.

The garnet-spinel peridotite transition and the garnet signature in MORB: There are two qualitatively different lines of evidence for residual garnet in MORB petrogenesis. U-Th systematics are set at the very onset of melting, and therefore only require that MORB incorporate a very small increment of garnet-equilibrated melt (McKenzie, 1985). In contrast, evidence for residual garnet based on Hf isotopes (Salters and Hart, 1989) and on REE in basalts (Beattie, 1993b; McKenzie and O'Nions, 1991) or in abyssal peridotites (Johnson et al., 1990) have been interpreted as requiring that MORB are mixtures of contributions from melting of spinel-bearing and garnet-bearing peridotite where a significant fraction of melt must be derived from garnet-bearing rock. The analysis presented above, however, indicates that melting in the garnet-spinel transition region is relatively unproductive. If these interpretations of the REE and Hf isotopes are correct, and MORBs do contain a significant quantity of melt from melting of garnet peridotite, this would require that melting begins significantly deeper than the depth range of the spinel-garnet transition. Experiments indicate that garnet is stable on the solidus of fertile peridotite beginning at a depth of 80±10 km (e.g., Green and Ringwood, 1970; Ito and Kennedy, 1967; Takahashi, 1986). The interval over which garnet and spinel coexist along the solidus is not well established and depends on compositional factors such as whole-

rock Cr content, but may be in the neighborhood of 10 km (e.g., Nickel, 1986). Consequently, if Hf isotope and REE distributions in MORB require significant melting of garnet peridotite, then the potentially unproductive character of the spinel-garnet transition region could require that melting begin deeper than 90 km. However, such great depths of initial melting are difficult to reconcile with prevailing ideas about the average depth and amount of melting in the MORB source region (Albarède, 1992; Kinzler and Grove, 1992b; Klein and Langmuir, 1987; Langmuir et al., 1992). One resolution of this dilemma, suggested by Hirschmann and Stolper (1995), is that the so-called garnet signature is contributed to MORB by partial melts of garnet *pyroxenites*, which are stable to significantly lower pressures than garnet *peridotites*. This would produce an imprint of residual garnet in MORBs without requiring significant melting at the great depths that would be required if this signature were contributed by extensive melting of garnet peridotites.

U-series disequilibria in MORB: Because garnet is the only major phase in peridotite that preferentially incorporates U relative to Th, observed ^{238}U-^{230}Th disequilibrium in MORB (e.g., Reinitz and Turekian, 1989; Newman, 1983; Condomines *et al.*, 1981; Ben Othman and Allègre, 1990) appear to require that melting begins in the presence of garnet. A key feature of the U-Th system is that, because U and Th are both very incompatible in all mantle minerals, $(^{230}Th)/(^{238}U)$ of MORB is influenced largely by the conditions prevailing at the onset of melting, as melt produced after the first increments of melting is largely devoid of U or Th. Quantitative evaluation of U series disequilibrium evolution during peridotite melting requires that the initial rate of melting be low, which in turn requires either that the rate of upwelling or the melt production per increment of upwelling (productivity) be very small during the initial stages of melting in the MORB source region (e.g., Beattie, 1993a; Beattie, 1993b; Iwamori, 1994; McKenzie, 1985; Spiegelman and Elliott, 1993). Because previous models have assumed constant melt productivities of

approximately 0.4%/km, they have had to postulate extremely low upwelling rates. For example, the models of Beattie (1993a) and Iwamori (1994) only generate $(^{230}Th)/(^{238}U)$ activity ratios comparable to typical MORB (1.2 ; Ben Othman and Allegre, 1990; Condomines et al., 1981; Newman et al., 1983; Reinitz and Turekian, 1989) if upwelling rates do not exceed approximately 1 cm/yr or 0.3 cm/yr, respectively. Such rates are less than the half-spreading rates of all but the slowest spreading ridges, and can be justified only if upwelling beneath ridges is distributed over tens to thousands of kilometers (Iwamori, 1994). The model of Spiegelman and Elliot (1993) incorporates chromatographic effects and can produce $(^{230}Th)/(^{238}U)$ similar to typical MORB at upwelling rates of up to 3 cm/yr, but only if melt upwells via porous flow over great distances. Some MORB have $(^{230}Th)/(^{238}U)$ between 1.4 and 1.8, however (Ben Othman and Allegre, 1990; Condomines et al., 1981; Newman et al., 1983; Reinitz and Turekian, 1989), and no model presented thus far is capable of generating such large degrees of U series disequilibrium for upwelling rates greater than 0.2-0.3 cm/yr.

Our analysis of the effects of solid-solid phase transitions on melt productivity suggests observed deviations of $(^{230}Th)/(^{238}U)$ from the equiline could be explained by low melt productivities at the onset of melting in the garnet-spinel transition zone rather than by extremely low upwelling rates that have been required by models (e.g., Beattie, 1993a; Iwamori, 1994; Spiegelman and Elliott, 1993) that assumed constant, relatively high melt productivities of ~0.4%/km. If melting begins in the garnet-spinel transition region and if the melt productivity in that region is similar to that modeled in the MELTS calculations, then observed U-series disequilibria may be created at reasonable upwelling velocities. For example, for a porosity of 0.1% and a melt productivity of 0.1%/km , the Beattie model predicts $(^{230}Th)/(^{238}U)$ of 1.2 at upwelling rates of 4 cm/yr and 1.5 at 1 cm/yr. At this porosity, $(^{230}Th)/(^{238}U)$ equal to 1.2 is reached even for upwelling rates of 10 cm/yr if the initial melt productivity is 0.04%/km, a rate that is not inconceivable in the garnet-spinel transition zone. For this melting rate, the largest degrees of $(^{230}Th)/(^{238}U)$

disequilibria recorded for MORB (1.4-1.8) could be generated at upwelling rates of 2-3 cm/yr. We emphasize that such extremely low melting rates would affect $(^{230}Th)/(^{238}U)$ only if melting *begins* in the garnet/spinel transition zone (a common feature of melt distributions inferred from REE inversion, McKenzie and O'Nions, 1991; White et al., 1992).

If melting begins deeper than the garnet-spinel transition zone, then the U/Th systematics of melts would be dominated by the rate of melting in the garnet-only zone. We note, however, that using MELTS, Hirschmann *et al.* (1994) calculated that the rate of melt production during the first few percent of fractional melting along an ascending adiabat is about 0.1%/km, one fourth the rate generally assumed, so even if melting began deeper in the garnet peridotite zone, observed U-Th disequilibria need not imply the low upwelling rates usually inferred.

Depth of final melting at ridges: There is considerable uncertainty about the depth at and means by which melting stops under mid-ocean ridges. Many petrologic models of mantle melting assume that melting continues to near the top of the mantle, at 7-15 km (Kinzler and Grove, 1992b; Klein and Langmuir, 1987; Langmuir et al., 1992; McKenzie and Bickle, 1988; Niu and Batiza, 1991), which is consistent with the relatively shallow average depths of melting inferred by examination of major element systematics of MORB in these models. In contrast, Shen and Forsyth (1995) argue that melting ceases at depths as great as 30-50 km, and that melting may cease at particularly great depth at slow spreading ridges and near fracture zones. McKenzie and O'Nions (1991) also suggest that conductive cooling generally causes melting to stop at about 30 km. Although inversions of REE distributions from MORB (Brodie et al., 1994; McKenzie and O'Nions, 1991; White et al., 1992) also typically indicate effective cessation of melting at depths near 25 km, this result is not robust since the models assume incorrectly that plagioclase is always present in peridotite shallower than 25 km, unless the residue experiences more than 30%

melt extraction at deeper levels. The inference by Grove *et al.* (1992) that some MORB have experienced significant fractional crystallization from depths as great as 18 km is also consistent with relatively deep cessation of melting due to conductive cooling, at least locally.

An additional observation that bears on this problem is that MORBs generally have at most small Eu anomalies (BVSP, 1981). There are at least three possible interpretations of this constraint. (1) The most likely explanation is that peridotites upwelling beneath ridges that reach the pressure at which plagioclase would form in fertile, subsolidus peridotite are extensively depleted and hence too poor in Na and Al and too enriched in Cr to actually stabilize plagioclase. In this case, there would be no melting in the presence of plagioclase and a Eu anomaly would not be generated, even if melting continued to the base of the crust. (2) Second, conductive cooling of the uppermost mantle could terminate decompression melting before plagioclase forms. If plagioclase forms in the subsolidus residue at a level shallower than that at which melting terminates by conductive cooling, the integrated melt composition would not be affected. Although conductive cooling is undoubtedly an important cause of cessation of melting beneath ridges, it is unlikely that plagioclase forms in subsolidus peridotite residues. Observations of plagioclase peridotites suggest that they do not form by isochemical metamorphism (Dick and Bullen, 1984). (3) A third possibility, suggested by our work, is that in cases where plagioclase does become stable during upwelling, its very formation shuts off melting. The most likely conditions under which this could occur are those where the potential temperature of the upwelling mantle is low (so relatively little melting has occurred at depth) and the spreading rate is high enough that conductive cooling does not extend to great depth. Areas where plagioclase could play a role in shutting off melting include the Mid-Cayman Rise (Klein and Langmuir, 1987), the Siqueros fracture zone (White et al., 1992), or the Arctic Ocean (Langmuir et al., 1992) (although these areas of thin crust are also areas of slow spreading). Formation of plagioclase could also plausibly terminate melting where the

upwelling mantle is particularly fertile (i.e., rich in alumina and normative plagioclase) or in other tectonic environments (back-arc spreading centers, regions of continental extension), where the degree of melting may be lower than for most mid-ocean ridges (McKenzie and Bickle, 1988; Stolper and Newman, 1994). Note that in regions where the spinel-plagioclase transition stops decompression melting, the residual peridotites would contain plagioclase, but the erupted basalts would still not have negative Eu anomalies, because during fractional fusion no melt would be generated in the presence of residual plagioclase.

The key point is that melting of plagioclase peridotite is an unlikely process in upwelling mantle. If melting is very extensive, then upwelling peridotites will be too depleted at pressures less than ~10 kbar to form plagioclase. If melting is not so extensive, and spinel peridotite begins to convert to plagioclase peridotite at $P \leq 10$ kbar, the precipitation of plagioclase will terminate melting. Either way, melting of plagioclase peridotite does not occur.

Dynamical implications: Numerous petrological and geochemical characteristics of MORB have been taken to indicate that melts migrate to the surface from considerable depth without fully re-equilibrating at shallow levels (Albarède, 1992; Beattie, 1993a; Hart, 1993; Johnson et al., 1990; Klein and Langmuir, 1987; McKenzie and O'Nions, 1991; Salters and Hart, 1989). Because grain-scale porous flow does not appear capable of transporting melts over the necessary distances without such equilibration, melt transport in macroscopic channels or regions of high porosity has been suggested to play an important role in MORB sources (Iwamori, 1994; Kelemen et al., 1995a; Spiegelman and Kenyon, 1992). However, mechanisms for segregating melt into conduits larger than the grain-scale are poorly understood (Phipps Morgan, 1987; Sleep, 1988; Sparks and Parmentier, 1991; Spiegelman, 1990; Spiegelman, 1991; Stevenson, 1989). Variations in productivity with depth during upwelling could affect the rate and mechanism of upward migration of melt and, in particular, a region where melt-bearing mantle undergoes freezing or where

productivity approaches zero during near-fractional melting could constitute a barrier to upward flow of melt from deeper in the melting regime. In this section, we speculate on how such barriers might promote the segregation of melt into macroscopic channels.

Experimental studies of texturally equilibrated partially molten peridotites suggest that the liquid phase is interconnected even at very low melt fractions, and therefore able to move via porous flow along grain boundaries (Kohlstedt, 1991; Riley and Kohlstedt, 1990; Spiegelman, 1993a; von Bargen and Waff, 1986). The permeability that characterizes this flow is uncertain, but is assumed to be related to melt fraction by a power law with an exponent greater than one (Frank, 1968; Kohlstedt, 1991; McKenzie, 1984; Turcotte and Ahern, 1978). A region with a melt fraction approaching zero therefore represents a potential barrier to porous flow. In a source region where melt production and segregation by porous flow and compaction are dynamically coupled, a low-productivity region is likely also to be a low-porosity and hence low-permeability zone, whether its productivity is actually zero or simply reduced compared to subjacent regions.

The implications of such a barrier are potentially complex, but an accumulation of melt from below would likely develop at the base of the zone of low productivity. Such accumulations of low-density melt would be unstable with respect to the overlying low-porosity zones, and we speculate that the unproductive zones would be breached episodically, likely in macroscopic conduits or high permeability zones. This could occur by chemical and physical interaction between the unproductive zone and the accumulated melt (as in the experiments of Riley and Kohlstedt, 1990). Such a reactive infiltration along an originally planar interface can be unstable with respect to elongated high-porosity fingers; i.e., since permeability increases with porosity, any high-porosity perturbation will capture extra flow, increasing local reaction rates and hence increasing porosity further (Kelemen et al., 1995a; Kelemen et al., 1995b). Once established in response to the accumulation of melt beneath the unproductive zones, these conduits could persist to shallower levels at which melt production resumes, thereby providing sites for rapid

magma transport over larger depth ranges than those associated with solid-solid phase transitions. Alternatively, the accumulating melt could traverse the low permeability zones as solitary porosity waves (Richter and McKenzie, 1984; Scott and Stevenson, 1984). This could also lead to development of persistent conduits based on Spiegelman's (1993a; 1993b) demonstration that such porosity waves in viscously deformable media grow in amplitude upon entering a region undergoing freezing, to the point where they could disrupt the matrix. It has been shown (Sparks and Parmentier, 1991; Spiegelman, 1990; Spiegelman, 1991) that an inclined freezing front at the top of the oceanic melting regime can cause the formation of high-porosity channels that allow rapid lateral migration of melt towards the ridge axis. In principle the same mechanism may operate at depth if an inclined freezing front is generated by lateral temperature variations at the garnet-spinel or spinel-plagioclase transitions (although over a plume this could cause lateral flow away from the plume axis, since a positive Clapeyron slope implies the transition is deepest at the hot plume axis). These various examples and possibilities illustrate that an interruption in melt productivity at a phase transition presents an opportunity to initiate segregation of melt into macroscopic conduits by several possible mechanisms. The key point is that simply by concentrating melt at a fixed location in pressure, opportunities are created to stimulate phenomena at lengthscales larger than a grain diameter.

Conclusions

1) Solid-solid phase transitions with positive Clapeyron slopes consume entropy in converting to the low-pressure assemblage. Hence there is a competition for entropy between pressure-release melting and solid-state reactions during isentropic ascent of the sources of basaltic magmas. Consequently, a decrease in melt productivity or even freezing can occur when a batch-melting, isentropically ascending parcel of mantle undergoes a solid-solid phase transition. If melt escapes as it is produced (i.e., fractional or near fractional fusion), melting ceases when the solid solid transition takes place and does

not resume until a finite interval of pressure has been traversed. These phenomena can be readily visualized and analyzed in one- and two-component systems, in which freezing occurs at invariant points (i.e., cusps in the solidus); this result contrasts with the widely held view that cusps lead to enhanced melting. Transitions with negative Clapeyron slopes do lead to an impulse of melting at the cusp. The magnitude of freezing or melting at a cusp depends on the entropy of fusion, the entropy of reaction, the modal abundance of the reacting minerals, and the amount of melt present before the transition.

2) Thermodynamic modeling of mantle melting using MELTS shows that the garnet-spinel and spinel-plagioclase transitions are regions of low-productivity or freezing, not of enhanced melting. Near-fractional fusion leads to a wider interval without melt production than does batch fusion. These models demonstrate that the insights from analysis of simple systems generalize to mantle melting, and confirm that "cusps" on the mantle solidus associated with the garnet-spinel and spinel-plagioclase transitions lead to diminished rather than enhanced melting.

3) Reduced melting at phase transitions has several implications for problems in MORB petrogenesis. First, melt production during upwelling is expected to be highly non-uniform. The reduction of productivity in the garnet-spinel transition region could allow the observed U-Th disequilibria in MORB to be produced without requiring extraordinarily low rates of mantle ascent. However, the low productivity of this depth range implies that if significant contributions of melt from garnet peridotite are invoked to account for the Lu-Hf systematics and REE patterns in MORB, melting must begin deep within the garnet stability zone, in conflict with constraints from the average depths and extents of melting in MORB sources. It is also possible that the spinel-plagioclase transition, where it occurs, would cause mantle melting to cease. Finally, we speculate that the barren or low-productivity zones predicted to be associated with both the garnet-spinel and spinel-plagioclase transitions may trigger segregation of melt into rapid transport (high permeability) conduits.

Table 1. Bulk Composition used in Model Calculations

SiO_2	46.40 wt. %
TiO_2	0.18
Al_2O_3	4.10
FeO*	7.61
MgO	38.14
CaO	3.24
Na_2O	0.33

Hart and Zindler (1986), minus Cr_2O_3 and K_2O, all Fe as FeO, renormalized to 100%. Cr_2O_3-bearing calculations contained 0.47 wt. % Cr_2O_3.

Figure 1. Schematic phase diagrams for one-component systems in the vicinity of a triple point where a subsolidus phase transition meets the melting reaction. (a) Pressure (P) vs. molar entropy (S) for the system SiO_2 in the vicinity of the coesite, quartz, liquid triple point. Shaded lines are phase boundaries (metastable extensions dotted), with horizontal lightly-shaded tie-lines marking fields where two phases coexist. The horizontal shaded line at 43.6 kbar is the triple point where β-quartz (Q), coesite (C), and liquid (L) coexist. Heavy black dashed line A and medium black dashed line B are isentropes; heavy black solid path C traces the residue during fractional melting with isentropic infinitesimal melting increments. Light black dotted lines are isotherms, labeled with the appropriate temperature. Solid entropy calculated from Berman (1988), liquid entropy from Richet and Bottinga (1986), with Cp and α for the liquid taken as constant; the diagram is calculated quantitatively but the uncertainty in extrapolating thermochemical data to these conditions is large. (b) P vs. temperature (T) for the system SiO_2 for the conditions shown in (a) . Paths restricted to univariant curves are slightly offset for clarity. Phase boundaries extrapolated from Boyd and England (1960). (c) Generic, schematic one-component system with negative Clapeyron slope of subsolidus reaction, P vs. S; β is the high-pressure phase, α the low-pressure phase. See (a) for key. (d) Same system as (c), P vs. T.

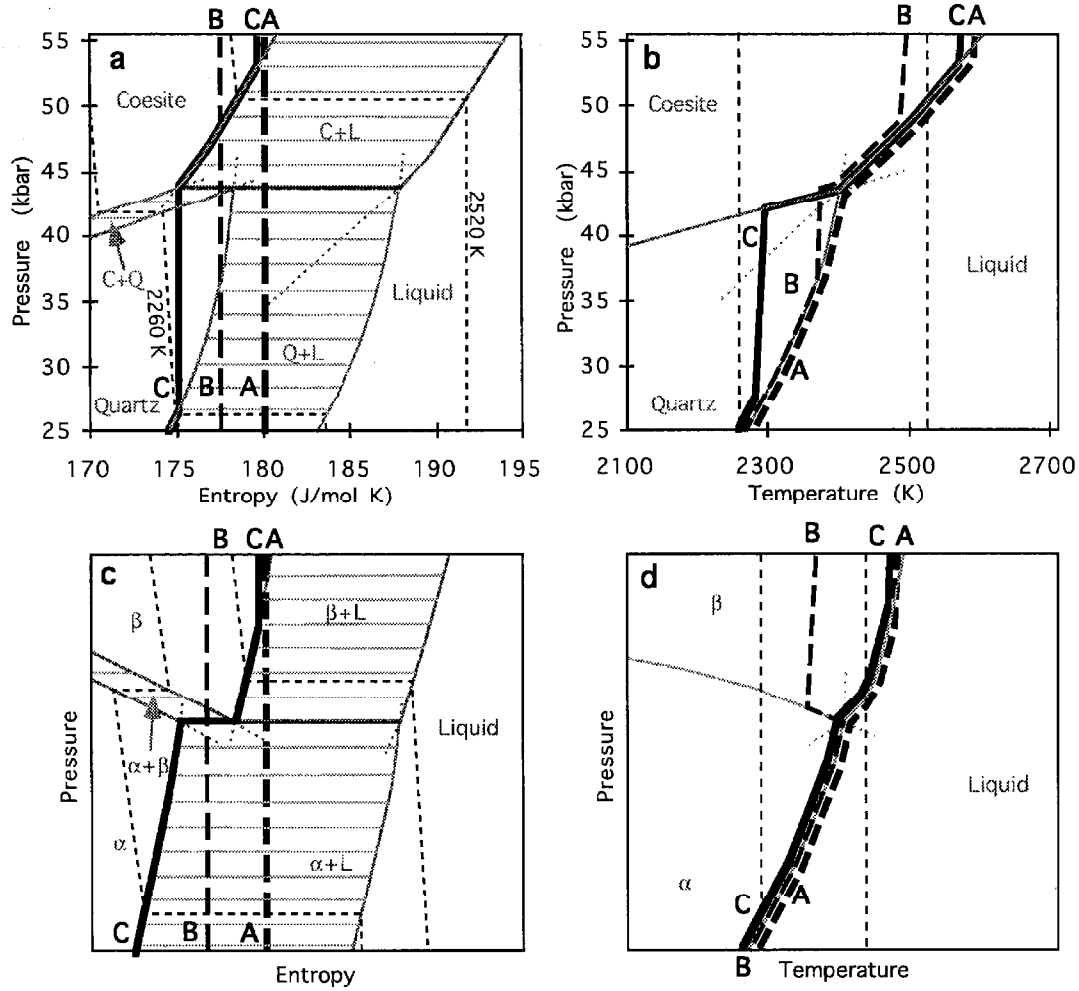

Chapter 2, Figure 1

Figure 2. In a one component system, the amount of melt coexisting with the low pressure phase α ($\phi_{L\alpha}$) at a pressure infinitesimally below the triple point vs. the amount of melt coexisting with the high pressure phase β ($\phi_{L\beta}$) at a pressure infinitesimally above the triple point contoured for constant values of $\Sigma \equiv \Delta S_{\alpha\beta}/\Delta S_{L\beta}$. $\Delta S_{\alpha\beta}$ is the entropy of phase α at the triple point minus the entropy of phase β at the same P and T. $\Delta S_{\alpha\beta}$ has the same sign as the Clapeyron slope of the subsolidus reaction. $\Delta S_{L\beta}$ is the entropy of fusion of β at the triple point. This figure illustrates the magnitude of freezing or melting at the triple point in a one-component system. For a particular one-component system, Σ is fixed, and this plot shows $\phi_{L\alpha}$ as a function of $\phi_{L\beta}$. For SiO_2 at the quartz-coesite-liquid triple point, $\Sigma \sim 0.25$.

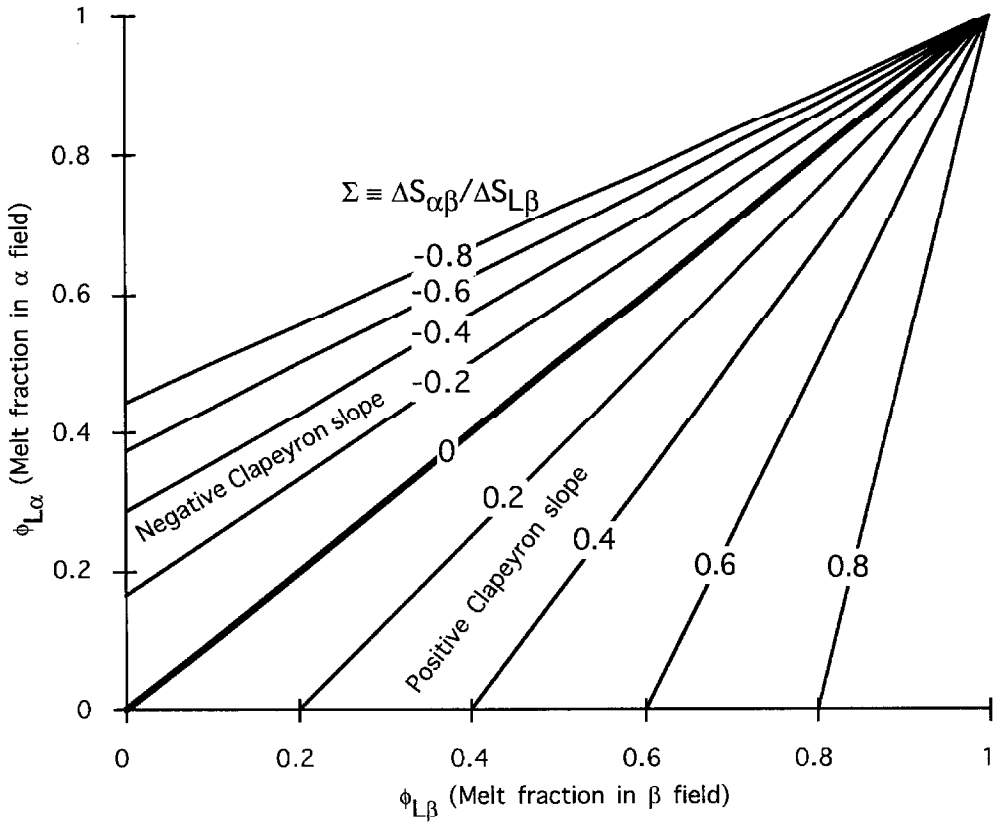

Chapter 2, Figure 2

Figure 3. Phase diagrams for the two-component system $NaAlSi_2O_6$-SiO_2. Jd = jadeite, Ab = albite, Q = quartz, C = coesite, L = liquid. (a) *P*-*T* projection showing univariant reactions, invariant point (I_{Ab}), and singular point (S_{Ab}) (Bell and Roseboom, 1969). Heavy black solid lines paths are isentropes; heavy dashed path is the trace of the residue during fractional melting with isentropic infinitesimal melting increments. Symbols on the ends of paths correspond to symbols marking *S*-*X* conditions in (d) and (e). (b) P = 34 kbar and (c) P = 33.3 kbar T vs. molar bulk composition (X_{SiO_2}) sections, after (Bell and Roseboom, 1969) (dashed curves inferred). (d) P = 34 kbar and (e) P = 33.3 kbar sections showing entropy S (per mole of oxygen) vs. X_{SiO_2}. Shaded regions are three-phase triangles. Heavy lines are stable phases (solids calculated from (Berman, 1988), liquid from (Richet and Bottinga, 1986); note that liquid has been approximated by mixing jadeite, albite, and silica melts without accounting for the entropy of mixing); liquid can exist alone anywhere above the liquid curve. Light lines are tie-lines showing two coexisting phases. Stars and asterisks corresponding to the isentropic paths in (a) are plotted at a fixed S and X_{SiO_2}. The darkly shaded circles and curved arrow corresponding to the heavy dashed path in (a) indicate the compositional and entropic evolution of the residue of fractional melting during decompression.

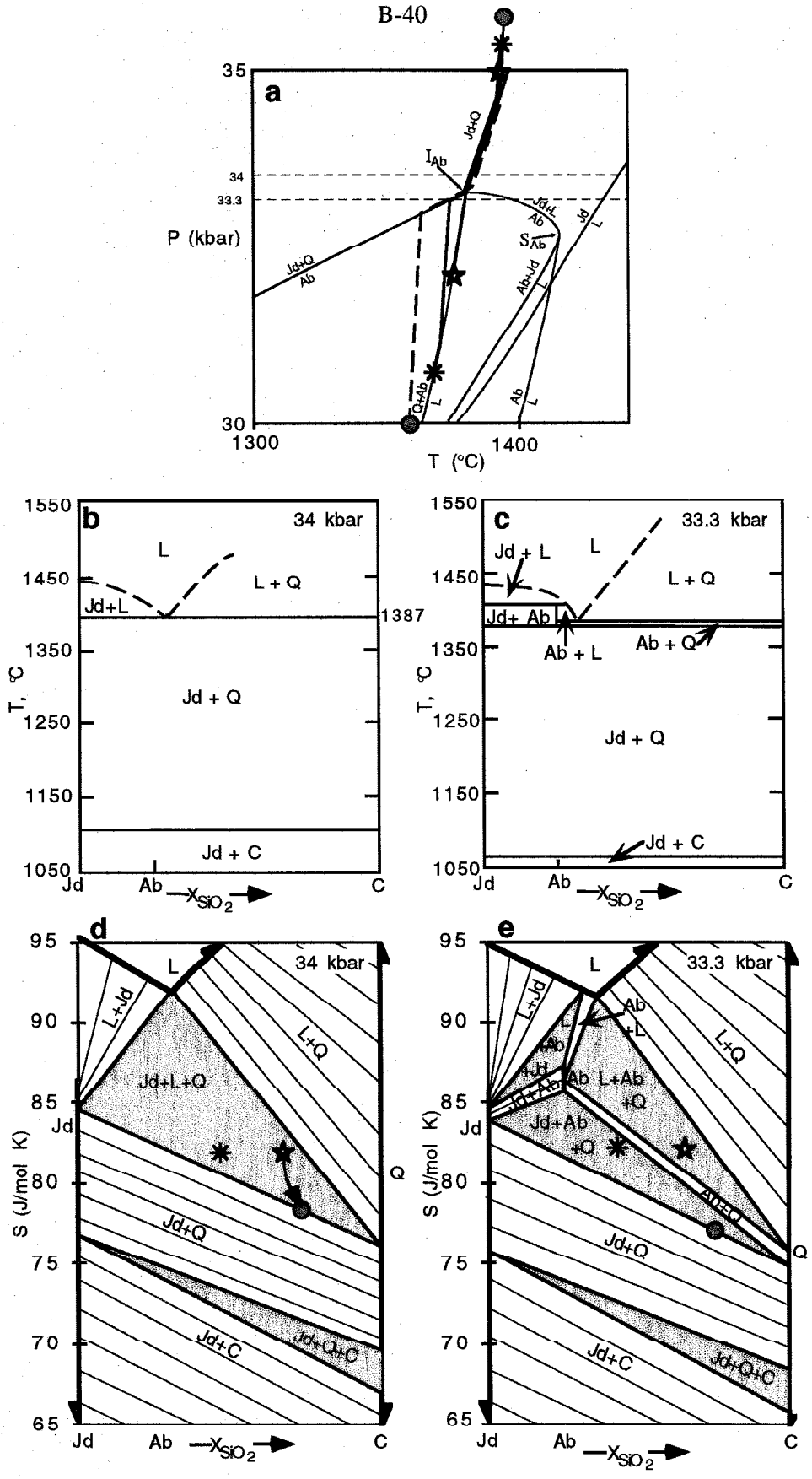

Chapter 2, Figure 3

Figure 4. Contour plot showing behavior of melt fraction at the invariant point I_{Ab} in the system jadeite-silica. Approaching the invariant point from higher pressure along the eutectic reaction Jd+Q = L, the system has molar melt fraction ϕ_{QJdL}, and has molar entropy S and bulk composition X_{SiO_2} that plot within the triangle Jd+Q+L. Leaving the invariant point, the system will either be subsolidus (triangle Ab+Jd+Q), or will consist of Q+Ab+L with molar melt fraction ϕ_{QAbL} or will consist of Ab+Jd+L with molar melt fraction ϕ_{AbJdL}. Contours (light solid lines) show the ratios $\frac{\phi_{QAbL}}{\phi_{QJdL}}$ and $\frac{\phi_{AbJdL}}{\phi_{QJdL}}$. Heavy solid lines indicate the boundaries of the three-phase triangles at the invariant point.

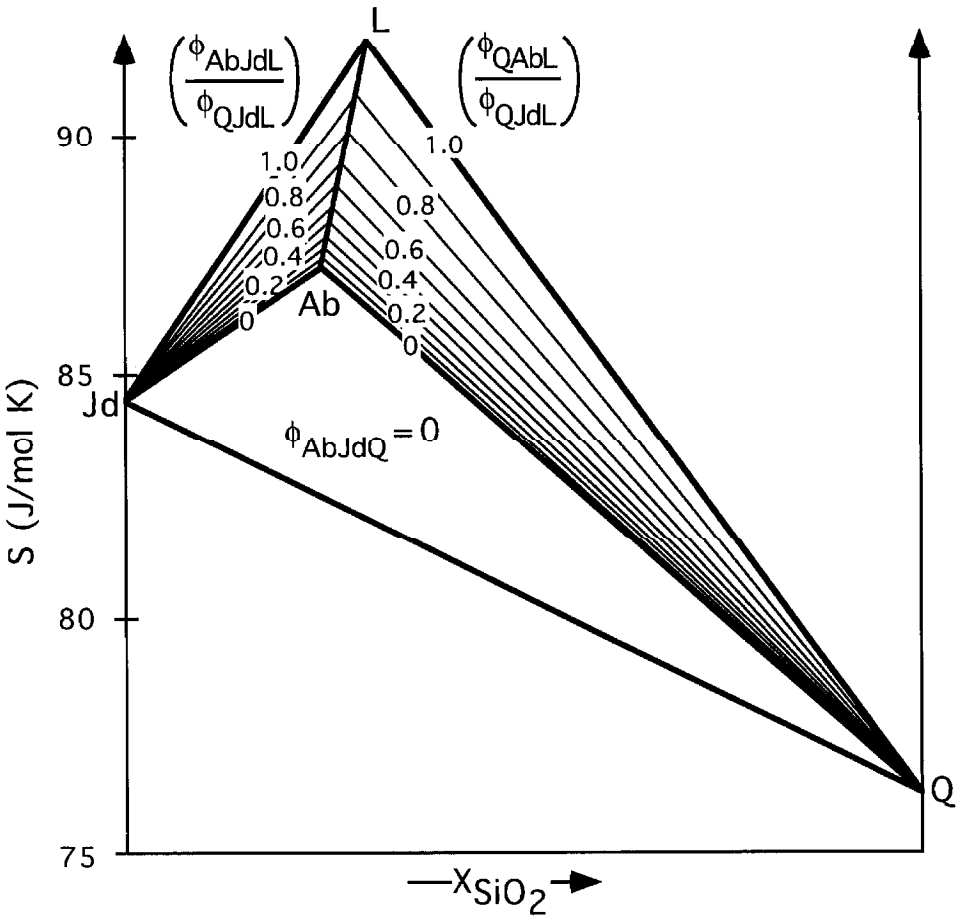

Chapter 2, Figure 4

Figure 5. Results of thermodynamic calculations of mantle melting at the spinel-plagioclase transition using MELTS and a fertile peridotite composition (see Table 1), with and without Cr_2O_3. Parts (a) through (d) show the Cr_2O_3-absent calculations; parts (e)-(h) show Cr_2O_3-bearing calculations. (a) T vs. P. The lower (solid) curve is a batch adiabat; the upper (dashed) curve is a finite-increment fractional melting path, with melt extraction events of 0.1% by volume. The short-dashed segment of the fractional path indicates a subsolidus region, where no melt is produced. (b) Modal abundance (wt %) of spinel and feldspar in the residue for the same (dashed) fractional and (solid) batch melting paths as in part (a). Modes of spinel and feldspar in the assemblage along the subsolidus part of the fractional path are indicated by short dashes. Plagioclase appears at 6 kbar along both paths; spinel goes out within 500 bars in the batch case and 1 kbar in the fractional case. (c) F vs. P. F is the total extent of melting experienced by the residue, calculated as integrated volume fraction. The (solid) batch adiabat and (dashed) fractional path are the same as those shown in part (a). (d) dF/dP (%/kbar) vs. P for the same paths; $dF/dP < 0$ indicates freezing during upwelling. Metastable batch melting of spinel lherzolite beyond the appearance of feldspar on the stable path is shown shaded. (e) As in (a), but for Cr_2O_3-bearing assemblage. (f) As in (b), for Cr_2O_3-bearing assemblage; spinel is now present throughout the pressure interval studied and plagioclase appears at 5 kbar along both batch and fractional paths. (g) As in (c), for Cr_2O_3-bearing assemblage. (h) As in (d), for Cr_2O_3-bearing assemblage.

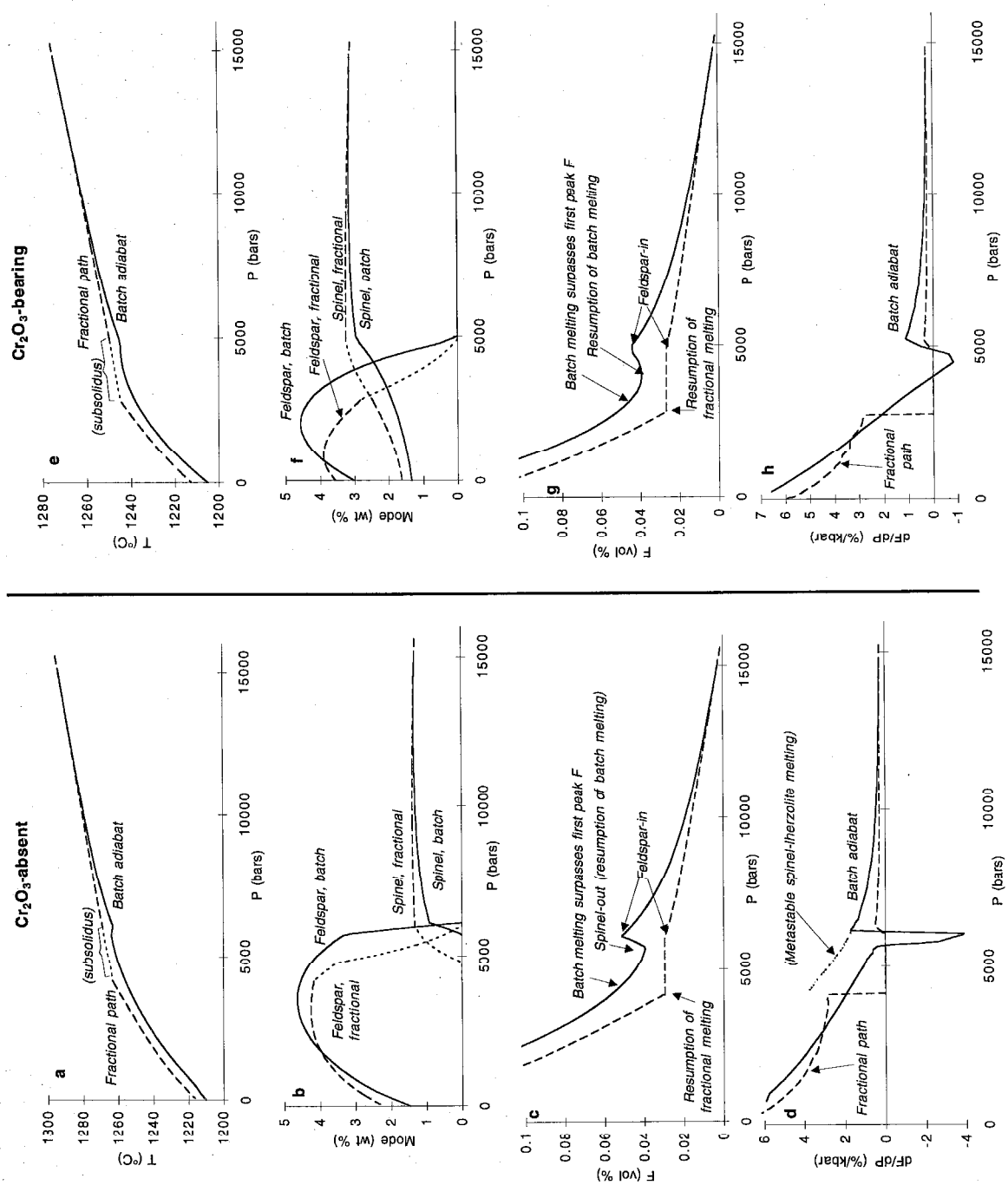

Chapter 2, Figure 5

Figure 6. Results of thermodynamic calculations of mantle melting at the garnet-spinel transition using MELTS and a fertile peridotite composition (see Table 1). (a) through (d) show results for a Cr_2O_3-free composition; (e)-(h) show a Cr_2O_3-bearing composition. Two starting entropies (or potential temperatures) were used for each composition — a "hot" mantle and a "cold" mantle. Batch and fractional melting calculations (melt extraction interval of 0.025% by volume) were performed for each composition and starting entropy. (a) T vs. P. The hot paths (shaded lines) cross the solidus at 45 kbar, the cold paths (black lines) at 28 kbar. For each case, a batch adiabat (solid lines) and a finite-increment fractional path (dashed lines) are plotted. (b) Modal abundance (weight %) of spinel and garnet in the residue during the melting paths shown in part (a); shading and dashing as in (a). The transition is quite sharp -- about 250 bars wide in all cases. (c) F (vol. %) vs. P for the same upwelling paths. F is the total extent of melting experienced by the residue. Note the plateaux corresponding to the transition intervals. (d) dF/dP (%/kbar) vs. P; Note that the "Hot, fractional" path dips below zero near the garnet-out point as the melt generated near spinel-in (less than the extraction threshold of 0.025% by volume) is refrozen. (e) As in (a), but for Cr_2O_3-bearing composition. In this calculation the cold paths intersect the solidus at 35 kbar, the hot paths at 50 kbar. (f) As in (b), for Cr_2O_3-bearing composition. Garnet is exhausted at 31 kbar along the cold paths, 32 kbar along the hot paths. Spinel is present in the residue throughout the pressure range studied; its modal abundances increases while garnet is present and decreases slowly thereafter. (g) As in (c), for Cr_2O_3-bearing composition. There are no plateaux, but there are subtle upward kinks at garnet-out. (h) As in (d), for Cr_2O_3-bearing composition. The gradual increase in productivity which characterizes adiabatic melting is interrupted by sudden doubling of productivity at the garnet-out point along each path. This demonstrates that the growth of spinel in the residual assemblage consumes entropy.

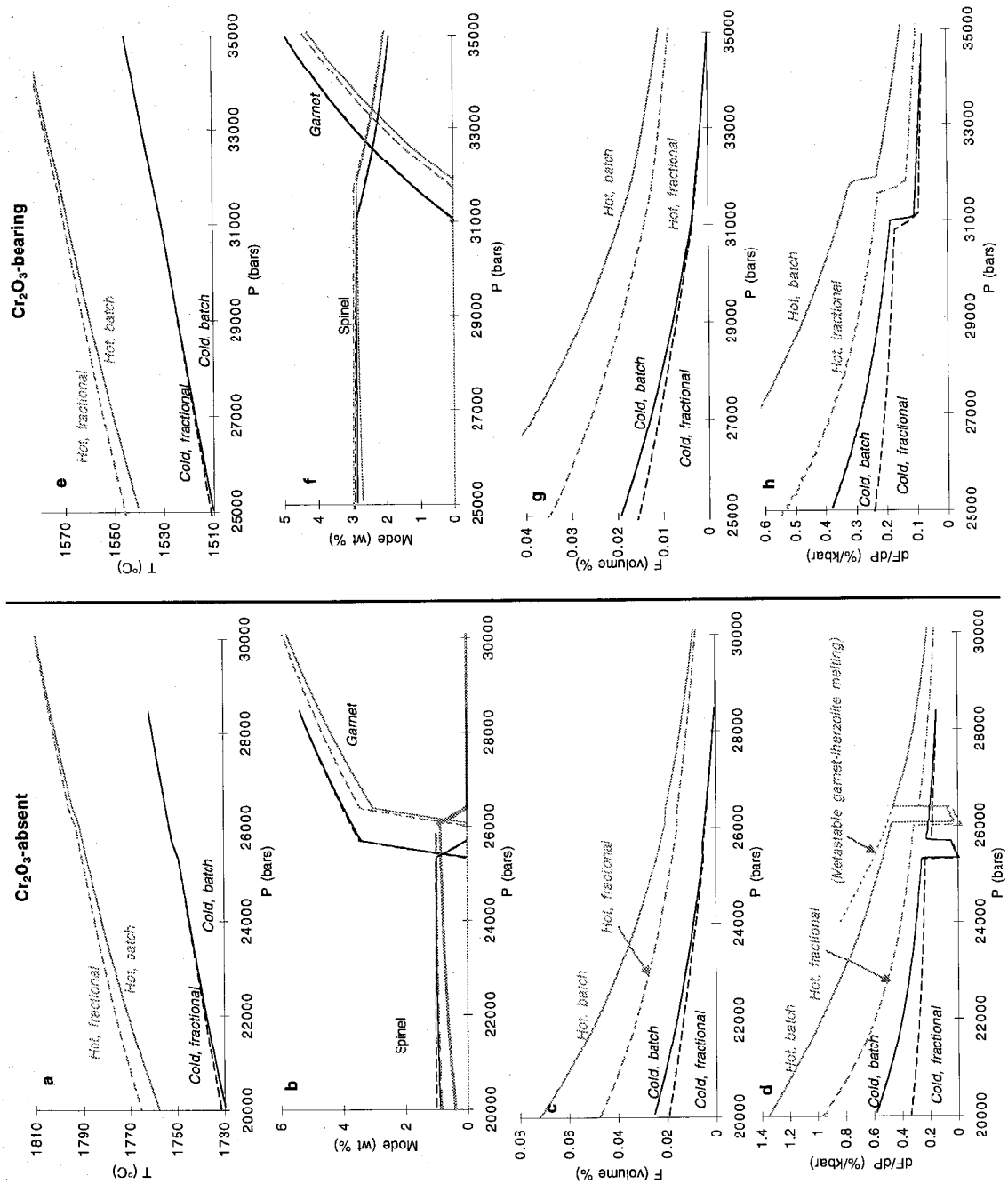

Chapter 2, Figure 6

Figure 7. Entropy content of the phases during isentropic passage through the garnet-spinel peridotite transition. The system is 100 grams of a Cr_2O_3-free fertile peridotite as in Figure 6a-d; entropy and phase equilibria are calculated by MELTS. The total entropy is always 264.1 J/K. (a) The total entropy content of each phase as a function of pressure. Note garnet going to zero where it disappears from the residue, spinel rising from zero where it appears in the assemblage. The entropy in the melt slowly increases at the system progressively melts. These changes in entropy are governed principally by changes in modal abundance; i.e., the specific entropy of each phase changes slowly. (b) The pressure derivative of the total entropy content of each phase, in J/K/kbar, plotted against pressure. Note that the liquid curve goes to zero during the transition, when melt productivity approaches zero and no further melting is occurring. The entropy changes are largest just before garnet is exhausted; this is the location where freezing is most likely (compare Figure 6d). This figure shows that solid-solid net transfers and exchanges dominate the entropy budget of the assemblage in the phase transition region.

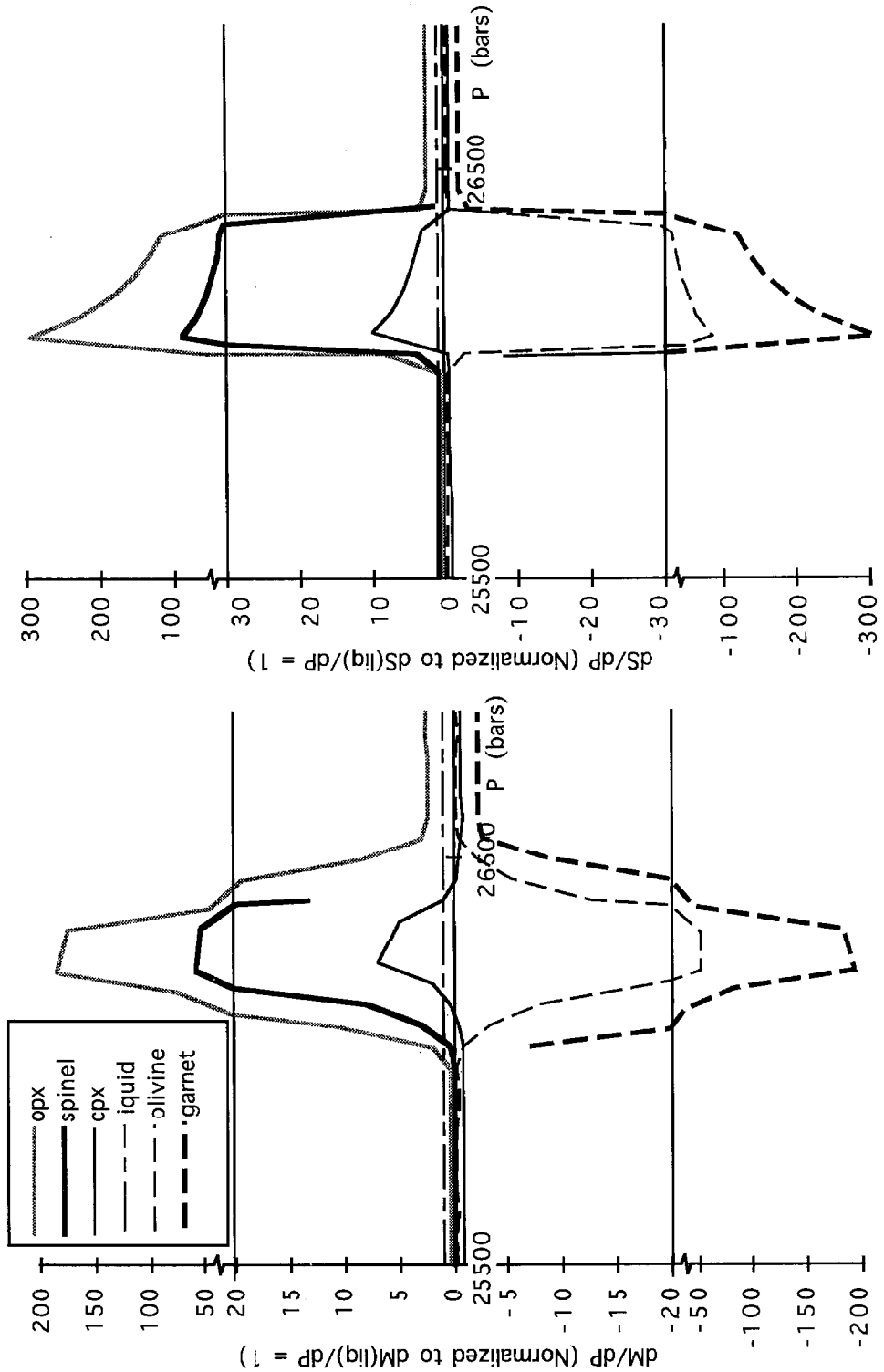

Chapter 1, Figure 7

Chapter 3. An analysis of variations in isentropic melt productivity

Abstract—The amount of melt generated per unit pressure drop during adiabatic upwelling, the isentropic melt productivity, cannot be determined directly from experiments and is commonly assumed to be constant or to decrease as melting progresses. From analysis of one- and two-component systems and from calculations based on a thermodynamic model of peridotite partial melting, we show that productivity for reversible, adiabatic (i.e., isentropic) depressurization melting is never constant; rather, productivity tends to increase as melting proceeds. Even in a one-component system with a univariant solid-liquid boundary, the $1/T$ dependence of $(\partial S/\partial T)_P$ and the downward curvature of the solidus (due to greater compressibility of liquids relative to minerals) lead to increased productivity with increasing melt fraction during batch fusion (and even for fractional fusion in some cases). Similarly, for multicomponent systems, downward curvature of contours of equal melt fraction between the solidus and the liquidus contributes to an increase in productivity as melting proceeds. In multicomponent systems, there is also a lever-rule relationship between productivity and the compositions of coexisting liquid and residue such that productivity is inversely related to the compositional distance between coexisting bulk solid and liquid. For most geologically relevant cases, this quantity decreases during progressive melting, again contributing to an increase in productivity with increasing melting. These results all suggest that the increases in productivity with increasing melt fraction (punctuated by drops in productivity upon exhaustion of each phase from the residue) predicted by thermodynamic modeling of melting of typical mantle peridotites using MELTS are neither artifacts nor unique properties of the model, but rather general consequences of adiabatic melting of upwelling mantle.

1. Introduction

The amount of melting experienced by upwelling mantle is one of the most important parameters required for understanding the dynamics of basalt production and the observed compositional variability of basalts at mid-ocean ridges and sites of hot spot magmatism. The key parameter is the "productivity" of the melting process (i.e., the amount of melt production per decrement of pressure; Hirschmann et al., 1994), which exerts important controls on the dynamics and style of melt extraction, particularly if it varies with depth (Asimow et al., 1995a; Spiegelman, 1993b). The productivity also relates the geometry of the melting region to the average depth of melt generation and to the total amount of melt produced, and therefore to the thickness of the oceanic crust (Langmuir et al., 1992). The motivation for this paper is that the primary information available from the study of igneous rocks, their compositions and volumes, cannot be interpreted in terms of source dynamics and geometry without an understanding of the factors influencing productivity in upwelling mantle.

Mantle upwelling at mid-ocean ridges and plumes in the absence of melt or fluid flow is usually approximated as an adiabatic process. To the extent that upwelling is slow relative to mass and thermal transfer in the ascending peridotite, the process can also be envisioned as reversible. Under these conditions, processes occurring in upwelling mantle can be approximated as isentropic (McKenzie, 1984; Verhoogen, 1965). Once melt or fluid migration is allowed to occur or the effects of viscous deformation of the solids are considered, the process is no longer locally adiabatic or isentropic, and indeed, no simple thermodynamic constraints can be applied to the general case. Nevertheless, certain idealized end-member processes, such as batch fusion or fractional fusion (in which each increment of melt production during upwelling can be approximated as adiabatic and reversible), can be evaluated relatively simply from a thermodynamic perspective. However, despite the apparent simplicity of the problem when posed thermodynamically

— e.g., for the reversible adiabatic case, pressure (P), entropy (S), and chemical composition are the independent variables in upwelling mantle and the equilibrium state is one of minimum enthalpy (H) — the general features of productivity during adiabatic depressurization of mantle peridotite (and even of simpler, model systems) are little understood. The difficulty is partly that adiabatic processes are not readily simulated by experiment; i.e., whereas it is relatively simple to do an experiment at fixed or known P, temperature (T), and chemical composition, there is no straightforward way to do an experiment at fixed or known S or H at high pressure. Another difficulty, however, is that there is, to our knowledge, no general treatment of adiabatic melting and its consequences even in simple systems, so there is no framework or background for understanding the behavior of complex natural systems undergoing this process. Although space limitations prevent us from presenting a complete treatment, the goal of this paper is to expose some of the key parameters entering into the process of *isentropic* melting of the mantle and, by illustrating some of the expected behaviors and what causes them, to help calibrate people's intuition about this important process.

2. Background and previous work

The simplest approach to estimating melt production in upwelling peridotite is to assume that melt fraction increases linearly as pressure decreases; i.e., isentropic productivity is assumed to be constant (Kinzler and Grove, 1992a; Klein and Langmuir, 1987; Niu and Batiza, 1991; Turcotte and Ahern, 1978). In other cases, plausible assumptions have been made that lead to decreasing productivity with progressive decompression; for example, McKenzie and Bickle (1988) inferred, based on available peridotite melting data, that melt production would be enhanced near the solidus of natural peridotite (similar to the behavior of a simple system at a eutectic or peritectic; see McKenzie and Bickle, 1990), and Langmuir et al. (1992) argued that melting is more

productive at high pressure because the solidus and liquidus are closer together. Although both of these effects could be important under some conditions, we show below that decreasing productivity during upwelling is exactly the opposite of what is expected in most natural cases; i.e., productivity is generally smaller at the initiation of decompression melting and increases with progressive decompression. Note that in this paper we restrict our attention to changes in productivity with progressive melting along particular adiabats; we leave comparisons among adiabats of different potential temperature for future work.

A widely used approach to estimating adiabatic melting paths is based on the assumption that at a given pressure the enthalpy of the metastable solid adiabat (a state that can be readily calculated from an initially stable subsolidus assemblage) and that of the stable partially molten adiabat are equal (Cawthorn, 1975; Hart, 1993; Hess, 1992; Langmuir et al., 1992; Longhi, 1992; Ramberg, 1972). In practice, these authors balanced the enthalpy required to melt the metastable solid against the enthalpy recovered by cooling to the stable partially molten assemblage. Although these authors presumably intended to calculate the amount of melt produced on reversible, adiabatic upwelling of peridotite, they actually calculated the amount of melt produced on a somewhat different adiabatic path. Consider Figure 1, where this melting path (informally labeled the "Hess/Langmuir melting path") is compared with isentropic upwelling in P-T space (Figure 1a) and in the less familiar but more informative H-S plane (Figure 1b). We have drawn Figure 1a for a multicomponent system, so that the melting paths do not coincide with the solidus, but for simplicity we have drawn Figure 1b for a one-component system. In H-S space, the locus of states of a phase at constant pressure fall on a curve whose slope is temperature (i.e., $(\partial H/\partial S)_P = T$). The coexistence of two phases at equilibrium requires equal T and equal P, so it is represented by a tie-line tangent to isobaric curves for the two phases. The isentropic path from stable state *1* on the solidus at P_0 to the stable, partially molten state *4* at P_f is vertical in H-S space. The Hess/Langmuir melting path, however, corresponds to a

path on Figure 1b from the stable state *1* at P_0 to the metastable solid state *2* at P_f (reached by a reversible adiabatic decompression), followed by a second path to the stable partially molten state *3* at P_f (which has the same enthalpy as state *2*). Figure 1b shows that state *3* is at a higher melt fraction (F), higher S, and higher H than state *4*. For a multicomponent system, state *3* can also be at a higher T than state *4* on the isentropic path. Hence the process that these authors actually approximated contains an *irreversible*, isobaric, adiabatic melting step (i.e., the adiabatic path from state *2* to state *3* at constant P and H leading to maximization of S), which leads to more melting than that produced by reversible adiabatic upwelling. Although the quantitative differences between these two paths are small, particularly at low degrees of melting, this example illustrates the importance of precise definition of the thermodynamics governing the melting process. Note that this treatment is not "wrong" in that it does follow an adiabatic path, just not the reversible one, and it is possible that such a path could be of petrologic or geophysical interest; e.g., at a solid-solid phase transformation if the transition is kinetically inhibited (Solomatov and Stevenson, 1994).

An alternative to this approach would be to estimate melt production during reversible (i.e., isentropic) upwelling by balancing S rather than H in equivalent calculations comparing the metastable solid assemblage and the stable partially molten assemblage (i.e., by breaking the isentropic path from state *1* to state *4* in Figure 1b into the sum of paths $1 \rightarrow 2$ and $2 \rightarrow 4$). Actual conversion of the metastable solid state *2* to final state *4* would require in this case an irreversible, non-adiabatic process at constant P and S leading to a minimization of H. The direct path from $1 \rightarrow 4$, on the other hand, is accomplished in a series of infinitesimal, reversible, adiabatic steps. Although both entropy-conserving and enthalpy-conserving calculations of this sort are conceptually simple, rigorous application of this approach to modeling adiabatic productivity in multicomponent systems would in practice be difficult because of the difficulty of incorporating into the calculation the

dependence of the thermodynamic parameters (heat capacities, entropy of fusion, etc.) on changes in melt, solid, and system composition, on residual mineralogy, and on temperature and pressure.

There have been several well-defined thermodynamic treatments of isentropic batch melting of decompressing peridotite (Albarède, 1992; Iwamori et al., 1995; McKenzie, 1984; Miller et al., 1991). These treatments use as inputs parameterizations of experimental data on isobaric productivity (i.e., $(\partial F/\partial T)_P$, where F is the melt fraction), the positions of the solidus and liquidus, and the entropy of fusion (assumed to be constant). These parameterizations are generally poorly constrained (particularly the isobaric productivity near the solidus) and the isentropic productivity functions that have been presented are consequently highly variable. For example, McKenzie (1984) favored models that yield roughly constant or strongly decreasing productivity during upwelling, while Iwamori et al. (1995) and Miller et al. (1991) presented models with complex productivity functions that largely reflect their fits to the solidus and liquidus and to the isobaric productivity function. Note that these treatments cannot easily incorporate the effects on melting of changes in the compositions or abundances of residual phases, of pressure dependent solid-solid phase changes (Asimow et al., 1995a), or of changing bulk composition, and thus, like the simple enthalpy- or entropy-balances described in the preceding paragraphs, they do not provide insight into the influence of these features of peridotite phase equilibria on productivity, which are likely to be substantial. Moreover, these treatments are not well-suited to evaluating the productivity of fractional fusion.

We have adopted in our work (Asimow et al., 1995a; Asimow et al., 1995b; Baker et al., 1995; Hirschmann et al., 1994) an approach based on a self-consistent thermodynamic model of multicomponent liquid-crystal equilibria. Using a modification of the MELTS code (Ghiorso and Sack, 1995), we minimize directly the enthalpy for a specific bulk composition at a given P and S. Because this treatment incorporates

internally consistent thermochemical models for the liquid and solid phases in mantle peridotites, it implicitly takes into account the phase and compositional changes that occur on melting of peridotite without having to incorporate them into parameterizations for the solidus and liquidus, the isobaric productivity, etc., which in natural peridotite are unlikely to be fit by simple or general functional forms. In addition, because the model is not linked to any particular bulk composition on which experiments have been conducted, it is equally applicable to batch and fractional melting and can be applied to a range of fertile through depleted peridotite compositions. Though the accuracy of MELTS predictions is at present imperfect, it has been shown to capture even some relatively subtle features of available melting experiments on peridotite (Baker et al., 1995; Hirschmann et al., 1994), and it thus is a promising vehicle for modeling peridotite phase equilibria and melting energetics. Contrary to the results of all previous treatments, MELTS predicts that isentropic productivity strongly increases with progressive melting; e.g., initial melting of a fertile peridotite is predicted to be extremely unproductive, with near-solidus isentropic productivity values near 0.25 %/kbar, rising to values of ~3 %/kbar near the exhaustion of clinopyroxene (Figure 7; see also Asimow et al., 1995a; Hirschmann et al., 1994).

3. Isentropic melting in simple systems

Given the wide range in productivity functions that have been proposed for melting during adiabatic decompression — ranging from constant (Kinzler and Grove, 1992a; Klein and Langmuir, 1987; Niu and Batiza, 1991; Scott and Stevenson, 1989; Sparks and Parmentier, 1991; Turcotte and Ahern, 1978), to decreasing as melting proceeds (Langmuir et al., 1992; Longhi, 1992; McKenzie, 1984; McKenzie and Bickle, 1988; McKenzie and Bickle, 1990), to increasing as melting proceeds (Asimow et al., 1995a; Asimow et al., 1995b; Hirschmann et al., 1994), to complex and irregular (Iwamori et al., 1995; McKenzie, 1984; McKenzie and O'Nions, 1991; Miller et al., 1991) — it is fair to

say that this phenomenon is poorly understood. In order to develop a more complete understanding of the relationship between melting energetics, phase equilibria, and productivity, in this section we examine the behavior of melting during isentropic upwelling of simple model systems. The melting behavior of these systems is easy to understand, yet surprisingly rich in insights that can be generalized to multicomponent systems. These simple systems thus provide a framework for understanding the productivity during upwelling of more complex natural systems. A key conclusion is going to be that the melting behavior of these simple systems strongly suggests that the productivity functions generated by the MELTS calculations capture at least qualitatively the behavior of the real mantle.

In the following discussions we consider both isentropic batch melting and fractional fusion; fractional fusion is envisioned as a sequence of infinitesimal isentropic melting steps, each followed by extraction of the melt phase, carrying its entropy out of the system with it. Both processes are defined by the restriction

$$d\boldsymbol{S} = S^l \, d\boldsymbol{M}; \tag{1}$$

i.e., the only changes we allow in the entropy of the system, $\boldsymbol{S}$ (extensive variables are boldface), are due to extraction of liquid and the resulting change is given by the specific entropy of the liquid, S^l, times the change in system mass, $\boldsymbol{M}$. The general forms we derive will apply to isentropic batch and incrementally isentropic fractional fusion as well as to any continuous melting or dynamic melting process (Langmuir et al., 1977) subject to the restriction that liquid mass is a function of no variables other than solid mass (e.g., $\boldsymbol{M}^l = 0$ for fractional fusion; $\boldsymbol{M}^l = \boldsymbol{M}^o - \boldsymbol{M}^s$ where $\boldsymbol{M}^o$ is the initial system mass, a constant, for batch fusion; and

$$\boldsymbol{M}^l = \begin{cases} \boldsymbol{M}^o - \boldsymbol{M}^s \text{ for } \boldsymbol{M}^s \geq (1 - f^*)\boldsymbol{M}^o \\ \left(\dfrac{f^*}{1 - f^*}\right)\boldsymbol{M}^s \text{ for } \boldsymbol{M}^s \leq (1 - f^*)\boldsymbol{M}^o \end{cases} \tag{2}$$

for continuous fusion where f^* is a constant retained melt fraction). Note that M^l refers to the mass of liquid remaining in the system; extracted liquid is considered no further. We use the quantity F to refer to the melt fraction by mass normalized to original source mass for all melting processes,

$$F = 1 - \frac{M^s}{M^o}, \tag{3}$$

and the quantity f to refer to the mass fraction of liquid that remains in the source region,

$$f = \frac{M^l}{M^l + M^s}; \tag{4}$$

i.e., for batch melting, $f=F$; for fractional melting, $f=0$; and for continuous melting as defined in (2), $f=F$ until F reaches f^* and $f=f^*$ thereafter.

3a. One-component systems

The isentropic behavior of a one-component system can be evaluated rigorously in a closed form. Taking P and T as the independent variables, for a single phase of one component we write

$$\mathrm{d}S^\phi = \left(\frac{\partial S^\phi}{\partial T}\right)_P \mathrm{d}T + \left(\frac{\partial S^\phi}{\partial P}\right)_T \mathrm{d}P = \frac{C_\mathrm{p}^\phi}{T}\mathrm{d}T - V^\phi \alpha^\phi \mathrm{d}P, \tag{5}$$

where S is specific entropy, C_p is isobaric heat capacity, V is specific volume, α is the isobaric coefficient of thermal expansion, and the superscript ϕ indicates the properties of a single phase. If we consider two phases, solid (s) and liquid (l), coexisting at equilibrium along a univariant curve (denoted 2ϕ), then for coexisting solid and liquid we have

$$\left(\frac{\mathrm{d}S^s}{\mathrm{d}P}\right)_{2\phi} = \frac{C_\mathrm{p}^s}{T}\left(\frac{\mathrm{d}T}{\mathrm{d}P}\right)_{2\phi} - V^s\alpha^s, \text{ and} \tag{6a}$$

$$\left(\frac{\mathrm{d}S^l}{\mathrm{d}P}\right)_{2\phi} = \frac{C_\mathrm{p}^l}{T}\left(\frac{\mathrm{d}T}{\mathrm{d}P}\right)_{2\phi} - V^l\alpha^l. \tag{6b}$$

For upwelling of a closed system at constant total specific entropy, S_o, the system must always satisfy

$$FS^l + (1-F)S^s = S_O. \tag{7}$$

Hence for batch melting

$$F = \frac{S_O - S^s}{S^l - S^s} = \frac{S_O - S^s}{\Delta S_{fus}} \tag{8}$$

where ΔS_{fus} is the specific entropy of fusion for a one-component system, which is in general a function of P and T.

3a (i). Constant coefficients. In the special case that ΔS_{fus} is constant (equivalent to requiring $C_p^l = C_p^s$ and $V^l\alpha^l = V^s\alpha^s$), the isentropic productivity for batch melting can be obtained by differentiation of equation (8):

$$-\left(\frac{\partial F}{\partial P}\right)_S = \frac{1}{\Delta S_{fus}}\left(\frac{C_p^s}{T}\left(\frac{dT}{dP}\right)_{2\phi} - V^s\alpha^s\right) = \frac{1}{\Delta S_{fus}}\left(\frac{C_p^s}{T}\left(\frac{\Delta V_{fus}}{\Delta S_{fus}}\right) - V^s\alpha^s\right), \tag{9}$$

where the second equality follows from the Clausius-Clapeyron equation for a one-component system. Since melting occurs over a range of pressure along a univariant curve with a finite slope, it also occurs over a range of temperatures. Hence equation (9) shows that even in the simplest possible case – a one-component system with constant ΔS_{fus}, ΔV_{fus}, C_p^s, and $V^s\alpha^s$ – isentropic productivity is not constant; i.e., it depends on temperature.

The magnitude of this effect can be estimated as follows. Neglecting the temperature difference due to the finite slope of the solid adiabat, the ratio of the temperature at the onset of isentropic melting to that at the completion of melting in a system with constant coefficients can be approximated by

$$\frac{T_0}{T_1} = exp\left(\frac{\Delta S_{fus}}{C_p^l}\right) \tag{10}$$

(Miller et al., 1991). If we take as typical values of the entropy of fusion ~R per atom and of the liquid heat capacity ~$3R$ per atom, we obtain $T_0/T_1 \sim 1.4$. For most silicates the $V^s\alpha^s$ term in equation (9) is very small, so melting at the completion of isentropic melting

in a one-component system would typically be ~1.4 times more productive than at the onset of melting.

Although fractional melting is neither isentropic nor reversible, as indicated above we define an idealized adiabatic fractional melting process as a series of infinitesimal isentropic melting steps, each followed by complete extraction of the liquid, carrying its entropy out of the system. We note that each infinitesimal increment of melting is equivalent to the initial increment of batch melting of a system that has been reduced by a factor $(1 - F)$ from the original mass of the system. Since F is defined as the mass fraction of the *original* system that is now liquid (equation 3), we obtain

$$-\left(\frac{dF}{dP}\right)_{Fractional} = \frac{1}{\Delta S_{fus}}\left(\frac{C_p^s}{T}\left(\frac{\Delta V_{fus}}{\Delta S_{fus}}\right) - V^s\alpha^s\right)(1 - F) \qquad (11)$$

(for a more rigorous derivation of productivity for incrementally isentropic processes, see the Appendix to this chapter). Thus, in a one-component system, productivity during fractional melting is initially the same as that of batch melting, but becomes steadily smaller (and asymptotically approaches 0 as the system approaches 100% melt) as upwelling proceeds. We emphasize that in a one-component system with constant coefficients, productivity during fractional fusion defined this way differs from batch productivity solely because of decreasing source mass. Note that the productivity per unit mass of solid, another way to define productivity, is always equal for batch and fractional melting in a one-component system with constant ΔS_{fus} (except in the case of solid-solid phase changes; see Asimow et al., 1995a).

We can obtain an expression suitable for batch and fractional melting as well as intermediate processes in which some but not all of the melt is left in the system (so-called continuous or dynamic melting; Langmuir et al., 1977) if we note that at any time the fraction of the original mass that remains in the system is $(1 - F)/(1 - f)$. For batch melting this term is equal to one and for fractional melting it reduces to $(1 - F)$. Thus, for

the general process of isentropic melting steps possibly followed by some melt extraction in the constant-coefficient one-component case (see the Appendix to this chapter for a more rigorous derivation),

$$-\left(\frac{dF}{dP}\right)=\frac{1}{\Delta S_{fus}}\left(\frac{C_p^s}{T}\left(\frac{\Delta V_{fus}}{\Delta S_{fus}}\right)-V^s\alpha^s\right)\frac{(1-F)}{(1-f)}. \qquad (12)$$

We will generally refer to $-(dF/dP)$ as the "isentropic productivity" even though for fractional fusion the process is only isentropic in each infinitesimal melting step.

To illustrate melting behavior in a one-component system, equations (9) and (11) have been applied to pure diopside (we neglect any incongruent melting behavior; Biggar and O'Hara, 1969; Kushiro, 1972). Using the properties given in Table 1 and taking the values of ΔS_{fus}, ΔV_{fus}, C_p^s, and $V^s\alpha^s$ at the 1 bar melting point to apply at all P and T, we obtained a linear melting curve (Figure 2a). The same phase relations are shown in S-P space in Figure 2b, where it should be noted that although the entropy difference between coexisting solid and liquid is constant, the boundaries of the two-phase field are not linear, reflecting the $1/T$ dependence in equations (6a) and (6b) (Asimow et al., 1995a). Choosing an isentrope that intersects the melting curve at 7 GPa, we obtained the productivity curves shown in Figure 2c for batch and fractional melting (for comparison, the hypothetical linear case is also shown), which have been integrated to yield the F vs. P curves shown in Figure 2d. Batch melting in this case yields a concave-up F vs. P curve, while the curve for fractional melting is concave down. Productivity at the completion of batch melting in this case is a factor 1.6 higher than the initial productivity. The upward curvature of the batch melting curve seen here will be referred to below as the "$1/T$ effect". This effect is of only secondary significance in multicomponent systems, but we draw attention to it here in order to illustrate the improbability of constant productivity for any isentropic melting process.

3a (ii): Variable coefficients. Figure 2c shows that for the case of constant coefficients, isentropic melting leads to increasing productivity in the batch case, reflecting the $1/T$ dependence, and decreasing productivity in the fractional case, reflecting decreasing source mass. We now apply the same analysis using more realistic variations in thermodynamic parameters as functions of P and T. In the case that ΔS_{fus} is not constant, equations (9) and (12) do not apply. Instead we begin from equation (1) and, as shown in the Appendix to this chapter, we derive the following general expression for any process of isentropic melting steps possibly followed by melt extraction in a one-component system:

$$-\left(\frac{dF}{dP}\right) = \frac{1}{\Delta S_{fus}}\left(\frac{C_p^s + f(C_p^l - C_p^s)}{T}\left(\frac{dT}{dP}\right)_{2\phi} - \left[V^s\alpha^s + f(V^l\alpha^l - V^s\alpha^s)\right]\right)\frac{(1-F)}{(1-f)}. \qquad (13)$$

For fractional melting in a one-component system with variable coefficients, f is zero, so (13) reduces to equation (11).

To examine the variable-coefficient case, we again used diopside as the example and treated it as a one-component system. The solidus curve predicted by the thermodynamic data given in Table 1 is shown in Figure 3a; the downward curvature results from the greater compressibility of the liquid relative to the solid. The same phase relations are shown in S-P space in Figure 3b; the curvature of each boundary of the two-phase field is higher than in the constant coefficient case, reflecting the $(dT/dP)_{2\phi}$ term in equations (6). Using these coefficients, we computed $F(P)$ from equation (8) and $-(dF/dP)$ from equation (13) subject to the constraint $f = F$ along the batch adiabat that intersects the solidus at 7 GPa. For fractional melting, we computed $-(dF/dP)$ along the path that intersects the solidus at 7 GPa using equation (13) subject to the constraint $f = 0$, and integrated to obtain $F(P)$. The results are shown in Figures 3c and 3d.

Comparison of Figures 2c and 3c shows that in systems with variable coefficients, the increase in productivity with increasing melt fraction due to the curvature of the solidus can be substantial for batch melting; in the case shown it leads to large (e.g., a factor of 5.7

between F=0 and F=.9) increases in productivity as melting proceeds. In fact, as shown by comparing the fractional fusion curves in Figure 2c and 3c, the increase in productivity due to curvature of the solidus in the more realistic case overwhelms the tendency for productivity to decrease due to the decreasing mass of the source and results in increasing productivity with progressive melting even for fractional fusion (although there must be a maximum and productivity must eventually decrease at high melt fraction, since melt fraction normalized by original source mass must for fractional melting asymptotically approach F=1 in equation 11). We note that equation (13) also shows that a solidus slope that is negative or less than the adiabatic gradient will generally lead to crystallization rather than melting with decreasing pressure at constant entropy (Albarède, 1983; Iwamori et al., 1995; Rumble, 1976).

The strong increase in productivity in the variable-coefficient one-component case reflects the increase in the slope of the solidus with decreasing pressure. The same effect is present in multicomponent systems, where the analogous controlling variable is $(\partial T/\partial P)_F$, the slope of a constant melt fraction contour; note that all such contours are collapsed onto the univariant solidus in P-T space in a one-component system but are arrayed between the solidus and the liquidus (and are not, in general, parallel to either) in multicomponent systems. The influence of the slopes of these contours on isentropic productivity will be referred to below as the "$(\partial T/\partial P)_F$ effect".

3b. Multicomponent systems

For the general case in a multicomponent system, the expression for -(dF/dP) for isentropic or incrementally isentropic melting paths with possible melt extraction is derived in the Appendix to this chapter:

$$-\frac{\mathrm{d}F}{\mathrm{d}P}=\left(\frac{\frac{C_{\mathrm{p}}^{s}+f(C_{\mathrm{p}}^{l}-C_{\mathrm{p}}^{s})}{T}\left(\frac{\partial T}{\partial P}\right)_{F}-\left[V^{s}\alpha^{s}+f(V^{l}\alpha^{l}-V^{s}\alpha^{s})\right]+\left(\frac{\partial S_{X}}{\partial P}\right)_{F}}{\left(\frac{C_{\mathrm{p}}^{s}+f(C_{\mathrm{p}}^{l}-C_{\mathrm{p}}^{s})}{\mathrm{T}\left(\frac{\partial F}{\partial T}\right)_{P}}\right)+\frac{(1-f)}{(1-F)}(S^{l}-S^{s})+\left(\frac{\partial S_{X}}{\partial F}\right)_{P}}\right), \qquad (14)$$

where the superscript s now refers to the bulk properties of the residual (usually polymineralic) solid assemblage and $(\partial S_X/\partial P)_F$ and $(\partial S_X/\partial F)_P$ are shorthand notation for terms that reflect the effects on S^l and S^s of changes in liquid and mineral compositions and of changes in the relative abundances of the minerals in the solid assemblage (see Appendix to this chapter; for related equations, see Iwamori et al., 1995; McKenzie, 1984; Verhoogen, 1965). Note that ΔS_{fus}, defined as the entropy difference between a solid and liquid of the same composition, does not appear in this expression. Most earlier thermodynamic treatments of adiabatic melting in multicomponent systems have equated $(S^l - S^s)$ or $(\partial S/\partial F)_{P,T}$ (which is equivalent to the sum of the last two terms in the denominator of (14)) with ΔS_{fus} for the bulk peridotite, which has undoubtedly led to inaccuracies. The essential first-order change from (13) is the presence of a term in the denominator involving the partial derivative of melt fraction with respect to temperature at constant pressure, $(\partial F/\partial T)_P$, which we call the isobaric productivity. In a one-component system, isobaric melting occurs at a unique temperature, so this quantity is infinite. Hence the first term in the denominator of (14) as well as the terms due to compositional and modal changes in the entropy of the phases vanish for one-component systems and this expression reduces to (13). For multicomponent systems, $(\partial F/\partial T)_P$ thus joins $(\partial T/\partial P)_F$ as a key source of variability in isentropic productivity. Note that the $1/T$ effect will

typically be of secondary importance in the multicomponent case, since it now contributes both to the numerator and denominator of the expression for (dF/dP).

In this section, we explore the origins and importance for isentropic productivity of variations in $(\partial F/\partial T)_P$ in a simple two-component binary phase loop and then in MELTS simulations of peridotite melting. We will emphasize that $(\partial F/\partial T)_P$ reflects changes in liquid and solid composition during melting via conservation of mass as expressed in the lever rule. We then demonstrate that variations in both $(\partial F/\partial T)_P$ and $(\partial T/\partial P)_F$ are needed for a reasonably accurate understanding of the variations in (dF/dP). We also show that variations of other parameters with melt fraction, including $(S^l - S^s)$, do not affect productivity variations by more than *ca.* 10%, even when phases are exhausted from the residue.

3c. Two-component systems.

Before considering isentropic melting, we first evaluate isobaric productivity in two-component systems. We approach the problem in this way because isobaric melting can be treated using familiar phase diagrams from which the effect of composition on productivity can be deduced easily and because we wish to isolate isobaric productivity from the other terms in the general expression for incrementally isentropic productivity (equation 14). In this exercise, we use as a model system a hypothetical binary *a*-*b* with complete solid solution in the solid and ideal mixing for both the liquid and solid solutions (Figure 4). End member *a* has the thermodynamic properties of diopside; end member *b* has similar properties, except the melting point at 1 bar is arbitrarily chosen to be 500 °C lower than that of *a*. Model parameters for the end members are listed in Table 1. We chose a complete solid solution model as our example rather than a eutectic or peritectic involving solid phases of fixed composition because all mantle phases are solid solutions and hence the phase loop captures the essential behavior of the natural system (except when a phase is exhausted on melting; see below); we chose this hypothetical binary rather than

the actual diopside-hedenbergite system because the exaggerated difference in melting points of the two end members allows the effects of a finite melting interval to be more easily seen.

3c (i). Isobaric melting. In a two component system, the productivity of isobaric melting with increasing temperature is simply a matter of conservation of mass. If we consider a system where the bulk composition is given by X_b, the mass fraction of component b, we can write

$$F\,X_b^l + (1-F)\,X_b^s = X_b \quad \text{or} \quad \mathrm{F} = \frac{(X_b - X_b^s)}{(X_b^l - X_b^s)}, \tag{15}$$

which is just a statement of mass balance (i.e., the familiar lever rule for graphical analysis of phase diagrams). For batch melting, differentiation of (15) leads to

$$\left(\frac{\partial F}{\partial T}\right)_P^{Batch} = -\left(\frac{\partial X_b^s}{\partial T}\right)_P\left(\frac{1}{X_b^l - X_b^s}\right) \quad \frac{(X_b - X_b^s)\left(\dfrac{\partial (X_b^l - X_b^s)}{\partial T}\right)_P}{(X_b^l - X_b^s)^2}. \tag{16}$$

For fractional melting the second term in (16) vanishes since the instantaneous solid composition is always equal to the bulk composition and source mass decreases as (1-F), which leads to

$$\left(\frac{\partial F}{\partial T}\right)_P^{Fractional} = \left(\frac{\partial X_b^s}{\partial T}\right)_P\left(\frac{1}{X_b^l - X_b^s}\right)(1\text{-}F). \tag{17}$$

(a more rigorous derivation of the expression for isobaric fractional melting requires starting from extensive variables as in the derivation in the Appendix to this chapter).

The inverse relationship between isobaric productivity and the compositional difference between coexisting liquid and solid (i.e., the $1/(X_b^l - X_b^s)$ factor) is generally the most important term in both equations (16) and (17) for the simple phase loop. The second term in (16) is important at high melt fraction (i.e., where $\mathrm{F} = (X_b - X_b^s)/(X_b^l - X_b^s)$ is large) or when the solids are fixed or nearly fixed in composition (note that the first term

goes to zero if the solid phases are fixed in composition); the derivative of solid composition in the first term is also important near the exhaustion of a phase from the residue when a multiphase residual assemblage is melting (see below). Equations (16) and (17) yield infinite $(\partial F/\partial T)_P$ during eutectic or peritectic melting.

The key effect of variable composition of the phases is to cause isobaric productivity to be small when the difference between liquid and solid compositions, $(X_b^l - X_b^s)$, is large. This is illustrated by the quantitative results (Figure 5) based on the calculated phase relations for our model binary phase loop (Figure 4a), in which the form of the melt fraction vs. temperature curve varies with bulk composition mostly according to whether the compositional difference between the liquid and solid initially increases or always decreases with increasing melt fraction. Melt fraction vs. temperature curves and isobaric productivity vs. temperature curves for batch and fractional melting of the bulk compositions X_b = 0.1, 0.25, 0.5, and 0.75 are shown in Figure 5. The dashed curves in Figures 5c and 5d plot the first term in equation (16); this is the initial isobaric productivity (i.e., at the solidus) as a function of bulk composition. The fractional fusion curves differ from the dashed curve only by a factor (1-F); the batch melting curves differ from the dashed curve according to the second term in (16), which increases with F and changes sign at the widest point on the phase loop (T=1393 K, $X_b^s = 0.15$, $X_b^l = 0.85$). Examination of the dashed curve in Figures 5c and 5d shows that in this example, the multiplication by $(\partial X_b^s/\partial T)_P$ in the first term of equation (16) contributes a strong asymmetry to the productivity function, which is otherwise dominated by the (nearly symmetric about 1393 K) inverse compositional distance term. The net effect of all these terms is that compositions with $X_b < 0.06$ show a melt fraction vs. temperature curve for batch melting that is always concave up (i.e., an isobaric productivity that always increases as melting proceeds). For fractional melting, productivity always increases for $X_b < 0.03$. For more b-rich bulk compositions, the melt fraction vs. temperature curves (such as those illustrated

in Figures 5a and 5b for X_b = 0.25, 0.5 and 0.75) are initially concave down, but concave up at higher F. The critical bulk X_b below which the melt fraction vs. temperature curve is everywhere concave up depends on the shape of the phase loop; in the diopside-hedenbergite system where the phase loop is much narrower, it occurs at $X_{Hd} \sim 0.4$ for batch melting and $X_{Hd} \sim 0.2$ for fractional melting. In the forsterite-fayalite system the corresponding values are $X_{Fa} \sim 0.14$ for batch melting and $X_{Fa} \sim 0.1$ for fractional melting. The location of this critical X_b cannot be read directly off the phase diagram; it depends on all the terms in (16) or (17) and does not correspond to the widest point on the phase loop. Note again that in the special case where the solid residue is fixed in composition (i.e., only batch melting is continuous in temperature), the first term in (16) vanishes and the difference in melt and solid composition always decreases with F, so the geometric effect leads to the melt fraction vs. temperature curve being everywhere concave up.

3c (*ii*). *Isentropic melting*. There is no simple two-dimensional phase diagram with which to portray isentropic melting for a binary loop. Inspection of the general expression for isentropic melting (equation 14) shows that the geometric effect related to the compositional distance between liquid and solid (i.e., the $(\partial F/\partial T)_P$ term discussed in the preceding paragraphs) is superimposed on the $1/T$ and $(\partial T/\partial P)_F$ effects that control isentropic productivity in one-component systems. The relationship among the terms in these equations can be visualized by examining Figures 4b through 4f. Figure 4b shows S vs. X_b at 1 bar for the model binary phase loop; Figures 4c through 4f show a series of simplified S vs. X_b sections on the same scale at successively higher pressures. With increasing pressure, the entire phase loop moves up (i.e., to higher values of specific entropy); in the one-component diopside-like end member a, this increase is illustrated in Figure 3b. Isentropic melting of a particular bulk composition can then be visualized as the movement of the loop over a particular fixed point (X_b = 0.1, S = 663 J/mol/K in this example) as pressure decreases.

Although the shape of the phase loop is complex and changes with pressure, its overall downward movement with decreasing pressure tends to contribute, for any composition, to increasing productivity with decreasing P (i.e., a concave up F vs. P diagram) just as it does in the one-component end members. This reflects the $1/T$ and $(\partial T/\partial P)_F$ dependencies described above. The melt composition effect is discernible in the rotation of the tie lines (in this case little influenced by decompression) towards the vertical from the center to the edges of the loop, which results in changes in the difference in composition between the solid and liquid with increased melting. Although it is not as easy to read as the diagrams for the isobaric melting case, examination of Figure 4 shows that for a-rich compositions, the compositional difference between solid and melt decreases with decreasing pressure (and increasing melt fraction). Just as in the isobaric melting case, this leads to a purely geometric contribution tending to increase productivity as pressure decreases. However, for more b-rich compositions, the compositional difference between solid and liquid initially increases with progressive isentropic melting; as a consequence, when this increase is quite pronounced, complex melt fraction vs. P functions (including initially decreasing productivity) can result from the combination of this with the $1/T$ and $(\partial T/\partial P)_F$ effects.

Results for isentropic melting in the model binary system are shown in Figure 6 for isentropic batch and fractional melting of the bulk composition $a_{90}b_{10}$ starting at 10 GPa. As anticipated in the above discussion of Figures 4c-f, isentropic productivity increases with progressive melting. For fractional melting, Figure 6c shows both the productivity normalized to original source mass, the usage we adopt, and the productivity relative to unit mass of solid present at any pressure (dotted line, labeled "local fractional"). It is interesting to note that (except exactly at the solidus where they are identical) the local productivity of fractional melting in this system is lower than the productivity of batch melting at low melt fraction but slightly greater at high melt fraction (similar to models of

peridotite melting; Hirschmann et al., 1994). Comparison of Figures 5 and 6 shows that the contribution of the $(\partial T/\partial P)_F$ effect can lead to increasing isentropic productivity at all F even for compositions such as X_b=0.1 that have initially decreasing isobaric productivity.

To demonstrate the contributions of the $(\partial T/\partial P)_F$ and $(\partial F/\partial T)_P$ terms to variations in isentropic productivity, we calculated productivity curves by substituting these quantities into equation (14), assuming all other parameters (C_p^s, C_p^l, T, f, $V^s\alpha^s$, $V^l\alpha^l$, and $(S^l - S^s)$) are constant at their values on the solidus at 10 GPa (although $(1\text{-}F)/(1\text{-}f)$ is also allowed to vary so that fractional melting is normalized properly and all terms due to compositional and modal changes in the entropy of the phases, i.e. $(\partial S_X/\partial P)_F$ and $(\partial S_X/\partial F)_P$, are set to zero). We also tried allowing only one of $(\partial T/\partial P)_F$ and $(\partial F/\partial T)_P$ to vary and holding the other constant along with the above list of parameters at its value on the solidus; the resulting 3 curves (labeled according to which quantity or quantities we allowed to vary) are shown in Figure 6d. Only when we allow both $(\partial T/\partial P)_F$ and $(\partial F/\partial T)_P$ to vary do we reproduce the isentropic productivity function reasonably well, demonstrating that variations of *both* parameters control the detailed shape of the productivity function. Note that the chosen bulk composition in this model system has a total isobaric melting interval (i.e., an average $(\partial F/\partial T)_P$) for $0.1 < X_b < 0.9$ comparable to that of natural peridotite (Takahashi, 1986); hence the quantitative importance of $(\partial F/\partial T)_P$ relative to other sources of productivity variation in equation (14) in this two-component system is comparable to its importance in peridotite melting.

3d. Multicomponent systems

Equation (14) shows how knowledge of $(\partial F/\partial T)_P$, $(\partial T/\partial P)_F$, and values of parameters such as $(S^l - S^s)$, C_p, T, and $V\alpha$ can be translated into predictions of isentropic productivity and its variability for any system of arbitrary compositional complexity and variance. There are, however, factors other than those we have considered in the model systems treated above that contribute to the variability of these parameters and thus to

variations in productivity during isentropic melting. For example, we have emphasized that the dominant term for isobaric melting along a binary phase loop is the inverse dependence on the compositional distance between liquid and solid. However, discontinuous reactions and phase exhaustion must also play important roles in productivity for polymineralic assemblages. We have not presented simple examples involving such phenomena, but they are readily treated in terms of the same parameters discussed above. For example, the exhaustion of a phase restricts the compositional variations available to the solid residue. This translates into a discontinuous drop in the rate of change of the composition of the solid with temperature (equivalent to the $(\partial X_b^s/\partial T)_P$ term in equations 16 and 17) and therefore results in a discontinuous drop in productivity even though the compositional distance (equivalent to $X_b^l - X_b^s$ in 16 and 17) is continuous. The effect of the derivative of bulk solid composition on productivity is also evident at the end of eutectic or peritectic melting in a simple system (where the change from infinite $(\partial X_b^s/\partial T)_P$ and $(\partial F/\partial T)_P$ to finite values results in a corresponding decrease in $-dF/dP$ in equation 14), at the loss of a phase during cotectic melting in a ternary system, and at the exhaustion of clinopyroxene during melting of natural peridotite. Note that in none of our simulations of batch fusion have we observed a *drop* in productivity except on phase exhaustion (or addition, as in the case of the spinel-plagioclase transition; Asimow et al., 1995a).

4. Model peridotite system

Given the simple rules developed above for one- and two-component systems and their generalization to multicomponent systems, we are now in a position to anticipate the productivity function of isentropically melting mantle peridotite during batch fusion and of incrementally isentropic fractional fusion. Although a rigorous analysis is needed to understand the interaction of all the variables controlling productivity in a complex, multicomponent system, the simple arguments developed here give considerable insight

into the overall behavior. For example, our analysis makes clear that isentropic productivity is very unlikely ever to be even approximately constant. In addition, it suggests that the concave up melt fraction vs. P functions predicted for peridotite melting by the MELTS algorithm (Asimow et al., 1995a; Hirschmann et al., 1994) are robust features of the behavior of natural peridotite.

We have examined quantitatively controls on productivity using the results of isentropic batch and fractional MELTS calculations on a model peridotite. We used a nine-component model composition in the system SiO_2-TiO_2-Al_2O_3-Cr_2O_3-Fe_2O_3-FeO-MgO-CaO-Na_2O (composition from Hart and Zindler, 1986). Choosing an adiabat that intersects the solidus at 22 kbar, we calculated batch melting by minimizing H at fixed S, P, and bulk composition to obtain T, F, and the compositions of coexisting liquid and solids. For fractional fusion, we searched in pressure for the point along the isentrope that has a fixed incremental melt fraction ($dF = 0.001$) and then took the entropy and composition of the residue as the reference for the next step. Batch isentropic productivity was calculated by differentiation of the F vs. P results, and fractional productivity was determined by dividing dF by the pressure difference between successive melt extractions. Figure 7 shows the calculated productivity and melt fraction as functions of pressure for batch and fractional melting.

We have evaluated the extent to which the sources of variation isolated above (i.e., $(\partial T/\partial P)_F$ and $(\partial F/\partial T)_P$) combine to control variations in MELTS-predicted peridotite productivity via an exercise similar to the analysis of the binary case above. We assumed all other parameters (C_p^s, C_p^l, T, f, $V^s\alpha^s$, $V^l\alpha^l$, and $(S^l - S^s)$, but not $(1\text{-}F)/(1\text{-}f)$, which normalizes fractional melting, or $(\partial S_X/\partial P)_F$ and $(\partial S_X/\partial F)_P$, which we neglect altogether by setting them to zero) in equation (14) to be constant (at their 11 kbar values, i.e., at the midpoint of the melting paths) and calculated the isentropic productivity along the melting path based on several different sets of values for $(\partial T/\partial P)_F$ and $(\partial F/\partial T)_P$: (i) the actual

value of $(\partial T/\partial P)_F$ at each point on the melting path, with $(\partial F/\partial T)_P$ held constant at its 11 kbar value; (ii) the actual value of $(\partial F/\partial T)_P$ at each point on the melting path, with $(\partial T/\partial P)_F$ held constant at its 11 kbar value; and (iii) the actual values of both $(\partial T/\partial P)_F$ and $(\partial F/\partial T)_P$ along the melting path. The resulting curves are shown in Figure 7, labeled by what was allowed to vary. For both batch and fractional fusion, shown in Figures 7a and 7b, case (ii) captures the general form of the isentropic productivity function, including the rise to a peak at the exhaustion of clinopyroxene and the sharp drop-off. Case (iii), however, shows much better quantitative agreement (although differences are noticeable where productivity is large), demonstrating as for the binary case presented earlier that variations in *both* $(\partial T/\partial P)_F$ and $(\partial F/\partial T)_P$ must be taken into account to approximate accurately the productivity function. The fits to melt fraction for case (iii) shown in Figures 7c and 7d are also very good, indicating that the overall amounts of melting during batch and fractional fusion of peridotite can be precisely modeled using equation (14) and that variations in T, $(S_l - S_s)$, C_p, $V\alpha$ and compositional derivatives are of secondary importance compared to $(\partial T/\partial P)_F$ *and* $(\partial F/\partial T)_P$. We emphasize that this exercise is entirely based on the internally consistent nature of the MELTS calculation; consequently, although it helps to isolate the key parameters in the peridotite productivity function as predicted by MELTS, it does not directly address the accuracy of the MELTS results for melt production in nature.

The good qualitative match to the isentropic productivity obtained solely by varying $(\partial F/\partial T)_P$ (Figures 7a and 7b) implies that the source of much of the variation in isentropic productivity can be understood by examining the controls on $(\partial F/\partial T)_P$. Just as in the two-component system discussed above, the shape of the isobaric productivity function reflects the compositions of coexisting melt and residue and is dominated by the rate of change of the compositional difference between them (except near the exhaustion of a phase in the more complex system). Near-solidus melts of peridotite differ significantly in

composition from the coexisting residue, and the composition of the liquid changes rapidly with increased melting at low melt fractions, becoming more similar to the composition of the residue with increased melting (e.g., in the sense that the melts become richer in normative olivine and poorer in normative plagioclase and incompatible elements, and thus more similar to peridotite; Baker and Stolper, 1994; Kushiro, 1996; Takahashi and Kushiro, 1983). Our analysis indicates that this "geometric effect", which influences the $(\partial F/\partial T)_P$ function and hence the isentropic productivity, is the main factor leading to low productivity near the solidus and the strongly concave up melt fraction vs. pressure function predicted by the MELTS calculations. It must be emphasized that peridotite melting is neither invariant nor pseudo-invariant (there are many more components than phases and hence in both MELTS calculations and experiments the compositions of liquids vary continuously at all melt fractions) and thus eutectic and peritectic melting are very poor models for peridotite. The important point is that the increase in isentropic productivity with progressive melting in these calculations is dominated by the tendency for the liquids to be initially very distant from the source composition (due especially to high concentrations of incompatible elements like Na_2O) and to move towards the bulk composition with progressive melting.

As illustrated by Figure 7, the discontinuous changes in isentropic productivity associated with phase exhaustion are also precisely mirrored by changes in isobaric productivity; in both cases this reflects the rate of change of the residual solid composition (analogous to the $(\partial X_b^S/\partial T)_P$ parameter in 16 and 17). As the exhaustion of clinopyroxene is approached during batch melting, the bulk residual solid composition changes significantly and its temperature derivative is large; the result is a very high productivity in this region. At the actual disappearance of clinopyroxene from the residue, the derivative of bulk solid composition decreases discontinuously, resulting in a drop in productivity. In the fractional case, the shape of the productivity function just before clinopyroxene

exhaustion is somewhat different (Figure 7a vs. 7b; note that this difference is not apparent in the F vs. P, Figure 7c vs. 7d); the decrease in productivity in anticipation of clinopyroxene exhaustion during fractional fusion probably reflects the fact that the jadeite component of clinopyroxene is nearly exhausted a few kilobars before the phase disappears, leading to a decrease in the temperature derivative of clinopyroxene composition and hence a decrease in both isobaric and isentropic productivity in advance of the much larger discontinuous drop at cpx-out. This example illustrates quite clearly a point made in the Introduction, that efforts to model or understand the productivity of peridotite melting that do not include the effects of phase equilibria and changing solid and liquid compositions as melting progresses are very unlikely to capture the essence of the isentropic melting process.

The predicted overall increase in isentropic productivity with melt fraction in the batch melting case, punctuated by drops in productivity upon exhaustion of phases from the residue, appears to be a general feature of simple systems with solid-solution, particularly when the solid solution(s) are close to the high-temperature end member(s). MELTS calculations suggest that it is also a robust feature of the more complex multicomponent peridotite system. The productivity function for fractional fusion can be more complex, but it is also likely to have a concave upward shape at low degrees of melting of relatively fertile peridotite. Note that productivity during fractional fusion of fertile peridotite, although lower than that of batch fusion at low melt fraction (but not exactly at the solidus, where they must be equal), is predicted to be comparable to that of batch fusion after several percent melting (Figures 7a and 7b; see also Hirschmann et al., 1994). Although contrary to most previous speculations (Langmuir et al., 1992; Niu and Batiza, 1991), recent experimental work appears to confirm this prediction (Hirose and Kawamura, 1994).

5. Conclusions

There is no thermodynamic basis for assuming a constant rate of melt generation during isentropic depressurization. Even in a simple one-component system, the isentropic productivity depends on $1/T$ and the slope of the solidus, leading to increasing productivity with progressive melting (i.e., the melt fraction vs. pressure function is concave up). Although other parameters appear in the general expression for isentropic productivity in multicomponent systems, the most important factors are the slopes of equal melt-fraction contours, $(\partial T/\partial P)_F$, and the isobaric productivity, $(\partial F/\partial T)_P$, both of which can be determined, in principle, from relatively straightforward phase equilibrium experiments. The isobaric productivity is the principal source of the variability of productivity during isentropic melting of peridotite, and it can be reduced to a simple statement of mass balance if the compositions of coexisting melt and residue are known. At low melt fractions, changes in the isobaric melt productivity are dominated by the decrease with progressive melting in the compositional difference between liquid and bulk residual solids.

Several authors have constructed models of peridotite melting in which $(\partial F/\partial T)_P$ is initially very high and decreases with progressive melting, based largely on analogy with low variance melting in simple systems (e.g., at a eutectic or peritectic). Thermodynamic modeling using MELTS, however, does not predict such behavior. In contrast, initial liquids are predicted to differ significantly in composition from the coexisting bulk solid and to move closer in composition to the residue with progressive melting, leading to low productivity at the solidus and increases in productivity with increasing melt fraction (i.e., the same variations in productivity found for analogous simple systems). The same effects carry over into isentropic productivity. There are additional complexities related to phase changes and phase exhaustions, but their impact on isentropic productivity can also be understood by examining these same effects.

In summary, analysis of simple systems and thermodynamic calculations on complex peridotite compositions lead us to predict that isentropic melting of typical mantle peridotites will be characterized by an overall increase in isentropic productivity with melt fraction in the batch melting case, punctuated by drops in productivity upon exhaustion of each phase from the residue. The productivity function for fractional fusion can be more complex, but we predict that the concave upward shape of the melt fraction vs. pressure curve predicted for the batch fusion case is also likely to be a characteristic of low degrees of fractional melting of relatively fertile peridotite.

Appendix to chapter 3

Here we derive a general expression for isentropic and for incrementally isentropic melt productivity in multicomponent systems. We consider only processes that obey the restriction

$$dS = S^l \, dM \tag{A1}$$

where S is the extensive entropy of the system, S^l is the specific entropy of the liquid phase, and M is the mass of the system. We also require that the mass of liquid in the source region, M^l, be a function only of the mass of solid in the source region, M^s, and constants such that

$$\frac{dM^l}{dM^s} = \left(\frac{\partial M^l}{\partial M^s}\right)_Y \text{ and } \left(\frac{\partial M^l}{\partial Y}\right)_{M^s} = 0 \tag{A2}$$

for any variable Y. For multicomponent systems, the superscript s refers to bulk properties of the polymineralic solid assemblage. These constraints limit the processes to those for which entropy change of the system only occurs by extraction of melt and for which there is a strict coupling between melt production and melt extraction. For example, for batch fusion, $dM=0$ (i.e., $dM^l = -dM^s$), so (A1) means that the process is isentropic. For fractional fusion, the mass of the system decreases due to removal of liquid (i.e., $dM = dM^s$), and the entropy of the system decreases by the amount carried away by the liquid;

since this is the only way in which the entropy of the system changes, fractional fusion subject to the constraint of (A1) can be envisioned as a series of infinitesimal increments of isentropic fusion followed by complete melt removal.

Given (A1) and (A2), the changes in the state of the system are entirely determined by two variables, so we can write the total differential of $\boldsymbol{S}$ in terms of P and $\boldsymbol{M^s}$:

$$\mathrm{d}\boldsymbol{S} = \left(\frac{\partial \boldsymbol{S}}{\partial P}\right)_{\boldsymbol{M}^s} \mathrm{d}P + \left(\frac{\partial \boldsymbol{S}}{\partial \boldsymbol{M}^s}\right)_{P} \mathrm{d}\boldsymbol{M}^s . \tag{A3}$$

Since $\boldsymbol{M} = \boldsymbol{M^l} + \boldsymbol{M^s}$, (A1) and (A3) lead to

$$\left(\frac{\partial \boldsymbol{S}}{\partial P}\right)_{\boldsymbol{M}^s} \mathrm{d}P + \left(\frac{\partial \boldsymbol{S}}{\partial \boldsymbol{M}^s}\right)_{P} \mathrm{d}\boldsymbol{M}^s = S^l \mathrm{d}\boldsymbol{M}^l + S^l \mathrm{d}\boldsymbol{M}^s . \tag{A4}$$

Dividing (A4) by dP, rearranging, and applying the chain rule

$$\frac{\mathrm{d}\boldsymbol{M}^l}{\mathrm{d}P} = \frac{\mathrm{d}\boldsymbol{M}^l}{\mathrm{d}\boldsymbol{M}^s}\frac{\mathrm{d}\boldsymbol{M}^s}{\mathrm{d}P} \tag{A5}$$

leads to an expression for the change in solid mass with pressure:

$$\frac{\mathrm{d}\boldsymbol{M}^s}{\mathrm{d}P} = \frac{\left(\frac{\partial \boldsymbol{S}}{\partial P}\right)_{\boldsymbol{M}^s}}{S^l + S^l \frac{\mathrm{d}\boldsymbol{M}^l}{\mathrm{d}\boldsymbol{M}^s} - \left(\frac{\partial \boldsymbol{S}}{\partial \boldsymbol{M}^s}\right)_{P}} . \tag{A6}$$

We now evaluate the partial derivatives that appear in (A6). We differentiate

$$\boldsymbol{S} = \boldsymbol{M}^s S^s + \boldsymbol{M}^l S^l \tag{A7}$$

to obtain

$$\left(\frac{\partial \boldsymbol{S}}{\partial P}\right)_{\boldsymbol{M}^s} = \boldsymbol{M}^s \left(\frac{\partial S^s}{\partial P}\right)_{\boldsymbol{M}^s} + \boldsymbol{M}^l \left(\frac{\partial S^l}{\partial P}\right)_{\boldsymbol{M}^s} + S^l \left(\frac{\partial \boldsymbol{M}^l}{\partial P}\right)_{\boldsymbol{M}^s} . \tag{A8}$$

The restriction (A2) causes the last term in (A8) to vanish. The evaluation of the remaining terms in (A8) is related to equations (6a) and (6b) in the text, except that partial derivatives at constant $\boldsymbol{M^s}$ appear in place of total derivatives along the 2-phase boundary, and more importantly we must now include derivatives that describe changes in phase compositions:

$$\mathrm{d}S^l = \left(\frac{\partial S^l}{\partial T}\right)_{P,X^l} \mathrm{d}T + \left(\frac{\partial S^l}{\partial P}\right)_{T,X^l} \mathrm{d}P + \sum_{i=1}^{n^l} \left(\frac{\partial S^l}{\partial X_i^l}\right)_{T,P,X_{j\neq i}^l} \mathrm{d}X_i^l \tag{A9a}$$

$$\mathrm{d}S^s = \left(\frac{\partial S^s}{\partial T}\right)_{P,X^s} \mathrm{d}T + \left(\frac{\partial S^s}{\partial P}\right)_{T,X^s} \mathrm{d}P + \sum_{k=1}^{n^s} \left[S^k d\gamma^k + \gamma^k \sum_{i=1}^{n^k} \left(\frac{\partial S^k}{\partial X_i^k}\right)_{T,P,X_{j\neq i}^k} \mathrm{d}X_i^k \right], \tag{A9b}$$

where X_i^l is the mass fraction of component i in the n^l component liquid phase and $\left(\frac{\partial S^l}{\partial X_i^l}\right)_{T,P,X_{j\neq i}^l}$ should be recognized as the partial specific entropy of component i in the liquid. In (A9b) S^s represents a weighted sum over n^s solid phases, γ^k is the mass fraction of the kth solid phase in the bulk solid assemblage, S^k is the specific entropy of the kth phase, X_i^k is the mass fraction of component i in the kth solid phase of n^k components, and $\left(\frac{\partial S^k}{\partial X_i^k}\right)_{T,P,X_{j\neq i}^k}$ is the partial specific entropy of component i in solid phase k. All of these new quantities are, in general, functions of temperature, pressure, and bulk composition. For brevity in what follows we define the entire last term in (A9a) as $\mathrm{d}S_X^l$ and the entire last term in (A9b) as $\mathrm{d}S_X^s$, since they represent the changes in S^l and S^s due to compositional and/or modal changes in the liquid and bulk solid respectively. We note that these terms have been neglected without comment in all previous treatments of isentropic melting of which we are aware. In most cases, first-order approximations of productivity remain reasonable when $\mathrm{d}S_X^l$ and $\mathrm{d}S_X^s$ are neglected.

From (A9a) and (A9b) we can obtain

$$\left(\frac{\partial S^l}{\partial P}\right)_{M^s} = \frac{C_\mathrm{p}^l}{T}\left(\frac{\partial T}{\partial P}\right)_{M^s} - V^l\alpha^l + \left(\frac{\partial S_X^l}{\partial P}\right)_{M^s} \tag{A9c}$$

$$\left(\frac{\partial S^s}{\partial P}\right)_{M^s} = \frac{C_\mathrm{p}^s}{T}\left(\frac{\partial T}{\partial P}\right)_{M^s} - V^s\alpha^s + \left(\frac{\partial S_X^s}{\partial P}\right)_{M^s}, \tag{A9d}$$

where the last terms are abbreviations for sums similar to those in (A9a) and (A9b) except $(\partial X_i^l/\partial P)_{M^s}$ is substituted for $\mathrm{d}X_i^l$, $(\partial\gamma^k/\partial P)_{M^s}$ for $\mathrm{d}\gamma^k$, and $(\partial X_i^k/\partial P)_{M^s}$ for $\mathrm{d}X_i^k$. Using the intensive variable $f = \boldsymbol{M}^l/(\boldsymbol{M}^l + \boldsymbol{M}^s)$ for the mass fraction of liquid in the system and combining (A8), (A9c), and (A9d) leads to

$$\left(\frac{\partial \boldsymbol{S}}{\partial P}\right)_{M^s} = (\boldsymbol{M}^s + \boldsymbol{M}^l)\left(\frac{C_\mathrm{p}^s + f(C_\mathrm{p}^l - C_\mathrm{p}^s)}{T}\left(\frac{\partial T}{\partial P}\right)_{M^s} - \left[V^s\alpha^s + f(V^l\alpha^l - V^s\alpha^s)\right] + f\left(\frac{\partial S_X^l}{\partial P}\right)_{M^s} + (1-f)\left(\frac{\partial S_X^s}{\partial P}\right)_{M^s}\right) \tag{A10}$$

and below for brevity we will use the definition $\left(\frac{\partial S_X}{\partial P}\right)_{M^s} \equiv f\left(\frac{\partial S_X^l}{\partial P}\right)_{M^s} + (1-f)\left(\frac{\partial S_X^s}{\partial P}\right)_{M^s}$.

Next we take the partial derivative of (A7) with respect to M^s at constant P:

$$\left(\frac{\partial S}{\partial M^s}\right)_P = S^s + S^l\left(\frac{\partial M^l}{\partial M^s}\right)_P + M^s\left(\frac{\partial S^s}{\partial M^s}\right)_P + M^l\left(\frac{\partial S^l}{\partial M^s}\right)_P . \qquad \text{(A11)}$$

To simplify (A11) we can obtain from (A9a) and (A9b):

$$\left(\frac{\partial S^l}{\partial M^s}\right)_P = \frac{C_p^l}{T}\left(\frac{\partial T}{\partial M^s}\right)_P + \left(\frac{\partial S_X^l}{\partial M^s}\right)_P \text{ and } \left(\frac{\partial S^s}{\partial M^s}\right)_P = \frac{C_p^s}{T}\left(\frac{\partial T}{\partial M^s}\right)_P + \left(\frac{\partial S_X^s}{\partial M^s}\right)_P , \qquad \text{(A12)}$$

where again the last terms in each expression are defined similarly to the last terms in (A9a) and (A9b) except that partial derivatives with respect to M^s at constant P replace all the total differentials, which together with the definition of f and (A2) lead to

$$\left(\frac{\partial S}{\partial M^s}\right)_P = S^s + S^l\frac{dM^l}{dM^s} + (M^s+M^l)\left(\frac{C_p^s+f(C_p^l-C_p^s)}{T\left(\frac{\partial M^s}{\partial T}\right)_P} + f\left(\frac{\partial S_X^l}{\partial M^s}\right)_P + (1-f)\left(\frac{\partial S_X^s}{\partial M^s}\right)_P\right), \qquad \text{(A13)}$$

and for further brevity we define $\left(\frac{\partial S_X}{\partial M^s}\right)_P \equiv f\left(\frac{\partial S_X^l}{\partial M^s}\right)_P + (1-f)\left(\frac{\partial S_X^s}{\partial M^s}\right)_P$.

We now substitute (A10) and (A13) into (A6) to obtain our final expression in terms of extensive mass variables:

$$-\frac{dM^s}{dP} = \frac{\frac{C_p^s + f(C_p^l - C_p^s)}{T}\left(\frac{\partial T}{\partial P}\right)_{M^s} - \left[V^s\alpha^s + f(V^l\alpha^l - V^s\alpha^s)\right] + \left(\frac{\partial S_X}{\partial P}\right)_{M^s}}{\left(\frac{C_p^s + f(C_p^l - C_p^s)}{T\left(\frac{\partial M^s}{\partial T}\right)_P}\right) - \frac{(S^l - S^s)}{(M^s+M^l)} + \left(\frac{\partial S_X}{\partial M^s}\right)_P}, \qquad \text{(A14)}$$

where we retain $S^l - S^s$ and $(\partial S_X/\partial M^s)_P$ instead of attempting to define the last two terms in the denominator as ΔS_{fus} since this does not correspond to the common understanding of the meaning of ΔS_{fus}. Now the definition of $F = 1 - (M^s/M^o)$, the fraction of the initial solid mass that has been melted, gives

$$\frac{dF}{dP} = -\frac{1}{M^o}\frac{dM^s}{dP}, \left(\frac{\partial F}{\partial Y}\right)_P = -\frac{1}{M^o}\left(\frac{\partial M^s}{\partial Y}\right)_P, \text{ and } \left(\frac{\partial Y}{\partial P}\right)_F = \left(\frac{\partial Y}{\partial P}\right)_{M^s}, \qquad \text{(A15)}$$

for any variable Y (including notably T and S_X, which can be shown using the definitions above), which relations together with the equation $(1 - F) / (1 - f) = (M^s+M^l) / M^o$ allow us to eliminate all extensive variables from (A14) and produce our final productivity equation:

$$-\frac{dF}{dP}=\left(\frac{\frac{C_p^s+f(C_p^l-C_p^s)}{T}\left(\frac{\partial T}{\partial P}\right)_F-\left[V^s\alpha^s+f(V^l\alpha^l-V^s\alpha^s)\right]+\left(\frac{\partial S_X}{\partial P}\right)_F}{\left(\frac{C_p^s+f(C_p^l-C_p^s)}{T\left(\frac{\partial F}{\partial T}\right)_P}\right)+\frac{(1-f)}{(1-F)}(S^l-S^s)+\left(\frac{\partial S_X}{\partial F}\right)_P}\right). \qquad \text{(A16)}$$

(A16) can be simplified directly for batch and fractional melting by taking $F=f$ and $f=0$, respectively. Furthermore, (A16) reduces to the correct form (equation 13) for one-component systems, where (i) it is straightforward to set $\Delta S_{fus}=(S^l-S^s)$ and there are no S_X terms since composition is constant and only one solid phase can participate in melting except at an invariant point, (ii) the last two terms in (A11) and hence the first term in the denominator of (A16) vanish since $(\partial T/\partial F)_P=0$ when isobaric melting takes place at a unique temperature, and (iii) $(\partial T/\partial P)_F=(dT/dP)_{2\phi}$ since all melting is restricted to the univariant two-phase curve. Finally, (A16) can be reduced to the constant coefficient one-component case (equation 12) since

$$\Delta S_{fus}(P,T)=\Delta S_{fus}(P_o,T_o)+\int_{T_o}^{T}\frac{(C_p^l-C_p^s)}{T}dT+\int_{P_o}^{P}(V^l\alpha^l-V^s\alpha^s)dP \qquad \text{(A17)}$$

means that constant ΔS_{fus} also requires $(C_p^l-C_p^s)=0$ and $(V^l\alpha^l-V^s\alpha^s)=0$.

We also include here the expression for calculating the P-T path of upwelling material undergoing any of the melting processes described by (A1) and (A2). For batch melting it is simple to show

$$\left(\frac{\partial T}{\partial P}\right)_S=\left(\frac{\partial T}{\partial P}\right)_F+\frac{\left(\frac{\partial F}{\partial P}\right)_S}{\left(\frac{\partial F}{\partial T}\right)_P} \qquad \text{(A18)}$$

(e.g., Albarède, 1992). A simple derivation beginning from the total differential of $\boldsymbol{M}^s$ expressed in terms of P and T followed by substitution of F for $\boldsymbol{M}^s$ leads to the corresponding result for (dT/dP) subject to (A1) rather than constant S:

$$\frac{dT}{dP}=\left(\frac{\partial T}{\partial P}\right)_F+\frac{\frac{dF}{dP}}{\left(\frac{\partial F}{\partial T}\right)_P}. \qquad \text{(A19)}$$

Table 1: Thermophysical properties of Di (Figure 2, 3) and *a*-*b* binary[a] (Figures 4,5,6)

parameter	diopside & *a* solids	*b* solid	di & *a* liqs	*b* liquid	units
S_o (298 K)	142.5 [b]	174.2			J/mol/K
H_o (298 K)	-3200.583 [b]	-2842.221			kJ/mol
V_o (1664 K)	69.11 [b]	same	82.34 [c]	same	m^3/mol x10^{-6}
T_{fus} (1 bar)	1664 K	1164 K			
ΔS_{fus} (1 bar)	82.88 [e]	same			J/mol/K
K_{T0}	90.7 [c]	same	21.9 [d]	24	GPa
K_T'	4.5 [c]	same	6.9 [d]	6.9	
α	3.2 x 10^{-5} [c]	same	6.5 x10^{-5} [c]	same	K^{-1}
Cp	305.41-160.49 $T^{-0.5}$ - 71.66 x10^5 T^{-2} + 92.184 x10^7 T^{-3} [b]	same	353 [c]	same	J/mol/K

a. For binary example, end member *a* is identical to diopside, end member *b* is selected to have a 1 bar melting point 500 K lower. Unreferenced quantities for *b* are chosen arbitrarily to give well-behaved binary phase-loop up to 10 GPa. b. Berman (1988). c. Rigden et al. (1989) and sources therein. d. Lange and Carmichael (1990). e. Stebbins et al. (1983).

Figure 1. Schematic comparison of enthalpy- and entropy-conservation during adiabatic melting. (a) In *P-T* space, a parcel of adiabatically upwelling mantle intersects its solidus at P_0, state *1*. At lower pressure P_f, the metastable extension of the solid adiabat is state *2*. The stable partially molten state *3* is obtained by an adiabatic, isobaric (i.e., isenthalpic) process whereby the enthalpy recovered by cooling from state *2* to state *3* equals that required to melt up to some degree of melting *F*. State *4* is reached by reversible, adiabatic (i.e., isentropic) melting from state *1*. (b) In *H-S* space, the difference between the two adiabatic processes (the isentropic path from $1 \rightarrow 4$, shown as a gray arrow, vs. the path from $1 \rightarrow 2 \rightarrow 3$, shown as black arrows) is shown for a hypothetical one-component system. The partially molten, stable state *4* is reached by adiabatic and reversible upwelling from the stable solid state *1* (on the solidus at P_0); the direct path from $1 \rightarrow 4$ is accomplished in a series of infinitesimal, reversible, adiabatic decompression steps; this state is clearly the minimum possible H for this S at P_f. State 2 is the metastable solid state at P_f reached by reversible, adiabatic (i.e., constant S) decompression from state 1 at P_0. State *3* is shown to be the stable, partially molten state on the tie-line between solid and liquid at P_f that has the same enthalpy as state *2* (reached by an irreversible, adiabatic, isobaric path at P_f that maximizes S). Clearly, state *3* has higher *H* and higher *S* than state *4*. Furthermore, application of the lever rule along the tie-line shows that state *3* has higher *F* than state *4*. Returning to (a), note that in a multicomponent system state *3* generally also has higher *T* than state *4*, although in a one-component system both states lie on the solidus and are indistinguishable in *P-T* space.

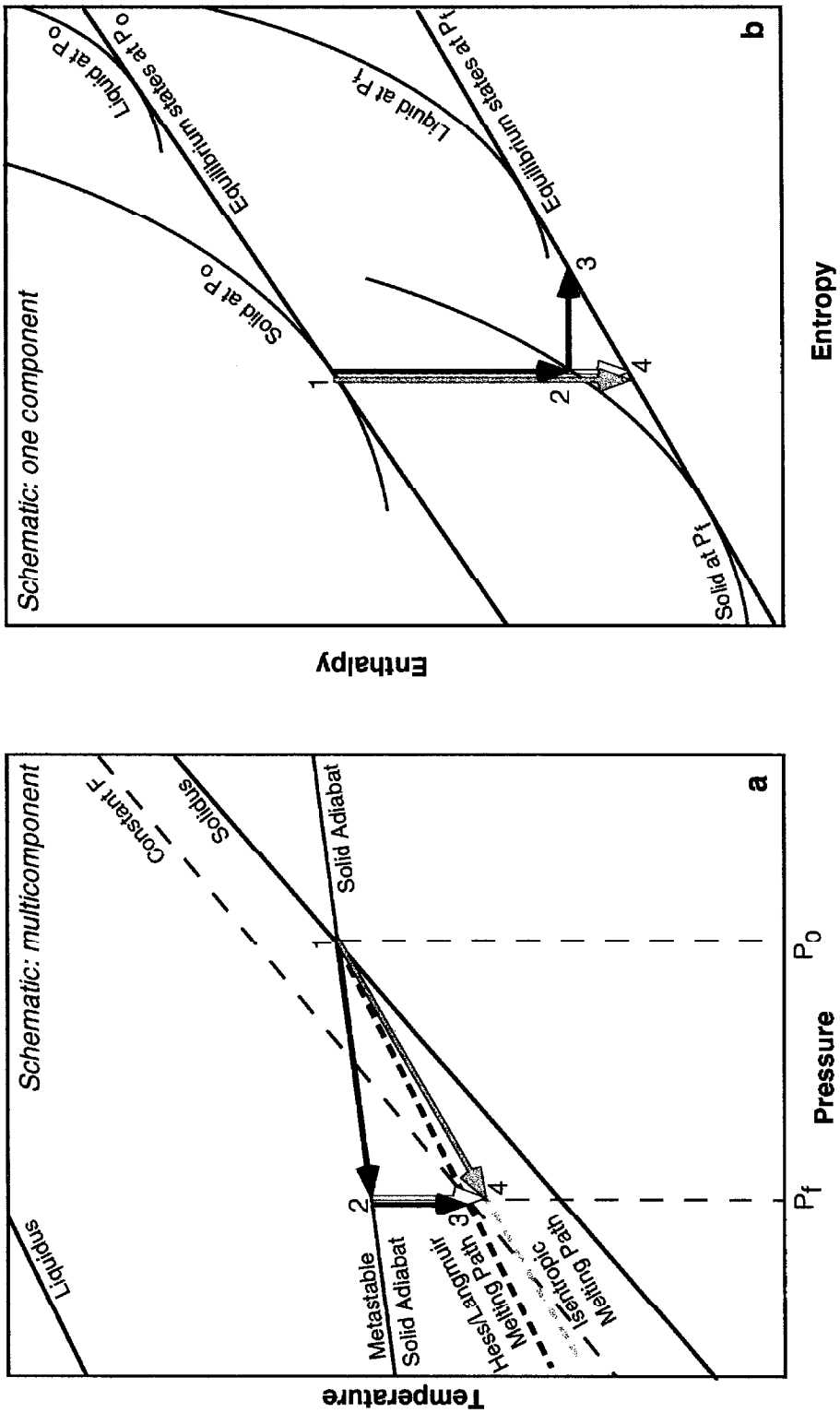

Chapter 3, Figure 1

Figure 2. Isentropic melting behavior of a hypothetical one-component system in which the heat capacity, $(dV/dT)_P$, ΔV_{fus}, and ΔS_{fus} of diopside at 1 bar and 1664 K are taken to obtain over all P and T. (a) The solidus is linear. It has been chosen to go through 7 GPa and 2338 K, close to the actual diopside solidus (Rigden et al., 1989). (b) Isentropic melting is best illustrated with an S-P plot. Batch melting follows a horizontal line on this figure. The reference isentrope shown as a heavy horizontal line intersects the solidus at 7 GPa. (c) The isentropic productivity (expressed as percent melting per kilobar pressure decrement) vs. P for batch and fractional paths that intersect the solidus at 7 GPa. The dashed line is for comparative purposes only; it does not correspond to any isentropic path. (d) Melt fraction vs. P for the same batch and fractional paths.

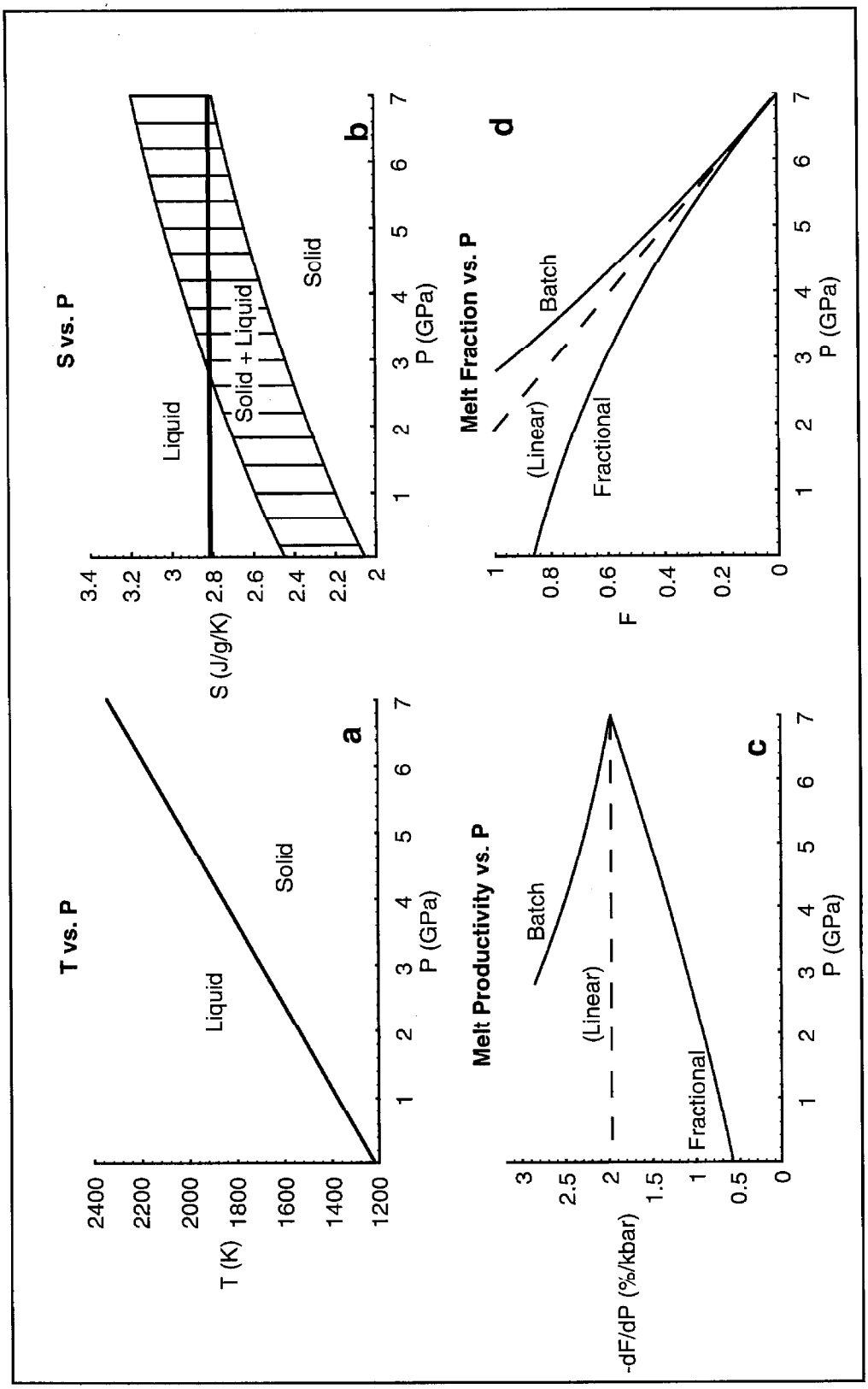

Chapter 3, Figure 2

Figure 3. Isentropic melting behavior of diopside using the thermodynamic data from Table 1. (a) The solidus is concave down, due to greater compressibility of the liquid relative to the solid. (b) The curvature of the solidus translates into greater curvature of the edges of the two-phase field in *S*-*P* space, compared to Figure 2b. The heavy horizontal line is an *S*-*P* path for batch melting. (c) The isentropic productivity vs. *P* for batch and fractional paths that intersect the solidus at 7 GPa. The dashed line is for comparative purposes only; it does not correspond to any isentropic path. (d) Melt fraction vs. *P* for the same batch and fractional paths.

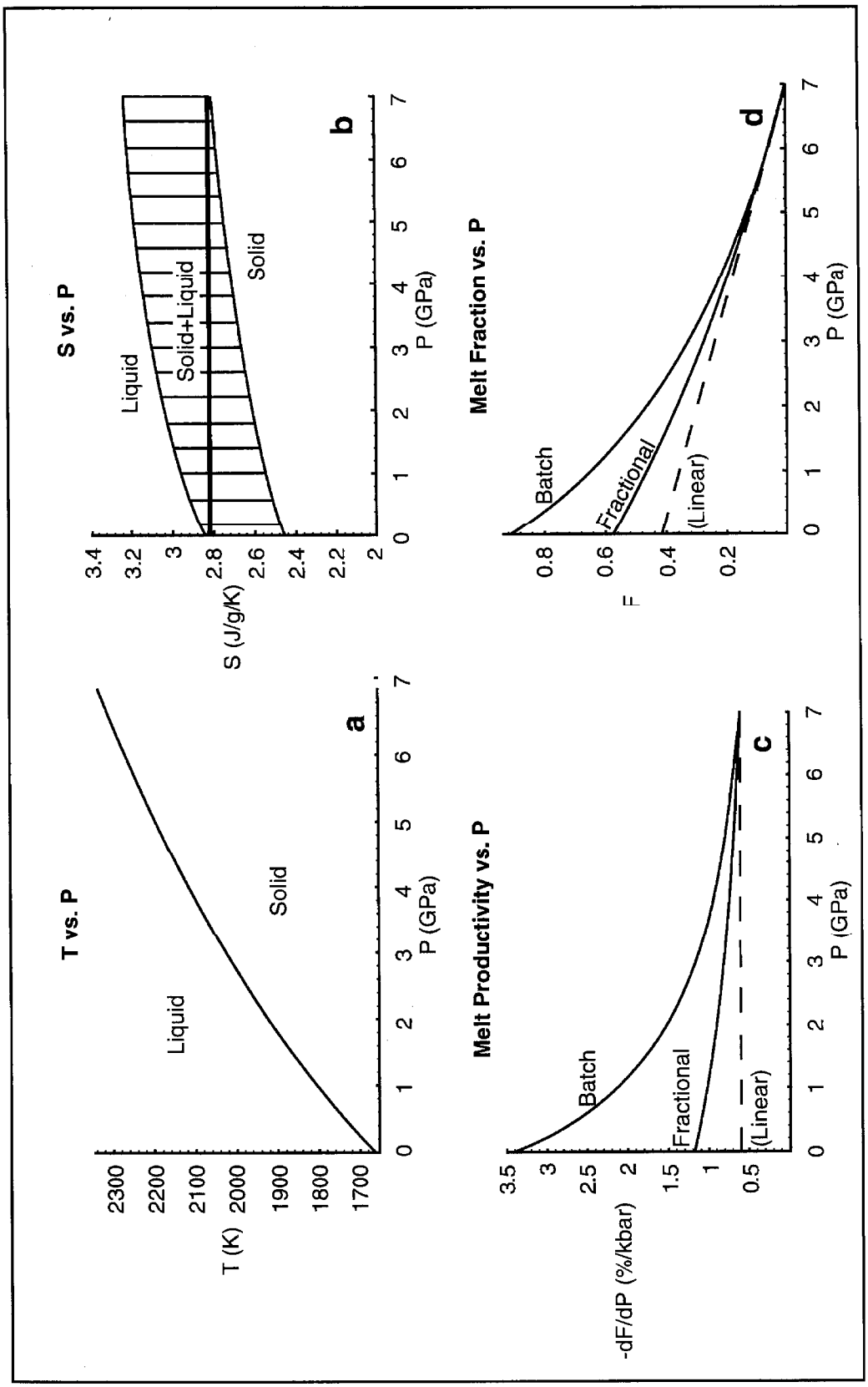

Chapter 3, Figure 3

Figure 4. Phase diagram of a two-component model system *a-b*; both solid and liquid are ideal solutions. Model data are in Table 1. (a) T vs. X_b at 1 bar. (b) S vs. X_b at 1 bar. Tie-lines in the two-phase field indicate entropy and composition of coexisting phases. (c)-(f) Analysis of isentropic melting is visualized by a series of S vs. X_b sections at P=1 bar, 3.3 GPa, 6.7 GPa, and 10 GPa with the point X_b=0.1, S=663 J/mol/K and the tie-line that passes through it at each pressure highlighted. The position of the point along the highlighted tie-line gives the melt fraction by the lever rule; this sequence illustrates the importance both of the movement of the phase loop as a function of pressure and the rotation of the tie-lines towards the vertical near the end members in determining melt fraction and productivity.

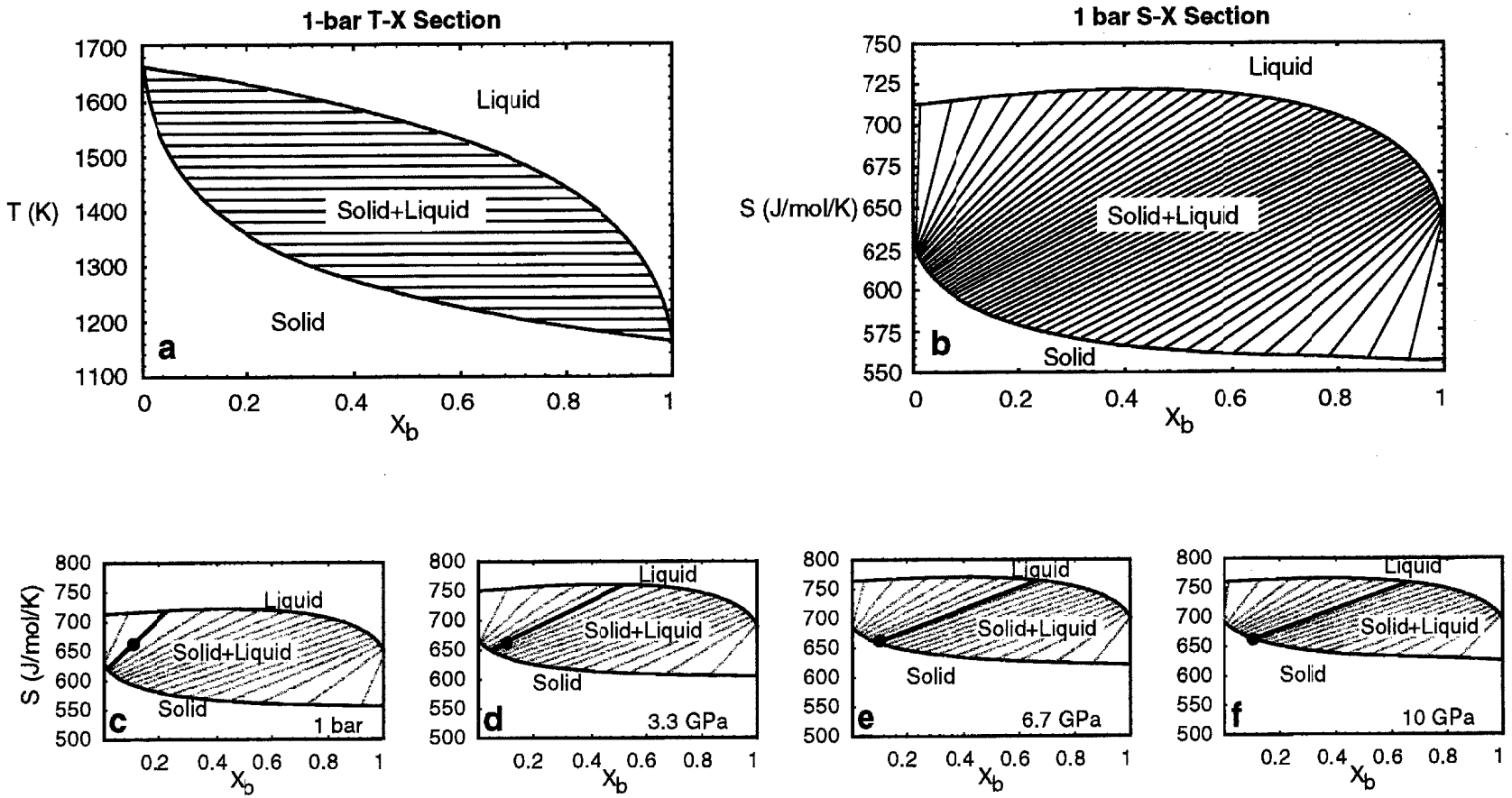

Chapter 3, Figure 4

Figure 5. Isobaric batch and fractional melting of the model binary system *a*-*b* at 1 bar according to the phase relations shown in Figure 4. X_b values indicate the bulk composition of the solid before the initiation of melting. (a) Batch melting, F vs. T. (b) Fractional melting, F vs. T. Note that all curves finish melting at $T = 1664$ K, the melting point of the *a* end member. (c) Isobaric productivity in percent melting per degree temperature increase for batch melting. The dashed curve shows the first term in equation (16) and is the locus of values of productivity on the solidus (F=0) for various bulk compositions. (d) Isobaric productivity for fractional melting. The values differ from the dashed solidus productivity curve only by a factor (1-F).

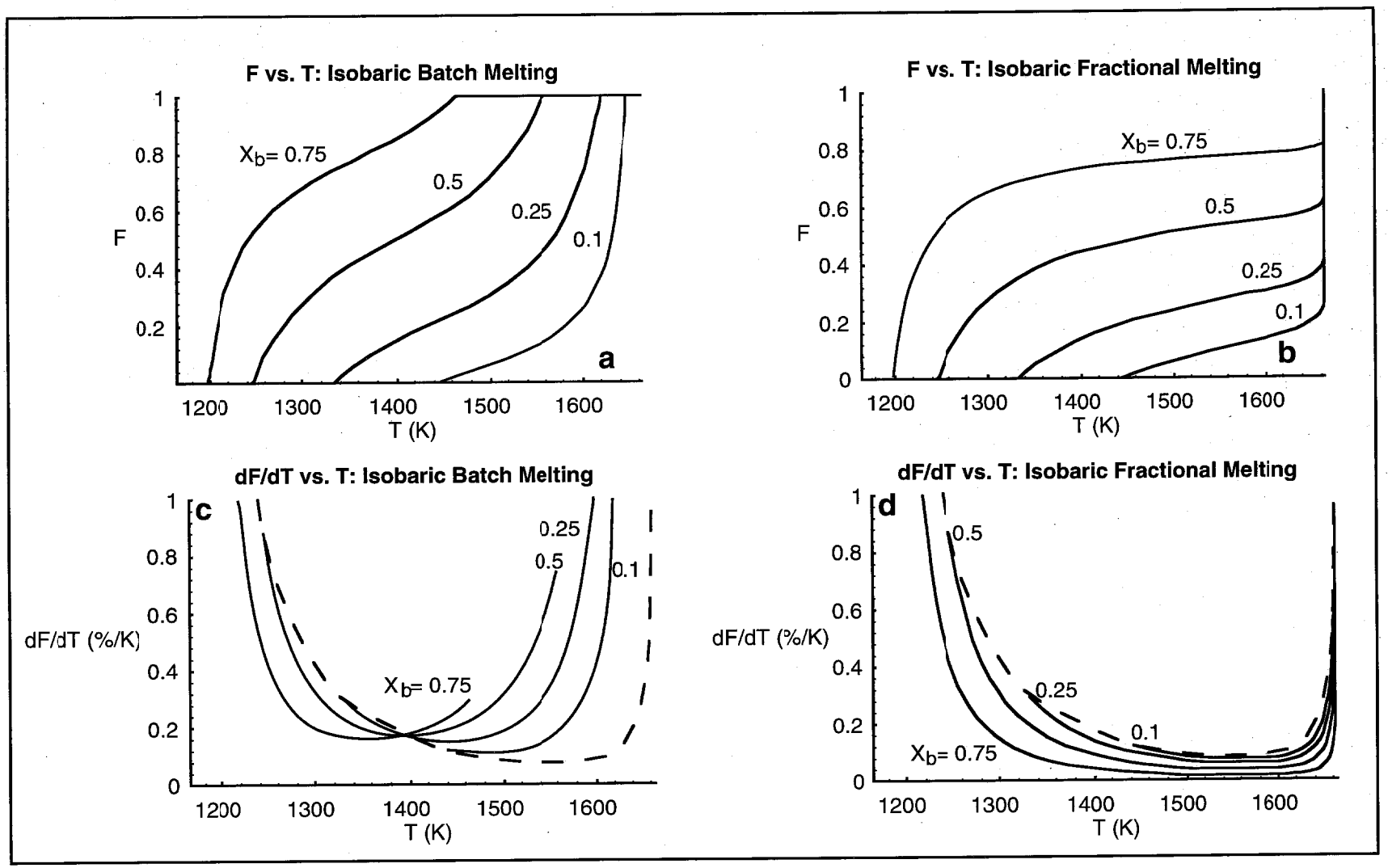

Chapter 3, Figure 5

Figure 6. Isentropic batch and incrementally isentropic fractional melting of the model binary system *a-b*. (a) T vs. P, showing the univariant melting curves for the end members and both batch and fractional isentropic melting paths for composition $a_{90}b_{10}$ that intersect the solidus at 10 GPa. (b) F vs. P, showing the upward curvature characteristic of increasing productivity. The dashed line is a linear extrapolation of the productivity at the solidus; it does not correspond to any isentropic path. (c) Isentropic productivity vs. P for batch and fractional melting. The dashed curve shows "local" fractional productivity of a unit mass of solid at any pressure; the light solid curve shows $-dF/dP$ for incrementally isentropic fractional melting, where F is normalized to the original source mass (see text). (d) Isentropic productivity vs. P for batch melting (heavy curve) compared to a calculation (light solid curve) of productivity based on equation (14) where all parameters except $(\partial T/\partial P)_F$ and $(\partial F/\partial T)_P$ were held constant at their values on the solidus at 10 GPa (see text for details). Also shown are calculations in which we allowed $(\partial T/\partial P)_F$ (dotted curve) or $(\partial F/\partial T)_P$ (dashed curve) to vary along the adiabat, holding the other quantity constant at its solidus value. Variations in $(\partial F/\partial T)_P$ capture the major qualitative features of the productivity, but $(\partial T/\partial P)_F$ variations are also required to get a good quantitative fit.

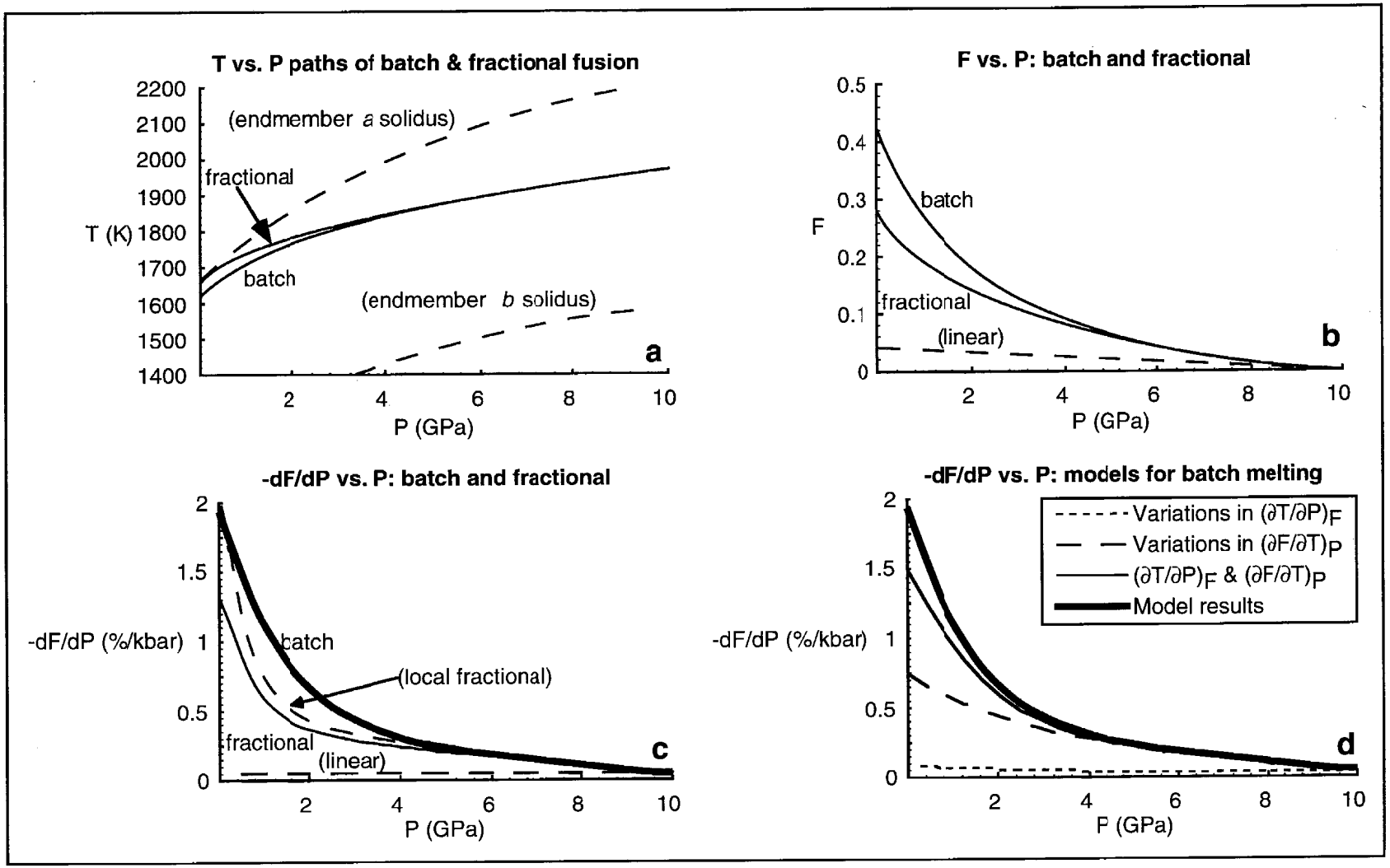

Chapter 3, Figure 6

Figure 7. Isentropic melting of 9-component model fertile peridotite (Asimow et al., 1995a; Hart and Zindler, 1986) based on calculations using MELTS. (a) Isentropic productivity vs. P during batch melting (heavy curve) compared with productivity predicted by equation (14) with all parameters except (i) $(\partial T/\partial P)_F$ (dotted curve), (ii) $(\partial F/\partial T)_P$ (dashed curve), or (iii) $(\partial T/\partial P)_F$ and $(\partial F/\partial T)_P$ (light solid curve) held constant at their values near the middle of the melting paths at 11 kbar (see text for details). (b) Analogous to (a) for fractional melting. (c) Melt fraction F vs. P for batch melting, compared to melt fraction expected by integrating the three curves in (a). (d) Analogous to (c) for fractional melting.

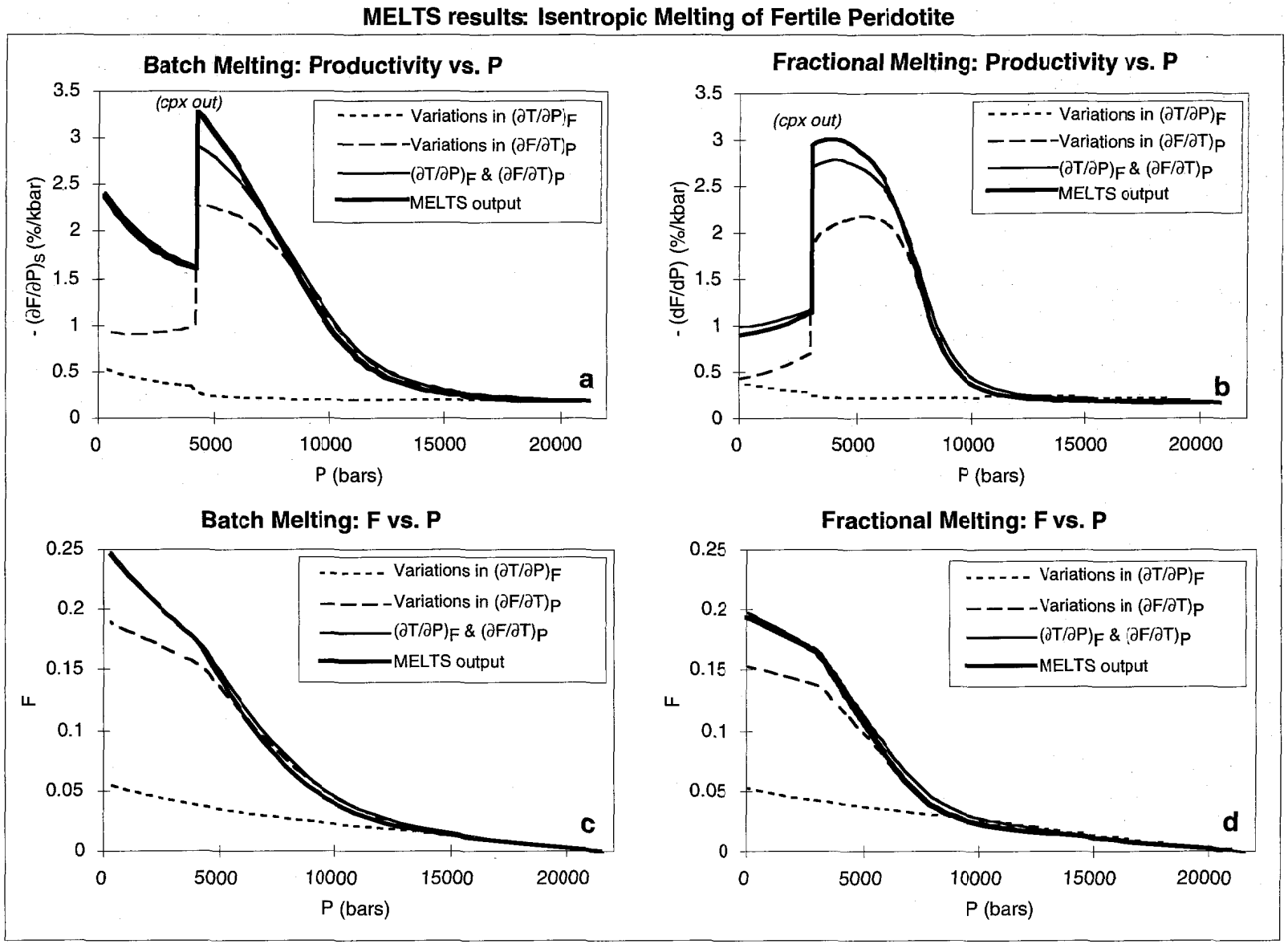

Chapter 3, Figure 7

Chapter 4. Steady-state mantle-melt interactions in one dimension

Abstract—Two phenomena in mantle-melt interaction during migration of the melt phase are explored in one dimension and steady-state. We begin by reconsidering the equivalence between 1-D steady equilibrium porous flow and batch melting. In the absence of diffusion and radioactive decay, conservation of mass flux requires that throughout the porous flow column the compositions of melt and solid and the distributions of trace elements are the same as would be generated by batch melting the source composition at the same pressure (P) and temperature (T). Furthermore conservation of energy requires that T and the extent of melting (F) as functions of P are independent of melt migration except for dissipative source terms due to compaction of the solid and gravitational energy release due to relative vertical flow of liquid and solid. When diffusion and dissipation are neglected the only effect of porous flow is to reduce the volume fraction (φ) of melt in the system and increase its velocity relative to the solid. This equivalence is used to greatly simplify two kinds of one-dimensional steady melt transport calculations. First we examine the effects of melt focusing, i.e., of increasing the flux of melt to simulate either a two-dimensional flow field with converging melt streamlines or the result of channeling by a reactive infiltration instability. Melt focusing modifies the mineralogy of the residual matrix as well as the erupted melt. We use MELTS calculations to reconsider the formation of discordant dunites and other phenomena by this mechanism and quantify the melt fluxes involved.

We then consider the case of fractional melting where the extracted melts mix and move upwards in chemically isolated channels but interact with the surrounding solids by thermal diffusion. This causes cooling and possibly partial crystallization of the migrating melts and heating accompanied by excess melting (beyond the adiabatic melt production) in the solid. A corollary of the independence of mass and energy flux in one-

dimensional steady flow and migration velocities is that, except for a gravitational term, the thermal effects of migrating fractional melts are the same whatever their migration velocity. Hence we can greatly simplify these calculations by moving the residuum and the accumulated fractional melt together at the same velocity. We also explore the maximum effect of the gravitational potential energy term in the infinite permeability limit. Using MELTS, we quantify the magnitude of the heat exchange between mantle and accumulated melt for peridotite in one-dimensional melting columns. The amount of melting in excess of the adiabatic productivity is small except where the ascending accumulated fractional melt crosses its liquidus and begins to crystallize. The relationship between the slope of the wet adiabat, the adiabatic melt productivity, and the possibility of crystallization from chemically isolated fractional melts is explored.

Introduction

It is now well-established that on the time scale of pressure-release melting of the earth's mantle, the liquid phase is usually able to move relative to the residual solid phases. This follows from experimental and theoretical studies of the equilibrium textures of olivine-dominated, partially molten systems, which suggest that the liquid phase is interconnected at melt fractions less than 1% (Kohlstedt, 1991; von Bargen and Waff, 1986; Waff and Bulau, 1979) and thus that even at very low melt fractions, melt can begin to move by porous flow, driven by density differences or by shear of the matrix (McKenzie, 1984; Richter and McKenzie, 1984; Spiegelman and McKenzie, 1987; Stevenson and Scott, 1991). For reasonable grain sizes and rates of solid-state diffusion in the residual minerals, the expected rates of grain-scale porous flow are such that the moving melt is expected to approach closely equilibrium with the matrix minerals (Navon and Stolper, 1987; Spiegelman and Kenyon, 1992).

There is, however, considerable evidence that erupted mid-ocean ridge basalts (MORBs) are *not* in major or trace element equilibrium with mantle residues at low pressure (Johnson et al., 1990; O'Hara, 1968; Stolper, 1980), suggesting that erupted magmas contain at least a component of melts that did not stay in intimate contact with residual peridotites all the way to the top of the upper mantle. Furthermore, the time scale on which basalts are segregated and erupted is short compared to the half-life of daughter products in the decay series of ^{238}U (Condomines et al., 1981; Newman et al., 1983; Reinitz and Turekian, 1989). Both of these lines of evidence suggest that not all of the melt produced under mid-ocean ridges is transported from depth to the crust by diffuse porous flow and that there must be mechanisms for rapid extraction and transport of melt from depth. Proposed mechanisms for such rapid extraction and transport include: high porosity regions formed by shear instability (Stevenson, 1989), reactive infiltration (Kelemen et al., 1995a; Kelemen et al., 1995b) or steepening of propagating porosity waves; (Scott and Stevenson, 1984; Spiegelman, 1993a; Spiegelman, 1993b); open channels formed by diking (Sleep, 1988); or a fractal hierarchy of melt pathways (Hart, 1993).

The transport rates required to produce the required degrees of chemical disequilibrium depend on the scale of the channels, which would differ for the various mechanisms listed in the last paragraph and which are, in any case, poorly constrained by observations of mantle rocks. Hence the values of adjustable parameters in most models of melt transport under ridges are chosen to give transport rates sufficient to yield chemical disequilibrium; i.e., they require a large chemical Peclet number (Spiegelman and Kenyon, 1992). Note, however, that since thermal diffusion is so much faster than chemical diffusion, there is a substantial parameter range for any model of rapid melt extraction where the melt would be expected to be in thermal equilibrium with the surrounding mantle even though it is not in chemical equilibrium with it. In this chapter,

I explore two related phenomena in rapid melt transport: (1) the effects of increasing melt flux in a region of focused flow given complete thermal and chemical equilibrium between the melt and the solid in a high-porosity channel, and (2) the effects of achieving thermal but not chemical equilibrium between flowing melt and country rock.

My treatment of these phenomena utilizes calculations based on the MELTS package of models and algorithms for equilibrium calculations in silicate systems (Ghiorso, 1994; Ghiorso and Sack, 1995). Within the internally consistent framework of MELTS, I can calculate the complete phase equilibria and energetics of arbitrary bulk compositions in multicomponent systems. It thus permits computation of effects (e.g., the effect of solid phase transitions, Asimow et al., 1995a; or the productivity of isentropic upwelling, Asimow et al., 1997) that generally are not accessible to calculation based only on direct parameterizations of experimental phase equilibrium data (e.g., Kinzler and Grove, 1992a; Klein and Langmuir, 1987; Langmuir et al., 1992; McKenzie and Bickle, 1988; Niu and Batiza, 1991) and that have previously only been dealt with by simple linear or dimensional analyses (e.g., productivity estimates in Hess, 1992; McKenzie, 1984; Turcotte and Ahern, 1978). Although earlier versions of MELTS (i.e., SILMIN) have been applied to the equilibrium porous flow problem (Kelemen, 1990; Kelemen et al., 1992; Kelemen and Ghiorso, 1986), improvements in the MELTS models and algorithms, together with the concept of the formal equivalence of this problem to batch melting (developed below), allow me to calculate the entire one-dimensional upwelling system rather than be restricted to a zero-dimensional view of the process as one of assimilation at fixed pressure and temperature (or enthalpy) as in the work of Kelemen. This one-dimensional calculation is better suited to characterizing the evolution of the residual mantle column in space and time as a function of increasing melt flux than the approach of Kelemen, which focused on the evolution of a single parcel of liquid progressively assimilating peridotite.

Although melt flow beneath mid-ocean ridges is at least two-dimensional (Ahern and Turcotte, 1979; Spiegelman and McKenzie, 1987), and probably includes a significant component of three-dimensional flow (Parmentier and Phipps Morgan, 1990; Phipps Morgan and Forsyth, 1988; Sparks and Parmentier, 1993), one-dimensional calculations provide a simple and useful framework for thinking about more complicated flow regimes. For example, a one-dimensional flow model (i.e., including thermal equilibration, but without melt focusing) likely provides a minimum estimate of the magnitude of heating of the country rock by migrating liquids at the axis of a mid-ocean ridge, since higher dimensional flows are thought to focus more melt to the axis (Spiegelman and McKenzie, 1987). Similarly, a one-dimensional model of focused porous flow simulates the effects of higher dimensional flows, the effect of which are essentially to add extra melt flux to a predominantly vertical axial flow. Finally, although there is no reason, *a priori*, to expect that melt extraction is a steady process (Scott and Stevenson, 1989), steady solutions of the sort we present provide a simple baseline for understanding time-dependent behaviors.

Equilibrium porous flow

I develop here a more general version of Ribe's (1985) proof that in a steady-state one-dimensional ascending column undergoing melting and equilibrium porous flow (i.e., melt and solid are always in equilibrium at all levels in the column) the extent of melting and the composition of the melt present (but *not* the amount of melt present) are independent of the melt migration rate and hence equivalent to batch melting (i.e., no melt migration). Ribe stated that this was an approximate result. We will see below the conditions under which this is an exact result (Spiegelman, 1996; see also Spiegelman and Elliott, 1993). To anticipate somewhat, let me state here what I am going to show: at equilibrium and steady-state in one dimension, at any point in the column (with its

particular P and T) the liquid and solid have compositions that are the same as would be obtained at the same P and T by batch melting of the source composition entering the base of the column. For trace elements whose partitioning is independent of P and T, only F need be specified and the porous flow system will yield the same phase compositions as batch melting of the source to the given F. For major elements or trace elements with variable partition coefficients, however, two of the three variables P, T, and F must be specified (and, as we shall see, the relationship between them in the one-dimensional column can depend on the details of the behavior of the column), but once two of these variables are specified, the compositions of the coexisting phases will correspond to batch melting of the source at the same conditions. Furthermore, except for dissipative source terms, conservation of entropy flux in the porous flow system reduces to the same entropy conservation law as batch melting, which means that when these source terms are neglected, then even for elements (major or trace) with variable partition coefficients, only one of the variables P, T, and F needs to be specified and the liquid and solid compositions are the same as those obtained by isentropic batch melting of the source composition from the same initial potential temperature. Nevertheless, even when the dissipative source terms in the energy equation are non-zero, the porous flow system still is restricted to liquid and solid compositions consistent with batch melting, although in this case the path through P-T-F space is different and two independent variables must be specified to relate the compositions to batch melts and residues of the source composition.

The system I consider is illustrated schematically in Figure 1, where z is the vertical distance measured upwards from the bottom of the column. A one-dimensional adiabatic column of solid mantle moving upwards with velocity $W(z)$ intersects its solidus at z_o, at which point its velocity is W_o. Once melt begins to form at this depth, it moves at velocity $w(z)$. As melting proceeds, the mass fraction of the solid residue that has been

melted (which we refer to as the extent of melting, F) can be defined using the concentration of a perfectly compatible tracer (pct) in the residue: $F \equiv 1 - X_o^{pct} / X_s^{pct}$ (Spiegelman, 1996). Note that because of the relative motions of solid and liquid, the porosity (i.e., the fraction of the volume that is occupied by liquid at any depth, φ) does not necessarily bear any simple relationship to F except in the case where the liquid is not permitted to move relative to the solid; i.e., if $w=W$, which is batch melting (in which case $F = \varphi\rho_f / [\varphi\rho_f + (1-\varphi)\rho_s]$). Although both F and φ have sometimes been termed the "melt fraction" in the literature (e.g., both usages appear in McKenzie, 1984), it is critical in what follows to distinguish clearly between them. In the most general case, where arbitrary liquids might be added or removed from a system, it might no longer be meaningful to call F the "extent of melting," but in all cases it can be defined as above and retains a definite physical meaning, i.e., one minus the mass of the solid in the residue divided by the original solid mass, which in nearly all cases will correspond to the fraction of the original solid mass that has been melted. My goal is to show under what conditions $F(z)$ and the compositions of coexisting solid and liquid do not depend on w-W or φ.

Conservation of mass flux

We begin in the same manner as McKenzie (1984), Ribe (1985), and Richter (1986) by stating the conservation of the mass of each component in the melt and the matrix, respectively:

$$\frac{\partial}{\partial t}\left[\varphi\rho_f X_f^n\right] + \frac{\partial}{\partial z}\left[\varphi\rho_f X_f^n w\right] = \Gamma^n \tag{1}$$

$$\frac{\partial}{\partial t}\left[(1-\varphi)\rho_s X_s^n\right] + \frac{\partial}{\partial z}\left[(1-\varphi)\rho_s X_s^n W\right] = -\Gamma^n, \tag{2}$$

where t is time, ρ is density, X_n is the concentration in mass units of the n^{th} component in our N-component system (normalized so that $\sum_{n=1}^{N} X_f^n = \sum_{n=1}^{N} X_s^n = 1$), and Γ^n is the rate of mass transfer of the n^{th} component from matrix to melt, where the subscripts f and s refer

to melt and solid (the solid assemblage may be polymineralic, but all solid phases move at the same velocity so only bulk properties of the solid assemblage are needed). At steady state,

$$\frac{\partial}{\partial z}\left[\varphi\rho_f X_f^n w\right] = \Gamma^n \tag{3}$$

$$\frac{\partial}{\partial z}\left[(1-\varphi)\rho_s X_s^n W\right] = -\Gamma^n. \tag{4}$$

Adding (3) to (4) and integrating from z_O to z subject to the boundary conditions $\varphi(z_o) = 0$, $\rho_s(z_o) = \rho_s^o$, $X_s^n(z_o) = X_o^n$, and $W(z_o) = W_o$ yields

$$\varphi\rho_f X_f^n w + (1-\varphi)\rho_s X_s^n W = \rho_s^o X_o^n W_o. \tag{5}$$

Summing the equivalent of equation (5) for each component from 1 to N gives a constraint on the total mass flux:

$$\varphi\rho_f w + (1-\varphi)\rho_s W = \rho_s^o W_o. \tag{6}$$

At this stage, Ribe (1985) assumed constant ρ_s and a two-component system with a single compositional variable. We proceed for the general n-component, variable density case. Eliminating w and W, respectively, between (5) and (6) and introducing the definition for each component $F^n = \left(X_o^n - X_s^n\right) / \left(X_f^n - X_s^n\right)$, we obtain

$$(1-\varphi)\rho_s W = (1 - F^n)\rho_s^o W_o \tag{7}$$

$$\varphi\rho_f w = F^n \rho_s^o W_o. \tag{8}$$

Since φ, ρ_f, ρ_s, ρ_s^o, w, W, and W_o are the same for all components n, (7) and (8) show that F^n has the same value when defined using any component, including a perfectly compatible tracer (for which $X_f^{pct} = 0$, so that $F^{pct} = F$ as defined above). This is a key result: at steady state in one dimension, all components give the same "extent of melting" as originally defined above based on a perfectly compatible tracer. Hence we can simply use F in place of F^n for all elements, so $FX_f^n + (1 - F)X_s^n = X_o^n$ and

$$(1-\varphi)\rho_s W = (1 - F)\rho_s^o W_o \tag{7'}$$

$$\varphi\rho_f w = F\rho_s^o W_o. \tag{8'}$$

The relationship between F and Γ^n follows from equating the partial derivative of (7') with respect to z with the sum of all N equations (4) (recall that $\sum_{n=1}^{N} X_s^n = 1$):

$$\sum_{n=1}^{N} \Gamma^n = \rho_s^o W_o \frac{\partial F}{\partial z}. \tag{9}$$

We are now in a position to show that given certain assumptions, various characteristics of the melting column are independent of w, W, and φ; i.e., they do not depend on the amount of melt present or the rate of melt migration.

Trace Elements: Consider conservation of an element that is governed by an equilibrium partitioning between the concentration in the melt and in the solid where the partition coefficient, $K^n = X_s^n/X_f^n$, need not be a constant (i.e., it can be an arbitrary function of P, T, and F). Then at steady state and equilibrium the sum of equations (3) and (4) is

$$\frac{\partial}{\partial z}\left[\varphi\rho_f X_f^n w + (1-\varphi)\rho_s K X_f^n W\right] = 0. \tag{10}$$

If we expand the products in (10) we can obtain

$$\varphi\rho_f w\frac{\partial X_f^n}{\partial z} + (1-\varphi)\rho_s W\frac{\partial\left(K^n X_f^n\right)}{\partial z} + X_f^n\frac{\partial}{\partial z}\left[\varphi\rho_f w\right] + K^n X_f^n\frac{\partial}{\partial z}\left[(1-\varphi)\rho_s W\right] = 0. \tag{11}$$

Then substitution of (7') and (8') into the last two terms in (11) gives

$$\varphi\rho_f w\frac{\partial X_f^n}{\partial z} + (1-\varphi)\rho_s W\frac{\partial\left(K^n X_f^n\right)}{\partial z} + X_f^n\rho_s^o W_o\frac{\partial F}{\partial z} + K^n X_f^n\rho_s^o W_o\frac{\partial(1-F)}{\partial z} = 0. \tag{12}$$

Substitution of (9) into (12) leads to the standard equation for one-dimensional steady-state trace element flux conservation in the absence of diffusion and production by radioactive decay (McKenzie, 1984; Ribe, 1985; Richter and McKenzie, 1984):

$$\varphi\rho_f w\frac{\partial X_f^n}{\partial z} + (1-\varphi)\rho_s W\frac{\partial}{\partial z}\left[K^n X_f^n\right] = \left(K^n - 1\right)X_f^n\sum_{n=1}^{N}\Gamma^n. \tag{13}$$

The term on the right-hand side for exchange of the trace element between solid and melt depends on the total mass of solid converted to melt and hence on the sum of all the Γ^n. If we substitute (7') and (8') into the first two terms in (12), we obtain another statement of conservation of flux in which w, W, and φ no longer appear,

$$F\frac{\partial X_f^n}{\partial z} + (1-F)\frac{\partial}{\partial z}\left[K^n X_f^n\right] = \left(K^n - 1\right)X_f^n\frac{\partial F}{\partial z}, \tag{14}$$

which can be rearranged as

$$\frac{\partial}{\partial z}\left[\left(K^n + (1-K^n)F\right)X_f^n\right] = 0. \tag{15}$$

Integrating (15) subject to the boundary conditions $F(z_o) = 0$, $K^n(z_o) = K_o^n$, and $X_f^n(z_o) = X_o^n/K_o^n$ (where X_o^n is both the concentration before melting begins and the concentration in the bulk solid at the beginning of melting) gives

$$\frac{X_f^n}{X_o^n} = \frac{1}{K^n + (1-K^n)F}, \tag{16}$$

which is identical to the result for batch melting. This shows that the concentration of a stable, non-radiogenic trace element in the liquid (and hence in the solid) as a function of F is independent of solid velocity, liquid velocity, permeability, and porosity as long as equilibrium is maintained (Ribe, 1985; Richter, 1986; Spiegelman and Elliott, 1993).

Major Elements: It is significant that (16) is obtained without any assumptions concerning the behavior of the partition coefficient K^n. Indeed, this generality means that the mass flux constraints require all elements to be partitioned in a manner that depends only on F and not on φ. In other words, even though the bulk composition of the column (i.e., $\varphi X_f^n + (1-\varphi)X_s^n$) varies with depth and depends on φ, the effective bulk composition that governs equilibration even of major element at all depths in the column is $FX_f^n + (1-F)X_s^n = X_o^n$, and thus, since this is the governing equation for batch fusion, even if melt and solid are moving differentially, their compositions are the same at each point in the column as would be obtained by batch fusion of the source composition at the same P and T (or the same P and F, or the same T and F; i.e., only two of these three are independent given the n mass conservation equations). It may seem strange that the compositions of the phases at a given P and T are the same in the steady state porous flow and batch fusion cases since the bulk compositions (i.e., of the solid plus liquid

assemblage) at these conditions differ for the two cases, but this is certainly a possible solution since one can change the amount of a phase present in a system at equilibrium without affecting the amounts or compositions of other phases and remain at equilibrium. This is in fact the unique solution, or at least as unique as the batch melting equilibrium, given the requirements of steady state, one dimension, and local equilibrium. Note also that, although the bulk composition depends on melt transport, the bulk solid compositions does not. Since the solid phase compositions and the bulk solid compositions are both independent of melt transport, it follows that the proportions of the phases in the solid assemblage are also independent of melt transport, a result we will use below to interpret melt focusing calculations.

Conservation of entropy flux

For elements whose partition coefficients are constant, the foregoing proves that the concentrations in liquid and solid in the porous flow case will be identical to batch melting at the same F (equation (16)). For elements with arbitrary, temperature- and pressure-dependent behavior, the porous flow case will be identical if we specify two variables among F, P, and T. However, the concentrations of such elements will be the same at given F *or* at given P only in the case that $F(P)$ and $T(P)$ are the same for batch melting and porous flow. Let us investigate the conditions under which this is true. McKenzie (1984) gives an equation for conservation of energy, which at steady-state and in one-dimension can be written

$$\begin{aligned} T(S_f - S_s)\sum_{n=1}^{N}\Gamma^n + T(1-\varphi)\rho_s W\frac{dS_s}{dz} + T\varphi\rho_f w\frac{dS_f}{dz} = \\ \frac{\partial}{\partial z}\left[k_T\frac{\partial T}{\partial z}\right] + \frac{\mu\varphi^2}{k}(w-W)^2 + (\zeta+\frac{4}{3}\eta)\left(\frac{\partial W}{\partial z}\right)^2 + H \end{aligned} \quad , \qquad (17)$$

where S_f and S_S are the specific entropies of the melt and matrix, k_T is the bulk thermal diffusivity, μ is the viscosity of the melt, k is the permeability, ζ is the bulk viscosity and

η the shear viscosity of the matrix, and H is the rate of internal heat generation. The four terms on the right-hand side of (17) represent, respectively, the contributions of thermal diffusion, gravitational potential energy dissipated by viscous flow of the melt, dissipation by compaction of the solid, and internal heat generation (e.g., by radioactivity) to the change in internal energy of the system. In this treatment we neglect internal heat generation as well as thermal diffusion (i.e., we assume $H = 0$ and $k_T = 0$).

Using (7'), (8'), and (9) and rearranging, we obtain

$$(S_f - S_s)\frac{dF}{dz} + (1-F)\frac{dS_s}{dz} + F\frac{dS_f}{dz} = \frac{1}{T\rho_s^o W_o}\left(\frac{\mu\varphi^2}{k}(w-W)^2 + (\zeta + \frac{4}{3}\eta)\left(\frac{\partial W}{\partial z}\right)^2\right). \quad (18)$$

Equation (18) can be used to find both the entropy and the temperature as functions of P or z.

Entropy: First, to obtain entropy, we integrate (18) subject to suitable boundary conditions:

$$(FS_f + (1-F)S_s) = S_s^o + \frac{1}{\rho_s^o W_o}\int_{z_o}^{z} \frac{1}{T}\left(\frac{\mu\varphi^2}{k}(w-W)^2 + (\zeta + \frac{4}{3}\eta)\left(\frac{\partial W}{\partial z}\right)^2\right)dz\,. \quad (19)$$

This states that, except for the dissipative source terms, the system acts identically to the ordinary isentropic batch melting case $(FS_f + (1-F)S_s) = S_s^o$. This result is precisely analogous to the foregoing results for mass and composition: the specific entropies of liquid and solid, like the compositions of liquid and solid, are the same (in the absence of the source terms) for porous flow and batch melting, even through the total entropy, like the bulk composition, may vary with depth in the porous flow case.

Temperature and melt productivity: To obtain a temperature equation, we expand the total differentials of S_f and S_S,

$$dS_s = \frac{C_p^s}{T}dT - \frac{\alpha_s}{\rho_s}dP + \sum_{n=1}^{N} S_s^n dX_s^n = \frac{C_p^s}{T}dT - \frac{\alpha_s}{\rho_s}dP + \sum_{n=1}^{N} S_s^n\left(\left(\frac{\partial X_s^n}{\partial F}\right)_P dF + \left(\frac{\partial X_s^n}{\partial P}\right)_F dP\right), \quad (20a)$$

$$dS_f = \frac{C_p^f}{T}dT - \frac{\alpha_f}{\rho_f}dP + \sum_{n=1}^{N} S_f^n dX_f^n = \frac{C_p^f}{T}dT - \frac{\alpha_f}{\rho_f}dP + \sum_{n=1}^{N} S_f^n\left(\left(\frac{\partial X_f^n}{\partial F}\right)_P dF + \left(\frac{\partial X_f^n}{\partial P}\right)_F dP\right), \quad (20b)$$

where α_s is the coefficient of thermal expansion and C_p^s the heat capacity of the bulk solid assemblage, S_s^n is the partial specific entropy of component n in the bulk solid assemblage (encompassing both modal and compositional effects)[1], and α_f, C_p^f, and S_f^n are the thermal expansion, heat capacity, and partial specific entropy of component n in the liquid phase. Let us introduce the shorthand notations

$$\left(\frac{\partial S_X^s}{\partial P}\right)_F = \sum_{n=1}^{N} S_s^n\left(\frac{\partial X_s^n}{\partial P}\right)_F, \quad \left(\frac{\partial S_X^f}{\partial P}\right)_F = \sum_{n=1}^{N} S_f^n\left(\frac{\partial X_f^n}{\partial P}\right)_F$$

$$\left(\frac{\partial S_X^s}{\partial F}\right)_P = \sum_{n=1}^{N} S_s^n\left(\frac{\partial X_s^n}{\partial F}\right)_P, \quad \left(\frac{\partial S_X^f}{\partial F}\right)_P = \sum_{n=1}^{N} S_f^n\left(\frac{\partial X_f^n}{\partial F}\right)_P.$$

for the compositional and modal entropy changes resulting from melting, summed over all components (see also chapter 3). Then (20) can be written

$$dS_s = \frac{C_p^s}{T}dT + \left(\left(\frac{\partial S_X^s}{\partial P}\right)_F - \frac{\alpha_s}{\rho_s}\right)dP + \left(\frac{\partial S_X^s}{\partial F}\right)_P dF \quad (21a)$$

$$dS_f = \frac{C_p^f}{T}dT + \left(\left(\frac{\partial S_X^f}{\partial P}\right)_F - \frac{\alpha_f}{\rho_f}\right)dP + \left(\frac{\partial S_X^f}{\partial F}\right)_P dF. \quad (21b)$$

Introducing these expansions into (18) gives

$$T\left(\frac{\partial S}{\partial F}\right)_{P,T}\frac{dF}{dz} + T\left[\left(\frac{\partial S_X}{\partial P}\right)_F - F\frac{\alpha_f}{\rho_f} - (1-F)\frac{\alpha_s}{\rho_s}\right]\frac{dP}{dz} + \left[FC_p^f + (1-F)C_p^s\right]\frac{dT}{dz} = \frac{1}{\rho_s^o W^o}\left(\frac{\mu\varphi^2}{k}(w-W)^2 + (\zeta + \frac{4}{3}\eta)\left(\frac{\partial W}{\partial z}\right)^2\right) \quad (22)$$

in which $(\partial S_X/\partial P)_F = F(\partial S_X^f/\partial P)_F + (1-F)(\partial S_X^S/\partial P)_F$ and in place of the conventional but ill-defined quantity ΔS_{fus} we use the well-defined quantity

---

[1] We can also write the modal and compositional effects separately. If the solid assemblage consists of J solid phases, where phase j has modal abundance γ^j, specific entropy S^j, and N^j components with concentrations X_n^j, then (20a) can be written

$$dS_s = \frac{C_p^s}{T}dT - \frac{\alpha_s}{\rho_s}dP + \sum_{j=1}^{J}\left[S^j d\gamma^j + \gamma^j\sum_{n=1}^{N^j}\left(\frac{\partial S^j}{\partial X_n^j}\right)_{T,P,X_{m\neq n}^j} dX_n^j\right].$$

$(\partial S/\partial F)_{P,T} = (S_f - S_s) + F\left(\partial S_X^f/\partial F\right)_P + (1 \quad F)\left(\partial S_X^S/\partial F\right)_P$ (see chapter 3 and Asimow et al., 1997). If we add the assumption of hydrostatic equilibrium, $dP/dz = g[\varphi\rho_f + (1-\varphi)\rho_s]$, then we have

$$T\left(\frac{\partial S}{\partial F}\right)_{P,T}\frac{dF}{dP} + T\left[\left(\frac{\partial S_X}{\partial P}\right)_F - F\frac{\alpha_f}{\rho_f} - (1-F)\frac{\alpha_s}{\rho_s}\right] + \left[FC_p^f + (1-F)C_p^s\right]\frac{dT}{dP} = \frac{1}{\rho_s^o W^o g[\varphi\rho_f + (1-\varphi)\rho_s]}\left(\frac{\mu\varphi^2}{k}(w-W)^2 + (\zeta + \frac{4}{3}\eta)\left(\frac{\partial W}{\partial z}\right)^2\right) \quad (23)$$

The terms on the left-hand side of (23) are due, respectively, to melting, adiabatic expansion, and advection. With the identity

$$\frac{dT}{dP} = \left(\frac{\partial T}{\partial F}\right)_P\frac{dF}{dP} + \left(\frac{\partial T}{\partial P}\right)_F, \quad (24)$$

we can solve (23) for melt productivity and temperature gradient separately. Substituting (24) into (23) and rearranging leads to

$$-\left(\frac{dF}{dP}\right) = \frac{\frac{FC_p^f + (1-F)C_p^s}{T}\left(\frac{dT}{dP}\right)_F - \left(F\frac{\alpha_f}{\rho_f} + (1-F)\frac{\alpha_s}{\rho_s}\right) + \left(\frac{\partial S_X}{\partial P}\right)_F + \frac{\frac{\mu\varphi^2}{k}(w-W)^2 + (\zeta + \frac{4}{3}\eta)\left(\frac{\partial W}{\partial z}\right)^2}{T\rho_s^o W^o g[\varphi\rho_f + (1-\varphi)\rho_s]}}{\frac{FC_p^f + (1-F)C_p^s}{T\,(dF/dT)_P} + \left(\frac{\partial S}{\partial F}\right)_{P,T}}, \quad (25)$$

which is identical to the productivity for isentropic batch melting except for the dissipative source terms at the end of the numerator (Asimow et al., 1997). Without writing it down explicitly, it is clear that substituting (25) back into (24) gives the temperature gradient. Since the velocity and porosity appear only in the dissipative source terms, equations (24) and (25) demonstrate that, as for trace elements in (16) above, the productivity and temperature gradient and hence F and T at any pressure in a one-dimensional steady-state equilibrium porous flow system are independent of melt and solid velocity, porosity, and permeability except in the dissipation terms. This is surprising in that (17) includes advective terms as well, but the constraints of one-dimensional conservation render the net advection independent of melt migration rates. Note that the solid dissipation term (i.e., due to matrix compaction) is dependent on

migration velocities, but is never strictly zero, even for batch melting with no melt migration: equation (6) demonstrates that W cannot be constant (i.e., the compaction rate $\partial W/\partial z$ is non-zero) unless the melt and solid densities are equal and constant[2]. Porous flow, however, in general requires substantially greater compaction rates than batch melting (consider equation (7'), which shows that, for small φ and $\rho_s \sim \rho_s^o$, W must change in proportion to (1-F) to conserve mass), so we would normally expect compaction to be a much greater heat source when porous flow is occurring. When there is no porous flow, the gravity term is exactly zero and dissipation in the melt is negligible. For the porous flow case, we can choose to neglect dissipation in the melt, but in so doing we must also neglect the effect of separation flow in a gravitational field.

In reaching expressions for -(dF/dP) and (dT/dP), it was necessary to substitute $dP/dz = g[\varphi\rho_f + (1-\varphi)\rho_s]$. The mechanical equilibrium due to overburden pressure depends on the density of the overlying column, which in turn depends on how much melt is present. Hence the above results do not hold exactly when expressed in distance terms (i.e., -(dF/dz) and (dT/dz) depend on φ even in the absence of dissipation). In what follows we use pressure as the vertical coordinate, since P is a significant thermodynamic parameter whereas z is not.

Summary

The formal equivalence between melt and solid composition and extent of melting as a function of P in a one-dimensional steady-state equilibrium porous flow system and during isentropic batch melting of the same source at the same potential temperature (which requires that -(dF/dP) and (dT/dP) are equal for the two cases) requires the following assumptions: (1) neglect of thermal and chemical diffusion in both the solid

---

[2] In one dimension, for a closed system, changes in W are the only means to accommodate changes in volume while conserving mass flux.

and melt phases (we have not shown that this is a necessary assumption), (2) no radioactive heating or transmutation of the elements (a necessary assumption, see Spiegelman and Elliott, 1993), (3) negligible heating by dissipation due to compaction of the solid matrix; and (4) negligible dissipation of gravitational potential energy due to vertical separation of fluid and solid of different densities. If (1) through (4) are assumed, then $F(P)$, $T(P)$, and phase compositions (and relative solid phase proportions) as functions of P (but *not* $\varphi(P)$) are independent of melt migration. Furthermore, relaxing assumptions (3) and (4) yields source terms only in the energy equation; mass is still conserved in the manner of batch melting. Hence melt migration in the absence of these last two assumptions explores a family of batch melting paths with the same bulk composition but different P-T and P-F paths.

Melt focusing

Although one-dimensional porous flow is unlikely in most natural settings, there are some two- and three-dimensional flows that can be approximately treated in one-dimension. At a mid-ocean ridge undergoing passive (plate-driven) flow, the streamlines of melt migration by porous flow can be focused towards the axis (Spiegelman and McKenzie, 1987). At the axis of the ridge, this situation may be approximated by one-dimensional vertical porous flow, with melt added to the column at various levels above the depth at which melting begins. On a smaller scale, study of infiltration of a porous medium by reactive melts has led to the recognition of a fingering instability in which narrow channels of high porosity and melt flux evolve (Aharonov et al., 1995; Kelemen et al., 1995a; Kelemen et al., 1995b). This situation can perhaps also be adequately modeled by one-dimensional vertical flow with melt added to the column either continuously or discretely at some level above that at which melting begins. I use the formal equivalence of one-dimensional steady equilibrium porous flow to batch melting

developed above to simplify greatly calculations involving melt focusing. It is not necessary to perform a simultaneous advection and equilibration calculation; instead each time melt is added to the system the problem is reduced to one of finding the equivalent set of independent variables (bulk composition and entropy or potential temperature) which when batch melted at the pressure of interest yields the new, higher melt-flux assemblage. The phase compositions and the modal abundance of each solid in the residue will be the same in the focused porous flow situation and in the suitably chosen batch melting calculation.

Discrete focusing

The case of a single focusing event, where melt is added to the column at a particular pressure, is the simplest to visualize. To illustrate, we consider a one-dimensional column undergoing isentropic upwelling that begins with the primitive upper mantle source composition of Hart and Zindler (1986). For this particular example, the solidus is encountered at 19 kbar. At 10 kbar, some additional quantity of melt with the same composition as the melt already present is added to the system at the current temperature of the system. The "focusing factor" Ω_D (D for discrete) in this case is just the ratio of melt mass after the addition of melt to the original melt mass at 10 kbar (by the same method we could study the neighboring columns that are depleted of melt by examining Ω_D values less than one). The composition and total entropy used to calculate the state of the system at pressures lower than 10 kbar are then simply the bulk composition and total entropy of the system at 10 kbar after the additional melt has been added. Figures 2a and 2b show the fraction of modal olivine and pyroxene, respectively, in the residue as a function of pressure for a range of values of Ω_D. Since the focusing event is at 10 kbar and changes only the amount of liquid, not the mode or composition of the residue, all curves on Figures 2a and 2b are identical at this point. The reference case

(Ω_D=1) begins at the solidus at 19 kbar with 48% olivine, 32% orthopyroxene (opx), 17% clinopyroxene (cpx), and 3% spinel. Olivine increases to 49% at 10 kbar and to 77% at 1 bar (expressed as mass fraction of the solid residue, not of the solid plus liquid system), while opx initially increases and then decreases, and cpx decreases (almost linearly as a function of melt fraction F, Figure 2d). These slopes reflect the stoichiometry of the melting reaction, which is cpx+spinel $\rightarrow$ olivine+opx+melt at high pressure and cpx+opx+spinel $\rightarrow$ olivine+melt at low pressure. For Ω_D=1, cpx is exhausted at 18% melting and 2.2 kbar, whereas opx remains in the residue throughout. In order to exhaust opx from the residue, it would be necessary to reach at least 35% melting (see chapter 5), but even systems with substantially higher potential temperature than this example are unlikely to reach such a high extent of melting, because beyond the exhaustion of cpx, the melt productivity is quite low as plotted in Figure 2c (Asimow et al., 1997; Hess, 1992; Langmuir et al., 1992). The low melt productivity of harzburgite assemblages is the fundamental barrier to creation of dunite by simple decompression melting. As Ω_D increases, however, the rate of increase in modal olivine and decrease in modal pyroxenes shallower than 10 kbar increases sharply, such that above Ω_D=6, olivine and spinel are the only remaining phases at 1 bar. As Ω_D increases further, the pressure at which opx is exhausted increases, to about 3 kbar at Ω_D=18.

The source of this effect is simple to understand, given the batch melting analogy developed above. Recall that, although the physical situation envisaged is one of equilibrium porous flow with a focusing event, these calculations were performed using isentropic batch melting. At the focusing event, the bulk composition and total entropy of the new, high melt-flux assemblage are substituted and batch melting continues. We can use this batch melting concept to interpret the results as well as to execute the calculation. For most purposes in melt transport calculations, F is best taken as a property of the solid residue (measured, for example, by the concentration of a perfectly

compatible tracer), in which case F would not be affected by the focusing event at 10 kbar. In this calculation, however, it is instructive to use the melt fraction of the equivalent batch melting calculation, $\tilde{F}$ (i.e., one minus the mass fraction of solids in the new, larger system after focusing), which differs at 10 kbar as a function of Ω_D (Fig 2d). Adding melt at 10 kbar changes the equivalent batch melting system to a more fertile bulk composition (in the sense that it contains more of the components that partition readily into liquid) at a higher melt fraction $\tilde{F}$. From this point of view, the modal changes leading to the formation of dunite by melt focusing result from the sum of three effects that help to overcome the barrier of the unproductive harzburgite region: (1) higher $-d\tilde{F}/dP$ in the lherzolite and harzburgite fields (Figure 2c); (2) exhaustion of cpx at higher pressure (which gives a larger pressure interval for harzburgite melting, Figure 2b); and (3) lower modal opx remaining at the exhaustion of cpx due to a change in the stoichiometry of the melting reaction (Figure 2d).

The reasons why $-d\tilde{F}/dP$ should increase with increasing focusing follow from the arguments developed in chapter 3 and Asimow et al. (1997). The isentropic melt productivity for batch melting, $-(dF/dP)_S$, is a complex function of many variables, but as long as no phases are exhausted, for a fixed composition it monotonically increases with increasing F during batch melting (Asimow et al., 1997). Thus, if we were to hold bulk composition constant and only move to a higher $\tilde{F}$, we would observe an increase in $-d\tilde{F}/dP$. Furthermore, at a given P and T, so long as the assemblage of residual phases is the same, a more fertile composition always yields a higher $-(dF/dP)$. Geometrically, this compositional effect is intuitively visible in, e.g., any two-component system and is due to the second-order term in the expression for isobaric productivity, $(\partial F/\partial T)_P$:

$$\left(\frac{\partial F}{\partial T}\right)_P^{Batch} = -\left(\frac{\partial X_b^s}{\partial T}\right)_P\left(\frac{1}{X_b^l - X_b^s}\right) - \frac{(X_b - X_b^s)\left(\frac{\partial (X_b^l - X_b^s)}{\partial T}\right)_P}{(X_b^l - X_b^s)^2} \qquad (26)$$

(Asimow et al., 1997). If this two-component a-b system is partially molten, bulk composition X_b must be in between liquid composition X_b^l and solid composition X_b^s. Hence moving the bulk composition closer to X_b^l by adding liquid must increase $(X_b - X_b^s)$ and hence isobaric productivity so long as $\partial((X_b^l - X_b^s)/\partial T)_P$ is negative, which is always true for peridotite. As discussed in chapter 3 (Asimow et al., 1997), a higher isobaric productivity leads to a higher isentropic productivity. Hence, keeping $\tilde{F}$ constant and only moving to a more fertile bulk composition leads to an increase in $-d\tilde{F}/dP$. When, in the focusing calculations, we both increase $\tilde{F}$ and enrich the bulk composition, these two effects act in the same direction: a more fertile composition at a higher $\tilde{F}$ must result in a higher $d\tilde{F}/dP$ wherever the assemblage of residual phases is the same, which is clearly seen in Figure 2c, both in the lherzolite range and the harzburgite range.

As Ω_D increases, cpx is exhausted at higher $\tilde{F}$ and at higher pressure (Figures 2b and 2d). Cpx persists to higher $\tilde{F}$ in more fertile assemblages, but the stoichiometric coefficient for cpx in the melting reaction does not depend substantially on the bulk composition (see Fig 2d., where reaction coefficients are represented by the slope of mass fraction of cpx vs $\tilde{F}$ lines), so the increase in $\tilde{F}$ required to exhaust cpx after focusing is nearly constant. Therefore, the enhancement in $d\tilde{F}/dP$ means that the necessary increase in $\tilde{F}$ is obtained over a smaller ΔP. The higher P of cpx-out leaves a larger pressure range over which to melt harzburgite, and hence contributes to making a dunite residue by 1 bar.

More importantly, though, at higher focusing factors there is less opx remaining at the exhaustion of cpx. This is due to a progressive change in the stoichiometry of the melting reaction with increasing focusing: as long as cpx remains in the residue, the mass of opx melted per unit change in $\tilde{F}$ increases with Ω_D (Figure 2d). The reaction coefficient for cpx, however, does not change very much. Hence the same increase in $\tilde{F}$ is required to proceed from the focusing point to the exhaustion of cpx, but the fraction of opx consumed over this range increases with Ω_D. Although the coefficient for opx after

loss of cpx does not change much, the smaller fraction of opx in the residue means that less melting in the harzburgite field is actually required to reach a dunite residue. The reason for the increase in reaction coefficient for opx can be understood in terms of the increase in $\tilde{F}$: for any fixed bulk composition, the coefficient for opx increases (and the coefficient for olivine decreases) during progressive decompression melting as the liquid composition increases in normative silica (indeed, according to MELTS it crosses from being an odd to an even reactant near $\tilde{F}$=0.06 for this potential temperature), but the coefficient for cpx is nearly constant. Furthermore, at constant $\tilde{F}$ the reaction coefficients are roughly the same in all the bulk compositions obtained by varying Ω_D (they are not exactly the same because the *P-T* paths diverge). Since focusing leads to an increase in $\tilde{F}$ at fixed pressure or at fixed fraction of opx in the residue, it increases the reaction coefficient for opx, without a noticeable change in the reaction coefficient for cpx.

These three effects act together to promote the exhaustion of opx: less melting of harzburgite is required because less opx remains when cpx is exhausted, a larger pressure range is available for harzburgite melting because cpx is exhausted at higher pressure, and the productivity in the harzburgite range is higher because $\tilde{F}$ is higher and the bulk composition is more fertile.

Continuous focusing

This brief examination of the discrete case of a single focusing event is sufficient to introduce a continuous focusing calculation, where a series of focusing events are performed as the system upwells. At small intervals in pressure, melt of the same composition as that already in the column is added to the system and a new bulk composition and total entropy obtained. This simulates a case where the flux of melt continuously increases upwards. The choice to add liquid of the same composition as that in the column is a simple case to study, but the issue of whether it describes a

physically reasonable higher-dimensional flow system is left for 2-D calculations such as those performed by Spiegelman (1996) for trace element transport. We consider only the case where the incremental focusing events are evenly spaced in pressure and all have the same Ω_D value. The continuous focusing column is characterized by the integrated focusing factor $\Omega_I = \Omega_D{}^m$, where m is the total number of incremental focusing events between the solidus and 1 bar. Note that Ω_I is not equal to the factor by which the mass of the system has increased, since each focusing event increases the mass of liquid, not the mass of the system, by a factor Ω_D. Neither is Ω_I equal to the ratio of the melt flux from the top of the focused column to the melt flux in the reference case, since the added melt triggers additional melting in the column. It is simply the product of focusing factors for all the discrete focusing events that are performed, and hence a measure of the total intensity of focusing. The results of two continuous focusing calculations with potential temperatures of 1300 °C and 1450 °C (solidus intersection pressures of 19 kbar and 35 kbar, respectively) are shown in Figures 3 and 4. The reference case $\Omega_I = 1$ for the colder example is the same as above. The effect of continuous focusing on the residual mode is seen to be similar to the single-focusing event calculation -- for values of Ω_I greater than one, modal olivine increases and modal pyroxenes decrease relative to the unfocused case. Above $\Omega_I = 4.4$ for the cold case (and $\Omega_I = 2$ for the hot case), the residue is dunite at 1 bar. The reasons for these modal changes are similar to the reasons for the corresponding behavior in the discrete focusing case: increased $d\tilde{F}/dP$ due to increasingly fertile bulk compositions at increasing $\tilde{F}$ (Figures 3c and 4c), leading to exhaustion of cpx at higher pressure and more productive melting of harzburgite, together with increased reaction coefficient for opx due to increasing $\tilde{F}$, reducing the quantity of opx remaining at the exhaustion of cpx (Figures 3d and 4d). The pressures at which the residue exhausts opx and cpx, respectively, increase with Ω_I in a non-linear manner, as shown in Fig 5: a small amount of focusing moves the cpx-out and opx-out points a large

distance in pressure, but further focusing is subject to diminishing returns. For each given potential temperature, there appears to be an upper limit to the pressure at which a dunite residue can be formed (about 5 kbar for a solidus at 19 kbar, about 8 kbar for a solidus at 35 kbar). This principle of diminishing returns in the pressure of opx-exhaustion as well as the small change in limiting pressure obtained by a large increase in solidus pressure may be related to the dependence of the phase relations of pressure, namely the expansion of the olivine phase volume at low pressure (Yoder, 1976). In this sense it is analogous to the observation that ordinary batch melting of this composition exhausts opx at higher melt fractions as it occurs at higher pressure, i.e., the adiabat which exhausts opx at 0.5 kbar does so at F=0.37, whereas the adiabat which exhausts opx at 1.5 kbar does so at F=0.40.

The minimum $\tilde{F}$ values for exhaustion of opx from the residue (i.e., when opx-out occurs at 1 bar) in the three cases of focusing discussed above (i.e., discrete focusing, cold continuous focusing, and hot continuous focusing) are 0.38, 0.46, and 0.40. These are remarkably close to the minimum melt fraction at which opx is exhausted at 1 bar by ordinary adiabatic batch melting of the source composition in the absence of focusing, F=0.36 (requiring, according to MELTS, a minimum potential temperature of 1500 °C and a solidus deeper than 60 kbar). As noted above, both batch melting and focusing calculations require higher F to exhaust opx at higher pressure. Hence a simple approximate criteria for quantifying the minimum focusing factor represented by a dunite channel is that the melt flux expressed as an apparent extent of melting (i.e., melt flux over melt plus solid flux, or $\tilde{F}$ of the appropriate analogous batch melting column) be greater than or equal to the F needed to exhaust opx by batch melting of the unmodified source composition at the pressure of interest. This is a strong constraint for the formation of dunites by this mechanism at high pressure, i.e., in the asthenosphere. It requires higher apparent melt fractions to reach dunite at high pressure than at low

pressure, and this implies a much deeper solidus and/or a large focusing factor: not only does the system have to achieve a certain critical melt fraction at higher pressure, but the critical melt fraction itself increases with pressure. Note that adiabatic fractional melting (a series of isentropic upwelling steps followed by extraction of the liquid, removing entropy from the system) cannot exhaust opx from the residue for any reasonable mantle potential temperature, as it requires the system to approach the peritectic point in the binary MgO-SiO_2 system at a real temperature of at least 1557°C and after ~40% melting, which implies a potential temperature of at least 1800°C.

Discussion

The characteristics of the dunites generated by the focusing process as modeled above are remarkably similar to discordant dunite veins observed in the mantle sections of many ophiolite sequences, including the Horoman peridotite (Takahashi, 1992; Takazawa et al., 1992), Trinity peridotite (Kelemen et al., 1992), Josephine peridotite (Kelemen and Dick, 1995) and, the best studied case, the Oman ophiolite (Kelemen et al., 1997 and references therein). Although these dunites may be present through up to 10 km of mantle section, and the present depth of exposure presumably gives a minimum depth of formation, it is difficult to estimate the actual depth at which dunites formed on geologic grounds, as they have generally been transposed into the foliation by continued mantle flow after emplacement (Kelemen et al., 1997). Petrological and geochemical similarities between these dunite veins and the model dunites generated by focused flow in MELTS include the forsterite content of the olivine (near Fo_{91}), the rare-earth element patterns (consistent with equilibrium with MORB, by contrast to the residues of fractional melting, which are extremely depleted in LREE), and, as shown in Figure 5, the spinel compositions (Kelemen et al., 1997; Kelemen et al., 1995a). This is encouraging in that it implies not only that melt focusing is a reasonable explanation for the formation of

these dunite veins but also that this type of modeling can be used to constrain the history of particular observed dunites. Since very little changes in a dunite once opx is exhausted, one can only hope to place a lower bound on the melt flux represented by a dunite vein: further melt flux beyond this point may leave no detectable trace. Thus, in applying models to interpret dunite veins from the field, two important goals are to establish the maximum pressure of formation and the minimum melt flux represented. This work shows that these two constraints are in fact correlated: to form a dunite at higher pressure requires a larger minimum melt flux.

Dunite bodies in ophiolite complexes have been interpreted as channels of focused melt extraction from the mantle (Kelemen and Dick, 1995; Kelemen et al., 1997) and therefore offer a possible explanation of the observation that liquids parental to MORB are not saturated with orthopyroxene except at pressures greater than about 8 kbar (O'Hara, 1968; Stolper, 1980). This interpretation requires that opx be exhausted from the focused melt flow channels by a pressure of 8 kbar. The results presented here imply that this requires both a hot mantle, which is in principle testable for any given ophiolite by observing the extent of depletion of the residual harzburgites, and focusing factors of tens to hundreds, which may be related to the areal extent of dunite as a fraction of the mantle section, although it is difficult to reconstruct the geometry at the spreading axis before transposition (see Kelemen et al., 1997).

The melt fluxes obtained from these calculations are probably too high and the pressure of formation at a given melt flux too low. The current MELTS calibration tends to overestimate the stability of opx relative to olivine (Hirschmann et al., 1997a). Thus the melt flux needed to form a dunite at a given pressure in MELTS is probably higher than that needed by natural melts in the mantle. Furthermore, since the overstability of opx in MELTS appears to increase with pressure (see chapter 5, figure 2), this model likely overstates the difficulty of making dunite at high pressure. Nevertheless, the

increase in opx stability relative to olivine is a real feature of basaltic phase equilibria (e.g., Yoder, 1976), so the increasing difficulty of making dunite residues at higher pressure is correct in sign if not necessarily in magnitude.

Thermal interactions

Although it is traditional to approximate pressure-release melting of the mantle as an isentropic (adiabatic and reversible) process (Asimow et al., 1997; Iwamori et al., 1995; McKenzie, 1984; Verhoogen, 1965), as discussed in the first section of this chapter there are several known sources of irreversible entropy production that remain to be included or quantified. McKenzie (1984) identified two physical processes that lead to such entropy production — viscous dissipation due to shear and compaction of the matrix and relative flow of melt and matrix. I deal here only with the second of these processes.

The relative vertical flow of melt and matrix adds two terms to the energy equation for fractional fusion: advection of heat by the melt and gravitational potential energy release (which in this inertia-less system is converted to heat through viscous dissipation in the melt). Based on simple arguments, McKenzie (1984) concluded that the total amount of extra melting generated by both advection and gravitational potential release was comparable to the effect of uncertainty in the entropy of fusion or to the effect of retaining 3% melt in the matrix, and hence that isentropic melting would suffice as a first approximation. I will show that, considered only in terms of the total amount of melt produced by a melting column, McKenzie's simple arguments are correct, although in part for reasons he did not consider, such as the limitation on melting along most normal mantle adiabats imposed by the exhaustion of clinopyroxene. The possibility of the liquid crossing its liquidus and beginning to crystallize (releasing its latent heat to cause further melting of the surrounding mantle), however, means that melt migration can, in principle, drive substantial changes in the composition and mean pressure of

segregation of the integrated melt and most significantly in the amount of liquid which actually reaches the crust. Given the complexities in the energetics of adiabatic melt production, I feel a complete self-consistent calculation with realistic models of liquid and solid phases is warranted.

The effect of advection of heat by the melt can be studied in a straightforward way because it is actually independent of the rate of melt migration. This is a simple corollary of the arguments developed above concerning batch melting. We showed that if there is no source term for mass or energy, then the constraints of one-dimension and steady-state imply that the fluxes of each mass component and of energy be constant with pressure and independent of the rate or presence of melt migration. In the fractional case, the same is true of energy, i.e., the heat flux carried by the melt is the same whatever its velocity. Thus we consider below only the case where the residual mantle and the accumulated fractional melt travel together at the same velocity, chemically isolated but thermally interacting. On the other hand, the gravitational potential release term is not independent of melt migration, but there is a well-defined maximum source for the case of infinite permeability. We will consider below the effect of a source term of this limiting magnitude.

Method

The numerical experiment used to evaluate the effects of heat advection is illustrated in Figure 7. The calculations proceeds in a series of discrete steps. A sample of mantle source material is isentropically decompressed at equilibrium until a small increment of melt (0.001% by volume) is present. The melt is then extracted into a separate reservoir which is initially empty. Thus the "mantle" reservoir and the accumulated fractional melt ("liquid," for brevity) reservoir begin at the same temperature, and the first increment of melt in the liquid reservoir begins on its liquidus.

Next, both the mantle and the liquid reservoirs are moved to lower pressure isentropically (each on its separate adiabat) until the mantle again achieves the critical melt fraction. Again the melt is extracted, and this time and henceforth it is mixed isenthalpically with the previously accumulated liquids. Now, in general, at this point the mantle and liquid reservoirs are at different temperatures. Here we make a choice; for the "no equilibration" case, nothing further happens before the two reservoirs are again decompressed on their separate adiabats. For all other cases, the mantle and liquid reservoirs are now brought to the same temperature at constant total enthalpy, an irreversible step. During this step, the mantle reservoir is kept at equilibrium; i.e., since it is right at its solidus following the extraction of melt, when heated by interaction with the liquid reservoir it generally produces some additional melt (which is for the moment left in the mantle reservoir). For the liquid reservoir, we make two further choices: whether to allow crystallization and, if so, whether to perform equilibrium or fractional crystallization. For the "no crystallization" case, the liquid reservoir is maintained as a (possibly metastable) liquid, whether or not it crosses its liquidus. For the "equilibrium crystallization" case, if the liquid reservoir is below its liquidus, it is permitted to crystallize any solid phase and this solid remains in the liquid reservoir in thermal and chemical equilibrium with the accumulated liquid. This crystallization is performed isenthalpically, and the latent heat of crystallization liberated enters into the total enthalpy balance resulting in an increase in temperature of the mantle and liquid reservoirs and additional melting in the mantle reservoir. For the "fractional crystallization" case, as solids form in the liquid reservoir they are extracted to yet a third chemically isolated reservoir, the "conduit walls." The conduit walls reservoir participates in the thermal equilibrium; i.e., its enthalpy is considered in maintaining constant total enthalpy during the thermal equilibration step and it stays at the same temperature as the mantle and liquid reservoirs (this reservoir is far below its solidus and does not melt during the

thermal equilibration step in any of the calculations performed here). At the end of the isenthalpic equilibration step, the individual entropies of all three reservoirs at the new temperature are calculated, and these are used as references for the next isentropic decompression step. This calculation is repeated until the pressure reaches 1 bar. I continue the calculation all the way to 1 bar in order to observe the range of possible behaviors in the plagioclase peridotite stability field, but this is not meant to imply that melting, much less adiabatic melting, continues to such a low pressure in any real environment. Much of the interesting behavior noted below for cold potential temperatures occurs entirely at pressures which in reality are in the lithosphere or oceanic crust. The conclusions with regard to normal mantle temperatures, however, are not sensitive to the pressure of final melting in these calculations.

In what follows below, four cases are compared for each potential temperature: (1) "no equilibration," (2) "no crystallization" (i.e., thermal equilibrium between the mantle and liquid reservoirs, but the liquid is not permitted to crystallize), (3) "equilibrium crystallization" (i.e., thermal equilibrium between the mantle and liquid reservoirs, and the liquid reservoir may crystallize if this is the stable equilibrium, but those crystals remain in the liquid reservoir), and (4) "fractional crystallization" (i.e. thermal equilibrium between mantle, liquid, and conduit walls reservoirs). The limiting gravitational energy source term can be added to any of these at each step of the decompression. In the "no equilibration" case, since it describes dissipation in the liquid, the gravity source simply makes the liquid hotter, but this does not feedback into melting.

An example calculation

Example *P-T* paths for the various cases are shown in Figure 8a-d for the Cr-free analogue of the Hart and Zindler (1986) primitive upper mantle source compositions and an adiabat that intersects its solidus near 17 kbar (i.e., a potential temperature of 1290

°C). The corresponding values of F and its derivative, $-(dF/dP)$, the melt productivity, are plotted against P in Figures 8e and 8f.

Case 1, no equilibration: The shape of the melting adiabat for the mantle reservoir in the "no equilibration" case is controlled by the melt productivity of incrementally isentropic fractional fusion, and the sources of variations in productivity and hence slope are explored in Asimow et al. (1997). On this cool adiabat, the fractional melting path encounters the spinel-plagioclase lherzolite transition at 5 kbar. It then exhausts plagioclase at 1.5 kbar and cpx just before finishing at 1 bar; these changes in the residual phase assemblage are all visible as drops in productivity in Figure 8f. The P-T path of the liquid reservoir differs from a simple liquid adiabat because liquids are added to it at each step at the temperature of the mantle reservoir; thus its shape mirrors the shape of the mantle P-T path. Nevertheless, the liquid reservoir evolves to a higher temperature than the mantle reservoir since it follows a non-melting adiabatic path during each decompression step. In the "no equilibration" case, the liquid reaches 1 bar at a temperature 25 K hotter than the mantle; this temperature excess represents the excess heat advected by the melt which can be recovered by the mantle when they are thermally equilibrated in the cases discussed below. If the gravitational source term is added to the no equilibration case, it does not feedback into the mantle reservoir since the gravitational energy is dissipated in the melt reservoir, but the resulting heating drives the liquid reservoir to a temperature at 1 bar 44 K hotter than the mantle reservoir. This temperature difference gives a good indication that the magnitude of excess heat from the gravitational source term is comparable to that available from thermal equilibration.

The liquidus temperature of the melt composition in the accumulated fractional melt in the liquid reservoir is also shown at each pressure in Figure 8a. Note that this is not the liquidus curve of any particular melt composition, since the liquid in the liquid

reservoir changes each time a new increment of melt is added. Nevertheless, the locus of liquidus temperatures shows some very important systematics. First, in the initial stages of melting, when the slope of the mantle adiabat is very low, the liquidus drops off more quickly than the wet adiabat. Hence, contrary to the assertion of Kinzler et al. (1993), cooling of fractional liquids to the temperature of the wet adiabat does not necessarily result in crystallization (see the "equilibrium crystallization" and "fractional crystallization" cases below). At higher extents of melting, however, the mantle adiabat is steeper (the result of increased melt productivity requiring larger absorption of latent heat by proportionately larger T decreases on the wet adiabat) and crosses the liquidus of the composition in the liquid reservoir near the pressure at which 5% total melting has taken place. At this level, crystallization from fractional liquids cooled to the temperature of the wet adiabat is possible. The constraint that fractional crystallization of accumulated fractional melts is thermally prohibited until the system reaches a certain critical melt productivity (and hence, in the MELTS model, a certain minimum extent of melting) limits the range of problems that can be solved by appeal to such deep crystallization. The argument of Kinzler et al. (1993) concerning excess olivine in residual peridotites is still valid in principle, and ought to be reconsidered with better constraints on the thermal environment. Note that for potential temperatures less than 1270 °C (not plotted in these figures), the liquidus of the liquid reservoir compositions crosses the liquid reservoir P-T path in the "no equilibration" case, and hence crystallization may occur from the fractional liquids even without any cooling by the surrounding mantle. This behavior has only been observed in the plagioclase lherzolite stability field.

Case 2, thermal equilibration, no crystallization: The case of thermal equilibration with no crystallization is shown in Figure 8b. The accumulated fractional liquid and mantle

reservoirs follow coincident *P-T* paths. Figure 8d compares the mantle reservoir *P-T* paths from the various cases (which is also the liquid reservoir *P-T* path for cases 2, 3, and 4); the mantle reservoir in the "no crystallization" case reaches 1 bar roughly 5 K hotter than the mantle reservoir in the "no equilibration" case and the liquid reservoir forced to the same temperature as the mantle reservoir in the "no crystallization" case reaches 1 bar 20 K cooler than the liquid reservoir in the "no equilibration" case. The liquid is metastable from 6 kbar to 1 bar, the range where it is below its liquidus, but crystallization is prohibited in this case. Figure 8f shows that thermal equilibration causes melting to be visibly more productive than the "no equilibration" case in the range 1.7-5 kbar, and as a result this case exhausts plagioclase from the residue earlier (and is then less productive in the pressure range 1.2-1.7 kbar, where the "no equilibration" case is still melting plagioclase lherzolite). The "no crystallization" case also exhausts cpx earlier than the "no equilibration" case (at 400 bars rather than 200 bars). The net result of these productivity changes and phase exhaustions, as shown in Figure 8e, is that the final melt fraction achieved at 1 bar (F_{max}) is almost identical to the "no equilibrium" case, although the mean pressure of melt production (not plotted) is slightly higher (by 150 bars, or 6 percent relative). One curious behavior not plotted here occurs for adiabats with potential temperatures less than 1250 °C. In these cases the barren zone at the spinel-plagioclase transition (Asimow et al., 1995a) is sufficiently wide that, liquid adiabats being steeper than dry solid adiabats, the liquid reservoir becomes cooler than the mantle reservoir. In this case thermal equilibration actually causes a small amount of cooling of the mantle reservoir and delays the onset of melting in the plagioclase field.

Cases 3 and 4, thermal equilibration, equilibrium or fractional crystallization: The *P-T* paths of mantle and liquid reservoirs in the "equilibrium crystallization" case are shown in Figure 8c; the "fractional crystallization" case looks similar, although the path

becomes slightly hotter after the exhaustion of plagioclase, as shown when the mantle reservoir *P-T* paths for all four cases are compared in Figure 8d. Crystallization of olivine and then plagioclase occurs after the coincident liquid reservoir and mantle reservoir *P-T* path crosses the liquidus temperature of the liquid reservoir. The amount of crystallization or resorption (which can occur in the equilibrium crystallization case) at each pressure depends on the relative slopes of the liquid reservoir liquidus path and the combined liquid reservoir and mantle reservoir *P-T* path; if the temperature difference is increasing, crystallization is likely to occur. Once crystallization begins, it therefore generally proceeds until a phase is exhausted from the residue, leading to a drop in productivity and a smaller slope of the mantle reservoir (and liquid reservoir) *P-T* path. After plagioclase or cpx is exhausted from the residue, crystallization stops because the mantle adiabat ceases to cool relative to the liquidus of the liquid reservoir. In the equilibrium case, with continued progress along a shallow, low-productivity path, the undercooling of the mantle and liquid reservoirs with respect to the liquidus of the liquid reservoir tends to decrease and resorption occurs. All the crystals in the liquid reservoir may be resorbed if the liquid and mantle reservoir *P-T* paths again become hotter than the liquidus of the liquid reservoir (which occurs for potential temperatures greater than 1330 °C).

When crystallization is occurring, it has a dramatic effect on productivity (Figure 8f). This is a simple consequence of enthalpy conservation: the enthalpy recovered by crystallizing in the liquid reservoir goes into melting the mantle reservoir. The total liquid mass in the two reservoirs may increase, remain constant, or decrease during this process, depending on the relationship between the enthalpy of crystallization of the assemblage crystallizing from the liquid reservoir, the enthalpy of fusion of the mantle reservoir, and the heat capacity of the system. The composition of the liquid remaining in the liquid reservoir can be shifted significantly by this crystallization; the direction of this

compositional shift depends on what minerals are crystallizing (olivine or olivine+plagioclase).

The large increase in productivity in Figure 8f for the equilibrium and fractional crystallization cases begins near 3 kbar, where plagioclase begins to crystallize rapidly. The small amount of olivine crystallization beginning at 6 kbar has a small effect (compare to the "no crystallization" case between 3 kbar and 6 kbar in Figure 8f). The productivity increase during plagioclase crystallization is larger in the fractional crystallization case; fractional crystallization liberates more enthalpy than equilibrium crystallization, even though the masses crystallized are equal. The productivity spike ends at 2.3 kbar in the equilibrium crystallization case and 2.4 kbar in the fractional case when the residue in the mantle reservoir exhausts plagioclase (which occurs first in the fractional crystallization case because of the larger productivity while plagioclase is fractionating from the liquid reservoir). Crystallization also stops at this point because productive melting of the mantle reservoir is no longer forcing the liquid reservoir to cool with respect to its liquidus.

Although the increase in productivity over the no crystallization case between 2 and 3 kbar in the cases with crystallization is large, the increase in maximum F achieved at 1 bar is extremely small (Figure 8e). Although the F curves for the various cases are visibly separate in the range 1-5 kbar, the kinks at the exhaustion of plagioclase from the residue in each case "refract" this visible difference to a very small difference at pressures below the kink. In effect, even though thermal equilibration and crystallization in the liquid reservoir add enthalpy to the mantle, its extent of melting is effectively limited by the exhaustion of phases. The high enthalpy of fusion of harzburgite prevents the added enthalpy from increasing the final melt fraction very much in this example, which happens to exhaust cpx in the "no equilibration" case just before reaching 1 bar.

The range of possible behaviors

The magnitude of the productivity effects of thermal equilibration and crystallization of the liquid reservoir vary with the potential temperature of the calculation in a variety of ways. The productivity of isentropic upwelling varies with pressure, as do the occurrence and intensity of subsolidus phase changes and the extent of melting needed to exhaust spinel, plagioclase, cpx, and opx from the residue. All these effects control the slope of the mantle adiabat, and hence its relationship to the liquidus path of the liquid reservoir and thus the occurrence and amount of crystallization. Certain phenomena, like the liquidus crossing the unequilibrated liquid reservoir *P-T* path and the unequilibrated liquid reservoir *P-T* path becoming cooler than the mantle adiabat while crossing the barren zone at the spinel-plagioclase transition, are restricted to certain ranges of potential temperature.

The net effects of thermal equilibration and crystallization are shown as functions of potential temperature in Figure 9. Figure 9a shows the maximum F (F_{max}, defined as the mass fraction of the mantle reservoir lost to melting; in cases with crystallization this is not necessarily related to how much melt contributes to the crust) achieved at 1 bar in each case; the basic observation is that excess heat sources such as thermal equilibration or crystallization from the liquid have negligible effects on the maximum melt fraction achieved for all those adiabats with potential temperature above 1275 °C. This surprising behavior is the result of the effective limitation of melting by the exhaustion of clinopyroxene. Although melting beyond this point is possible, the isentropic (and isobaric) productivity is quite low and the amount of enthalpy that would need to be added to the mantle by thermal equilibration or crystallization to produce significant melting is correspondingly large. Therefore, a more sensitive indicator of the magnitude of heating is shown in Figure 9b by the pressure of exhaustion of cpx from the residue. 1275 °C is seen to be the maximum potential temperature for cpx to remain in the residue

in the "no equilibration" case at 1 bar (and is also the maximum potential temperature for significant differences in F_{max} between the four cases), which confirms the notion that the suppression of further melting by the exhaustion of cpx is what limits the effect of thermal equilibration and crystallization on F_{max}. Figure 9b also shows that there are increases in the pressure of cpx-out and hence by implication in the depth at which melting takes place resulting from thermal equilibration for all potential temperatures. Again the effect becomes more significant at lower potential temperatures, where cpx-out may be depressed by 1 kbar or more.

Although the increase in melt fraction due to thermal equilibration and crystallization is generally small, crystallization in the mantle has an additional effect in that it may prevent some of the melt extracted from the residue from reaching the crust. Only the material that is in the liquid reservoir and in the liquid phase at the end of these calculations (at 1 bar, which is unrealistic) is considered to become part of the oceanic crust. Thus all mass that crystallizes in the fractional crystallization case and any crystals not resorbed in the equilibrium crystallization case are considered to remain in the mantle and therefore do not contribute to crustal thickness. For passive flow melting regime geometry, Figures 9c and 9d plot crustal thickness[3] and mean melt fraction F_B (Plank et al., 1995) in the aggregate melt that contributes to the crust against potential temperature for the four cases (and also show the effect of the gravitational term at T_P=1290 °C). The effects of crystallization are significant up to a potential temperature of about 1300 °C, 25 degrees hotter than the limit for significant changes in F_{max}. These figures define three regimes. At potential temperatures above 1300 °C, negligible crystallization occurs because the liquid reservoir path does not cross the liquidus or does so only for a small

[3] Note that in this calculation melting continues to 1 bar, whereas the crustal thicknesses shown below in chapter 5 are for melting regimes that stop at 0.2 GPa. The difference is quite significant. The reader is asked not to attempt to interpret the crustal thickness or F_B vs. potential temperature relationship shown here in terms of the properties of real oceanic crust, where melting certainly stops at a pressure greater than 1 bar!

pressure range, with a small amount of undercooling and very minor olivine crystallization. Between 1265 °C and 1300 °C, the loss of mass to crystallization in both the equilibrium and fractional cases is larger than the amount of extra melting induced by recovering the heat of crystallization. Hence there is a reduction in crustal thickness of up to 1 km. Below 1265 °C, the enthalpy balance of melting and crystallization is such that for the fractional crystallization case, more melt results than is lost to the conduit walls, and there is an increase in crustal thickness relative to cases without crystallization, again of about 1 km. This crossover at 1265 °C represents the point where, averaged over the pressure where crystallization is occurring, the enthalpy of crystallization recovered in the liquid reservoir balances the enthalpy of fusion of the mantle reservoir and the heat capacity of the system. The details of this balance are sufficiently complex that a full calculation may be necessary to predict the effects, but a simple interpretation is that the small temperature range over which plagioclase lherzolite melts (see chapter 5, figure 1) implies that at lower potential temperatures, where more of the melting occurs in the plagioclase lherzolite stability field and more plagioclase forms in the residue, the addition of enthalpy to the residue is more effective in producing excess melting.

Gravitational source term

Although the magnitude of the source of dissipation due to vertical separation in a gravity field depends on the extent of melt migration, there is a well-defined maximum limit to this term for the case of infinite permeability. Using D'Arcy's law

$$\varphi(w - W) = \frac{k}{\mu}\nabla(P + \rho_f g\hat{z}), \tag{26}$$

together with (8') and (9), the energy source due to melt migration in a gravitational potential in equation (17) can be rewritten:

$$\left(\frac{\mu\varphi^2(w - W)^2}{k\rho_s^o W^o}\right) = \left(\frac{F}{\rho_f} + \frac{\varphi}{(1-\varphi)}\frac{(1-F)}{\rho_s}\right)\nabla(P + \rho_f g\hat{z}). \tag{27}$$

The limit of infinite permeability corresponds to $\varphi = 0$, since melt is removed instantaneously as it is produced and migrates at infinite velocity. Furthermore, ignoring dynamic pressures, in this limit the hydrostatic pressure gradient $\nabla P = -\rho_S g$. Thus we can write a maximum value for the gravitational energy source term:

$$\left(\frac{\mu\varphi^2(w-W)^2}{k\rho_s^o W^o}\right) \leq \left(\frac{F(\rho_f - \rho_f)g}{\rho_f}\right), \tag{28}$$

or a corresponding maximum for the entropy source term by dividing by T. This is the differential form. Added together over a whole column, to the extent that g and the densities are nearly constant, the total entropy source is proportional to the integral of $F\mathrm{d}P$. We illustrate the effect of a source term of this limiting magnitude for one representative potential temperature, 1290 °C (the same case shown in Figure 8), for the "thermal equilibration" case only.

The magnitude of extra melting beyond the thermal equilibration case due to the addition of the limiting gravitational source term is seen in Figure 8f to be comparable, for this potential temperature, to the effect of thermal equilibration alone in the absence of crystallization from the ascending liquid. This is consistent with the excess temperatures of the liquids at 1 bar in the "no equilibration" case with and without gravity of 25 and 44 degrees, respectively (Figure 8a, see above). Addition of the gravity term increases the pressure of cpx-out (and the mean pressure of melting) by a few hundred bars, and has negligible effect on F_{max}, F_B, or crustal thickness (Fig 9). The effects of thermal equilibration and gravity seem to scale similarly with potential temperature; for a potential temperature of 1430 °C (melting begins at 30 kbar), the excess temperatures of the liquid reservoir above the mantle reservoir at 1 bar in the no equilibration case are 32 and 62 degrees.

Summary

The two sources of irreversible entropy production due to melt migration recognized by McKenzie (1984) (i.e., advection of heat by the fractionated liquids and gravitational energy release) appear to be comparable to one another in magnitude across a wide range of potential temperatures. Both are negligible for hot mantle since the extent of melting is anyway mostly limited by the drop in productivity when cpx is exhausted from the residue. For abnormally cold mantle, if melting continues to shallow levels (in these calculations it was continued to 1 bar), there may be increases of up to ~10% (relative) in F_{max} and ~200 m in crustal thickness as the result of each effect. When thermal interactions occur, however, there are additional effects due to the possibility of crystallization from the accumulated fractional liquid. This can cause local increases of >100% in the productivity of melting (e.g., Figure 8f, between 2.5 and 3 kbar), but the balance between liquid gained by extra melting and lost by crystallization prevents large increases in crustal thickness by this mechanism except for exceptionally cold mantle, where crystallization of plagioclase from the accumulated fractional liquid drives rapid melting of plagioclase lherzolite at low pressure. For more moderate mantle temperatures, the net effect of this deep crystallization is to reduce crustal thickness.

Although we have not introduced any new physics into the evaluation of the gravity term, our estimate of its magnitude is smaller than that of McKenzie (1984) for either the same F_{max} or the same pressure of initial melting. This is a consequence of the strongly increasing productivity function during progressive decompression melting in MELTS calculations. As mentioned above, the total entropy source due to gravity is roughly proportional to the integral of $F\mathrm{d}P$. Clearly, for the same F_{max} and the same pressure range of melting, the area under the F(P) curve is much smaller for a strongly concave-up curve than for a linear or concave-down curve (compare the curves in Figure 8e to the area under a straight line from F=0 at 17 kbar to F=F_{max} at 1 bar). The same is

true of our estimates of the effect of thermal equilibration when compared to constant or decreasing-productivity models. Since much of the liquid in a MELTS model of polybaric melting is produced at relatively shallow levels in the melting regime, much of the liquid does not ascend very far along a liquid adiabat, and so less superheat is available. In a rough sense, the weighted sum of the total distance that each increment of liquid ascends after being separated from the mantle residue should predict the order of magnitude of the excess heat that can be recovered through thermal equilibration with the liquid. This quantity also scales with the integral of $F\mathrm{d}P$, and hence is smaller in the MELTS model than in simple linear estimates because of the increasing productivity.

Conclusions

1. In the absence of diffusion, one-dimensional steady-state equilibrium porous flow is required by conservation of mass to yield melt and residue compositions identical to those attainable by batch melting of the source composition. Except for dissipative source terms due to solid compaction and gravity, energy conservation also requires the temperature and extent of melting at any pressure to equal those achieved by isentropic closed-system upwelling. This analogy between steady 1-D melt transport and batch melting enables some simple calculations of melt migration phenomena.

2. When melt flow is focused into a channel but maintains equilibrium with the residue in the channel, then compared to simple 1-D flow, this is equivalent to batch melting of increasingly fertile bulk compositions at higher extents of melting. Both effects contribute to higher melt productivity $-\mathrm{d}F/\mathrm{d}P$ and a larger coefficient for orthopyroxene in the melting reaction and hence faster removal of orthopyroxene from the residue. A small amount of melt focusing can easily leave a dunite residue if melting continues to 1 bar. Generating a dunite residue at typical asthenospheric pressures,

however, requires a combination of hot mantle potential temperature and extremely high focusing factors ($>10^2$).

3. At least in one dimension, the approximation of isentropic upwelling is reasonably robust even when melt and residue undergo relative motion (although we have not treated dissipation due to solid compaction or shear). The gravitational energy release due to melt migration and the advection of heat by the melt phase are both small effects in terms of total extent of melting produced for normal mantle potential temperatures that reach the exhaustion of clinopyroxene. However, the possibility that the migrating liquid may cross its liquidus and partially crystallize when melt productivity in the surrounding mantle is high enough implies that the composition and mean pressure of the final aggregate melt and the crustal thickness are dependent on thermal effects associated with melt migration.

Figure 1. Cartoon representing one-dimensional equilibrium porous flow columns. The system is adiabatic and all diffusion is neglected. The vertical coordinate z increases upwards from z_o at the bottom, which is the depth at which the adiabat intersects the solidus and melting begins. The fraction of liquid by volume, $\phi(z)$, is represented by the width of the "liquid" field as a fraction of the width of the column. The extent of melting $F(z)$ is represented by the concentration of a perfectly compatible tracer (stippling in the solid field). The composition of the liquid is indicated by the concentration of an incompatible element (shading in the liquid field). The vertical velocity of the solid $W(z)$ is shown by black-headed arrows and at z_o is equal to W_o. The vertical velocity of the liquid $w(z)$ (shown by white-headed arrows) is controlled by D'Arcy's law. The case on the left has permeability (k) set to zero and therefore is simply batch melting, with $W=w$ and $\varphi = F\rho_s / [F\rho_s + (1-F)\rho_f]$ everywhere. The case on the right has a non-zero permeability which is an increasing function of ϕ, hence $w>W$ and increases upwards. Conservation of mass flux requires that $\varphi < F\rho_s / [F\rho_s + (1-F)\rho_f]$ where $w>W$, but F and the composition of liquid and solid do not depend on f or w.

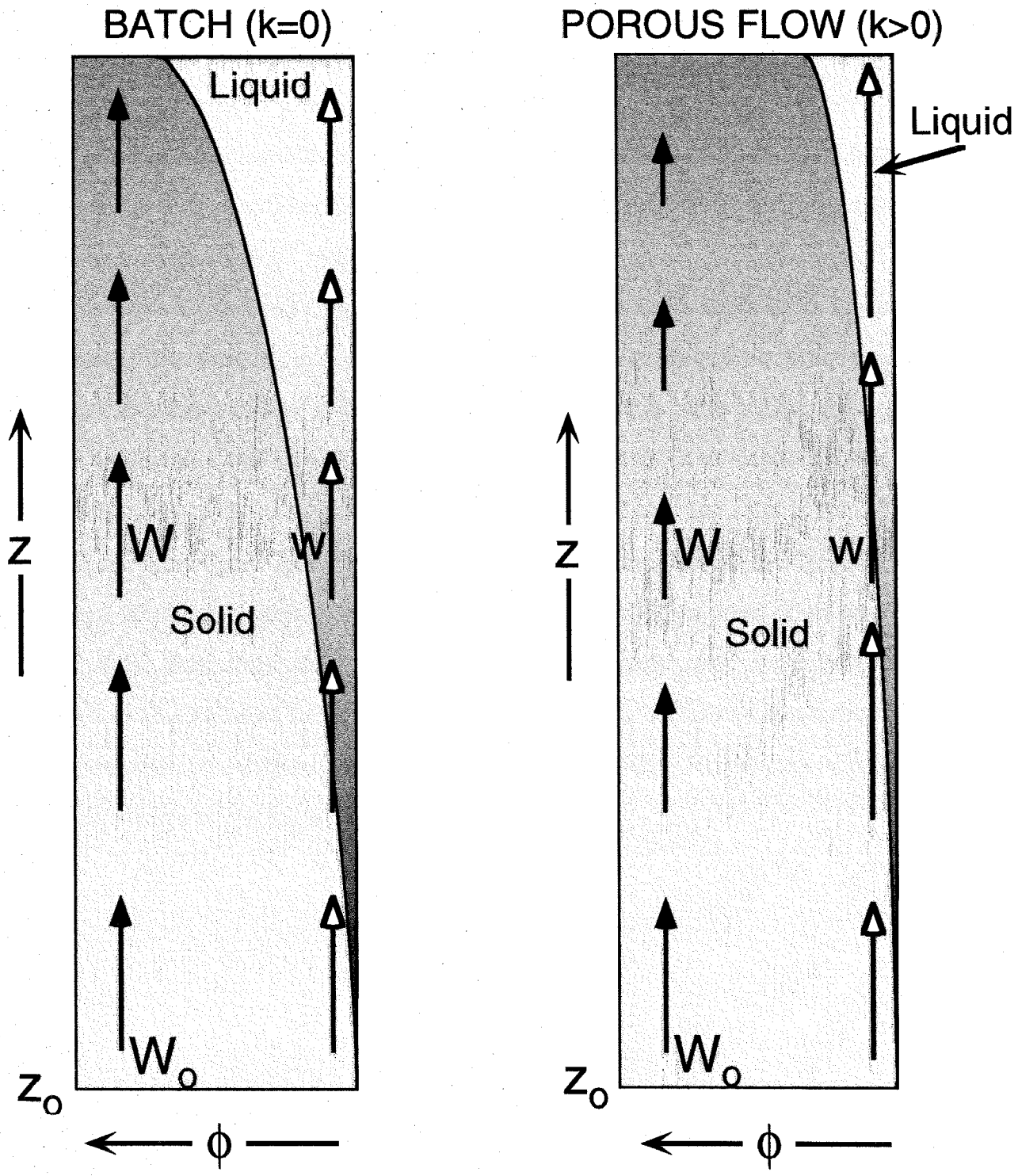

Chapter 4, Figure 1

Figure 2. The effect of a discrete focusing event that adds melt to a 1-D steady equilibrium porous flow column at 10 kbar. The system begins melting at 19 kbar. (a) Mass fraction of olivine in the residual assemblage as a function of pressure; various curves at pressures lower than 10 kbar represent various values of the focusing factor Ω_D, the ratio of melt mass after focusing at 10 kbar to melt mass before focusing at 10 kbar. Modal olivine of ~0.98 indicates a dunite with ~2% spinel. (b) Mass fractions of orthopyroxene (opx) and clinopyroxene (cpx) in the residual assemblage as functions of pressure. The focusing event at 10 kbar is indicated. The dashed black line marks the modal abundance of opx at the exhaustion of cpx for each value of Ω_D. (c) Apparent melt productivity ($-d\tilde{F}/dP$) vs. Pressure. $\tilde{F}$ is the mass fraction of melt in the equivalent batch melting calculation, i.e., if the relative velocity of melt and solid is zero, $\tilde{F}$ is the mass fraction of melt actually present. As long as the residual assemblage remains the same, ($-d\tilde{F}/dP$) increases monotonically with Ω_D. (d) Mass fractions of opx and cpx in the residue plotted against $\tilde{F}$ on a reversed scale. The stoichiometric coefficient of cpx (slope on this diagram) in the melting reaction is roughly constant with respect to $\tilde{F}$ and Ω_D, whereas the coefficient of opx increases with $\tilde{F}$ and Ω_D. Hence less opx remains at the exhaustion of cpx for higher values of Ω_D.

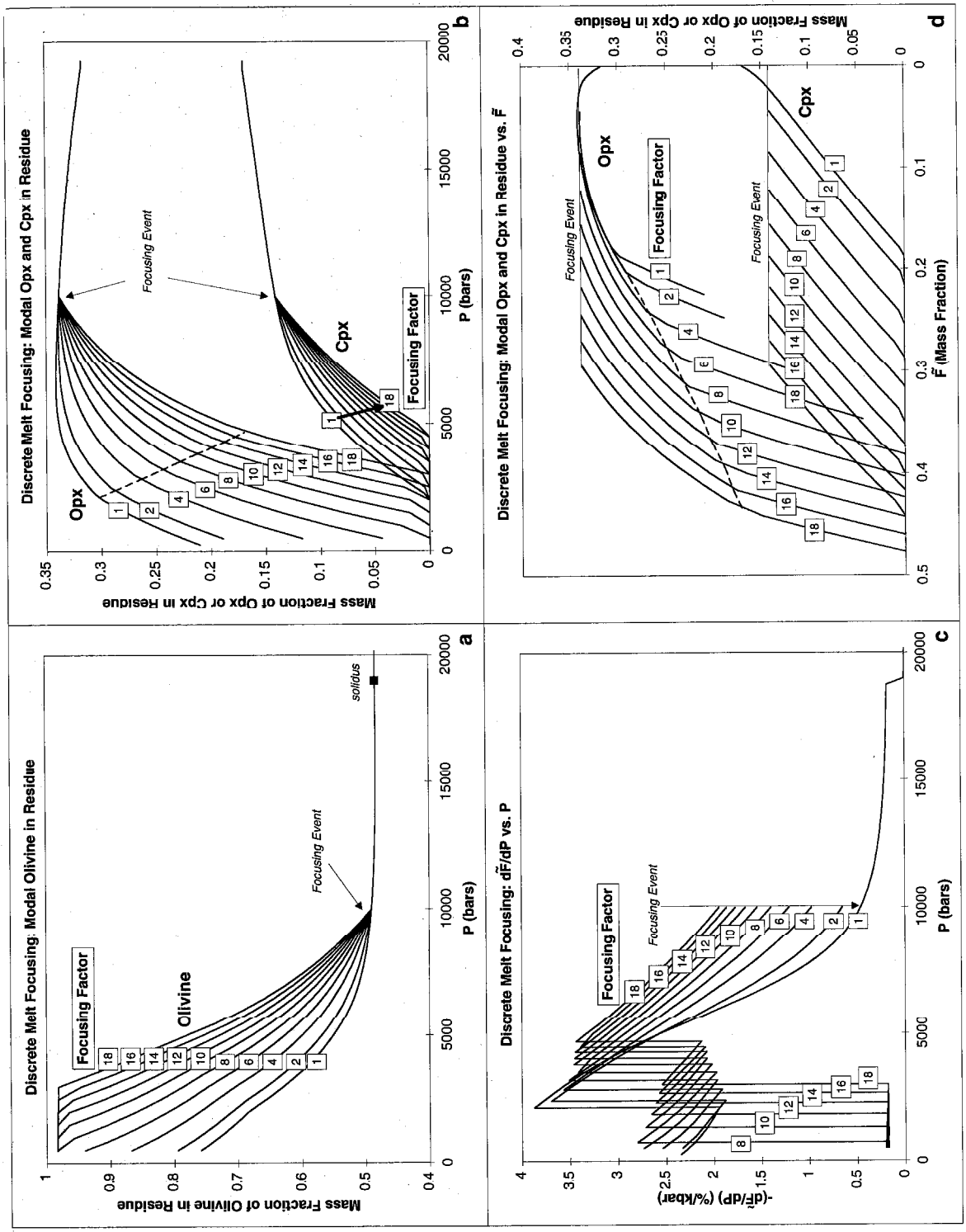

Chapter 4, Figure 2

Figure 3. The effect of continuous focusing of melt into a 1-D steady equilibrium porous flow column. The system begins melting at 19 kbar; every 0.5 kbar the melt flux is increased by a small factor. The product of all these incremental focusing factors over the entire column is the integrated focusing factor Ω_I. (a) Mass fraction of olivine in the residual assemblage as a function of pressure. (b) Mass fractions of orthopyroxene (opx) and clinopyroxene (cpx) in the residual assemblage as functions of pressure. The dashed black line marks the modal abundance of opx at the exhaustion of cpx for each value of Ω_I. (c) Apparent melt productivity ($-d\tilde{F}/dP$) vs. pressure. As long as the residual assemblage remains the same, ($-d\tilde{F}/dP$) increases monotonically with Ω_I. (d) Mass fractions of opx and cpx in the residue plotted against $\tilde{F}$ on a reversed scale. The stoichiometric coefficient of cpx (slope on this diagram) in the melting reaction is roughly constant with respect to $\tilde{F}$ whereas the coefficient of opx increases. Hence as the exhaustion of cpx moves to higher $\tilde{F}$ with increasing Ω_I, less opx remains at the exhaustion of cpx.

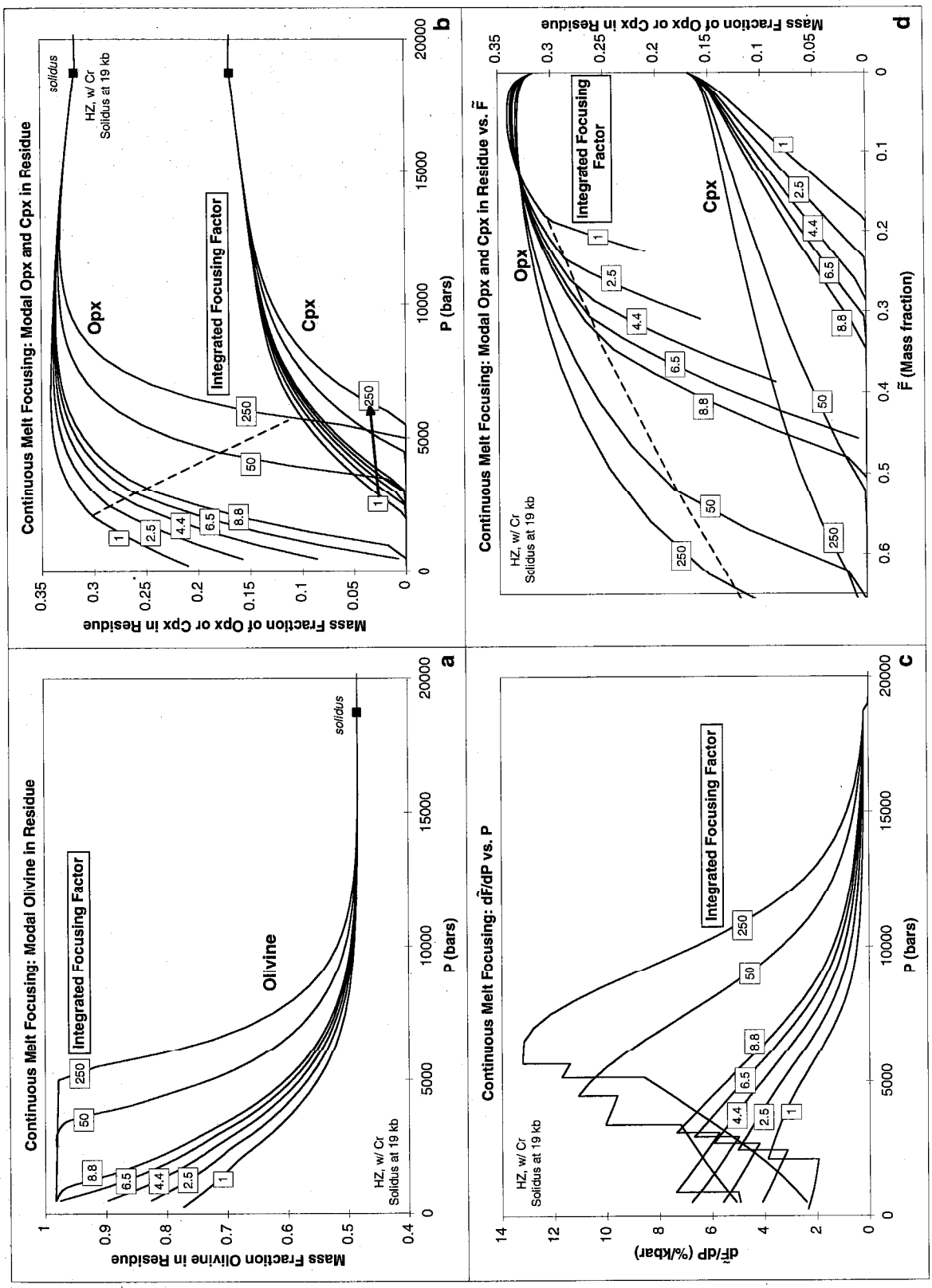

Chapter 4, Figure 3

Figure 4. The effect of continuous focusing of melt into a 1-D steady equilibrium porous flow column as in Figure 3, except this system begins melting at 35 kbar, in the garnet peridotite stability field. Note the changes in productivity and melt reaction stoichiometry at the exhaustion of garnet at 31 kbar (spinel is always present, since this composition contains Cr_2O_3).

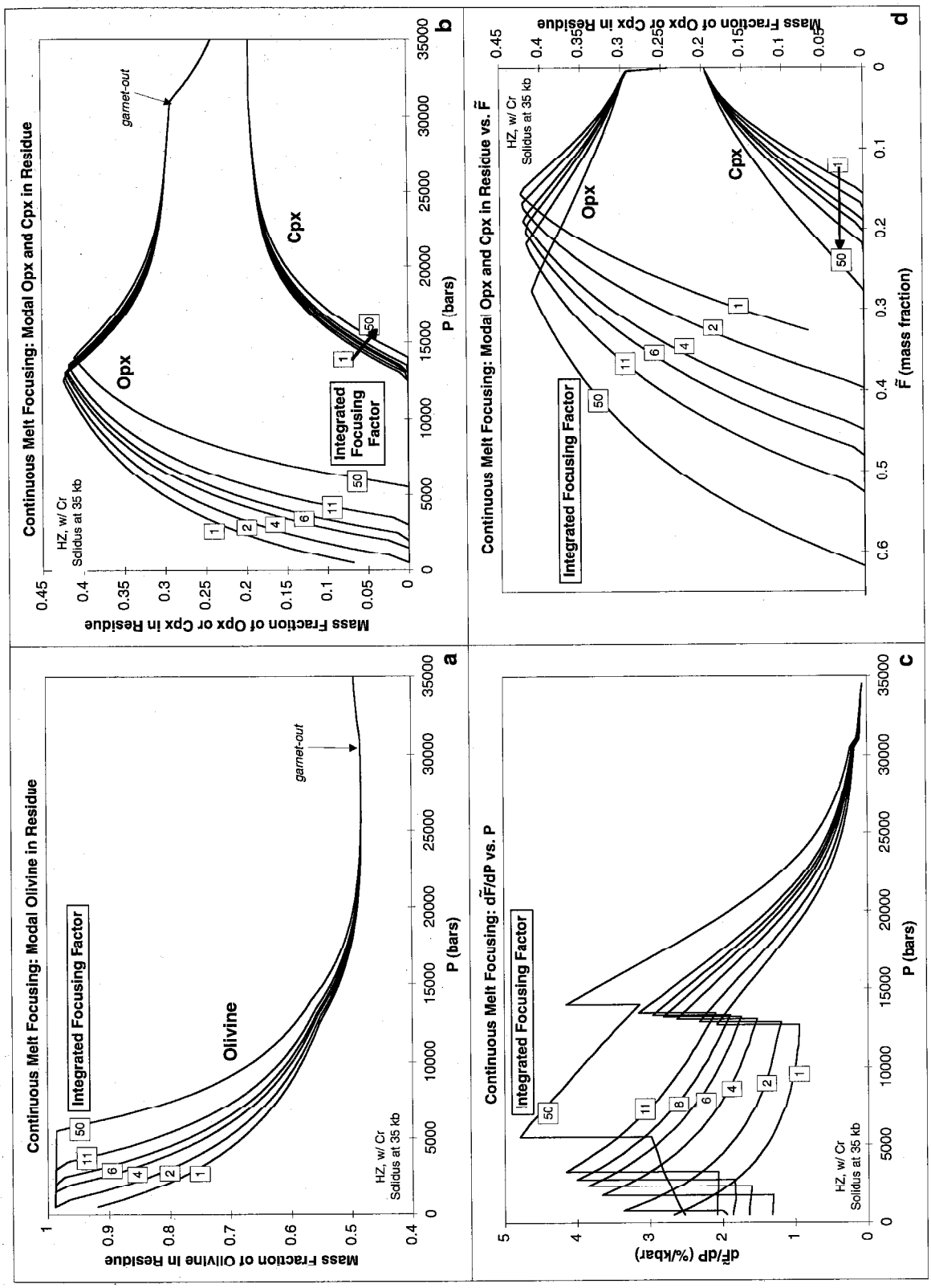

Chapter 4, Figure 4

Figure 5. Summary of the effect of continuous melt focusing (Figures 3 and 4) on the residual phase assemblage. As a function of integrated focusing factor, Ω_I, the plotted curves for the cold mantle (19 kbar solidus intersection) and hot mantle (35 kbar solidus intersection) cases divide the residual columns into lherzolite (olivine+spinel+opx+cpx), harzburgite (olivine+spinel+opx), and dunite (olivine+spinel) fields. This figure indicates both the increase in pressure of cpx-out with increasing Ω_I; the narrowing of the harzburgite field with increasing Ω_I; and the diminishing returns of increasing Ω_I, leading to an approximate limiting pressure for opx-out and cpx-out for each potential temperature.

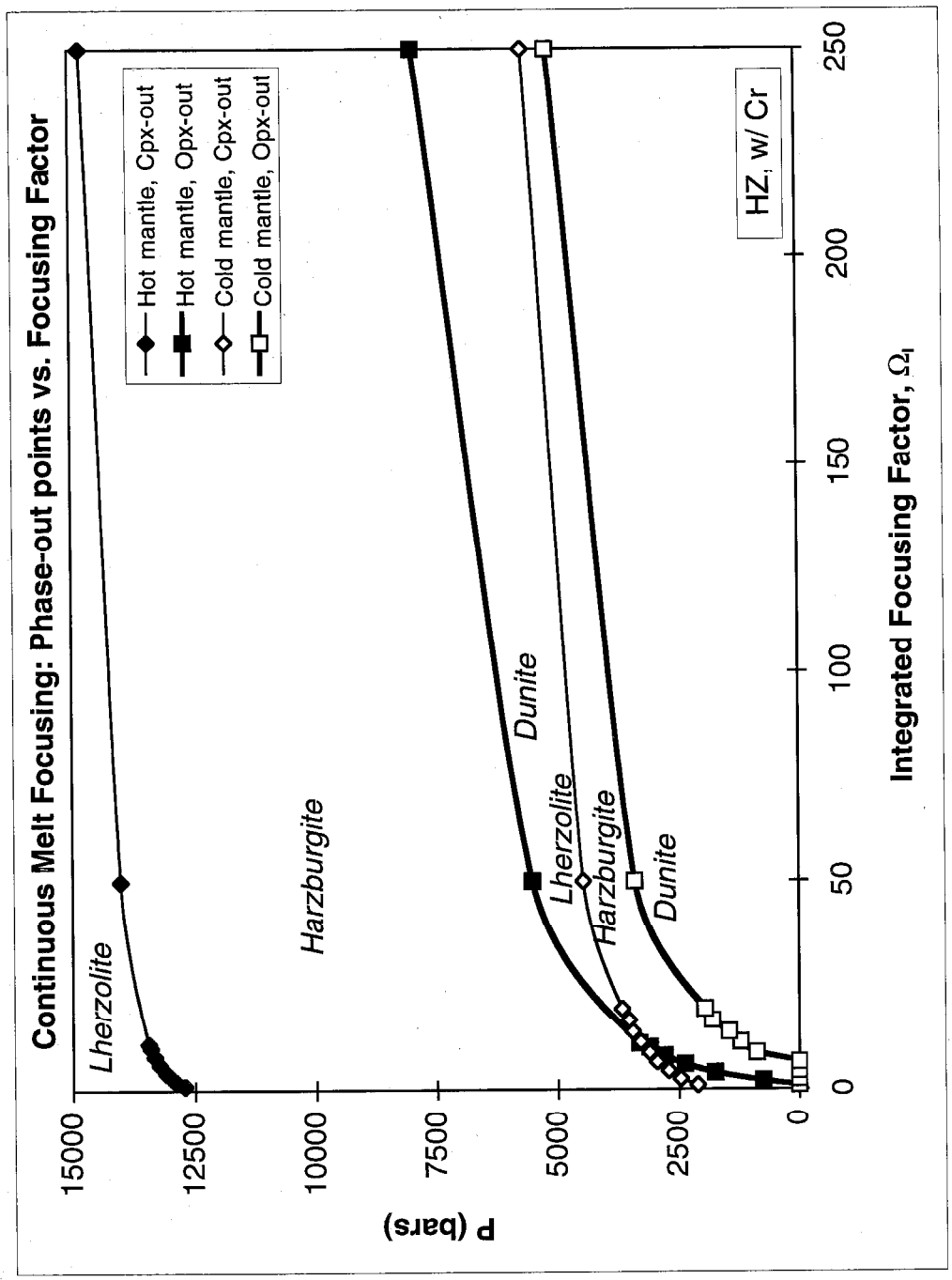

Chapter 4, Figure 5

Figure 6. Composition of spinel, Cr# (molar Cr/[Cr+Al]) vs. TiO_2 (wt %), in residues of adiabatic fractional melting and melt focusing calculations as described in the text. The colored curves show evolution of the residues as functions of pressure in the upwelling columns; for the focusing calculations the points of cpx-out and opx-out are shown. Oman ophiolite data from Kelemen (reference). The Oman harzburgites, interpreted as residues of fractional melting, have moderate Cr# and low TiO_2; the model fractional melting residues pass through this field. The Oman dunites, interpreted as channels of focused flow, have high Cr# and high TiO_2; the model focusing paths reach this field near the transition to dunite.

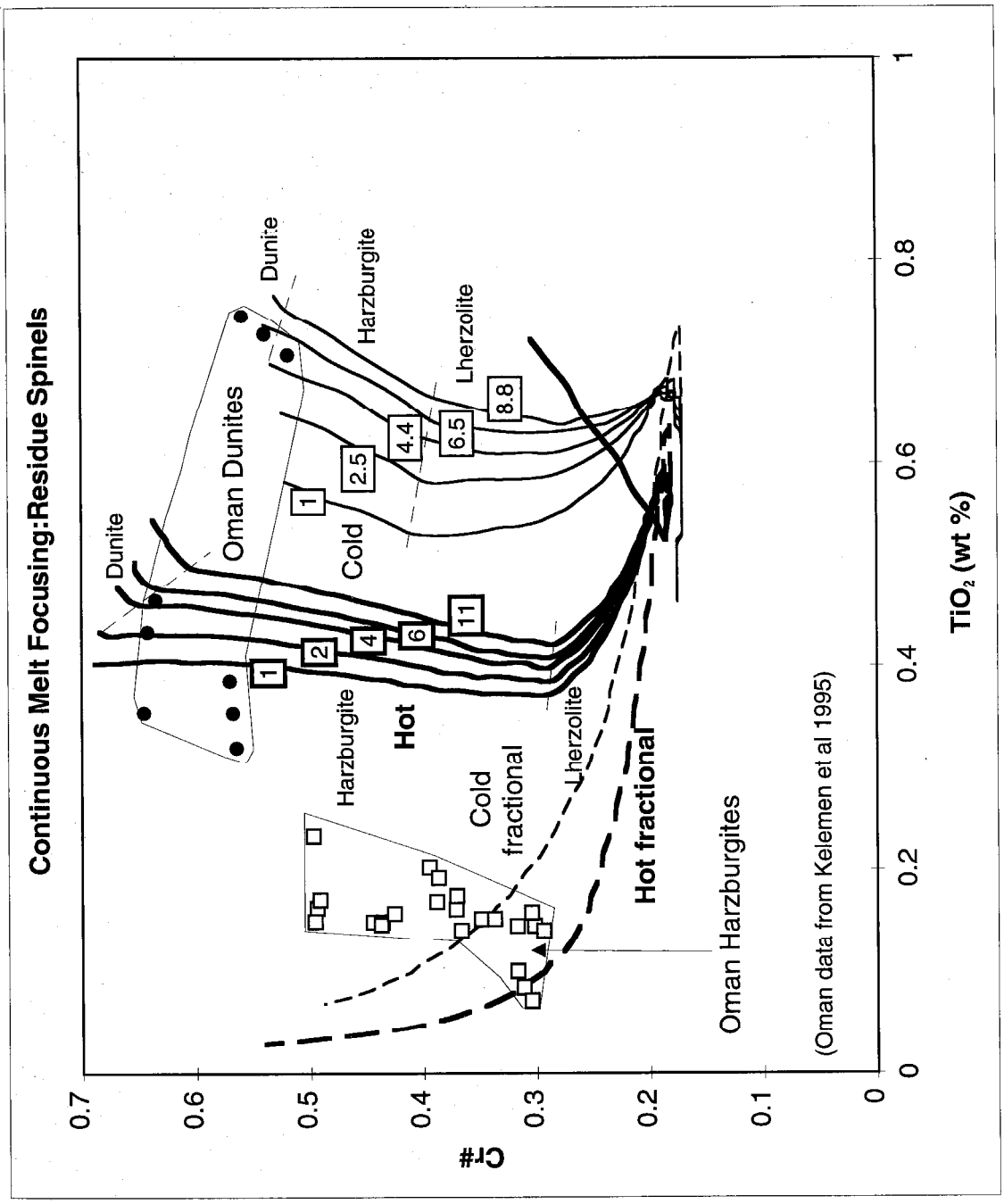

Chapter 4, Figure 6

Figure 7. Schematic drawing representing the calculation of thermal equilibrium between ascending mantle, the liquid reservoir containing accumulated fractional melts, and possibly a reservoir of crystals fractionated from the melt. The system is enclosed in an insulating box through which no heat flows. The reservoirs move together, but this represents any steady one-dimensional solution in which relative flow between mantle and liquid takes place, as long as there is either no thermal interaction or perfect thermal equilibration (see text). In each incremental step, the pressure is lowered reversibly and each reservoir moves up isentropically. Any melt that forms in the mantle reservoir is extracted to the liquid reservoir and mixed isenthalpically with its previous contents. Then, optionally, the mantle and liquid reservoirs may be brought to the same temperature at constant total enthalpy. Furthermore, if the liquid in the liquid reservoir crosses below its liquidus, it may either be (1) kept as a metastable liquid, (2) allowed to isenthalpically crystallize at equilibrium and carry its crystals with it (they might later be resorbed), or (3) allowed to fractionally crystallize in which case the crystals are removed to the third chemically isolated reservoir, the "conduit walls." The conduit walls continue to participate in the thermal equilibrium, i.e., the total enthalpy of the three reservoirs is held constant except during the isentropic vertical motion step.

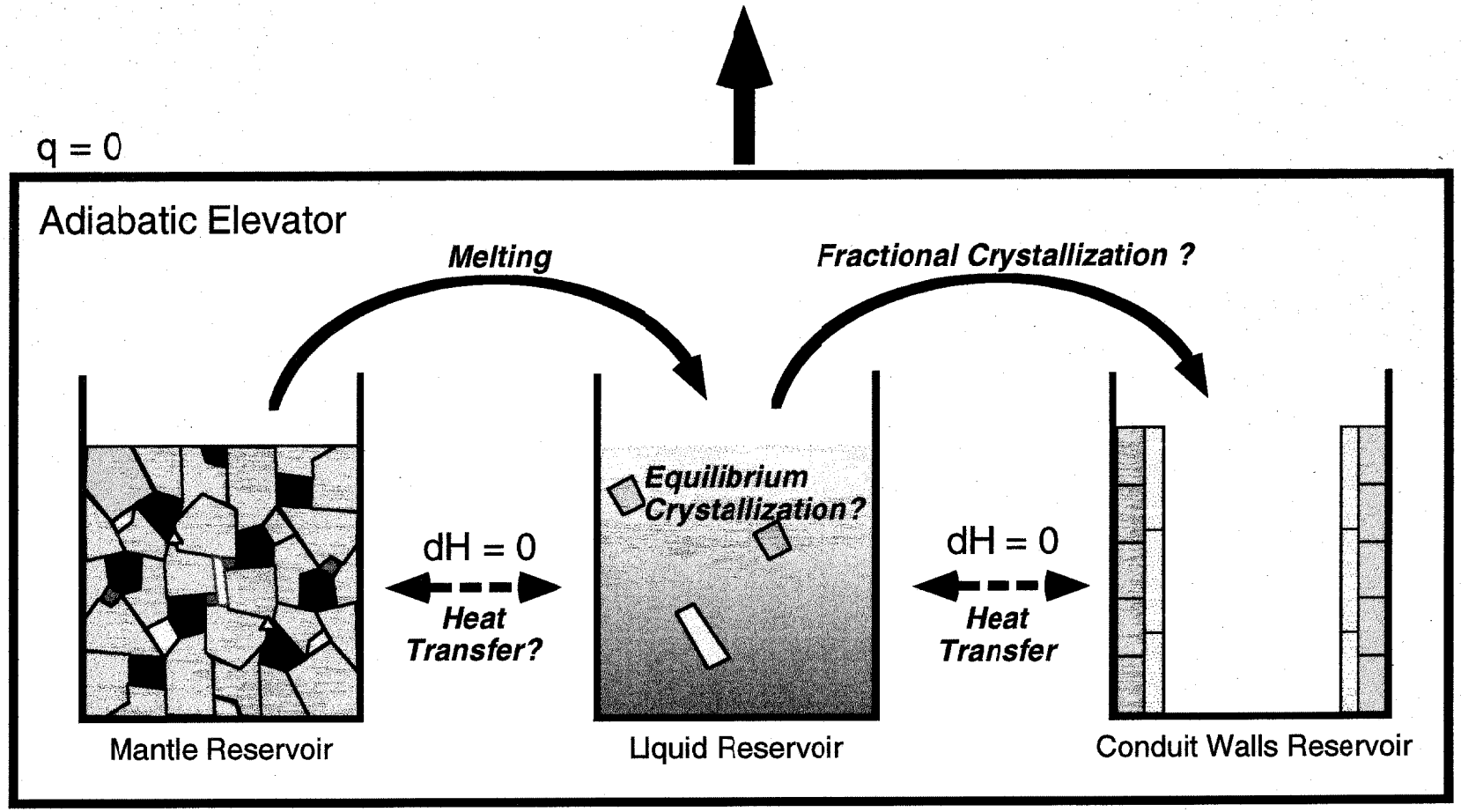

Chapter 4, Figure 7

Figure 8. Illustration of the effects of thermal equilibration between accumulated fractional melt and the mantle. The four cases, "no equilibration," "thermal equilibration, no crystallization," "thermal equilibration, equilibrium crystallization," and "thermal equilibration, fractional crystallization" are explained in the text. In this example, all cases begin melting at 17 kbar. (a) The "no equilibration" case; the *P-T* paths of the mantle and liquid reservoirs are plotted together with the locus of liquidus temperatures of the liquid reservoir at each pressure. The path of the liquid when gravitational energy is dissipated in this reservoir is also shown. (b) The "thermal equilibration, no crystallization" case, in which mantle and liquid reservoirs are brought to the same temperature at each pressure. The liquid is metastable below 6 kbar but is not permitted to crystallize. Gravity causes a small amount of heating at the end of the path. (c) The "thermal equilibration, equilibrium crystallization" case; the amount of crystallization that occurs is generally related to the undercooling of the liquid reservoir with respect to the liquidus curve. Gravity causes a small amount of heating at the end of the path. (d) The *P-T* paths of the mantle reservoir in the four cases (without gravity) are compared; for cases with thermal equilibration this is also the path of the liquid reservoir. The four cases only differ significantly below 3 kbar. (e) Melt fraction F vs. P for the four cases without gravity and for the "thermal equilibration, no crystallization" case with gravity. The differences are small, especially at low pressure where all the cases have exhausted plagioclase and clinopyroxene. The inset shows an enlargement of the low-pressure part of the plot. (f) Melt productivity $-(dF/dP)$ vs. P for the same five cases as (e). Here the differences are clearly visible. Each curve shows three drops in productivity, at the spinel-plagioclase transition (5-6 kbar), plagioclase-out (1.5-2.5 kbar), and cpx-out (0-1 kbar). The higher productivity cases experience each productivity drop at higher pressure. The large productivity spike in the crystallization cases is due to the crystallization of plagioclase+olivine from the liquid reservoir. The inset enlarges the low-pressure part of the figure for clarity.

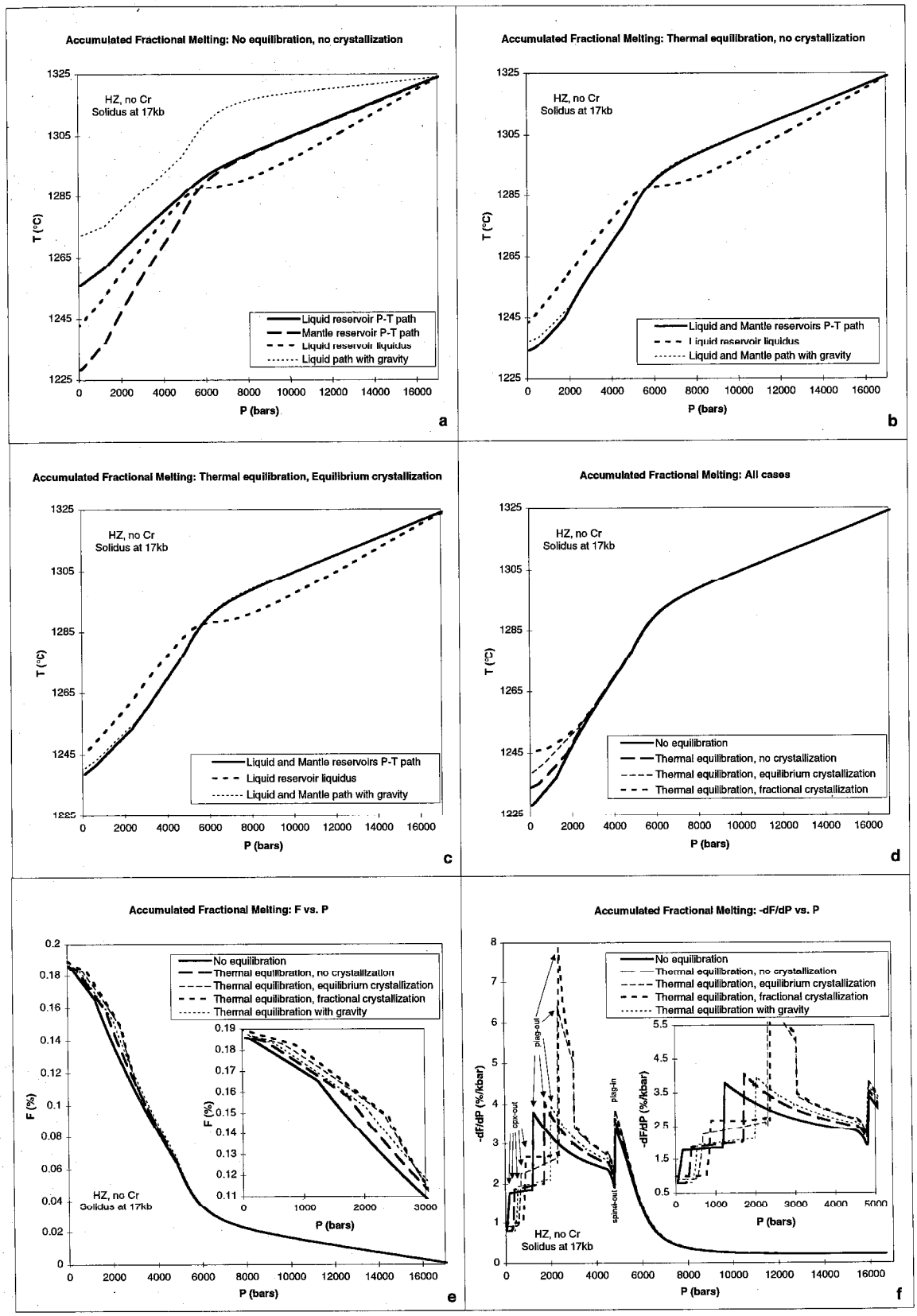

Chapter 4, Figure 8

Figure 9. The effects of thermal equilibrium, possible crystallization, and gravity on melt production in accumulated fractional melting systems. The abscissa in each case is potential temperature, a monotonic function of solidus intersection pressure and of total initial entropy. Each figure shows four cases across a range of potential temperatures (see text): "no equilibration," "thermal equilibration, no crystallization," "thermal equilibration, equilibrium crystallization," and "thermal equilibration, fractional crystallization." For one potential temperature (the same as the example calculations in Figure 8), the case of thermal equilibration plus gravity with no crystallization is shown (x symbol). (a) F_{max}, the melt fraction by mass reached at 1 bar measured by the total extracted from the mantle residue. (b) The pressure at which clinopyroxene is exhausted from the residue. (c) The crustal thickness from a two-dimensional passive flow melting regime, measured by the bulk melt fraction remaining after any crystallization in the mantle. (d) The mean melt fraction F_B in the accumulated two-dimensional melt that contributes to the crustal thickness in (c).

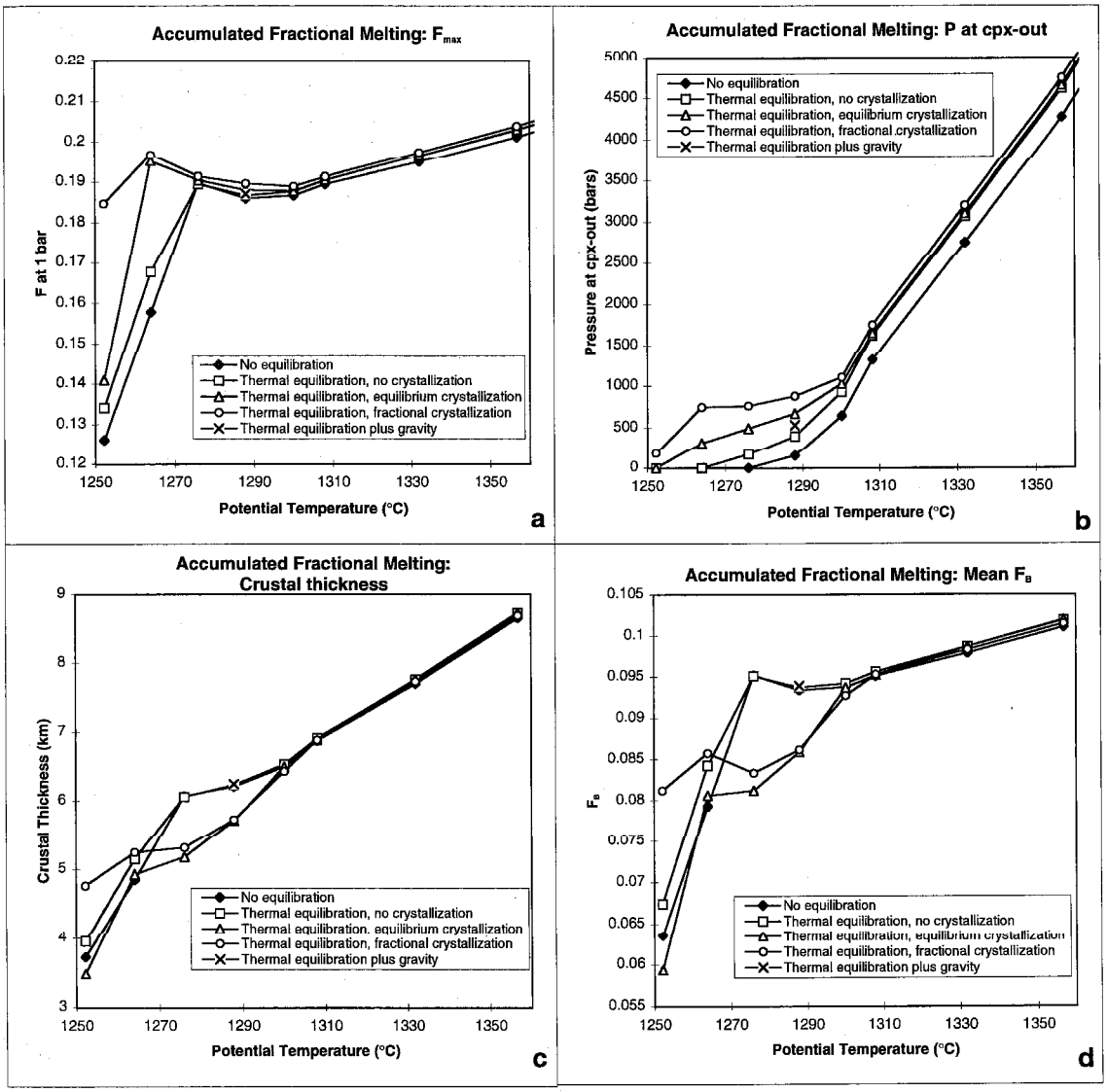

Chapter 4, Figure 9

Chapter 5. Thermodynamic calculation of the composition and mean properties of mid-ocean ridge basalts

Abstract – The composition, mean pressure, mean melt fraction, and crustal thickness of mid-ocean ridge basalts (MORBs) are calculated from the MELTS model of silicate-liquid equilibria. We consider polybaric, isentropic batch and incrementally isentropic fractional melting of a range of source compositions from fertile to depleted for a range of potential temperatures (i.e., pressures of initial melting) and pressures of final melting. The compositions and amounts of liquid as functions of pressure are added together for idealized active flow (one integration of fractional melts) and passive flow (two integrations of fractional melts or one integration of batch melts) to produce model primary aggregate liquids. The output of these polybaric models are compared to the output of other parameterizations of MORB production; the results differ both because the melt compositions predicted by MELTS differ from the compositions extrapolated by published parameterizations, most notably at small melt fractions, and because the self-consistent energy balance in the MELTS approach results in strong variations in melt productivity during progressive melting. The relationships among potential temperature, final pressure, mean pressure, mean extent of melting, and crustal thickness are reconsidered for a variety of models. The effects of unusually fertile or depleted source composition are discussed.

Introduction

Langmuir et al. (1992) identified three functions that must be combined to create a forward model capable of predicting primary MORB composition and volume: a chemistry function, a melting function, and a mixing function. The chemistry function specifies the liquid composition as a function of pressure (P) and temperature (T), and possibly depends on source composition as well. The melting function specifies the melt fraction (F) for a single parcel of source as a function of P and T. The mixing function is a representation of the two-dimensional form of the melting regime and specifies how the

individual increments of liquid are to be weighted to create the aggregate primary melt. These three functions are often constructed independently, but in fact the chemistry and melting functions are intimately dependent on one another since both must satisfy mass balance and both are controlled by the same thermodynamics of solid-liquid equilibrium. There are several published attempts to create chemistry, melting, and mixing functions from parameterization of experimental peridotite melting data (Kinzler, 1997; Kinzler and Grove, 1992a; Kinzler and Grove, 1992b; Klein and Langmuir, 1987; Langmuir et al., 1992; McKenzie and Bickle, 1988; Niu and Batiza, 1991). The thermodynamic approach to forward modeling replaces the chemistry and melting functions with the self-consistent predictions of MELTS. For discussion of the suitability of MELTS as presently calibrated for this purpose, see Baker et al. (1995) and Hirschmann et al. (1997b; 1997a). In general, MELTS predicts trends of compositions vs. melt fraction that are similar to trends observed in experiments, but the trend is frequently offset in T and in certain oxides: at 10 kbar SiO_2 is about 4% too low and MgO about 2% too high (Baker et al., 1995). The error in SiO_2 appears to increase with increasing pressure (see figure 2), which implies that the T and MgO errors also increase with pressure, as they all result from a common source (Hirschmann et al., 1997a). Given the inaccuracies in MELTS, we prefer to use it as presently calibrated as a tool to study trends and directions (i.e., the relationship among various variables), rather than to predict specific compositions. Quantitative modeling of absolute values of compositional variables, potential temperature, etc., will depend on improving or customizing the calibration.

The mixing function depends on geodynamic considerations such as the form of the solid flow field and melt extraction pathways. For what follows I want to focus on the insights gained from thermodynamic modeling of chemistry and melting and so I use only the simple end-member mixing functions associated with perfect active and perfect passive flow (see chapter 1, figure 2). The end-member case of active flow is a columnar melting regime in which any mantle that crosses the solidus subsequently flows all the way to the

top. For batch melting the aggregate melt from an active flow is identical to the equilibrium melt composition at the final pressure of melting; for fractional melting, the aggregate melt from an active flow system is obtained by integrating once. The end-member case of passive flow is a triangular melting regime in which flowlines farther from the axis turn horizontal and cease melting at deeper levels. The aggregate melt for batch melting in passive flow is obtained by integrating the compositions once; for fractional melting the compositions must be integrated twice (McKenzie and Bickle, 1988).

Even these simple mixing functions, however, enable us to examine the differences between two competing views on the principal controls on variation among mid-ocean ridge segments. Klein and Langmuir (1987) and other authors (Klein and Langmuir, 1989; Langmuir et al., 1992; McKenzie and Bickle, 1988; Plank and Langmuir, 1992) consider that, except perhaps at extremely slow-spreading ridges, melting continues to a shallow depth, perhaps the base of the crust, at all ridge segments. The variation among ridges is then attributed to substantial variations in the potential temperature of the upwelling mantle (a range of 200-250 °C, Klein and Langmuir, 1987; or 300 °C, McKenzie and Bickle, 1988), which controls the intersection of the adiabat with the solidus and the initial pressure of melting. Shen and Forsyth (1995), on the other hand, attribute the main trend of variation among ridges to the effectiveness of cooling from the surface and hence to the final pressure of melting. The total variation in temperature among non-hotspot affected ridges is then thought to be ~60 °C (Shen and Forsyth, 1995). A consistent model based on this view generally includes a significant role for heterogeneous source compositions (Niu and Batiza, 1991) and implies a correlation of extent of melting with spreading rate (Niu and Batiza, 1993; Niu and Hékinian, 1997a; Niu and Hékinian, 1997b). With apologies to other authors who have discussed similar models, we will refer in what follows to these two concepts as "Klein and Langmuir-type" and "Shen and Forsyth-type" melting regimes.

Discussion of variability and correlation among MORB compositions requires, first, correcting for the effects of fractionation, and second, distinguishing local variability among samples from global variability among regional averages of samples. In this work I predict only primary compositions and compare them to other authors' model primary aggregate liquids. I make no attempt at this time to fractionate these model liquids in order to compare them to actual MORB data or MORB data corrected for fractionation (e.g., to 8% MgO; Klein and Langmuir, 1987). I take this approach at present because, first, the model compositions from MELTS are difficult to compare quantitatively to actual samples due of offsets and errors in the model, and second, given that the errors in MELTS vary with pressure, primary liquids from high pressure do not behave well if MELTS is used for fractionation calculations at low pressure. Nevertheless, much can be learned from examination of primary liquids, since the effects of fractionation are relatively minor for several of the elements of interest.

The assumptions behind comparisons of aggregate liquids from model melting regimes with regional averages of MORB compositions (Klein and Langmuir, 1987; see also McKenzie and O'Nions, 1991) are (1) that one can correct for imperfections in the mixing of liquids with a sufficiently large population of samples, which should approach the mean composition for a ridge segment, and (2) that the physical parameters controlling the mean composition vary little along individual ridge segments. The correlations among these regional averages are generally termed "global trends." There is also, however, a rich source of information in the variations in composition among individual samples from a given ridge segment. These correlations are termed "local trends," and are generally interpreted as unmixed increments of melt sampled from various places in the melting regime (Klein and Langmuir, 1989), although it is equally valid to consider them as imperfect mixtures of the various melts which make up the average composition of the segment. One can examine the possible spectrum of local variability by examining all the incremental melt compositions and partial mixtures among them that can be produced

from a model melting regime, but the unlimited variety of partial mixing schemes that can be described makes it more difficult to choose the particular local trend that should result from a model melting regime.

In this chapter, I begin by introducing phase diagrams in *P-T* and *P-S* space that set up the framework for all MELTS predictions of polybaric melting by showing where each assemblage of phases is predicted to be stable as well as the contours of equal melt fraction above the solidus (the importance of which is discussed in chapter 3 and Asimow et al., 1997); strictly speaking, these diagrams show only batch processes since they are drawn for constant bulk compositions. The idea of interplay between the novel chemistry and melting functions predicted by MELTS is introduced by comparison to the SiO_2 vs. melt fraction (F) plot of Klein and Langmuir (Klein and Langmuir, 1987) for batch melting. A brief discussion of the differences between isentropic batch melting and isentropic fractional melting (as we define it, see chapters 2 and 3; Asimow et al., 1995a; Asimow et al., 1997) introduces the comparison of mean properties of the melting regime — i.e., mean pressure, mean extent of melting, and crustal thickness — as functions of initial pressure of melting (i.e., potential temperature) and final pressure of melting. This is followed by predictions of the correlation of these physical variables with compositional trends in the primary aggregate liquids, particularly Na_2O and FeO*. Finally I consider the effects of variable source composition on aggregate liquid compositions, extending the discussion of Hirschmann et al. (1997b), which is based on reasoning from isobaric melting only.

Isentropic Batch Melting

Figure 1 shows maps of the stable phase assemblages for a model primitive mantle source composition (Hart and Zindler, 1986), with and without Cr_2O_3. The axes in Figures 1a and 1c are P and entropy (S), or equivalently P and potential temperature (T_P, the calculated temperature of the metastable solid assemblage, allowing all subsolidus

reactions to come to equilibrium, at 1 bar with the given total S). "Ordinary" temperature (T) is plotted in Figures 1b and 1d for reference, but P and S are the appropriate independent variables for isentropic melting processes (Asimow et al., 1995a; Asimow et al., 1997; McKenzie, 1984; Verhoogen, 1965). Any vertical line on a P-S isopleth diagram corresponds to a batch isentropic path. Contours of constant melt fraction by mass, F, are plotted in the supersolidus region of each map. The isentropic melt productivity at any point is inversely proportional to the spacing of these contours where they intersect a vertical path. Hence these diagrams show at a glance all possible isentropic batch melting paths for this source composition and the full range of mantle potential temperatures. The temperatures in the following discussion are subject to the errors noted in Baker et al. (1995) and Hirschmann et al. (1997a) and are likely to be 50-100 °C hotter than the correct temperatures. For $T_P < 1125$ °C no melting occurs anywhere; it is interesting (and not previously anticipated) that this minimum temperature, roughly the same for the Cr-bearing and Cr-absent cases, is not determined by the solidus temperature at 1 bar or at the base of the crust but rather by the location of the 6-phase point olivine+opx+cpx+spinel+plag+liquid, i.e., the point of the cusp on the solidus. This is the point on the solidus with the lowest entropy, and so it defines the lowest mantle entropy that intersects the solidus.

Melting paths with $T_P < 1225$ °C freeze completely at the spinel-plagioclase transition (Asimow et al., 1995a). These paths achieve peak melt fractions in the spinel peridotite field less than F=.025. Those paths hotter than $T_P \sim 1175$ °C would begin melting again in the plagioclase stability field if isentropic decompression continued all the way to 1 bar. All paths up to $T_P \sim 1300$ °C encounter plagioclase in the residue for at least a small interval. $T_P \sim 1250$ °C is the minimum for exhaustion of cpx from the residue. For the Cr-bearing case, $T_P > 1425$ °C is required for melting to begin in the garnet field; for the Cr-absent case garnet is present on the solidus for $T_P > 1380$ °C.

The most salient feature of these diagrams is the shape of the solidus. Although simple considerations of phase diagram topology dictate that there must be a cusp in the solidus at the appearance of plagioclase, the magnitude of the temperature drop associated with this cusp according to MELTS is extremely large and surprising. The depth of the cusp is likely to be somewhat exaggerated in MELTS because it overestimates the incompatibility of Na in the spinel peridotite field (Hirschmann et al., 1997a). This shape has never been observed in experimental determinations of peridotite solidi, but examination of the melt fraction contours shows that the shape as determined by experiment would be extremely sensitive to the minimum melt fraction required to identify melting in an experiment. At F=.01, the temperature drop at the cusp is predicted to be only half as big as that on the solidus itself. By F=.05 there is no temperature drop or negatively sloped region at all. Experimental determinations of the solidus, especially if the interpretation is colored by the expectation of "eutectic-like" (Yoder, 1976) behavior, are unlikely to have resolved the large difference in temperature between F=.01 or even F=.05 and F=0.

The difficulty imposed by the inadequate treatment of Cr_2O_3 in MELTS (Hirschmann et al., 1997a) is well illustrated by these diagrams. In the present version of MELTS, spinel is the only mantle phase that accommodates Cr_2O_3, whereas at elevated pressures in natural systems, clinopyroxene and garnet are significant reservoirs for Cr_2O_3. Hence when Cr_2O_3 is included in the calculation, spinel is excessively stable. Spinel is present as part of the assemblage everywhere on Figures 1a and 1b, and persists nearly to the liquidus. Since this spinel must be in Cr/Al exchange equilibrium with the other phases, it draws in Al_2O_3 as well, which makes plagioclase and garnet less stable than they would otherwise be. On the other hand, when Cr_2O_3 is excluded from the bulk composition, as in Figures 1c and 1d, spinel is insufficiently stable and hence garnet and plagioclase are too stable. In this case, the garnet-spinel transition region is artificially narrow and spinel disappears from the residue near 10% melting, before the exhaustion of

cpx. We have generally worked around this problem by performing duplicate calculations in Cr-bearing and Cr-absent bulk compositions. When similar behavior is observed in both cases, we conclude that errors in spinel stability are not seriously affecting our results.

Previous attempts to estimate liquid compositions during isentropic batch melting have been based essentially on the idea of choosing a path through a chemistry function (i.e., liquid composition as a function of (P, F) or (P, T)) fitted to isobaric melting data, where the path is set by the (independently estimated) melting function -(dF/dP) or perhaps by an estimate of the thermal gradient during melting (dT/dP). For example, Klein and Langmuir (1987) illustrated the construction of such a model for SiO_2 as functions of F and P, based on fitted isobaric curves and an estimated isentropic productivity of 1.2 %/kbar (Figure 2b). MELTS generates isentropic batch melting paths directly, without a decoupling between the chemistry and melting functions. The result (Figure 2a) differs considerably from that of Klein and Langmuir (1987) for two distinct reasons. First, the isobaric melting curves are clearly different in that they show high SiO_2 at low F (Baker et al., 1995), especially at the low pressure end of the spinel peridotite field (Hirschmann et al., 1997c), a feature that was not apparent in experimental data available in 1987. Second, the isentropic productivity is not constant at 1.2 %/kbar; instead it systematically increases along each melting path from as little as 0.25 %/kbar on the solidus to a maximum near 3%/kbar at the exhaustion of clinopyroxene from the residue (Asimow et al., 1997; Hirschmann et al., 1994). Hence the isentropic paths cross the isobaric melting curves at an increasing rather than constant rate with increasing F. These two novel aspects combine to predict concave-up isentropic paths on Figure 2, in contrast to Klein and Langmuir's concave-down paths. I emphasize, however, that although this figure is useful for building intuition and as a contribution to the debate about batch melting experiments on fertile peridotite compositions, it is probably not directly relevant to MORB petrogenesis. This is because the consequences of fractional melting on liquid and residue compositions are dramatic as we will see below. Thus the idea of using batch melting

isobars (Figure 2b) or isentropes (Figure 2a) to predict compositions from fractional fusion is less useful than was once thought. Figure 2 also shows that the error in liquid SiO_2 contents predicted by MELTS, although a constant offset at each pressure (Baker et al., 1995), is pressure dependent. There appears to be very little error at 2 kbar (comparing isobars in Figure 2a and 2b), and the error increases smoothly to the value of 4% observed by Baker et al. (1995) at 10 kbar and ~6% at 15 kbar.

Incrementally Adiabatic Fractional Melting

Fractional melting cannot be a locally isentropic process, in that escaping melts remove entropy from the system. Here, as in chapters 2 and 3, I model fractional melting as an idealized process of infinitesimal isentropic batch melting steps followed by extraction of any liquid formed (see Asimow et al., 1995a; Asimow et al., 1997). The composition and entropy of the residue of each step serves as the reference for the next increment. The extension to continuous fusion, where some amount of melt remains behind, is straightforward (Asimow et al., 1997).

All prior attempts to construct models of polybaric fractional melting have been based on compositions and melt fractions from batch melting experiments. Those that use compositions directly from batch melting experiments (Klein and Langmuir, 1987; McKenzie and Bickle, 1988) include none of the compositional effects of fractional melting and make first-order estimates of the difference in productivity and P-T paths between batch and fractional melting. Other parameterizations that use major element partition coefficients fitted to batch melting experiments (Langmuir et al., 1992; Niu and Batiza, 1991) attempt to account for the evolution of residue composition and/or variations in liquid composition to first order, but are inaccurate to the extent that partition coefficients may vary with solid phase compositions or liquid components not modeled. The method of Kinzler and Grove (Kinzler, 1997; Kinzler and Grove, 1992a; Kinzler and Grove, 1992b) is likely to approximate the compositional effects of fractional melting well within

the compositional range over which the four-phase liquid saturation surfaces are calibrated, but still depends on poorly constrained estimates of fractional melt productivity and *P-T* paths.

Figure 2c gives an indication of the likely magnitude of the differences between batch and fractional melting. For the same solidus intersection pressures as the polybaric isentropic batch melting paths in Figure 2a, I have shown liquid SiO_2 vs. F for the incremental fractional melt compositions and the integrated fractional melt. Conventional petrological wisdom holds that integrated fractional melts are similar to batch melts, but this is only true for highly incompatible elements and only when partition coefficients are constant. In this polybaric case, where productivity and *P-T* paths are different for batch and fractional processes and where SiO_2 partitioning depends strongly on bulk composition, batch and integrated fractional melts are substantially different.

Mean Properties of Melting Regimes

Two-dimensional models of mid-ocean ridge melting can often be simply characterized by mean properties of the erupted melt (see chapter 1, figure 2), e.g., the mean pressure of extraction ($\bar{P}$) and the mean extent of melting F_B or F_V (see Plank et al., 1995), as well as total crustal thickness (Z_c). For any model (e.g., active or passive, batch or fractional), the relationship between these overall characteristics of the erupted melt and the basic physical parameters (solidus pressure P_o, pressure of final melting P_f) depends on the melt productivity. The non-linear melting function (i.e., non-constant $-dF/dP$) predicted by this work results in non-linear relationships among P_o, P_f, $\bar{P}$, F_B, F_V, and Z_c. I show below the relationships among all these variables for the reference case of perfect fractional melting, passive flow (hence double integrations of composition), and the Hart and Zindler (1986) source composition. Then I explore some possible differences due to batch melting, active flow, and source heterogeneity.

Figure 3 compares melting regimes with constant final pressure of melting (set to 2 kbar) and variable initial pressures of melting resulting from variations in potential temperature. $\bar{P}$, F_B, and Z_C are plotted against P_O in Figures 3a-c and against potential temperature in Figures 3d-f. Both the Cr-bearing and Cr-absent source compositions are shown; the results are similar in all important respects. Hence, the following discussion is not sensitively dependent on details of spinel stability. The model of Langmuir et al. (1992) is shown for comparison; this model has a slight decrease in productivity with decreasing pressure (not readily visible in Figure 3), but yields relationships on these diagrams similar to constant productivity models. The MELTS model and the Langmuir et al. model agree quite well in many respects in the "normal" range of solidus pressures near 20 kbar, but differ for anomalously hot or cold mantles. The disagreement for abnormally cold conditions is not surprising given the novel behavior predicted by MELTS for low F (which shows up most strongly in integrated melts with low F_B) and the influence of the spinel-plagioclase transition (which dominates at low potential temperature and is absent in the Langmuir et al. formulation). The disagreement for hotter mantle is due both to the difference between the solidus curve calculated by MELTS (see Figure 1) and the linear form assumed by Langmuir et al. (which changes the relationship between potential temperature and solidus intersection pressure, particularly as both parameters increase) and to the nonlinear productivity function predicted by MELTS. In particular, the decrease in productivity beyond the exhaustion of clinopyroxene (cpx) is a much more significant limitation to the achievement of large melt fractions in MELTS than in the Langmuir model. This results in the flattening of the F_B values attained by MELTS for increasingly hot mantle and solidus intersections deeper than 30 kbar and hence in the nearly linear relationship between crustal thickness and solidus pressure beyond 30 kbar (compared to the nearly quadratic relationship in the Langmuir et al. model). Little confidence should be placed in the results of either MELTS or direct experimental parameterizations beyond pressures of 30 kbar given the paucity of experimental data on

peridotite melting at these pressures and the low-order equations of state used in MELTS, but the very low productivity of melting beyond the exhaustion of clinopyroxene is a robust result (and occurs, even for these hot adiabats, at pressures where MELTS is more reliable). Considering the uncertainties, it is satisfying that MELTS predicts reasonable behavior in the normal mantle range given the independent method by which it is derived.

All the curves in Figure 3 reflect the behavior of MELTS in two regimes. For solidus pressures greater than about 17 kbar, i.e., potential temperatures greater than about 1280 °C, plagioclase does not appear in the residue during fractional melting (this value is lower than the limit for plagioclase to appear on batch melting adiabats as in Figure 1) and there is no gap in the melting regime associated with the spinel-plagioclase peridotite transition (Asimow et al., 1995a). In this "normal" range, the curvature of the trends results from the non-linear productivity of adiabatic fractional melting (Asimow et al., 1997) and from the shape of the solidus (see Figure 1). For solidus pressure lower than 17 kbar (T_P < 1280 °C), the spinel-plagioclase peridotite transition plays an increasingly important role in modifying the amount of melt produced and the pressure range over which melt production occurs. In a simple ideal passive flow model (see cartoon in Figure 4), the transition first divides the melting region into two disconnected regions, an upper triangle and a lower trapezoid. With decreasing potential temperature, the bottom of the triangle retreats upward and the top of the trapezoid retreats downwards, i.e., the transition shuts off melting at deeper levels and melting resumes at shallower levels (see Figure 1). This effect manifests in Figure 3 as a rapid drop in crustal thickness and mean extent of melting and a turnaround in mean pressure of melting. The loss of the shallower parts of the melting region results in increasing mean pressures of melting with decreasing potential temperature or solidus pressure in this range. At a certain critical location (the kink in the Figure 3 curves at T_P=1225 °C and P_O=14 kbar), the upper triangle disappears; i.e., the pressure at which melting in the plagioclase field would resume becomes shallower than the imposed minimum pressure of melting. From this point to the minimum melting

point at T_P = 1100 °C, the lower trapezoid shrinks until the solidus pressure equals the pressure of plagioclase appearance on the solidus near 10 kbar.

Figure 5 presents the form of variations in mean pressure, mean extent of melting, and crustal thickness in melting regimes controlled by the final pressure of melting, as envisioned by Shen and Forsyth (1995) and Niu and Hékinian (1997a), for three different potential temperatures (1500 °C, 1385 °C, and 1240 °C, corresponding to pressures of initial melting of 60 kbar, 25 kbar, and 15 kbar). The dashed lines on Figure 5a show constant productivity models for comparison. For a potential temperature of 1385 °C (P_O = 25 kbar), a range of final melting pressures from 0 to 9 kbar is needed to generate crustal thicknesses from 10 to 3 km. For a potential temperature of 1500 °C (P_O = 60 kbar), a range in final melting pressures from 3 to 25 kbar generates a range in crustal thicknesses of 25 to 3 km.

These figures address the key issue of the range in potential temperatures sampled by oceanic ridges. Klein and Langmuir (1987) estimated the total range from the Cayman Trough (crustal thickness ~3 km) to Iceland (crustal thickness 10-16 km, Klein and Langmuir, 1987; or 16-25 km, Langmuir et al., 1992) at 250 °C (on compositional grounds as well as crustal thickness considerations), whereas Shen and Forsyth (1995) constructed a model that explains the global range of major element variation in MORB with a temperature range of <60 °C and substantial variations in the final pressure of melting. Figure 3 considers only models with constant final pressure of melting equal to 2 kbar, but our model requires a temperature range less than 200 °C to enclose a range in crustal thickness from 3 km to 25 km. This corresponds to a range of 35 kbar in solidus intersection pressures, which is (counter-intuitively) much greater than the 20 kbar range in P_O implied by a 250 °C potential temperature range in the model of Langmuir et al. (1992). This is primarily the result of the curvature of the solidus in MELTS, which results in a rapid increase in depth of initial melting above T_P=1450 °C.

The global range of potential temperatures is not readily obtainable from Shen and Forsyth-type melting regimes without some constraint on the physically possible range of final pressure of melting. In principle, crustal thicknesses of 3-25 km can be generated from a perfectly isothermal subsolidus mantle (say, T_P = 1500 °C, with a solidus intersection at 60 kbar) if pressure of final melting spans a range from 3 kbar to 25 kbar (Figure 5c). If the globally uniform potential temperature were instead 1385 °C (P_o = 25 kbar), then it would only be necessary to shut off melting at a depth of 9 kbar in order to restrict crustal thickness to 3 km, but the maximum obtainable crustal thickness for this potential temperature is 10 km. It would seem that if oceanic crustal thicknesses do in fact approach 25 km anywhere, then even with variations of up to about 10 kbar in the pressure of final melting, a potential temperature range in the global mantle of over 100 °C is still required. We return below to the issue of variations in initial and final pressure of melting after considering variations in aggregate liquid composition. These cannot be distinguished from discussion of mean physical properties alone, since mean pressure and mean extent of melting are not directly measured like crustal thickness or axial depth but rather are inferred from averaged MORB compositions.

Aggregate Primary Melt Compositions

The number of free parameters in my models is small, but there is still a many-dimensional space of possible primary melt compositions. Here I attempt to show the effects of variations in P_o, P_f, and source composition (along a one-dimensional enrichment/depletion vector) for batch and fractional melting in active and passive flow regimes, i.e., three free parameters for each of four cases.

Figure 6 presents Na_2O and FeO* as functions of P_o, Z_c, F_B, and $\bar{P}$ in the primary aggregate liquids produced by fractional melting and passive flow with constant P_f = 2 kbar from MELTS and from the models of Langmuir et al. (1992) and Kinzler (1997). Both Cr-bearing and Cr-absent calculations are shown; the results are quite similar. Na_2O

is conventionally taken as an indicator of extent of melting, and Figure 6a shows that the three models agree reasonably well near $F_B = 0.1$. MELTS never reaches mean melt fractions as high as $F_B = 0.2$, and so is unable to produce $Na_2O < 2.3$ wt.% in a primary liquid from melting regimes of this type. At low mean melt fractions, MELTS predicts substantially higher Na_2O than the model of Langmuir et al.; this is at least partly due to inaccuracies in Na partitioning in MELTS (Hirschmann et al., 1997a). FeO* is sensitive to the mean pressure of melting, as emphasized by Langmuir and Hanson (1980) and Klein and Langmuir (1987); Figure 6b shows that MELTS also reproduces fairly well the relationship between FeO* and $\bar{P}$ expressed in the Langmuir et al. and Kinzler models. The slope of the relationship predicted by MELTS is somewhat steeper, and at very low potential temperatures, there is an ambiguity created by the effects of the spinel-plagioclase transition; i.e., in the region discussed above in connection with Figures 3 and 4 where mean pressure increases with decreasing potential temperature, FeO* continues to decrease smoothly. In my models FeO* appears to be a more reliable indicator of the pressure of initiation of melting than of the mean pressure in regions where the relationship between these latter two variables is not straightforward.

When FeO* and Na_2O of the aggregate primary liquid are plotted against solidus pressure (Figure 6c) or crustal thickness (Figure 6d), the results differ from previous models because both the FeO*-$\bar{P}$ and Na_2O-F_B relations and the F_B-$\bar{P}$-P_o-Z_c relations differ as shown above. In particular, for a given solidus pressure P_o, MELTS always predicts higher Na_2O and lower FeO* in the aggregate melt from a 2-D passive flow melting regime than simpler models because of the very low productivity of melting near the solidus. This results in F_B and $\bar{P}$ that are always lower than the Langmuir et al. model at given P_o. Plotted against crustal thickness, MELTS predicts that Na_2O is again uniformly higher than the Langmuir et al. and Kinzler models. This is the result both of the high Na_2O values at given F_B from MELTS (which moves the Na_2O vs. Z_c curve up) and also the wide interval of melting required to reach a given F_B (crustal thickness is

proportional to the product of F_B and $P_f - P_o$, so MELTS predicts a larger crustal thickness for the same F_B, which moves the Na_2O vs. Z_c curve to the right). FeO*, however, agrees well with the Langmuir et al. model at high crustal thicknesses and in the limit of zero crustal production, but is low in the normal range of Z_c from 3 to 7 km. This is a fundamental outcome of the increasing productivity predicted by MELTS. For melting regimes that do not exhaust clinopyroxene at great depth and for a given F_B and $P_f - P_o$, MELTS strongly weights its melt production towards the shallower part of the melting regime. This results in lower $\bar{P}$ and lower FeO*.

Figure 6e plots Na_2O against FeO* for primary aggregate liquids (compare Chapter 1, Figure 1). When these liquids are fractionated to 8.0% MgO (which we have not attempted in this work), a successful model ought to produce the global trend of Klein and Langmuir (1987). The uniformly high Na_2O and the FeO* that agrees with the Langmuir et al. primary melts at high potential temperature but decreases more quickly combine to give a Na_2O vs. FeO* trend that is much more shallowly sloped than the predictions of Langmuir et al. (1992) or Kinzler (1997). Both of these models match the global trend reasonably well. The MELTS model does not at this stage. It is not clear whether this is entirely attributable to the behavior of Na_2O, whether there are other confounding problems with the model, or whether in fact the conventional Klein and Langmuir-type explanation for the global trend is problematic.

The relationship between Na_2O and crustal thickness is replotted in Figure 7 with the axes transposed and a logarithmic scale for Z_c. Crustal thickness was plotted against $Na_{8.0}$ for regionally averaged MORBs in this way by Klein and Langmuir (1987), McKenzie and Bickle (1988), Langmuir et al. (1992), and Forsyth (1992); Figure 7a is a reproduction of Figure 52 of Forsyth (1992). None of these authors was able to match the entire global data array with one curve. Both Klein and Langmuir (1987) and Langmuir et al. (1992) resorted to a range of source compositions with initial Na_2O concentrations varying from 0.26% to 0.30% in order to spread their predicted data field to a width of

0.5% $Na_{8.0}$ in the aggregate liquid. McKenzie and Bickle (1988) found a curve that was too steep to fit the high Na_2O end of the data array. Forsyth (1992) pointed out that a single trend with active flow, giving crustal thickness proportional to F_B (rather than F_B^2 as in passive flow models) accounts for all the data except Iceland and the Cayman Trough. Although we have not fractionated our primary liquids to 8.0% MgO for direct comparison to data, and although our Na_2O values are uniformly high, the sharply curved trend predicted by our model suggests that productivity variations may hold the key to reconciling the entire global trend with a single model. Recalling that crustal thickness is proportional to the product of F_B and the thickness of the melting interval, the high slope at the low-Na, high-Z_c end of the array is due to the flattening of the F_B vs. P_o curve (Figure 3e) at large P_o in our model.

The global Na_2O-FeO* systematics resulting from integration of MELTS liquids in Shen and Forsyth-type melting regimes, with globally constant initial pressure of melting and variations in the final pressure of melting, are shown in Figure 8. Na_2O increases with increasing final pressure of melting (Figure 8a), due to the corresponding decrease in F_B (Figure 5b). FeO*, on the other hand, is roughly constant as a function of initial pressure of melting except for the hottest potential temperature (1500 °C) shown. In this case, FeO* increases substantially only for P_f greater than 15 kbar, and decreases for P_f greater than 33 kbar. In a Na_2O vs. FeO* plot (Figure 8b), the global trends generated by variations in P_f at constant P_o are nearly vertical trends except for the hottest potential temperature, in which case it has a negative slope for P_f up to 33 kbar. The prediction of the MELTS model for this type of global systematic is substantially different from the corresponding prediction of the Langmuir et al. (1992) chemistry and melting model, as shown in Figure 8b by the light solid curve, which has P_o = 25 kbar. MELTS achieves much higher Na_2O values than the Langmuir et al. model at low melt fractions (i.e., P_f approaching 25 kbar), and always has increasing FeO* with increasing P_f, for P_o = 25 kbar, whereas the Langmuir et al. model increases and then decreases. Nevertheless,

calculated with MELTS or with the Langmuir et al. model, the Na_2O vs. FeO* trends generated by Shen and Forsyth-type variations in P_f for a homogeneous mantle source do not resemble the global trend of MORB data.

Effects of Source Heterogeneity on Aggregate Melt Compositions

In principle, the ability to compute aggregate liquids from multiple source compositions is one of the most promising applications of MELTS to the study of variations in MORB compositions. Opinions differ widely as to whether major element heterogeneity of the sources of MORBs constitutes a major contributor to the spectrum of variability in erupted liquids: Langmuir et al. (1992) argue that heterogeneity does not control the global trend of regionally averaged compositions or the local trend observed at slow-spreading ridges, but may explain the local trend on the fast-spreading East Pacific Rise. Shen and Forsyth (1995) maintain, based on K_2O/TiO_2 and $(Sm/Yb)_N$ arguments, that the global trend is mostly a manifestation of source heterogeneity. Niu and Hékinian (1997a; 1997b), while advocating a physical picture of ridge melting similar to Shen and Forsyth, dismiss the possibility that source heterogeneity controls major element trends such as CaO/Al_2O_3. Several issues related to the effect of source heterogeneity on isobaric melting trends according to MELTS are discussed in Hirschmann (1997b). Here I extend this discussion to consider integrated melt compositions from isentropic or incrementally isentropic polybaric passive-flow and active-flow melting regimes and hence the likely effects of source heterogeneity on MORB compositions.

The compositional heterogeneity observed in natural peridotites (Herzberg et al., 1988) is large and complex, and cannot be reduced to a single vector in composition space (Figure 9). Nevertheless, for simplicity I have chosen a one-dimensional array of source compositions to illustrate the effects of source variations along the general trend from enriched to depleted. I chose a constant basaltic component to add or subtract from the Hart and Zindler (1986) primitive upper mantle composition (labeled filled point),

generating the lines shown in Figure 9, which either overlay or parallel the major trend of chemical variation in natural peridotites. In what follows I use five compositions along this line corresponding to the Hart and Zindler composition with 5% or 10% by mass of the basaltic component added or subtracted; the resulting five compositions are plotted in Figure 9 (open circles) for comparison with the field of observed peridotite compositions in the Herzberg database (small points). Also shown and labeled are experimental mixes mm3 (Baker and Stolper, 1994) and DMM1 (Wasylenki et al., 1996) and sample R123 (Frey et al., 1985), a particularly enriched peridotite from the Ronda massif.

*Na_2O-FeO**

The Na_2O-FeO* systematics of aggregate primary liquids from the MELTS model are explored in the light of variable source composition in Figures 10-11. Figure 10 shows Na_2O vs. FeO* in primary aggregate melts for Klein and Langmuir-type melting regimes (constant Z_f=5 km, variable potential temperature) with active and passive flow fields, batch and fractional melting, and five different source compositions. Each composition generates a negative correlation as expected for global trend systematics. The passive flow case generates higher Na_2O and, at moderate potential temperatures for fractional melting, higher FeO* than the active flow case because small degree melts from high pressure make a larger contribution to the mean. This difference is less apparent at very low potential temperatures, where the total sampled ranges of extent of melting and pressure are small, and at high potential temperature for FeO* because for both active and passive cases there is very little contribution in this range from low pressure melts (due to the exhaustion of cpx). Comparing the batch melting cases to the fractional cases confirms the conclusion of Langmuir et al. (1992) that batch melting generates a smaller range in FeO* in integrated melts than fractional melting, although this effect is only pronounced for active flow; for passive flow the difference is minor.

The contours of constant potential temperature across various source compositions in Figure 10 have, generally, steep positive slopes for passive flow and fractional melting (Figure 10b). This is consistent with the original qualitative argument in Klein and Langmuir (1987) and the quantitative calculation in Langmuir et al. (1992) that source heterogeneity ought to produce positive correlations between Na_2O and FeO* contents in a global trend sense. For active flow and/or batch melting, however, the potential temperature contours have a variety of slopes. At high potential temperatures, the contours show negative slopes for the depleted compositions and positive slopes for the enriched compositions. At low potential temperatures, the contours have positive slopes for all compositions. In no case do the constant T_p contours of heterogeneity variation correspond to the typical slopes of local trends, either for slow-spreading ridges (low positive slopes, Brodholt and Batiza, 1989; Klein and Langmuir, 1989) or fast-spreading ridges (negative slopes sub-parallel to the global trend, Langmuir et al., 1992). This treatment is unlikely, however, to be useful for observing the effect of heterogeneity on local systematics, since it considers integrated compositions from compositionally uniform melting regimes. If heterogeneity were present on a local scale, the melts from various compositional domains would mix rather than retain the separate identities plotted in Figure 10.

Figure 11 presents Na_2O-FeO* systematics for Shen and Forsyth-type melting regimes with constant potential temperature (1325 °C) and varying final depths of melting, a view which may be more useful for examining local systematics. Figure 11a plots incremental fractional melt compositions, Figure 11b plots singly integrated compositions for active flow melting regimes and fractional melting, and Figure 11c plots doubly integrated compositions for passive flow fractional melting regimes. Figures 11d and 11e show batch melting in the active flow and passive flow cases. Each heavy curve proceeds from the solidus to the surface, and a point along it represents the composition (or integrated composition) that would be obtained if melting were to stop at that depth.

Variations in final depth of melting for each source composition produce S-shaped curves with generally steep slopes. These trends do not obviously correspond to any global or local systematics of MORBs except perhaps for the most enriched compositions over the lowest range of Z_f, although it is likely that these curves are too steep given the underestimate of the partition coefficient for Na in MELTS.

Contours of constant final depth of melting in Figure 11 portray one manner in which source heterogeneity might be related to the slow-spreading local trend of Klein and Langmuir (1989). The total range of source heterogeneity considered generally gives a range in FeO* values at constant Na_2O or at constant Z_f of ~1.25%, which is comparable to the lengths of most slow-spreading local trends (see chapter 1, figure 1) and to the estimate of 0.5-1% given by Langmuir et al. (1992) based on their chemistry function. Since the MELTS modeling also considers the effect of heterogeneity on productivity, more quantitative statements can in principle be made about the range in Na_2O and the slope due to heterogeneity. The constant depth contours (i.e., heterogeneity vectors) on Figures 11b, 11c, and 11e have positive slopes and ranges of 2-5% in Na_2O, which is much larger (and hence the slope much steeper) than the typical range of <1% $Na_{8.0}$ of a slow-spreading local vector (Klein and Langmuir, 1989). Batch fusion and active flow yields constant Z_f contours with low negative slopes. Although the sign of the slope of many of these heterogeneity vectors is consistent with slow-spreading local trends, heterogeneity of the source at constant potential temperature does not generate trends that have the right magnitude of slope to explain the enigmatic slow-spreading local trends of Klein and Langmuir (1989). The particular constant-depth contours shown, however, represent very particular assumptions about the way increments of melt might mix to produce individual samples observed to compose a local trend; these contours assume that melts from each source retain their separate identity to the depth at which they are segregated. Different mixing scenarios could in fact produce low positive slopes with the necessary range in FeO*. Note that this calculation assumes further that each source

composition follows its own adiabatic path. In an adiabatic mantle that is isothermal below the solidus, once melting begins each source composition will follow a distinct *P-T* path controlled by its local melt productivity. If there is any thermal interaction between the domains, the result will be different from that shown in Figure 11 (Hirschmann and Stolper, 1995). Hence it remains difficult to assign any particular interpretation to slow-spreading local trends; the most that can be said is that heterogeneity of the source composition can contribute to the range in $Fe_{8.0}$ among samples from a given segment.

CaO/Al_2O_3

Recent work by Niu and Hékinian (1997a) has used CaO/Al_2O_3 values in MORB as indicators of extent of melting in order to argue for a global correlation between extent of melting and spreading rate. Hirschmann et al. (1997b), however, showed that, whereas CaO/Al_2O_3 is a monotonic indicator of extent of melting up to the exhaustion of cpx for any given source composition, when comparing different sources its behavior is complex and counter-intuitive. In particular, since CaO is controlled by the modal abundance of cpx, it is higher in liquids from more depleted sources, even though the source compositions have less CaO. Al_2O_3 behaves as a more ordinary incompatible element, and is lower in melts from more depleted sources with less Al_2O_3. Hence CaO/Al_2O_3 during progressive isobaric melting is significantly higher at melt fractions up to the exhaustion of cpx in liquids produced from more depleted sources, and does not depend in any simple way on the CaO/Al_2O_3 of the source composition.

Figure 12abc shows that high CaO/Al_2O_3 at a given extent of melting is also obtained for fractional melts produced along isentropic polybaric paths with constant potential temperature (1325 °C in this example), even when these compositions are integrated once or twice to describe progressively shallower final depths of melting (Shen and Forsyth-type melting regimes with active and passive flow). The incremental fractional melt compositions show a steep rise from very low CaO/Al_2O_3 at the solidus to

a gently increasing plateau value between 0.8 and 1.0 until the exhaustion of cpx, where they begin to drop steeply. The essential effect of integration in this case is to hide the effect of melting beyond the exhaustion of cpx; although CaO/Al_2O_3 decreases in the incremental fractional melts beyond this point, the productivity is low and very little is contributed to the integrated compositions. Hence CaO/Al_2O_3 in these integrated compositions monotonically increases for each source with increasing F_{max}, i.e., progressive shallowing of the final depth of melting. One consequence of this averaging, however, is that the effect of heterogeneity is exaggerated: for a constant F_{max} of 0.1, a range of CaO/Al_2O_3 from 0.35 to 0.85 is produced by a range of 20% enrichment or depletion in a basaltic component in the source. Similarly, a CaO/Al_2O_3 of 0.6 in consistent with F_{max} ranging from 0.02 to 0.25.

The behavior of CaO/Al_2O_3 turns out to be similar in integrated liquids with Klein and Langmuir-type global systematics (i.e., with constant final depth of melting and varying potential temperatures). When the increments of fractional melt from the entire melting regime are mixed during active flow (Figure 13b) or passive flow (Figure 13c), the trends of CaO/Al_2O_3 against F_{max} for varying potential temperature are like those shown in Figure 12: at fixed F_{max}, more depleted sources yield higher CaO/Al_2O_3. CaO/Al_2O_3 in these cases is sensitive to both extent of melting and source composition. As for the Shen and Forsyth-type systematics, a constant F_{max} can yield a large range of CaO/Al_2O_3 (the range increases with F_{max} for passive flow), and a CaO/Al_2O_3 of, say, 0.6 in consistent with F_{max} ranging from 0.04 (for a depleted source) to 0.2 (for an enriched source). On the other hand, in Klein and Langmuir-type systematics, the last increments of fractional liquid (produced at the final depth of melting, 5 km) behave quite differently as a function of F_{max} for various potential temperatures (Figure 13a). These CaO/Al_2O_3 values do not show the low values apparent at the solidus at high pressure, and instead for very low potential temperatures show values between 0.8 and 1.0, gently increasing with potential temperature before dropping steeply above the potential temperature where

plagioclase and cpx are no longer present in the residue at 5 km due to depletion of the residue by fractional melting lower in the melting regime. This behavior is partly the result of a coincidence, that plagioclase and cpx are exhausted at nearly the same extent of melting at $P \sim 2$ kbar (see Figure 1), and is perhaps unlikely to describe the systematics of any erupted MORB liquids.

This analysis of integrated liquid compositions from heterogeneous sources is contrary to the contention of Niu and Hékinian (1997a) that — CaO and Al_2O_3 being major oxides and hence less variable in source compositions than incompatible minor elements — CaO/Al_2O_3 should be a more reliable indicator of extent of melting in oceanic basalts than $Na_{8.0}$ (i.e., less likely to be confounded by source heterogeneity). We find instead, CaO and Al_2O_3 being major elements and hence correlated with modal abundances and phase equilibria, that CaO/Al_2O_3 is strongly contaminated by reasonable variations in source composition. Tests to deconvolve the effects of source heterogeneity from extent of melting are likely to require consideration of multiple chemical and isotopic indicators (see Hirschmann et al., 1997b).

FeO^*-K_2O/TiO_2

Hirschmann et al. (1997b) also showed that at any given MgO content (including, notably, MgO = 8.0 wt%), the batch melts produced from depleted sources are lower in FeO* than liquids produced from enriched sources. Hence, they argued, the negative correlation between K_2O/TiO_2 (considered a reliable and increasing function of source enrichment) and $Fe_{8.0}$ (i.e., FeO* corrected to 8.0 wt % MgO to account for fractionation) in regionally averaged basalts observed by Shen and Forsyth (1995, reproduced in Figure 14a) is unlikely to be due to mantle heterogeneity. This calls into question their attempt to eliminate the effects of heterogeneity on the global trend by correcting $Fe_{8.0}$ to a constant K_2O/TiO_2. For polybaric isentropic fractional melting integrated to describe passive flow or active flow, with either variable Z_f (Figure 12ef) or variable Z_o (Figure 13ef), the

observation remains true to the extent that one-dimensional integrated compositions and two-dimensional integrated compositions from more depleted sources all have lower FeO* at fixed MgO content (or Na_2O contents, see Figure 11). However, for individual increments of fractional melt, this is violated at low P_f in Shen and Forsyth-type melting regimes (Figure 13d) and at high T_P in Klein and Langmuir-type melting regimes (Figure 14d), but this reversed region is inevitably lost by integration, and certainly will not characterize regionally averaged compositions. Hence we concur that the Shen and Forsyth (1995) observation of a negative correlation between $Fe_{8.0}$ and K_2O/TiO_2 is unlikely to be the result of source heterogeneity.

Although we generally exclude K_2O from our modeling, Figure 14b shows the result of a calculation in which we have treated K as a simple trace element with a constant bulk D of 0.01. TiO_2 and FeO* are calculated in the normal manner from MELTS. The K_2O contents of natural peridotites are extremely scattered and define no clear trend against MgO or Mg#. For this calculation, we chose K_2O (Figure 9) such that the K_2O/TiO_2 ratio of the source increased with enrichment in other fertile components (from 0.06 for the composition depleted by 10% basalt extraction, to 0.18 for the Hart and Zindler primitive upper mantle, to 0.30 for composition enriched by 10% basalt addition). As shown in Figure 14b, my results for Klein and Langmuir-type melting regimes with varying potential temperature and constant final depth of melting yield a large range in K_2O/TiO_2 values (0.1 to greater than 1.0) in integrated primary melt compositions. At least for liquids that only fractionate olivine, FeO* changes little with fractionation and K_2O/TiO_2 should be constant, so the primary liquids plotted in Figure 14b should resemble compositions fractionated to 8% MgO. The large range in K_2O/TiO_2 is contrary to the calculation of Shen and Forsyth (1995), which used constant partition coefficients for both K and Ti and held solidus pressure constant, resulting in a much smaller range in K_2O/TiO_2 (~0.05-.01). This difference is not surprising in that (1) MELTS predicts strong variations in the partition coefficient of Ti (Hirschmann et al., 1997b) and (2) the

quantity of very incompatible elements available to be sampled by a passive flow melting regime is dominated by the area of the low melt fraction "wings" of the melting regime, which in turn is sensitive to the initial pressure of melting (Langmuir et al., 1992). We find that each homogeneous source composition yields a negatively correlated, roughly hyperbolic, relationship between K_2O/TiO_2 and FeO*. Variations in the source composition, as expected, do yield positive slopes, rather than the negative slope observed in the data, along constant potential temperature contours except for the most depleted composition considered. Although there is a superficial resemblance between the shape of the global trend we calculate for FeO* vs. K_2O/TiO_2 and the data for $Fe_{8.0}$ vs. K_2O/TiO_2 collected by Shen and Forsyth (1995), there are several notable differences. First, if all melts produced in the mantle are integrated to produce the crust and there is some K_2O in the source composition, there is no way for our models to produce average crust with K_2O/TiO_2 near zero as seen in the data. A better model will need to consider the effect of removing some low-melt fraction increments of liquid from the aggregate primary melt, perhaps by dynamical effects that lead to imperfect focusing and mixing of melts at the axis (e.g., Spiegelman, 1996). Second, our trend for any fixed composition falls off to low FeO* much more quickly than the observed data. This is related to the steeper FeO* vs. mean P trends obtained from MELTS than from other models, and prevents us from reaching any quantitative conclusion about the origin of the K_2O/TiO_2 variations. Nevertheless it is clearly possible to generate large variation in K_2O/TiO_2 from a homogeneous source and the general slope of the observed global correlation of $Fe_{8.0}$ against K_2O/TiO_2 is consistent with control by potential temperature, not source heterogeneity.

$(Sm/Yb)_N$

Shen and Forsyth (1995) also observed a negative correlation between $(Sm/Yb)_N$ and $Fe_{8.0}$ in regionally averaged MORB compositions. Since $(Sm/Yb)_N$ is considered to

be controlled by the extent of melting that takes place in the garnet field (Ellam, 1992), which ought to positively correlate with the initial pressure of melting if all else is held equal, this is taken as evidence that $Fe_{8.0}$ is not a good indicator of mean pressure of melting. It is clear, however, that $(Sm/Yb)_N$ also varies with extent of melting, since Sm is more incompatible than Yb whether garnet is present or not. Hence if garnet plays no role, then the conventional global trend of Klein and Langmuir-type melting regimes predicts a negative correlation between these two variables. Since MELTS makes novel predictions about the productivity variations during polybaric melting that begins in the garnet field, we calculated the integrated composition across a range of potential temperatures to test whether the extent of melting effect or the garnet effect dominates the $(Sm/Yb)_N$ of the integrated melt composition. The results in Figure 15 for the Cr-bearing Hart and Zindler source composition (the Cr-absent case is similar) using the partition coefficients for Sm and Yb of McKenzie and O'Nions (1995) shows that a negative correlation is expected at low potential temperatures where the extent of melting effect is strongest and a positive correlation is expected at high extents of melting where garnet begins to have an effect. The effect of garnet in the two-dimensional aggregate composition, however, does not appear until crustal thickness greater than 10 km; i.e., I do not find a positive correlation for normal MORB melting regimes. The magnitude of variation seen is somewhat smaller than that observed by Shen and Forsyth (1995), who find $(Sm/Yb)_N$ values from 0.95 to 1.35 (the highest values appear to require a more enriched source than the one in this calculation), and the trend from MELTS extends to much lower FeO* (since potential temperatures probably colder than any actual ridge are included and MELTS gives low FeO in this range). Nevertheless, contrary to the argument of Shen and Forsyth (1995), this result clearly shows that a negative correlation between $(Sm/Yb)_N$ can result from standard Klein and Langmuir-type systematics, even when residual garnet is considered.

Conclusions

1) The effects of the spinel-plagioclase peridotite transition become increasingly important for very low potential temperatures. The extreme depression of the solidus and negative slope through the region 5 - 10 kbar represents an experimentally testable prediction of this aspect of the MELTS model. It will be necessary, however, to develop the ability to experimentally recognize the onset of melting at very low melt fractions (<1%).

2) The variable productivity and curved solidus predicted by MELTS translate into non-linear relations among the potential temperature and initial pressure of melting, as well as non-linear relations among initial and final pressure of melting and mean pressure of melting, mean extent of melting, and crustal thickness. Since crustal thickness is the only one of these variables that can be directly measured, these relations are not testable by themselves, but depend on progress in interpreting melt compositions or perhaps consideration of residual peridotite compositions.

3) The novel productivity behavior of MELTS is convolved with melt compositions that reflect some behaviors absent from previous parameterizations to produce novel integrated melt compositions as functions of initial and final pressures of melting. One interesting result is that the relationship between the logarithm of crustal thickness and Na_2O is strongly curved, consistent with the variation of $Na_{8.0}$ data from MORB worldwide. Hence it may be possible to reconcile all crustal thickness data without recourse to source heterogeneity. Once these primary liquids are fractionated or observed liquids are corrected for fractionation to a common basis of comparison, these results can be used both to test and improve the MELTS model and to test hypotheses for the form of mid-ocean ridge melting regimes.

4) CaO/Al_2O_3 in aggregate melts is extremely sensitive to source compositions. A reasonable range of heterogeneity in the source can confound the simple dependence on melt fraction seen for each source composition.

5) K_2O/TiO_2 and FeO* correlate positively in aggregate primary melts as the source composition is varied and negatively as potential temperature is varied. We find it unlikely that regional averages in $Fe_{8.0}$ are controlled by source heterogeneity in the sense inferred by Shen and Forsyth (1995).

6) Global variation in $(Sm/Yb)_N$ in aggregate primary melt is dominated by the effect of extent of melting for normal ridges. Only at abnormally hot potential temperatures, sufficient to generate >10 km of oceanic crust, does the effect of residual garnet become dominant. This result is principally due to the low productivity of melting near the solidus and in the garnet-spinel transition region. Hence a negative correlation between $(Sm/Yb)_N$ and FeO* is broadly consistent with the Klein and Langmuir (1987) analysis of the global trend being dominated by potential temperature variation.

Figure 1. Maps of the stable phase assemblages predicted by MELTS for constant bulk compositions. In the region where liquid is present, the mass fraction of liquid (F) is contoured. Contours at 1% intervals for F up to 0.04 are shown dotted. Contours at 5% intervals for F above 0.05 are shown dashed. (a) and (b) use the primitive upper mantle compositions of Hart and Zindler (1986), (c) and (d) use a Cr-free equivalent. The axes in (a) and (c) are pressure (P) on the vertical axis and entropy (S) and potential temperature on the top and bottom horizontal axes. Vertical lines on these diagrams show isentropic batch melting paths. In (b) and (d) the horizontal axis is temperature (T). Abbreviations: Ol, olivine; Opx, orthopyroxene; Cpx, clinopyroxene; Sp, spinel; Gt, garnet; Pl, plagioclase; Liq, liquid.

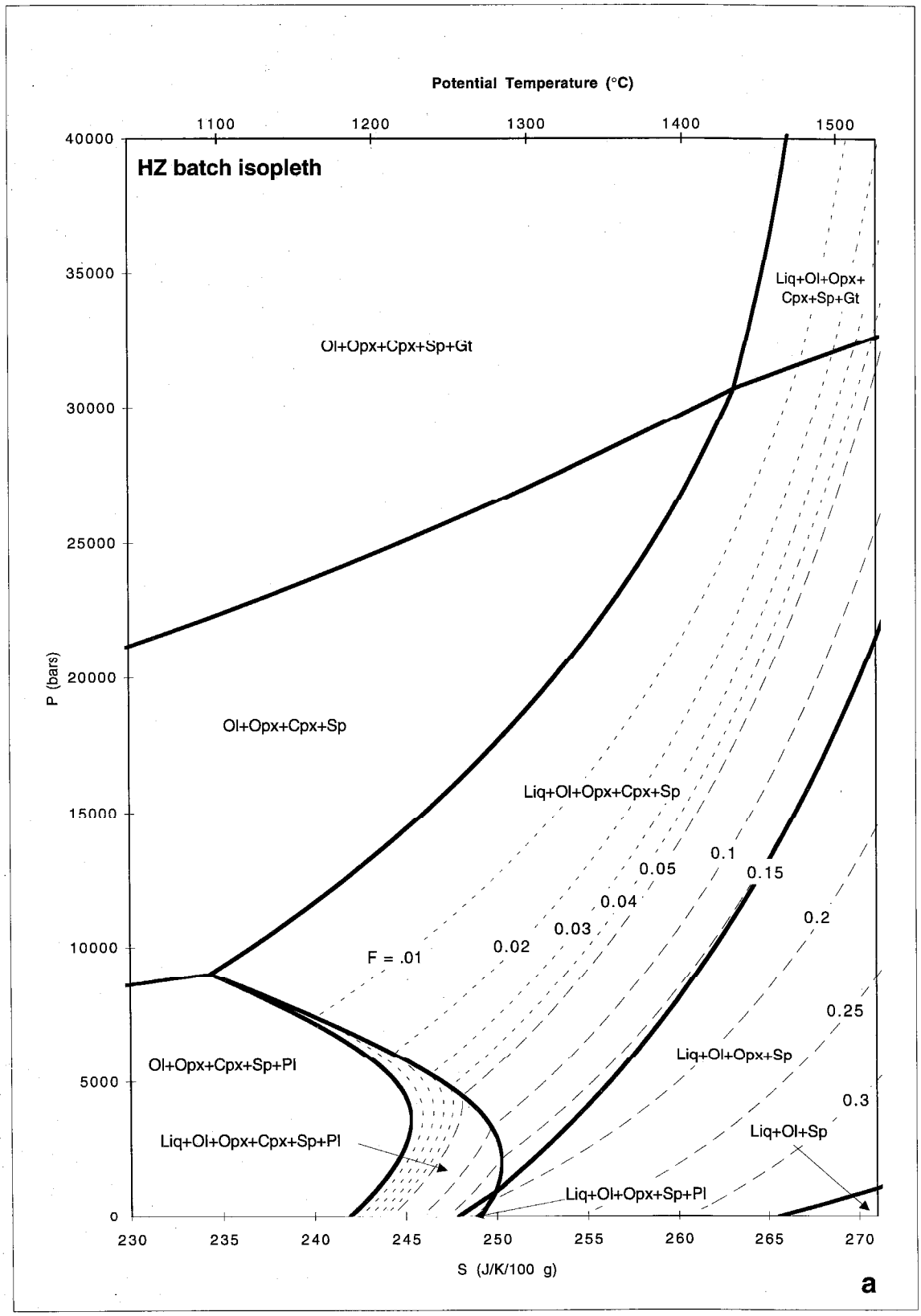

Chapter 5, Figure 1a

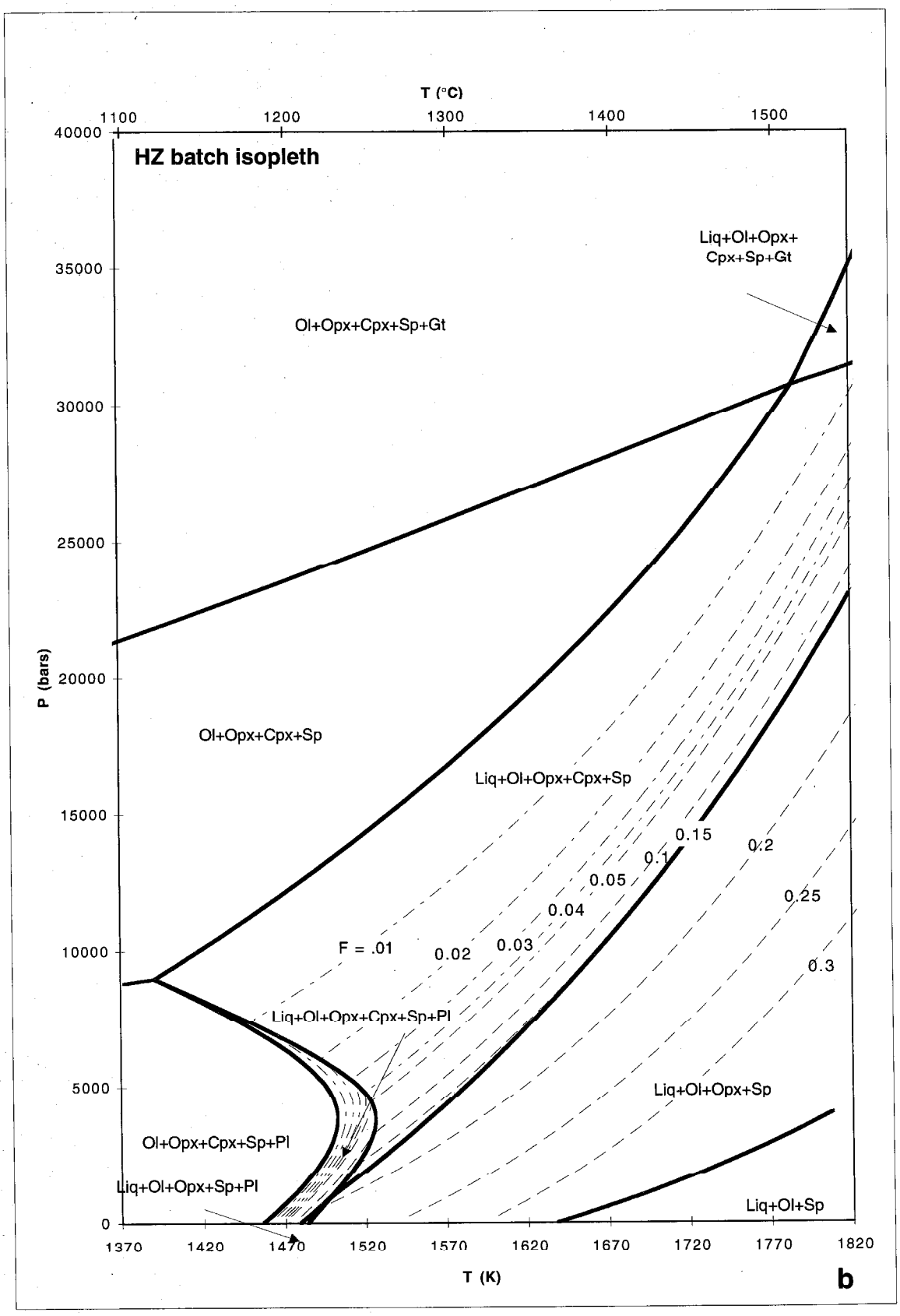

Chapter 5, Figure 1b

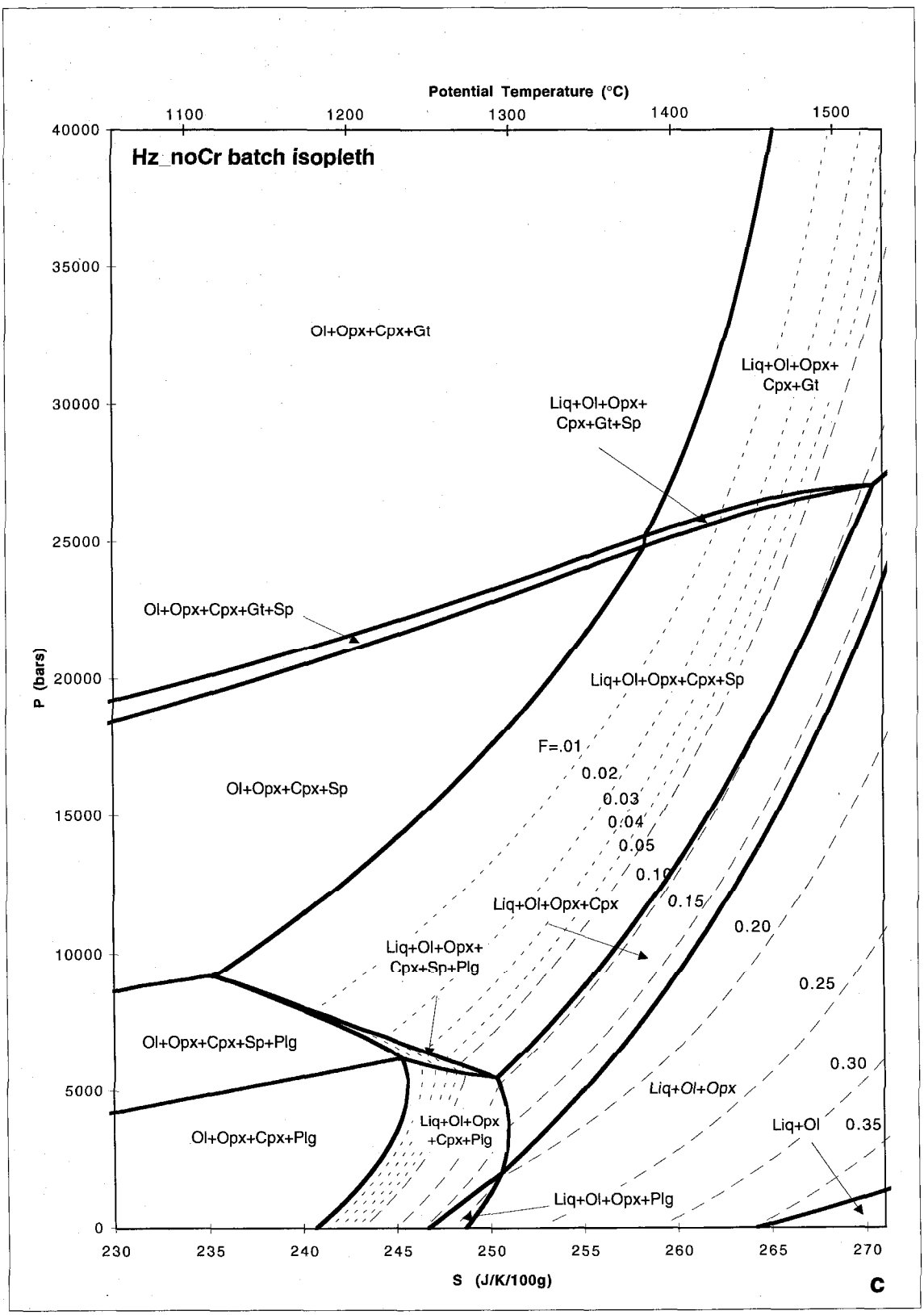

Chapter 5, Figure 1c

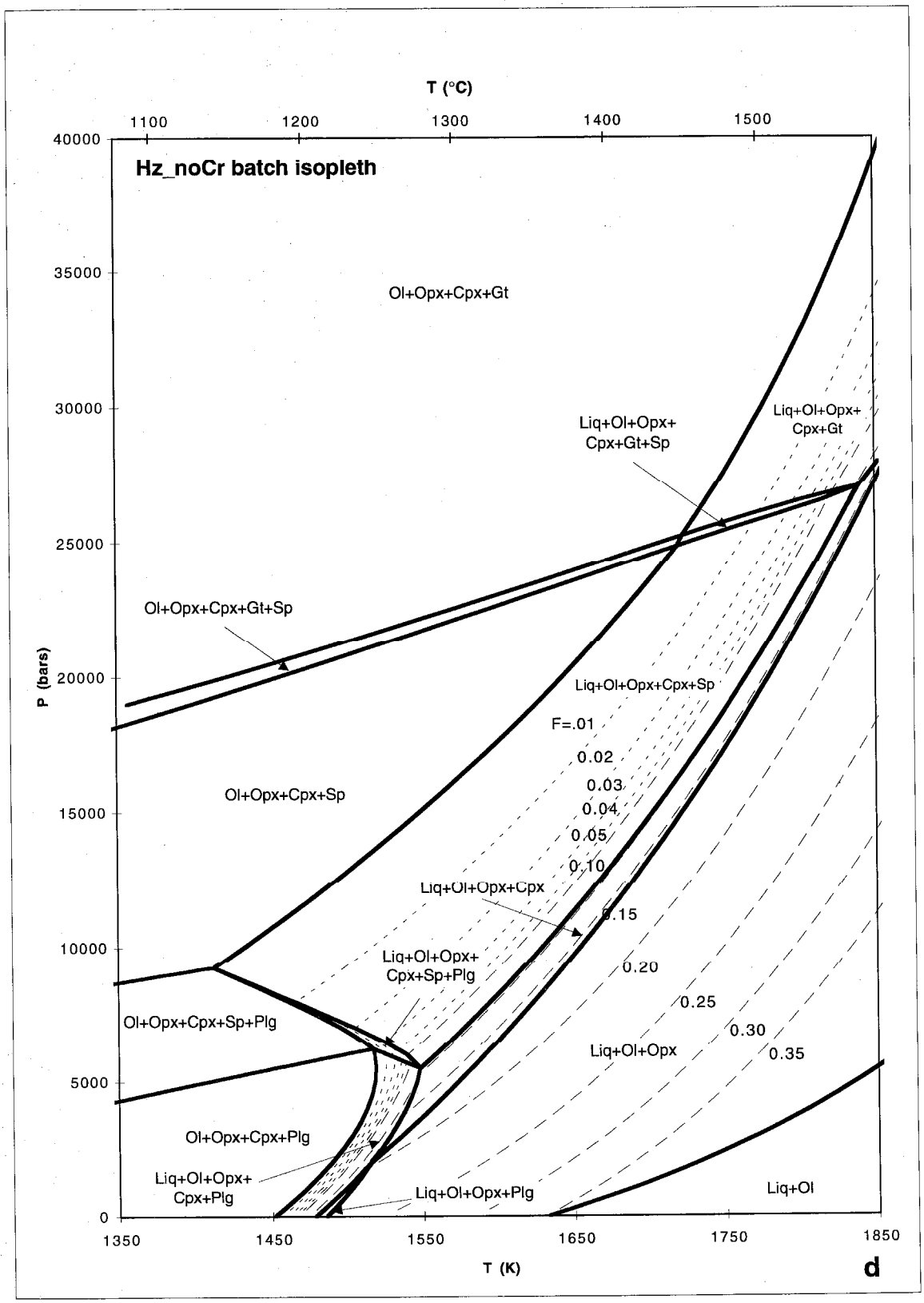

Chapter 5, Figure 1d

Figure 2. SiO_2 in silicate liquids from melting of peridotite vs. extent of melting F. (a) MELTS predictions for batch melting Cr-free Hart and Zindler (1986) composition. Light curves are isobaric paths at the labeled pressures. Bold curves are isentropic paths beginning at the labeled solidus intersection pressure P_o. The P_o=14 kbar path intersects the spinel-plagioclase transition and freezes completely before melting resumes in the plagioclase peridotite field. (b) Fits to isobaric batch melting data and estimated polybaric paths from Klein and Langmuir (1987). This calculation assumes a productivity $-(dF/dP)$ of 1.2 %/kbar. (c) Adiabatic (incrementally isentropic) fractional melting according to MELTS: incremental melt compositions are shown as light solid curves, integrated fractional melts are shown as heavy curves. The batch melting paths from (a) are shown for comparison as light dashed lines; the integrated fractional melts are substantially different from batch melting both in that lower melt fractions are achieved and SiO_2 content follows a different path.

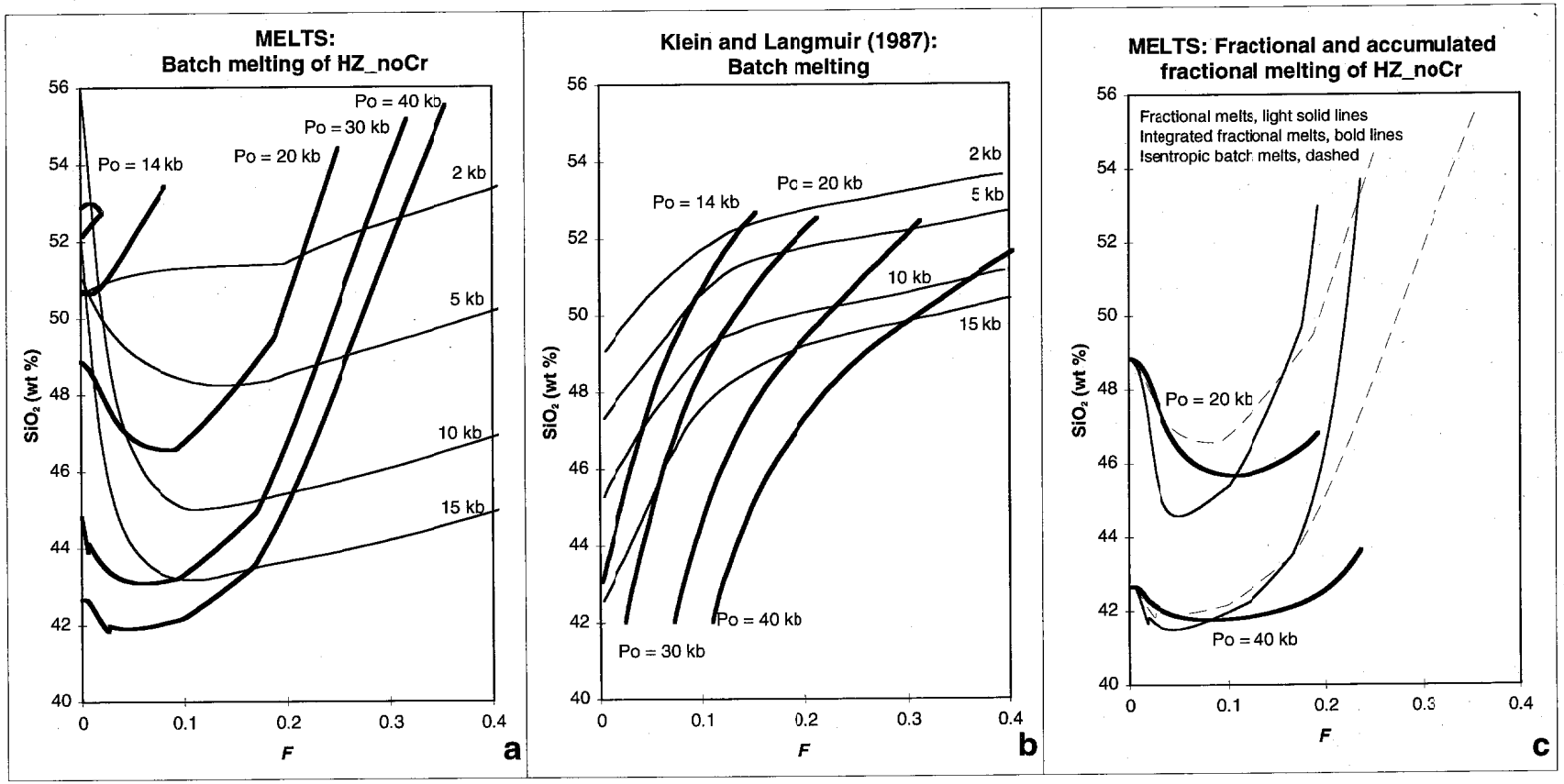

Chapter 5, Figure 2

Figure 3. Mean properties of two-dimensional integrated melting regimes with passive flow, constant final pressure of melting (2 kbar) and varying potential temperature and initial pressure of melting (Klein and Langmuir-type melting regimes). Both the Cr-bearing (HZ) and Cr-free (HZ_noCr) source compositions after Hart and Zindler (1986) are shown. MELTS results are compared to the model of Langmuir et al. (1992) as a representative of a broad class of models with nearly constant productivity. (a) Mean pressure $\bar{P}$ vs. solidus intersection pressure P_o. (b) Mean melt fraction F_B (see Plank et al., 1995) vs. P_o. (c) Crustal thickness (Zc, calculated according to the formalism of Klein and Langmuir, 1987) vs. P_o. (d) Mean P vs. potential temperature (T_P). (e) F_B vs. T_P. (f) Z_c vs. T_P.

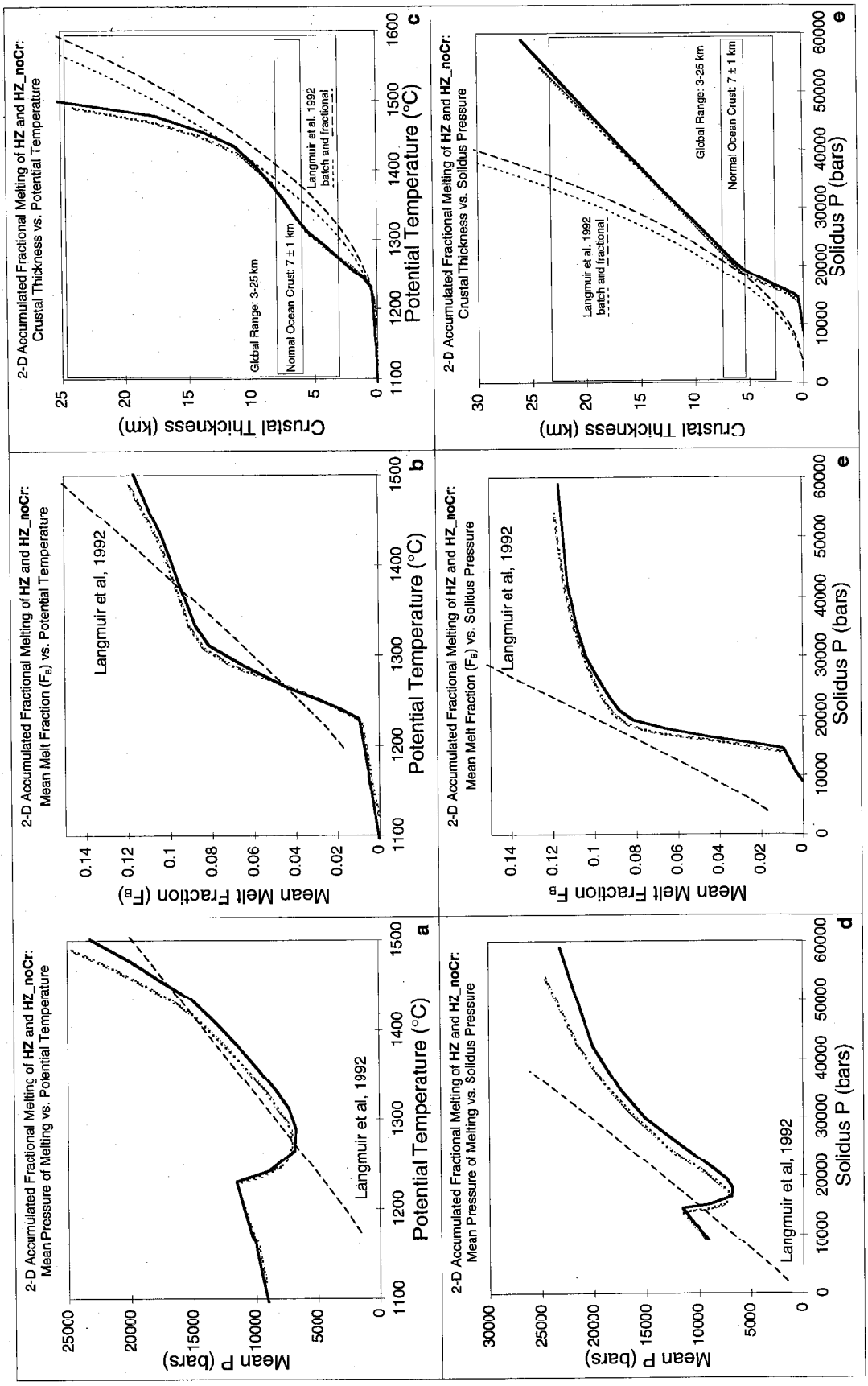

Chapter 5, Figure 3

Figure 4. Cartoon of passive flow melting regimes at mid-ocean ridge and the effect of the spinel-plagioclase transition region. The simple triangular melting regime generated by corner flow is modified for low potential temperature (shallow solidus pressure) by a barren region caused by the endothermic spinel-plagioclase transition region (see Asimow et al., 1995a). As potential temperature decreases, the barren zone widens until the upper part of the melting regime, in the plagioclase stability field, disappears. Compare to Figure 1; the barren zone is controlled by the shape of the solidus as a function of potential temperature.

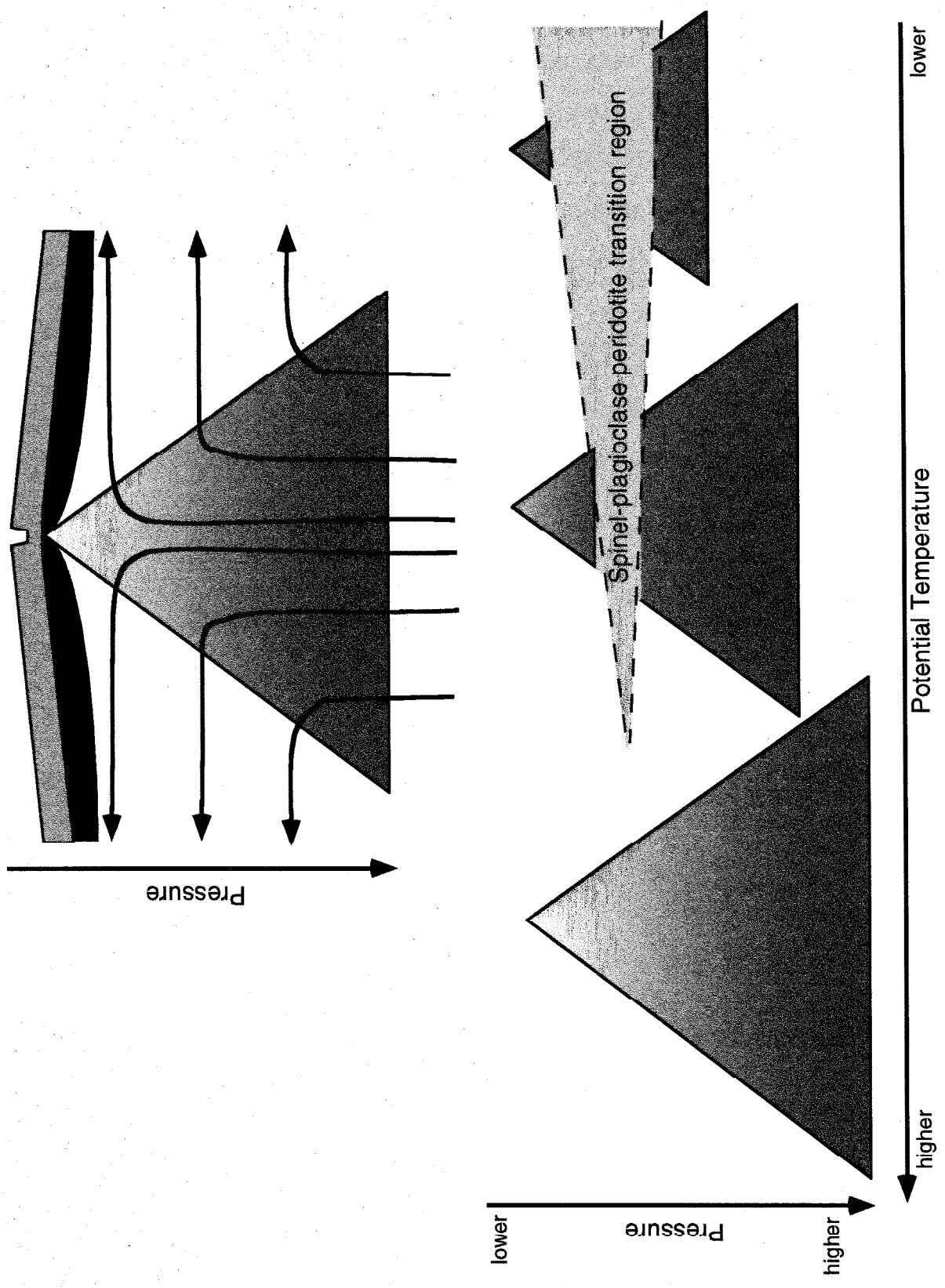

Chapter 5, Figure 4

Figure 5. Variations of mean properties of the melting regime with variations in the final pressure of melting (Shen and Forsyth-type melting regimes) for passive flow and the Cr-bearing HZ source composition. Three potential temperatures are shown, although the intent is to see how global mean properties would correlate if potential temperature were constant. (a) Mean pressure vs. Final pressure of melting (P_f). The result from the melting model of Langmuir et al. (1992) is shown (dashed) for comparison; the nearly constant productivity in their model leads to nearly linear trends on this diagram. (b) F_B vs. P_f. (c) Crustal thickness vs. P_f. For a globally uniform solidus pressure of 25 kbar, variation in P_f from 0 to 9 kbar would be needed to generate a range in crustal thicknesses from 10 to 3 km. For a globally uniform solidus pressure of 60 kbar, variation in P_f from 3 to 25 kbar would generate a range in crustal thickness from 25 to 3 km.

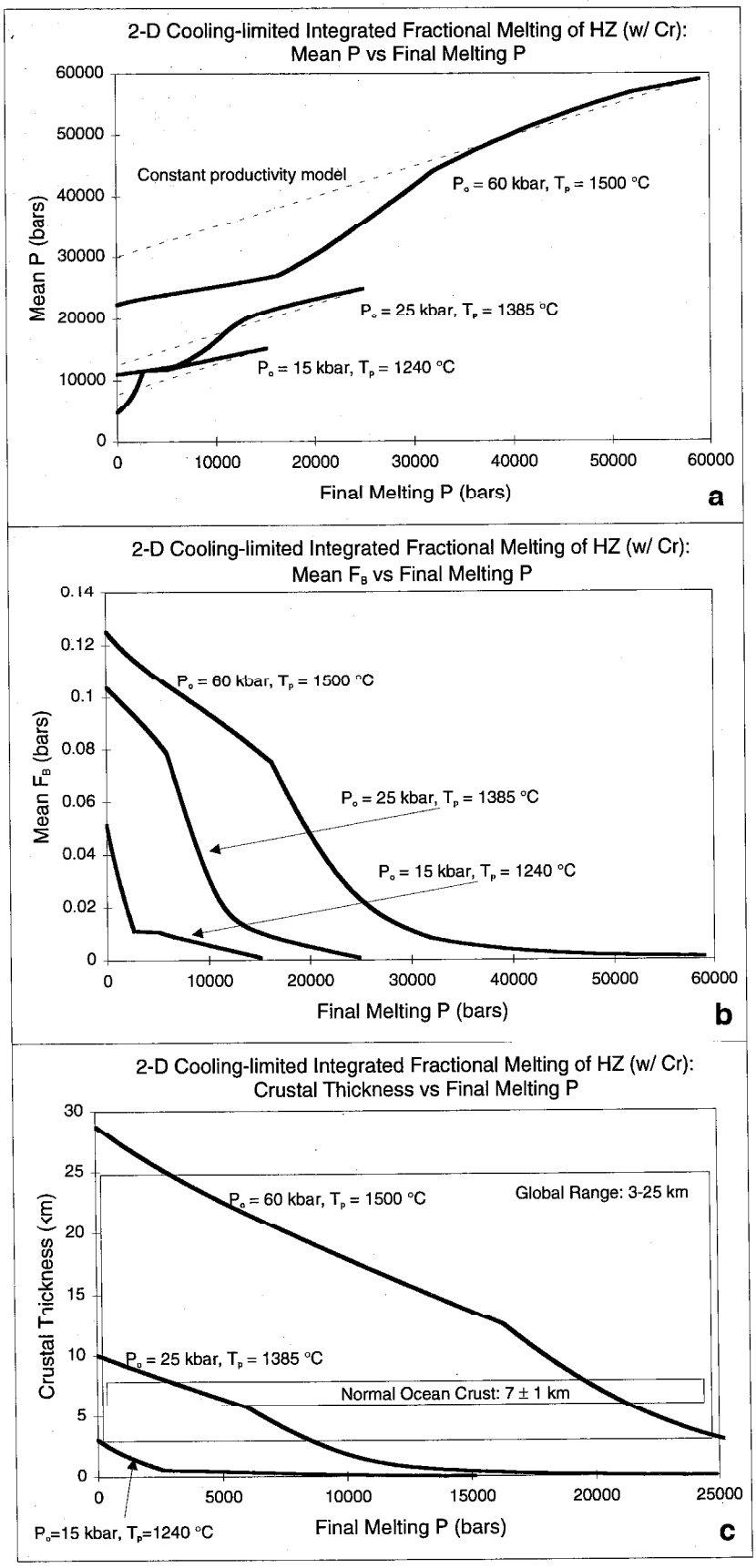

Chapter 5, Figure 5

Figure 6. Na_2O and FeO* systematics for primary aggregate liquids in the reference case of passive flow and Klein and Langmuir-type global systematics. These quantities have not been fractionated to 8% MgO. The models of Langmuir et al. (1992) and Kinzler (1997) for adiabatic fractional melting are shown for comparison. (a) Na_2O vs. F_B. (b) FeO* vs. mean P. (c) Na_2O and FeO* vs. P_o. (d) Na_2O and FeO* vs. crustal thickness. (e) Na_2O vs. FeO*.

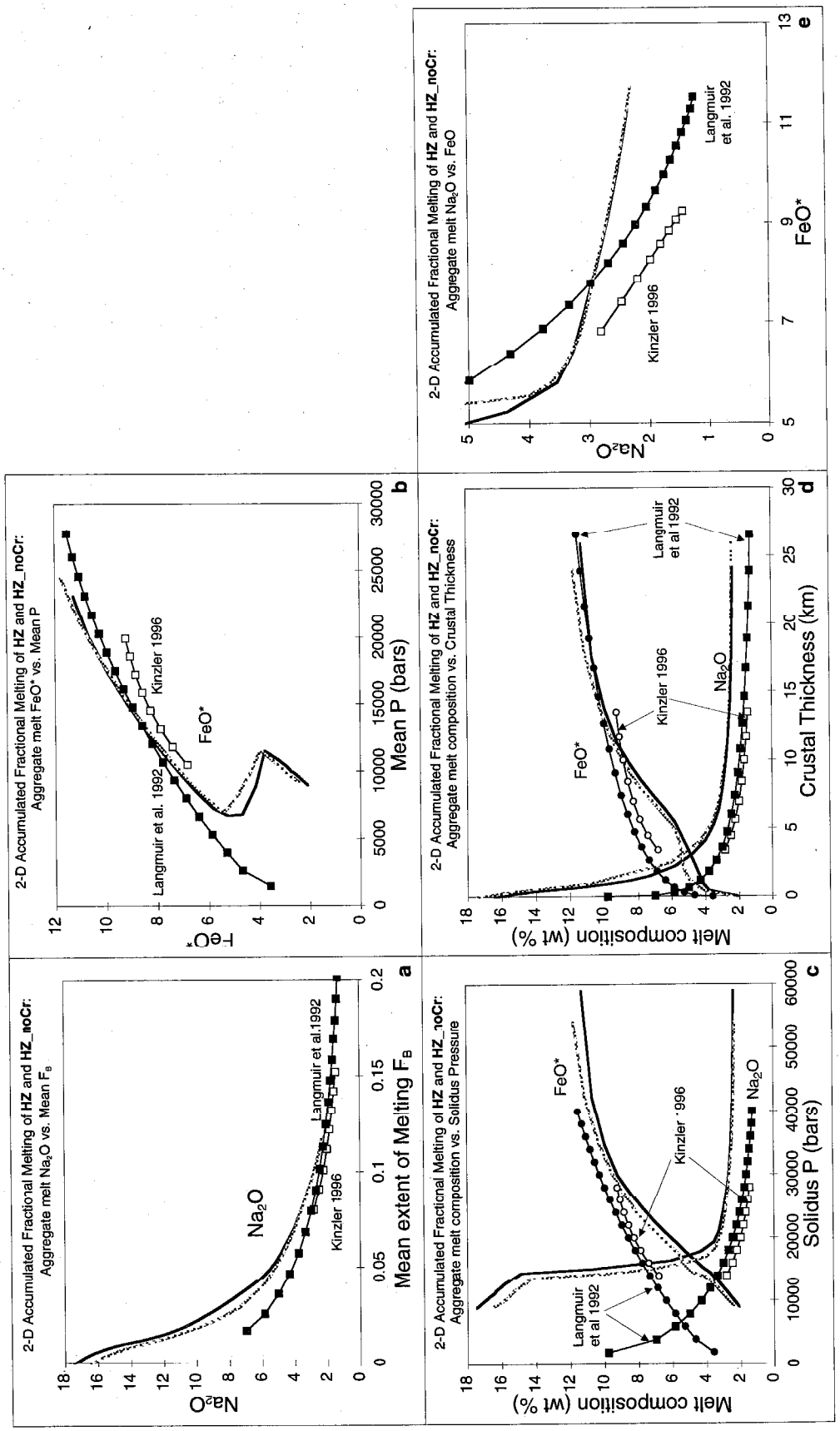

Chapter 5, Figure 6

Figure 7. (a) Crustal thickness (log scale) vs. $Na_{8.0}$ for regionally averaged MORB, the global data set of Klein and Langmuir (1987), supplemented by Forsyth (1992), together with model calculations from the same papers and that of McKenzie and Bickle (1988). None of these models can explain the global data array with a uniform source composition and melting model. (b) Crustal thickness (log scale) vs. Na_2O in primary aggregate melts from MELTS, Klein and Langmuir (1987) and Langmuir et al. (1992). The curvature of the MELTS results is in the right sense to explain the global correlation.

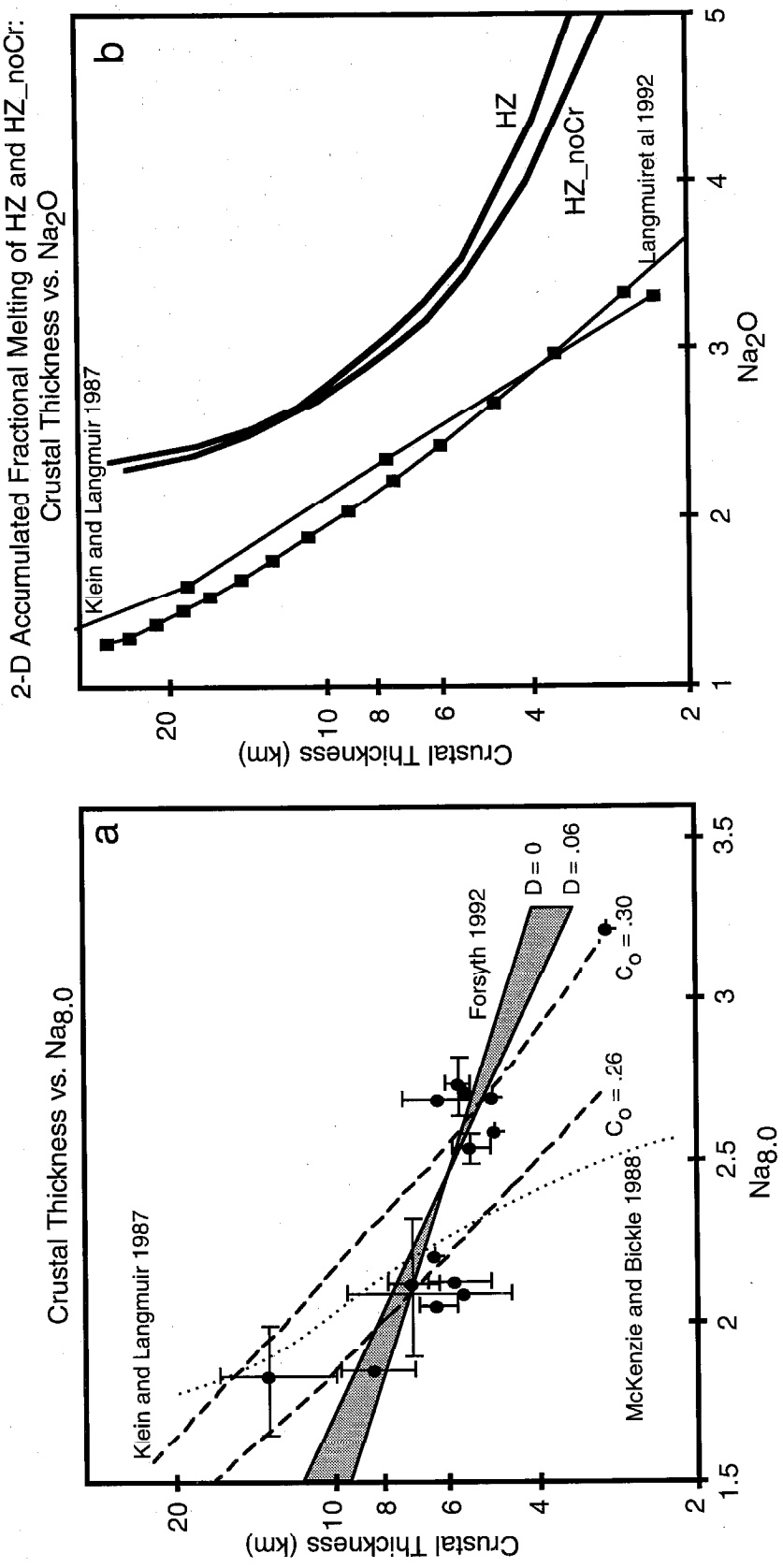

Chapter 5, Figure 7

Figure 8. Compositional trends expected from Shen and Forsyth-type melting regimes with variable final pressure of melting with passive flow and uniform HZ source composition. Three different potential temperatures are plotted, as in Figure 5, although the intent is to evaluate global systematics at constant potential temperature. (a) Na_2O and FeO* vs. P_f. FeO* is remarkably insensitive to the final pressure of melting. (b) Na_2O vs. FeO. The locus of points at P_f = 2 kbar for various potential temperature is also shown, labeled "Klein and Langmuir," as is the result of the Langmuir et al. (1992) model for a melting regime of this type with P_o=25 kbar.

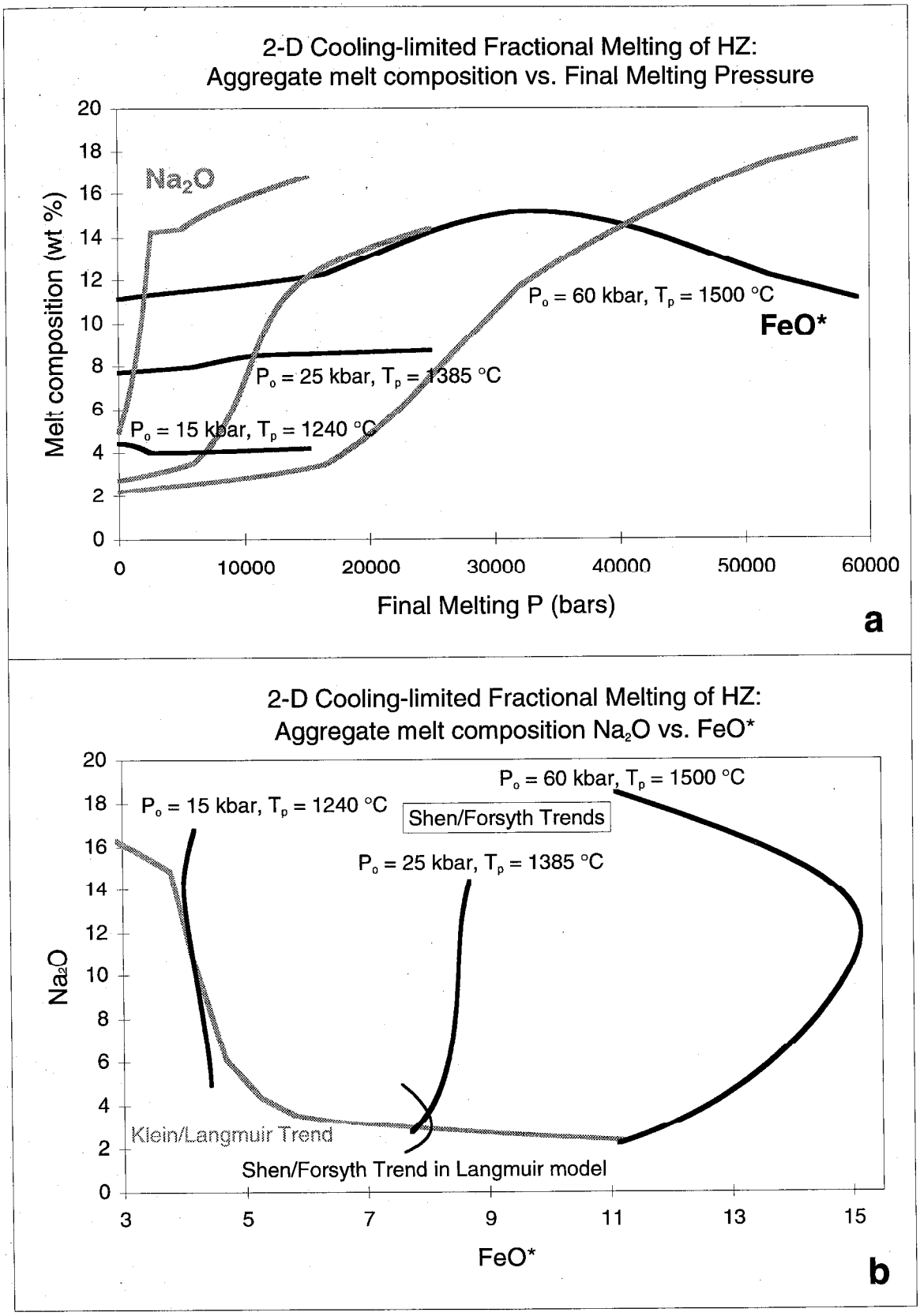

Chapter 5, Figure 8

Figure 9. Compositional heterogeneity in a global sample of peridotites (Herzberg et al., 1988), small points. The lines represent addition and subtraction of a uniform basaltic component from the primitive upper mantle composition (here called HZ) of Hart and Zindler (1986). This component was chosen so that the enrichment/depletion trend would parallel the principal trends of variation in the peridotite data. It is offset from the bulk of the data in those elements for which the starting composition is not in the center of the data array. The open circles show the five compositions used in calculations of the effects of source heterogeneity herein, i.e., HZ + 10% basalt, HZ + 5% basalt, HZ, HZ - 5% basalt, and HZ - 10% basalt. The labeled black dots, from left to right, are enriched peridotite R123 (Frey et al., 1985), HZ, experimental mix mm3 (Baker and Stolper, 1994), and experimental mix DMM1 (Wasylenki et al., 1996).

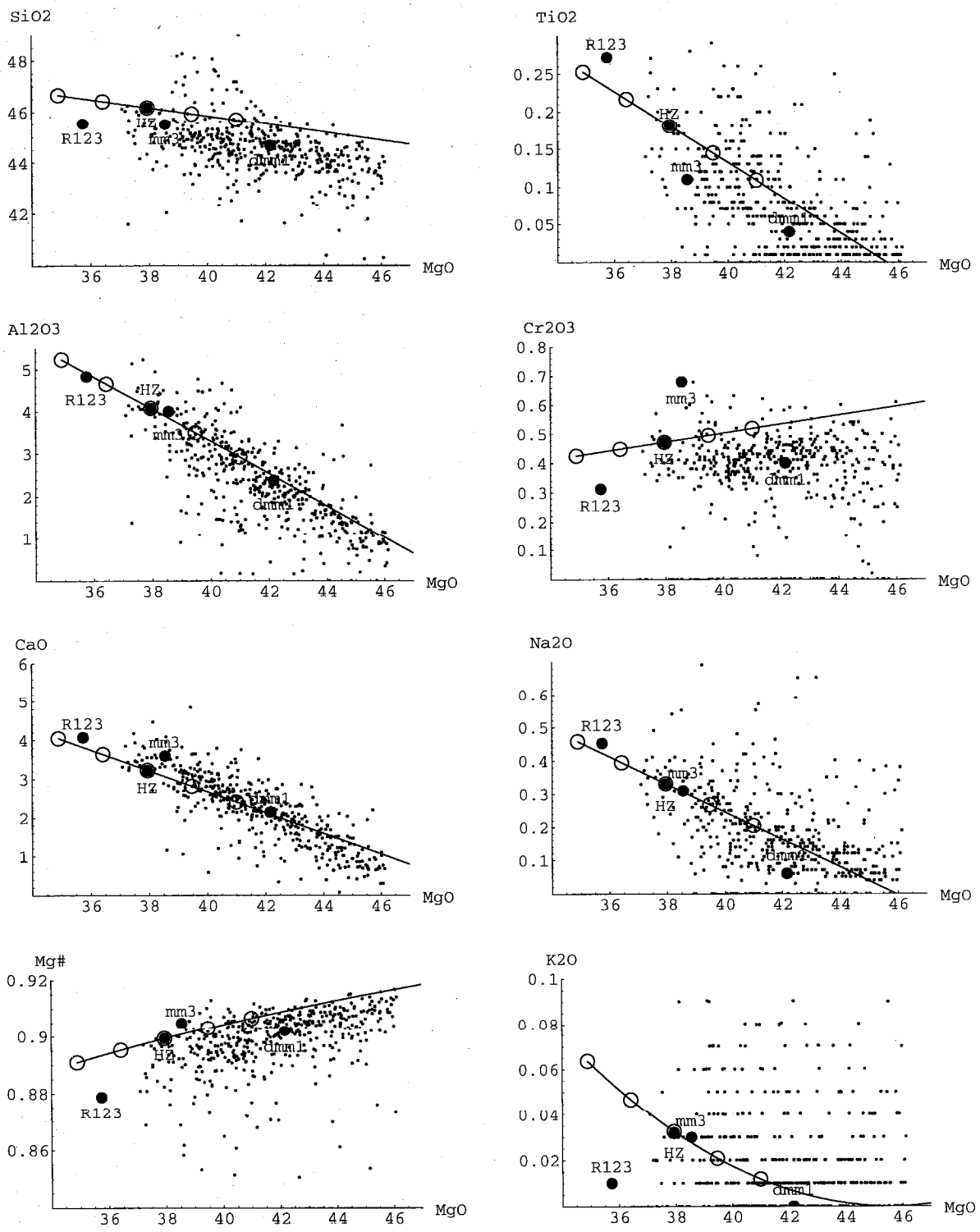

Chapter 5, Figure 9

Figure 10. Na_2O vs. FeO* for primary integrated liquid compositions for (a) active flow and fractional melting, (b) passive flow and fractional melting, (c) active flow and batch melting, and (d) passive flow and batch melting, all for melting regimes with constant final depth of melting (5 km), variable potential temperature (1200 to 1600 °C) and five different source compositions (see Figure 9). The heavy curves with negative slopes are for each source and various potential temperatures. The light curves are contours of constant potential temperature and varying source composition.

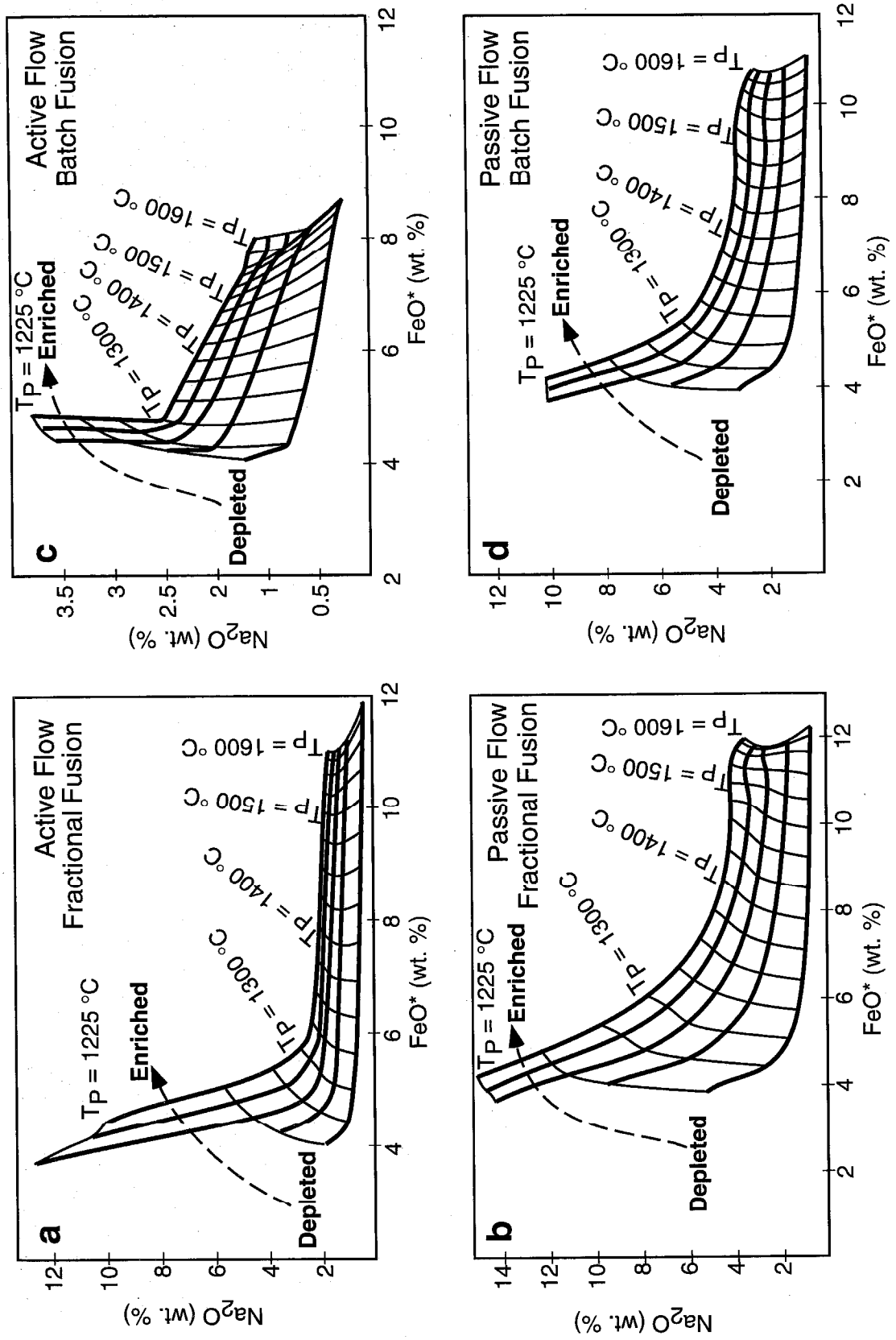

Chapter 5, Figure 10

Figure 11. Na_2O vs. FeO* for melting regimes various source compositions, with constant potential temperature (1325 °C) and varying final depth of melting. (a) shows incremental fractional melt compositions, (b) shows integrated compositions for active flow and fractional melting, (c) shows aggregate compositions for passive flow and fractional melting, (d) shows active flow and batch melting, and (e) shows passive flow and batch melting. The bold S-shaped curves in each case show variation from the solidus depth to 5 km in the final pressure of melting for each source composition. The light, shallowly sloped curves in (b)-(e) show constant final depth of melting contours for various source compositions.

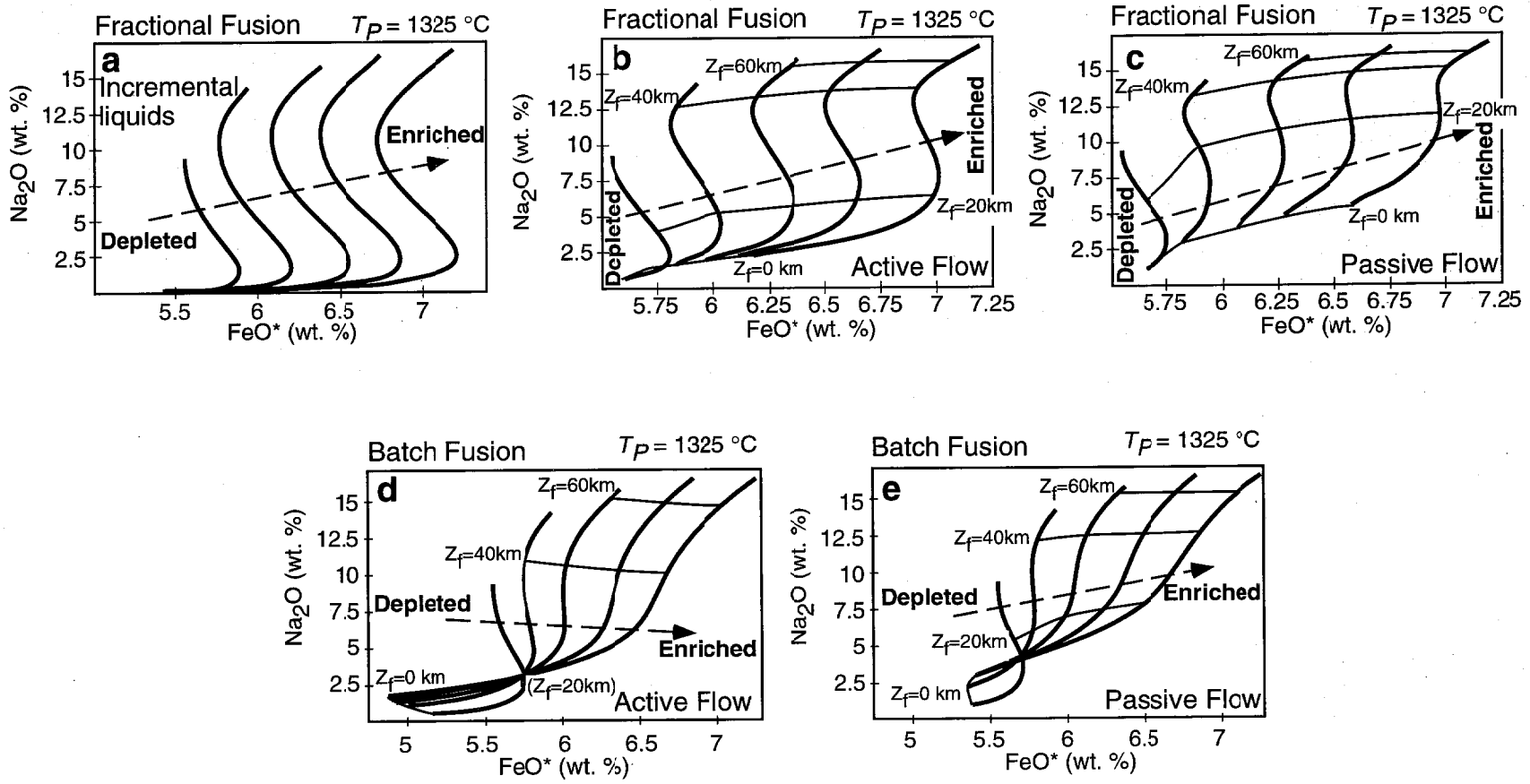

Chapter 5, Figure 11

Figure 12. Primary melt compositions in Shen and Forsyth-type melting regimes for five different source compositions (see Figure 9). The potential temperature is 1325 °C for all curves. (a) and (d) show incremental fractional melts. (b) and (e) show integrated compositions for active flow. (c) and (f) show aggregate compositions for passive flow. (a), (b), and (c) plot CaO/Al_2O_3 against F_{max}, the extent of melting achieved at the final pressure of melting. (d), (e), and (f) plot FeO* against MgO. The direction from depleted to enriched and from low P_f to high P_f is indicated in each case.

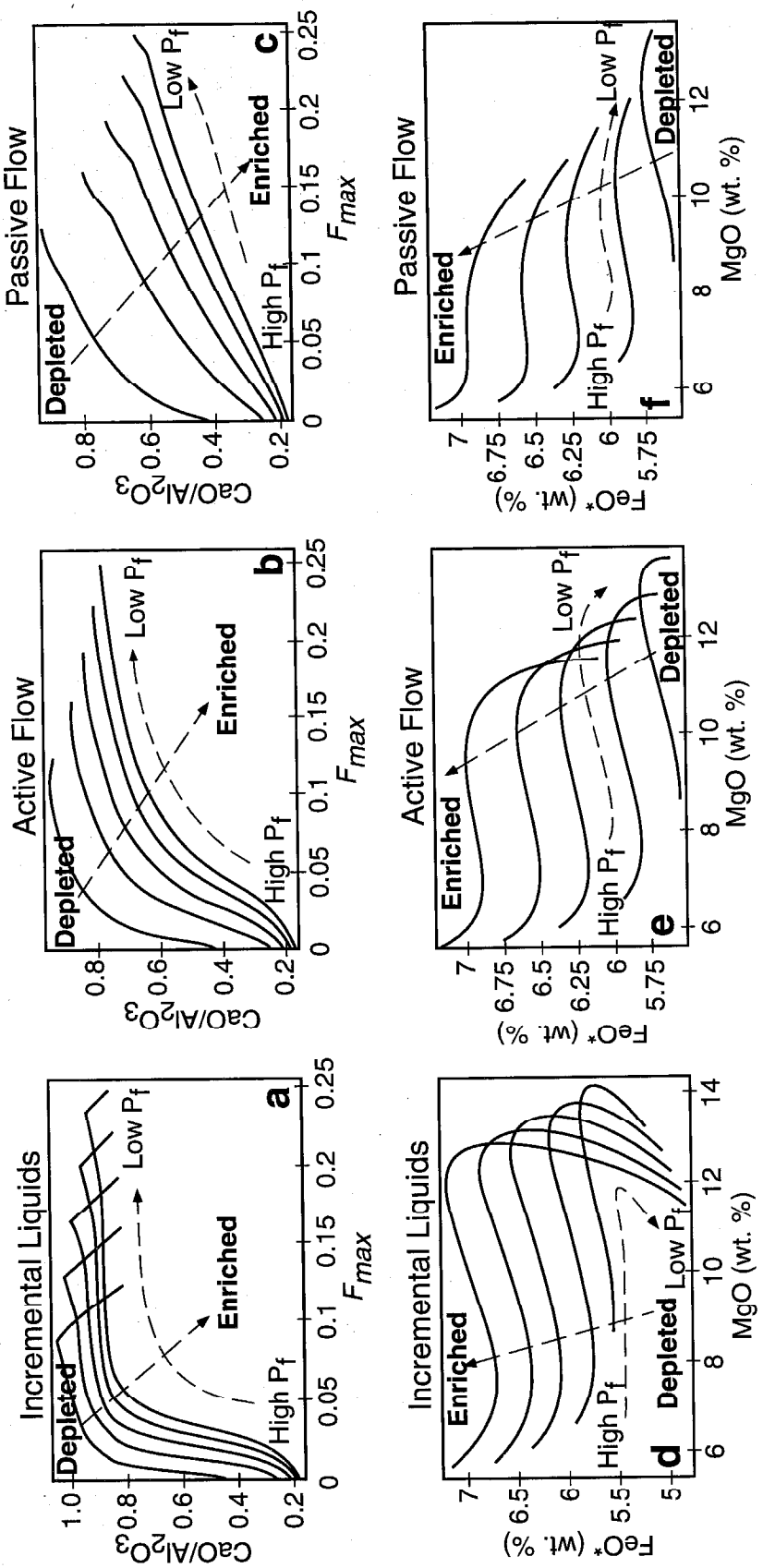

Chapter 5, Figure 12

Figure 13. Primary melt compositions in Klein and Langmuir-type melting regimes for five different source compositions (see Figure 9). Final pressure of melting is 5 km for all curves. Potential temperature varies from 1200 to 1600 °C along each curve. (a) and (d) show the incremental fractional melt produced at 5 km. (b) and (e) show integrated compositions for active flow. (c) and (f) show aggregate compositions for passive flow. (a), (b), and (c) plot CaO/Al_2O_3 against F_{max}, the extent of melting achieved at the final pressure of melting. (d), (e), and (f) plot FeO* against MgO. The direction from depleted to enriched and from low T_P to high T_P is indicated in each case.

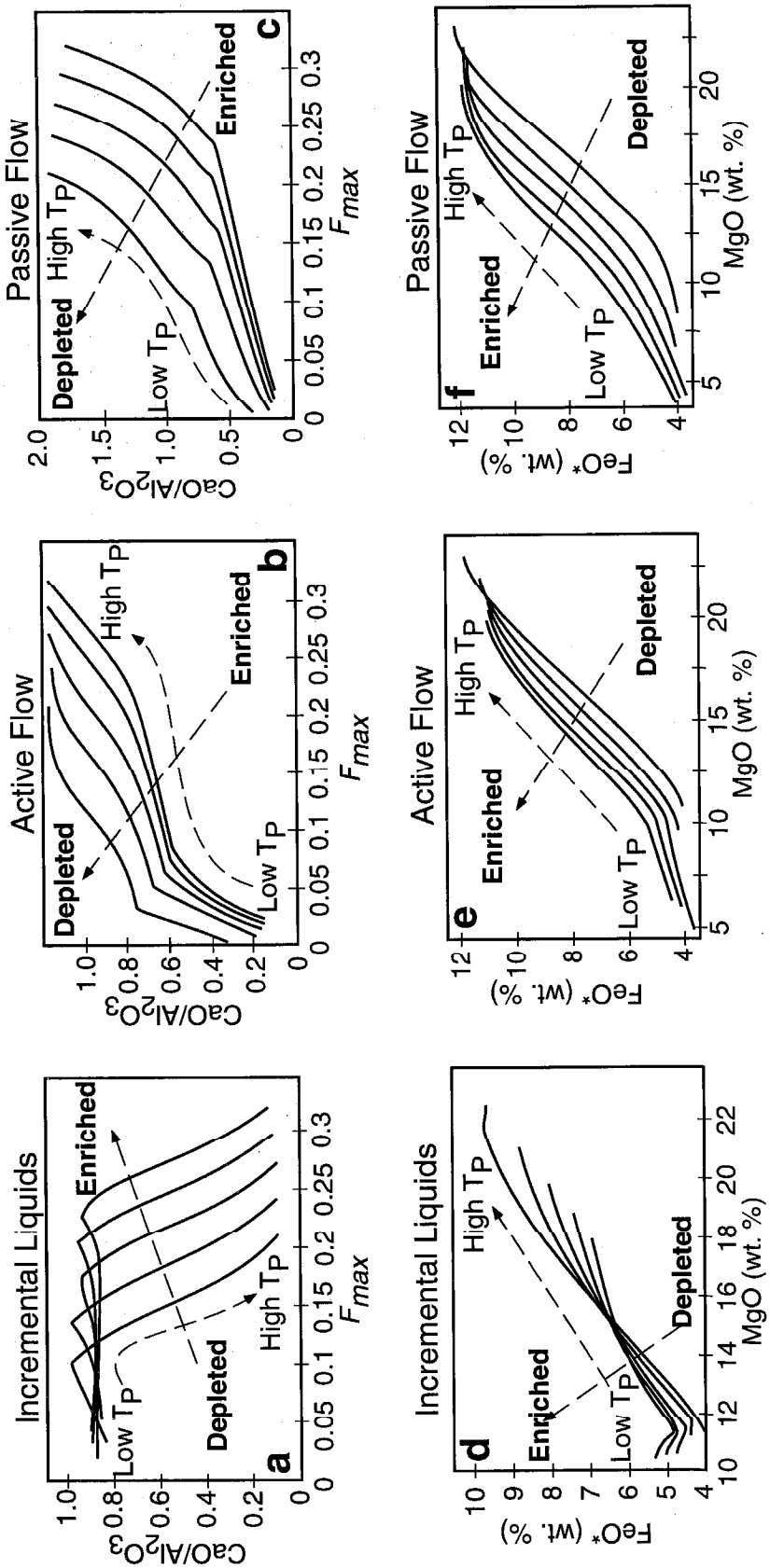

Chapter 5, Figure 13

Figure 14. (a) $Fe_{8.0}$ vs. K_2O/TiO_2 for regionally averaged basalt compositions, from Shen and Forsyth (1995), showing also the data of Niu and Batiza (1993). (b) FeO* vs. K_2O/TiO_2 for primary aggregate liquids predicted by MELTS from passive flow, fractional melting, Klein and Langmuir-type melting regimes for five different source compositions. Light lines with positive slope show the effect of heterogeneity at constant potential temperature.

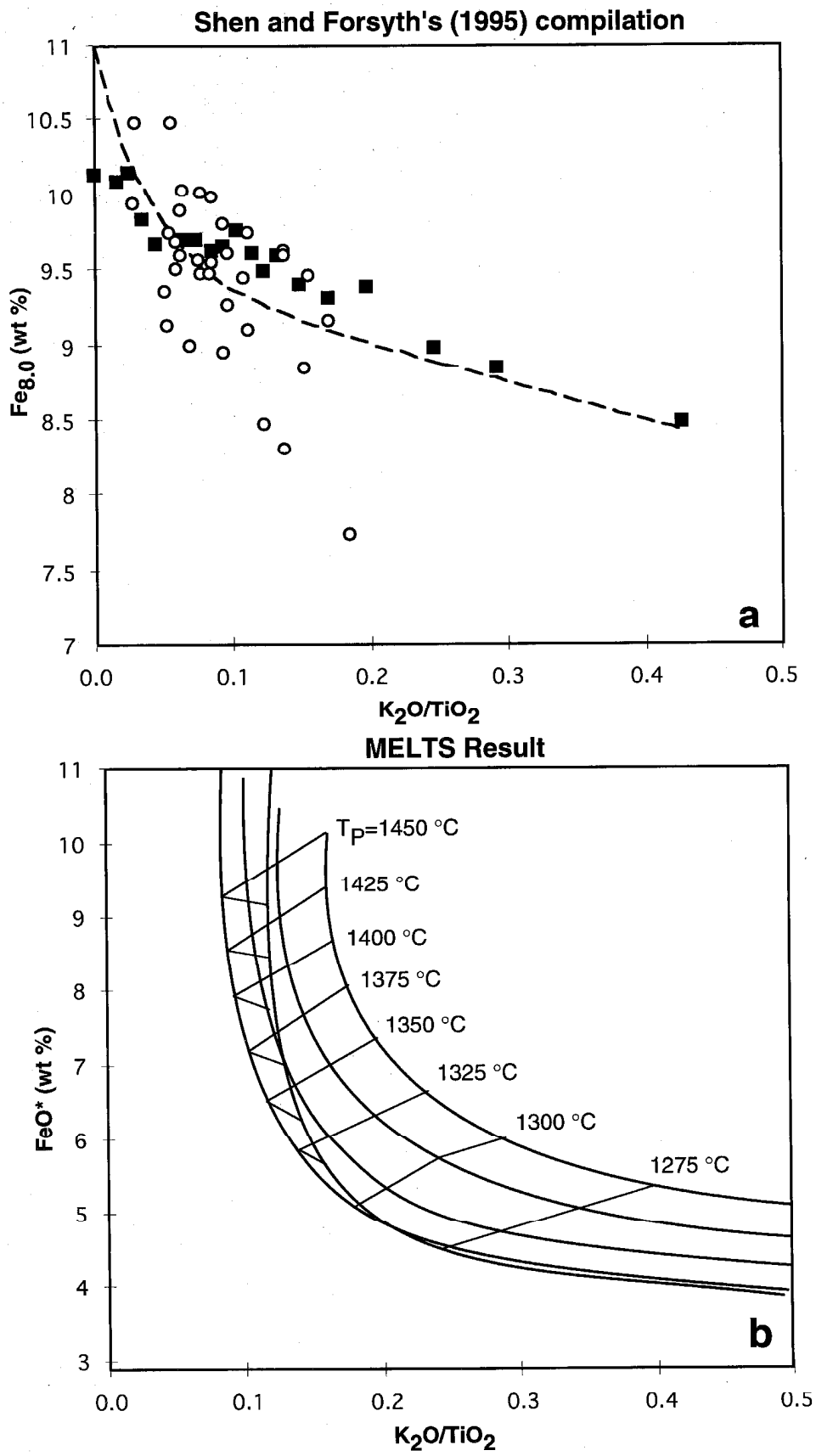

Chapter 5, Figure 14

Figure 15. $(Sm/Yb)_N$ (i.e., chondrite normalized) vs. (a) crustal thickness and (b) FeO* in the primary aggregate liquid, for Klein and Langmuir-type passive flow fractional melting regimes. The negative slope at low potential temperature is an extent of melting effect; the positive slope at high potential temperature reflects the influence of residual garnet.

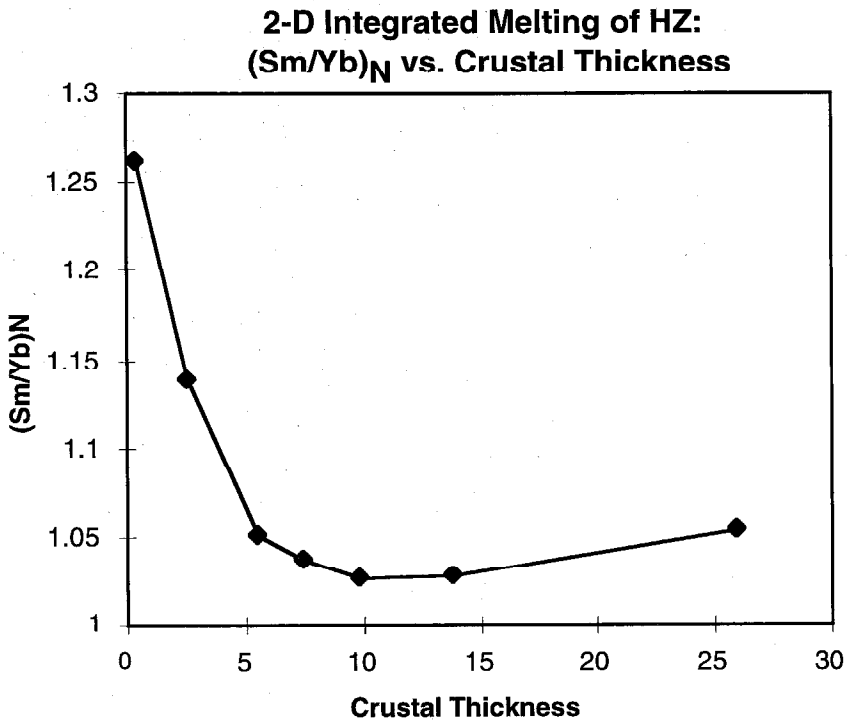

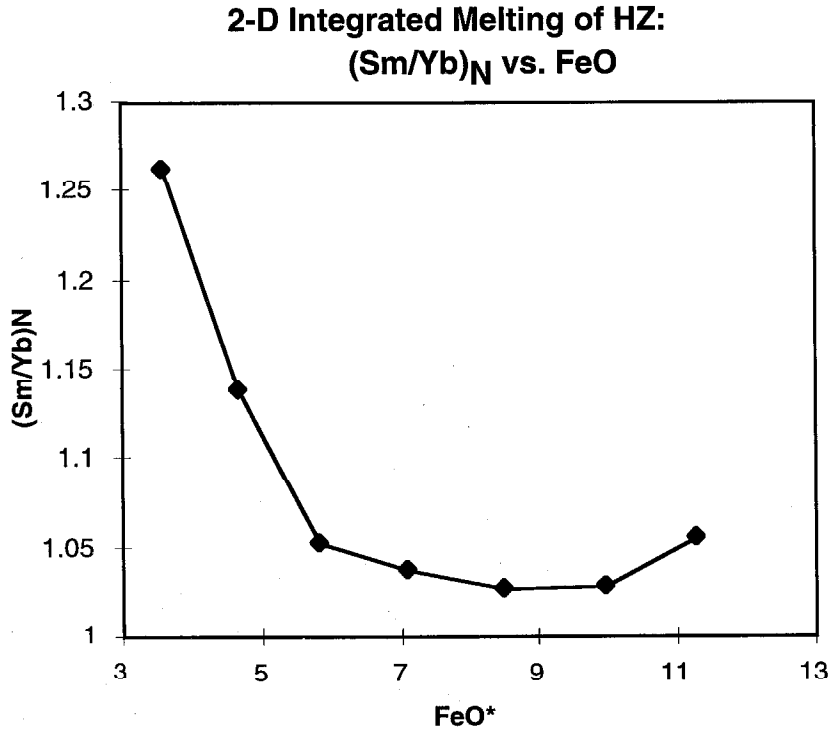

Chapter 5, Figure 15

References

Aharonov E., Whitehead J. A., Kelemen P. B. and Spiegelman M. (1995) Channeling instability of upwelling melt in the mantle. *J. Geophys. Res.* **100**, 20433-20450.

Ahern J. L. and Turcotte D. L. (1979) Magma migration beneath an ocean ridge. *Earth Planet. Sci. Lett.* **45**, 115-122.

Albarède F. (1983) Limitations thermiques à l'ascension des magmas hydratés. *C. R. Acad. Sci. Paris* **296**, 1441-1444.

Albarède F. (1992) How deep do common basaltic magmas form and differentiate? *J. Geophys. Res.* **97**, 10,997-11,009.

Asimow P. D., Hirschmann M. M., Ghiorso M. S., O'Hara M. J. and Stolper E. M. (1995a) The effect of pressure-induced solid-solid phase transitions on decompression melting of the mantle. *Geochim. Cosmochim. Acta* **59**, 4489-4506.

Asimow P. D., Hirschmann M. M., Ghiorso M. S. and Stolper E. M. (1995b) Isentropic melting processes in the mantle. In *Plume 2 Conference* (ed. D. L. Anderson et al.). pp. 12-14. Terra Nostra **3/1995**. Alfred-Wegener-Stiftung.

Asimow P. D., Hirschmann M. M. and Stolper E. M. (1997) An analysis of variations in isentropic melt productivity. *Philosophical Transactions of the Royal Society of London* **A355**, 255-281.

Baker M. B., Hirschmann M. M., Ghiorso M. S. and Stolper E. M. (1995) Compositions of low-degree partial melts of peridotite: Results from experiments and thermodynamic calculations. *Nature* **375**, 308-311.

Baker M. B. and Stolper E. M. (1994) Determining the composition of high-pressure mantle melts using diamond aggregates. *Geochim. Cosmochim. Acta* **58**, 2811-2827.

Beattie P. (1993a) Uranium-thorium disequilibria and partitioning on melting of garnet peridotite. *Nature* **363**, 63-65.

Beattie P. (1993b) The generation of uranium series disequilibria by partial melting of spinel peridotite: constraints from partitioning studies. *Earth Planet. Sci. Lett.* **117**, 379-391.

Bell P. M. and Roseboom E. H. (1969) Melting relationships of jadeite and albite to 45 kilobars with comments on melting diagrams of binary systems at high pressures. *Mineralogical Society Special Paper* **2**, 151-161.

Ben Othman D. and Allegre C. J. (1990) U-Th isotopic systematics at 13 °N east Pacific Ridge segment. *Earth Planet. Sci. Lett.* **98**, 129-137.

Berman R. G. (1988) Internally-consistent thermodynamic data for minerals in the system Na_2O-K_2O-CaO-MgO-FeO-Fe_2O_3-Al_2O_3-SiO_2-TiO_2-H_2O-CO_2: representation, estimation, and high temperature extrapolations. *J. Petrol.* **89**, 168-183.

Biggar G. M. and O'Hara M. J. (1969) Solid solutions at atmospheric pressure in the system CaO-MgO-SiO2 with special reference to the instabilities of diopside, akermanite, and monticellite. *Prog. Exp. Pet. 1st Rep.*, 89-96. NERC, London.

Boyd F. R. and England J. L. (1960) The quartz-coesite transition. *J. Geophys. Res.* **65**, 749-756.

Brodholt J. P. and Batiza R. (1989) Global systematics of unaveraged mid-ocean ridge basalt compositions: Comment on "Global correlations of ocean ridge basalt chemistry with axial depth and crustal thickness." *J. Geophys. Res.* **94**, 4231-4239.

Brodie J., Latin D. and White N. (1994) Rare earth element inversion for melt distribution: sensitivity and application. *J. Petrol.* **35**, 1155-1174.

Brown J. M. (1996) Mineral physics interpretations of the upper mantle. *EOS, Transactions American Geophysical Union* **77**, F483.

BVSP (1981) *Basaltic Volcanism on the Terrestrial Planets*. Pergamon.

Carr M. H. (1975) The volcanoes of Mars. *Scientific American* **234**, 32-43.

Cawthorn R. G. (1975) Degrees of melting in mantle diapirs and the origin of ultrabasic liquids. *Earth Planet. Sci. Lett.* **27**, 113-120.

Condomines M., Morand P. and Allègre C. J. (1981) ^{230}Th-^{238}U disequilibria in oceanic tholeiites from 21 °N on the East Pacific Rise. *Earth Planet. Sci. Lett.* **55**, 393-406.

Cross W., Iddings J. P., Pirsson L. V. and Washington H. S. (1902) A quantitative chemico-mineralogical classification and nomenclature of igneous rocks. *J. Geol.* **10**, 555-690.

Currie K. L. (1991) GENORM - a generalized norm calculation. *Computers and Geosciences* **17**, 77-89.

Ellam R. M. (1992) Lithospheric thickness as a control on basalt geochemistry. *Geology* **20**, 153-156.

Engel A. E., Engel C. G. and Havens R. G. (1965) Chemical characteristics of oceanic basalts and the upper mantle. *Geol. Soc. Amer. Bull.* **76**, 719-734.

Falloon T. J., Green D. H., Hatton C. J. and Harris K. L. (1988) Anhydrous partial melting of a fertile and depleted peridotite from 2 to 30 kb and application to basalt petrogenesis. *J. Petrol.* **29**, 1257-1282.

Flower M. J. F. (1981) Thermal and kinematic controls on ocean-ridge magma fractionation: contrasts between Atlantic and Pacific spreading axes. *J. geol. Soc* **138**, 695-712.

Forsyth D. W. (1992) Geophysical constraints on mantle flow and melt generation beneath mid-ocean ridges. In *Mantle Flow and Melt Generation at Mid-Ocean Ridges* (ed. J. Phipps Morgan et al.). pp. 1-66. Am. Geophys. Union, Geophys. Monogr. **71**.

Frank F. C. (1968) Two-component flow model for convection in the earth's upper mantle. *Nature* **220**, 350-352.

Frey F. A., Bryan W. B. and Thompson G. (1974) Atlantic Ocean floor: Geochemistry and petrology of basalts from Legs 2 and 3 of the Deep Sea Drilling Project. *J. Geophys. Res.* **79**, 5507-5527.

Frey F. A., Suen C. J. and Stockman H. W. (1985) The Ronda high-temperature peridotite: geochemistry and petrogenesis. *Geochim. Cosmochim. Acta* **49**, 2469-2491.

Ghiorso M. S. (1994) Algorithms for the estimation of phase stability in heterogeneous thermodynamic systems. *Geochim. Cosmochim. Acta* **58**, 5489-5501.

Ghiorso M. S., Hirschmann M. M. and Sack R. O. (1994) New software models thermodynamic models of magmatic systems. *EOS Trans. AGU* **75**, 571-576.

Ghiorso M. S. and Sack R. O. (1995) Chemical mass transfer in magmatic processes IV. A revised and internally consistent thermodynamic model for the interpolation and extrapolation of liquid-solid equilibria in magmatic systems at elevated temperatures and pressures. *Contrib. Mineral. Petrol.* **119**, 197-212.

Goodwin A. M. (1977) Archean volcanism in the Superior province, Canadian shield. *Geol. Assoc. Can. Spec. Paper* **16**, 205-241.

Green D. H. and Ringwood A. E. (1970) Mineralogy of peridotitic compositions under upper mantle conditions. *Phys. Earth. Planet. Interiors* **3**, 359-371.

Grove T. L., Kinzler R. J. and Bryan W. B. (1992) Fractionation of mid-ocean ridge basalt (MORB). In *Mantle Flow and Melt Generation at Mid-Ocean Ridges* (ed. J. Phipps Morgan et al.). pp. 281-310. Am. Geophys. Union Geophys. Monogr. **71**.

Hart S. R. (1993) Equilibration during mantle melting: A fractal tree model. *Proc. Natl. Acad. Sci.* **90**, 11914-11918.

Hart S. R. and Zindler A. (1986) In search of a bulk-earth composition. *Chem. Geol.* **57**, 247-267.

Head J. W. (1976) Lunar volcanism in space and time. *Reviews of Geophysics and Space Physics* **14**, 265-300.

Head J. W., Crumpler L. S., Aubele J. C., Guest J. E. and Saunders R. S. (1992) Venus volcanism: Classification of volcanic features and structures, associations, and global distribution from Magellan data. *J. Geophys. Res.* **97**, 13153-13197.

Herzberg C., Feigenson M., Skuba C. and Ohtani E. (1988) Majorite fractionation recorded in the geochemistry of peridotites from South Africa. *Nature* **332**, 823-826.

Hess P. C. (1992) Phase equilibria constraints on the origin of ocean floor basalt. In *Mantle Flow and Melt Generation at Mid-Ocean Ridges* (ed. J. Phipps Morgan et al.). pp. 67-102. Geophys. Monogr. **71**. Am. Geophys. Union.

Hirose K. and Kawamura K. (1994) A new experimental approach for incremental batch melting of peridotite at 1.5 GPa. *Geophys. Res. Lett.* **21**, 2139-2142.

Hirschmann M. (1991) Thermodynamics of multicomponent olivines and the solution properties of $(Ni,Mg,Fe)_2SiO_4$ and $(Ca,Mg,Fe)_2SiO_4$ olivines. *Amer. Mineral.* **76**, 1232-1248.

Hirschmann M. M., Asimow P. D., Ghiorso M. S. and Stolper E. M. (1997b) Calculations of peridotite partial melting from thermodynamic models of minerals and melts. II. Applications to mantle melting, *in prep.*

Hirschmann M. M., Baker M. B. and Stolper E. M. (1997c) The effect of alkalis on the silica content of mantle-derived melts. *Geochim. Cosmochim. Acta* **submitted**.

Hirschmann M. M., Ghiorso M. S., Wasylenki L. E., Asimow P. D. and Stolper E. M. (1997a) Calculations of peridotite partial melting from thermodynamic models of minerals and melts. I. Methods and comparison to experiments, *in prep.*

Hirschmann M. M. and Stolper E. M. (1995) A possible role for garnet pyroxenite in the origin of the "garnet signature" in MORB.

Hirschmann M. M., Stolper E. M. and Ghiorso M. S. (1994) Perspectives on shallow mantle melting from thermodynamic calculations. *Min. Mag.* **58A**, 418-419.

Hirth G. and Kohlstedt D. L. (1996) Water in the oceanic upper mantle: Implications for rheology, melt extraction and the evolution of the lithosphere. *Earth Planet. Sci. Lett.* **144**, 93-108.

Ito K. and Kennedy G. C. (1967) Melting and phase relations in a natural peridotite to 40 kilobars. *American Journal of Science.* **265**, 519-538.

Iwamori H. (1994) ^{238}U-^{230}Th-^{226}Ra and ^{235}U-^{231}Pa disequilibria produced by mantle melting with porous and channel flows. *Earth Planet. Sci. Lett.* **125**, 1-16.

Iwamori H., McKenzie D. P. and Takahashi E. (1995) Melt generation by isentropic mantle upwelling. *Earth Planet. Sci. Lett.* **134**, 253-266.

Jaques A. L. and Green D. H. (1980) Anhydrous melting of peridotite at 0-15 kb pressure and the genesis of tholeiitic basalts. *Contrib. Mineral. Petrol.* **73**, 287-310.

Johnson K. T. M., Dick H. J. B. and Shimizu N. (1990) Melting in the oceanic upper mantle: An ion microprobe study of diopsides in abyssal peridotites. *J. Geophys. Res.* **95**, 2661-2678.

Kelemen P. B. (1990) Reaction between ultramafic rock and fractionating basaltic magma I. Phase relations, the origin of calc-alkaline magma series, and the formation of discordant dunite. *J. Petrol.* **31**, 51-98.

Kelemen P. B. and Dick H. J. B. (1995) Focused melt flow and localized deformation in the upper mantle: juxtaposition of replacive dunite and ductile shear zones in the Josephine peridotite, SW Oregon. *J. Geophys. Res.* **100**, 423-438.

Kelemen P. B., Dick H. J. B. and Quick J. E. (1992) Formation of harzburgite by pervasive melt/rock reaction in the upper mantle. *Nature* **358**, 635-641.

Kelemen P. B. and Ghiorso M. S. (1986) Assimilation of peridotite in zoned calc-alkaline plutonic complexes: evidence from the Big Jim complex, Washington Cascades. *Contrib. Mineral. Petrol.* **94**, 12-28.

Kelemen P. B., Hirth G., Shimizu N., Spiegelman M. and Dick H. J. B. (1997) A review of melt migration processes in the adiabatically upwelling mantle beneath oceanic spreading ridges. *Phil. Trans. Royal Soc. London A* **355**, 283-318.

Kelemen P. B., Shimizu N. and Salters V. J. M. (1995a) Extraction of MORB from the mantle by focused flow of melt in dunite channels.

Kelemen P. B., Whitehead J. A., Aharonov E. and Jordahl K. A. (1995b) Experiments on flow focusing in soluble porous media, with applications to melt extraction from the mantle.

Kinzler R. J. (1997) Melting of mantle peridotite at pressures approaching the spinel to garnet transition: Application to mid-ocean ridge basalt petrogenesis. *J. Geophys. Res.* **102**, 853-874.

Kinzler R. J. and Grove T. L. (1992a) Primary magmas of mid-ocean ridge basalts 1. Experiments and Methods. *J. Geophys. Res.* **97**, 6885-6906.

Kinzler R. J. and Grove T. L. (1992b) Primary magmas of mid-ocean ridge basalts 2. Applications. *J. Geophys. Res.* **97**, 6907-6926.

Kinzler R. J., Niu Y.-L. and Langmuir C. II. (1993) Modal mineralogy and composition of abyssal peridotites: problems and solutions. *EOS Trans. AGU* **74**, 623.

Klein E. M. and Langmuir C. H. (1987) Global correlations of ocean ridge basalt chemistry with axial depth and crustal thickness. *J. Geophys. Res.* **92**, 8089-8115.

Klein E. M. and Langmuir C. H. (1989) Local versus global variations in ocean ridge basalt composition: A reply. *J. Geophys. Res.* **94**, 4241-4252.

Kohlstedt D. (1991) Structure, rheology, and permeability of partially molten rocks at low melt fractions. In *Mantle Flow and Melt Generation at Mid-Ocean Ridges* (ed. J. Phipps Morgan et al.). pp. 103-122. Am. Geophys. Union, Geophys. Monogr. **71**.

Kress V. C. and Carmichael I. S. E. (1991) The compressibility of silicate liquids containing Fe_2O_3 and the effect of composition, temperature, oxygen fugacity and pressure on their redox states. *Contrib. Mineral. Petrol.* **108**, 82-92.

Kushiro I. (1972) Determination of liquidus relations in synthetic silicate systems with electron probe analyses: The system forsterite-diopside-silica at 1 atm. *Amer. Mineral.* **57**, 51-74.

Kushiro I. (1996) Partial melting of a fertile mantle peridotite at high pressure: and experimental study using aggregates of diamond. In *Earth Processes: Reading the*

isotopic clock (ed. A. Basu and S. Hart). pp. 109-122. Geophys. Monogr. **95**. Am. Geophys. Union.

Lange R. L. and Carmichael I. S. E. (1990) Thermodynamic properties of silicate liquids with emphasis on density, thermal expansion and compressibility. In *Modern Methods of Igneous Petrology: Understanding Magmatic Processes* (ed. J. Nicholls and J. K. Russell). pp. 25-64. Rev. Mineral. **24**. Mineralogical Society of America.

Langmuir C. H., Bender J. F., Bence A. E., Hanson G. N. and Taylor S. R. (1977) Petrogenesis of basalts from the FAMOUS area: Mid-Atlantic Ridge. *Earth Planet. Sci. Lett.* **36**, 133-156.

Langmuir C. H. and Hanson G. N. (1980) An evaluation of major element heterogeneity in the mantle sources of basalts. *Phil. Trans. Royal Soc. London A* **297**, 383-407.

Langmuir C. H., Klein E. M. and Plank T. (1992) Petrological systematics of mid-ocean ridge basalts: Constraints on melt generation beneath ocean ridges. In *Mantle Flow and Melt Generation at Mid-Ocean Ridges* (ed. J. Phipps Morgan et al.). pp. 183-280. Geophys. Monogr. **71**. Am. Geophys. Union.

Lawson C. L. and Hanson R. (1974) *Solving Least Squares Problems*. Prentice-Hall.

Longhi J. (1992) Origin of green glass magmas by polybaric fractional fusion. *Proc. Lunar Planet. Sci.* **22**, 343-353.

McKenzie D. P. (1984) The generation and compaction of partial melts. *J. Petrol.* **25**, 713-765.

McKenzie D. P. (1985) ^{230}Th-^{238}U disequilibrium and the melting process beneath ridge axes. *Earth Planet. Sci. Lett.* **72**, 149-157.

McKenzie D. P. and Bickle M. J. (1988) The volume and composition of melt generated by extension of the lithosphere. *J. Petrol.* **29**, 625-679.

McKenzie D. P. and Bickle M. J. (1990) A eutectic parameterization of mantle melting. *J. Phys. Earth* **38**, 511-515.

McKenzie D. P. and O'Nions R. K. (1991) Partial melt distributions from inversion of rare earth element concentrations. *J. Petrol.* **32**, 1021-1091.

McKenzie D. P. and O'Nions R. K. (1995) The source regions of ocean island basalts. *J. Petrol.* **36**, 133-159.

McSween H. (1994) What we have learned about Mars from SNC meteorites. *Meteoritics* **29**, 757-779.

Miller G. H., Stolper E. M. and Ahrens T. H. (1991) The equation of state of a molten komatiite, 2, Applications to komatiite petrogenesis and the Hadean mantle. *J. Geophys. Res.* **96**, 11849-11864.

Natland J. H. and Melson W. G. (1980) Compositions of basaltic glasses from the East Pacific Rise and Siqueiros fracture zone, near 9°N. *Init. Reports DSDP* **54**, 705-725.

Navon O. and Stolper E. M. (1987) Geochemical consequences of melt percolation - the upper mantle as a chromatographic column. *J. Geol.* **95**, 285-307.

Newman S., Finkel R. C. and MacDougall J. D. (1983) ^{230}Th-^{238}U disequilibrium systematics in oceanic tholeiites from 21 °N on the East Pacific Rise. *Earth Planet. Sci. Lett.* **65**, 17-33.

Nickel K. G. (1986) Phase equilibria in the system SiO_2-MgO-Al_2O_3-CaO-Cr_2O_3 (SMACCR) and their bearing on spinel/garnet lherzolite relationships. *N. Jb. Miner. Abh.* **155**, 259-287.

Niu Y.-L. and Batiza R. (1991) An empirical method for calculating melt compositions produced beneath mid-ocean ridges: application to axis and off-axis (seamounts) melting. *J. Geophys. Res.* **96**, 21,753-21,777.

Niu Y.-L. and Batiza R. (1993) Chemical variation trends at fast and slow spreading mid-ocean ridges. *J. Geophys. Res.* **98**, 7887-7902.

Niu Y.-L. and Hékinian R. (1997a) Spreading-rate dependence of the extent of melting beneath ocean ridges. *Nature* **385**, 326-329.

Niu Y.-L. and Hékinian R. (1997b) Basaltic liquids and harzburgitic residues in the Garrett Transform – A case study at fast-spreading ridges. *Earth Planet. Sci. Lett.* **146**, 243-258.

O'Hara M. J. (1968) Are ocean floor basalts primary magmas? *Nature* **220**, 683-686.

Papike J. J., Hodges F. N., Bence A. E., Cameron M. and Rhodes J. M. (1976) Mare basalts: crystal chemistry, mineralogy and petrology. *Reviews of Geophysics and Space Physics* **14**, 475-540.

Parmentier E. M. and Phipps Morgan J. (1990) Spreading rate dependence of three-dimensional structure in oceanic spreading centers. *Nature* **348**, 325-328.

Phipps Morgan J. (1987) Melt migration beneath mid-ocean ridge spreading centers. *Geophys. Res. Lett.* **14**, 1238-1241.

Phipps Morgan J. (1997) The generation of a compositional lithosphere by midocean ridge melting and its effect on subsequent off-axis hotspot upwelling and melting. *Earth Planet. Sci. Lett.* **146**, 213-232.

Phipps Morgan J. and Forsyth D. W. (1988) Three-dimensional flow and temperature perturbations due to a transform offset: Effects on oceanic crustal and upper mantle structure. *J. Geophys. Res.* **93**, 2955-2966.

Plank T. and Langmuir C. H. (1992) Effects of the melting regime on the composition of oceanic crust. *J. Geophys. Res.* **97**, 19749-19770.

Plank T., Spiegelman M., Langmuir C. H. and Forsyth D. W. (1995) The meaning of "mean F": Clarifying the mean extent of melting at ocean ridges. *J. Geophys. Res.* **100**, 15045-15052.

Presnall D. C. (1980) A double partial-melt zone beneath mid-ocean ridges. *Phys. Earth. Planet. Interiors* **23**, 103-111.

Presnall D. C., Dixon J. R., O'Donnell T. H. and Dixon S. A. (1979) Generation of mid-ocean ridge tholeiites. *J. Petrol.* **20**, 3-35.

Presnall D. C. and Hoover J. D. (1987) High pressure phase equilibrium constraints on the origin of mid-ocean ridge basalts. In *Magmatic processes: Physiochemical principles* (ed. B. O. Mysen). pp. Geochemical Society Special Publication **1**.

Press W. H., Teukolsky S. A., Vetterling W. T. and Flannery B. P. (1992) *Numerical Recipes in C: The Art of Scientific Computing; 2nd Edition.* Cambridge University Press.

Ramberg H. (1972) Mantle diapirism and its tectonic and magmagenic consequences. *Phys. Earth. Planet. Interiors* **5**, 45-60.

Reinitz I. and Turekian K. K. (1989) $^{230}Th/^{238}U$ and $^{226}Ra/^{230}Th$ fractionation in young basaltic glasses from the East Pacific Rise. *Earth Planet. Sci. Lett.* **94**, 199-207.

Rhodes J. M., Dungan M. A., Blanchard D. P. and Long P. E. (1979) Magma mixing at mid-ocean ridges: Evidence from basalts drilled near 22°N on the Mid-Atlantic Ridge. *Tectonophys.* **55**, 35-62.

Ribe N. M. (1985) The generation and composition of partial melts in the earth's mantle. *Earth Planet. Sci. Lett.* **73**, 361-376.

Richet P. and Bottinga Y. (1986) Thermochemical properties of silicate glasses and liquids: a review. *Reviews of Geophysics* **24**, 1-25.

Richter F. M. (1986) Simple models for trace element fractionation during melt segregation. *Earth Planet. Sci. Lett.* **77**, 333-344.

Richter F. M. and McKenzie D. P. (1984) Dynamical models for melt segregation from a deformable matrix. *J. Geol.* **92**, 729-740.

Rigden S. M., Ahrens T. J. and Stolper E. M. (1989) High-pressure equation of state of molten anorthite and diopside. *J. Geophys. Res.* **94**, 9508-9522.

Riley G. N. and Kohlstedt D. L. (1990) An experimental study of melt migration in an olivine-melt system. In *Magma transport and storage* (ed. M. Ryan). pp. 77-86. Wiley.

Rudnick R. (1995) Making continental crust. *Nature* **378**, 571-578.

Rumble D. (1976) The adiabatic gradient and adiabatic compressibility. *Carn. Inst. Wash. Yb.* **75**, 651-655.

Sack R. O. and Ghiorso M. S. (1989) Importance of considerations of mixing properties in establishing an internally consistent thermodynamic database: Thermochemistry of minerals in the system Mg_2SiO_4-Fe_2SiO_4-SiO_2. *Contrib. Mineral. Petrol.* **102**, 41-68.

Sack R. O. and Ghiorso M. S. (1991a) Chromian spinels as petrogenetic indicators: Thermodynamics and petrological applications. *Amer. Mineral.* **76**, 827-847.

Sack R. O. and Ghiorso M. S. (1991b) An internally consistent model for the thermodynamic properties of Fe-Mg titanomagnetite-aluminate spinels. *Contrib. Mineral. Petrol.* **106**, 474-505.

Sack R. O. and Ghiorso M. S. (1994a) Thermodynamics of multicomponent pyroxenes: I. Formulation of a general model. *Contrib. Mineral. Petrol.* **116**, 277-286.

Sack R. O. and Ghiorso M. S. (1994b) Thermodynamics of multicomponent pyroxenes: II. Phase relations in the quadrilateral. *Contrib. Mineral. Petrol.* **116**, 287-300.

Sack R. O. and Ghiorso M. S. (1995) Thermodynamics of multicomponent pyroxenes: III. Calibration of $Fe^{2+}(Mg)_{-1}$, $TiAl(MgSi)_{-1}$, $TiFe^{3+}(MgSi)_{-1}$, $AlFe^{3+}(MgSi)_{-1}$, $NaAl(CaMg)_{-1}$, $Al_2(MgSi)_{-1}$ and $Ca(Mg)_{-1}$ exchange reactions between pyroxenes and silicate melts. *Contrib. Mineral. Petrol.* **118**, 271-296.

Salters V. J. M. and Hart S. R. (1989) The hafnium paradox and the role of garnet in the source of mid-oceanic-ridge basalts. *Nature* **342**, 420-422.

Scott D. R. and Stevenson D. J. (1984) Magma solitons. *Geophys. Res. Lett.* **11**, 1161-1164.

Scott D. R. and Stevenson D. J. (1989) A self-consistent model of melting, magma migration and buoyancy-driven circulation beneath mid-ocean ridges. *J. Geophys. Res.* **94**, 2973-2988.

Shen Y. and Forsyth D. W. (1995) Geochemical constraints on initial and final depths of melting beneath mid-ocean ridges. *J. Geophys. Res.* **100**, 2211-2237.

Sleep N. H. (1988) Tapping of melt by veins and dikes. *J. Geophys. Res.* **93**, 10255-10272.

Solomatov V. S. and Stevenson D. J. (1994) Can sharp seismic discontinuities be caused by non-equilibrium phase transformations? *Earth Planet. Sci. Lett.* **125**, 267-279.

Sparks D. W. and Parmentier E. M. (1991) Melt extraction from the mantle beneath spreading centers. *Earth Planet. Sci. Lett.* **105**, 368-378.

Sparks D. W. and Parmentier E. M. (1993) The structure of three-dimensional convection beneath oceanic spreading centers. *Geophysical Journal International* **112**, 81-91.

Spiegelman M. (1990) Focusing on freezing: a new mechanism for lateral melt migration at mid-ocean ridges. *EOS Trans. AGU* **71**, 1849.

Spiegelman M. (1991) 2-D or not 2-D: Understanding melt migration near a sloping, freezing boundary. *EOS Trans. AGU* **72**, 265.

Spiegelman M. (1993a) Flow in deformable porous media. Part I Simple analysis. *J. Fluid Mech.* **247**, 17-38.

Spiegelman M. (1993b) Flow in deformable porous media. Part 2: Numerical analysis -- the relationship between shock waves and solitary waves. *J. Fluid Mech.* **247**, 39-63.

Spiegelman M. (1996) Geochemical consequences of melt transport in 2-D: The sensitivity of trace elements to mantle dynamics. *Earth Planet. Sci. Lett.* **139**, 115-132.

Spiegelman M. and Elliott T. (1993) Consequences of melt transport for uranium series disequilibrium in young lavas. *Earth Planet. Sci. Lett.* **118**, 1-20.

Spiegelman M. and Kenyon P. (1992) The requirements for chemical disequilibrium during magma migration. *Earth Planet. Sci. Lett.* **109**, 611-620.

Spiegelman M. and McKenzie D. (1987) Simple 2-D models for melt extraction at mid-ocean ridges and island arcs. *Earth Planet. Sci. Lett.* **83**, 137-152.

Stebbins J. F., Carmichael I. S. E. and Weill D. J. (1983) The high-temperature liquid and glass heat contents and heats of fusion of diopside, albite, sanidine, and nepheline. *Amer. Mineral.* **68**, 717-730.

Stevenson D. J. (1989) Spontaneous small-scale melt segregation in partial melts undergoing deformation. *Geophys. Res. Lett.* **16**, 1067-1070.

Stevenson D. J. and Scott D. R. (1991) Mechanics of fluid-rock systems. *Annual Reviews of Fluid Mechanics* **23**, 305-339.

Stolper E. M. (1980) A phase diagram for mid-ocean ridge basalts. *Contrib. Mineral. Petrol.* **74**, 13-27.

Stolper E. M., McSween H. Y. and Hays J. F. (1979) A petrogenetic model of the relationships among achondritic meteorites. *Geochim. Cosmochim. Acta* **43**, 589-602.

Takahashi E. (1986) Melting of a dry peridotite KLB-1 up to 14 GPa: Implications on the origin of peridotitic upper mantle. *J. Geophys. Res.* **91**, 9367-9380.

Takahashi E. and Kushiro I. (1983) Melting of a dry peridotite at high pressures and basalt magma genesis. *Amer. Mineral.* **68**, 859-879.

Takahashi N. (1992) Evidence for melt segregation towards fractures in the Horoman mantle peridotite complex. *Nature* **359**, 52-55.

Takazawa E., Frey F. A., Shimizu N., Obata M. and Bodinier J. L. (1992) Geochemical evidence for melt migration and reaction in the upper mantle. *Nature* **359**, 55-58.

Toulmin P., Baird A. K., Clark B. C., Keil K., Jr. H. J. R., Christian R. P., Evans P. H. and Kelleher W. C. (1977) Geochemical and mineralogical interpretation of the Viking inorganic chemical results. *J. Geophys. Res.* **82**, 4625-4634.

Turcotte D. L. and Ahern J. L. (1978) A porous flow model for magma migration in the asthenosphere. *J. Geophys. Res.* **83**, 767-772.

Verhoogen J. (1965) Phase changes and convection in the Earth's mantle. *Phil. Trans. Royal Soc. London A* **258**, 276-283.

von Bargen N. and Waff H. S. (1986) Permeabilities, interfacial areas and curvatures of partially molten systems: results of numerical computations of equilibrium microstructures. *J. Geophys. Res.* **91**, 9261-9276.

Waff H. S. and Bulau J. R. (1979) Equilibrium fluid distribution in an ultramafic partial melt under hydrostatic stress conditions. *J. Geophys. Res.* **84**, 6109-6114.

Wasylenki L. E., Baker M. B., Hirschmann M. M. and Stolper E. M. (1996) The effect of source depletion on equilibrium mantle melting. *EOS Trans. AGU* **77**, F847.

Watson S. and McKenzie D. P. (1991) Melt generation by plumes: A study of Hawaiian volcanism. *J. Petrol.* **32**, 501-537.

Weaver J. and Langmuir C. H. (1990) Calculation of phase equilibrium in mineral-melt systems. *Computers and Geosciences* **16**, 1-19.

White R. S., McKenzie D. P. and O'Nions R. K. (1992) Oceanic crustal thickness from seismic measurements and rare earth element inversions. *J. Geophys. Res.* **97**, 19683-19715.

White R. S. and McKenzie D. P. (1989) Magmatism at rift zones: the generation of volcanic continental margins and flood basalts. *J. Geophys. Res.* **94**, 7685-7729.

White R. S. and McKenzie D. P. (1995) Mantle plumes and flood basalts. *J. Geophys. Res.* **100**, 17543-17585.

Wyllie P. J. (1988) Solidus curves, mantle plumes, and magma generation beneath Hawaii. *J. Geophys. Res.* **93**, 4171-4181.

Yoder H. S. (1976) *Generation of Basaltic Magma*. National Academy of Sciences.

Appendix 1. New algorithms for subsolidus calculations

A previously published set of algorithms, MELTS, for finding equilibrium in multicomponent magmatic systems (Ghiorso, 1994; Ghiorso and Sack, 1995) needed extensions in order to function in the subsolidus regime. Methods are presented for (1) selecting an initial guess assemblage that satisfies the bulk composition constraints, (2) detecting saturation of new phases (including liquid) in an assemblage, (3) adding and removing phases from the assemblage without adjusting the bulk composition, and (4) constraining the assemblage to a fixed fugacity of oxygen. These methods have been added to the MELTS software, allowing it to calculate heterogeneous phase equilibria with or without liquid, closed or open to oxygen, and with fixed intensive variables (P,T), (P,S), (P,H), or (V,T). Applications include fractional melting calculations, metamorphic phase equilibria, and geophysical models of subsolidus regions of the earth.

The basic mathematical problem solved by MELTS is to find the equilibrium assemblage of phases by minimizing the appropriate energy potential, subject to constraints on bulk composition; pressure or volume; temperature, enthalpy or entropy; and optionally oxygen fugacity. The liquid phase serves several special functions in MELTS as implemented in version 2.0.x and earlier by Ghiorso and Sack (1995). These functions need to be replaced with more general implementations in order for the algorithm to function without a liquid phase. The liquid has the special property of unlimited freedom of compositional variation within the space spanned by its components. Hence an *ex nihilo* initial guess assemblage that satisfies the bulk composition constraints is always available by attributing the entire assemblage to liquid. Likewise, the compositional freedom of the liquid phase makes it an ideal reservoir phase for adding or removing small amounts of any component in order to add or remove other phases from the assemblage without adjusting the bulk composition. Since in MELTS 2.0.x the number of liquid components is equal to the number of system components, the

chemical potential of any system component can be obtained by a simple algebraic transformation from the chemical potential of the liquid components. The chemical potentials of the system components, in turn, are needed to detect saturation of new phases and determine whether to add them to the assemblage. Finally, the fugacity of oxygen is determined, and for open systems buffered, using a parameterization of the Fe^{3+}/Fe^{2+} ratio in the liquid phase. Below I discuss general replacements for all these special functions of the liquid.

1. Initial guess

Finding an initial guess that satisfies the constraints is often the most difficult part of a multidimensional constrained minimization procedure. The constraints in this case are (1) that the total amount of each oxide (or system component) in the system must equal the quantity of that oxide (or system component) in the prescribed bulk composition and (2) that all phases be within their allowable range of stoichiometry. In the magmatic case, unless a previous solution is available, one can always take as an initial guess that the entire system consists of liquid (Ghiorso, 1994). Bulk compositions are then limited to those within the space of liquid compositions where the liquid solution model functions. Stoichiometric constraints on solids are typically much more rigorous, and only in special cases is it feasible to assign the bulk composition to a single solid phase. Hence a method is needed for deriving initial guess mineral assemblages where all minerals are legal and the total composition is known. I suggest two methods -- a norm calculation and a liquid initial guess. The former is more efficient, the latter is more general.

The problem of assigning a bulk composition in oxide weight percent to a set of mineral components is a familiar one to petrologists. The CIPW norm calculation (Cross et al., 1902) is the best known, but a similar procedure can be defined for any set of phases and phase components (e.g., Currie, 1991), and a range of composition space

bounded at least by these end members. At the end of this Appendix, I give a set of rules which can partition any peridotitic and many basaltic compositions into two pyroxenes ((Ca, Mg, Fe^{2+}, Fe^{3+}, Na)^{M1}(Mg, Fe^{2+}, Fe^{3+}, Al)^{M2}(Si, Ti, Al)$_2{}^{Tet}O_6$), olivine ((Mg, Fe, Ca, Ni, Co, Mn)$_2SiO_4$) or quartz, and between one and three of feldspar ((Na, K)$AlSi_3O_8$-$CaAl_2Si_2O_8$), garnet ((Ca, Mg, Fe^{2+})$_3Al_2Si_3O_{12}$), and spinel ((Mg, Fe^{2+})(Fe^{3+}, Cr, Al)$_2O_4$-Fe_2TiO_4) at the user's discretion. The phase components involved are those used by MELTS for these phases. The initial guess produced by a norm calculation can be tailored to include the phases that are stable at equilibrium if known; this saves considerable computation time. In general, however, it simply produces an entry point to a minimization algorithm that must be further equipped with the means to add and drop phases as needed.

When the composition is outside the range anticipated by available norm calculations it is best to use a completely molten system as the initial guess. When the equilibrium assemblage is totally unknown this may be more efficient than a norm initial guess using minerals that will subsequently have to be dropped. It is also likely to be more efficient than any mathematical procedure for assigning initial guesses that lacks petrological insight. Constrained minimization proceeds according the method used in MELTS (Ghiorso and Sack, 1995), adding saturated phases one at a time, until the liquid is exhausted. At this point, assuming a method is available to partition the mass contained in the last, trivial batch of liquid into the available solids (see below), one arrives at an assemblage of solid phases that meets the bulk composition and phase stoichiometry constraints. This is a valid initial guess for further minimization in the subsolidus. It often produces an assemblage quite close to the equilibrium assemblage. Note that this procedure can be applied with some confidence at quite low temperatures, as long as the liquid solution model does not behave pathologically when extrapolated below the calibrated range of temperature.

It is possible to define general algorithmic procedures for assigning bulk compositions to solid phases, but without the application of petrologic constraints, such a method will not produce an initial guess as useful as either of the above procedures.

2. Detecting phase saturation

Ghiorso (1994) describes a method for detecting saturation of single or multicomponent, ideal or non-ideal solids with respect to a liquid phase able to dissolve all the components present in the solid. This method uses the chemical potentials of the liquid components as a reference for the solids to be tested. It is straightforward to extend the method to any solid assemblage on the condition that this assemblage is in (at least metastable) heterogeneous equilibrium. Hence we require the potential minimization step of the equilibrium-seeking procedure to reach convergence with the initial solid assemblage before we can test for the saturation of additional phases. In practice this is not a significant difficulty.

We require the chemical potential of each of *nc* system components in the solid assemblage. Let the solid assemblage contain *m* phase components (when two or more phases of the same mineral coexist, its components need only be counted once in this procedure). The requirement that the assemblage be in heterogeneous equilibrium translates into a requirement that the chemical potentials of the system components are well-defined. These chemical potentials are obtained from the solution of an over-constrained but consistent least squares problem (if each system component is present in exactly one solid, then the matrix of the least squares problem is square). Let the vector μ_{sol} of length *m* contain the chemical potentials of the *m* solid phase components present in the assemblage, obtained from their respective standard-state properties and activity-composition models. Construct the *m* by *nc* matrix $\mathbf{T}_{sys}$ whose rows contain the stoichiometric coefficients which transform the phase components (in the same order as

the elements of μ_{sol}) into the system components. The vector of chemical potentials of system components μ_{sys} is obtained by solving

$$\mathbf{T}_{sys}\mu_{sys} = \mu_{sol}. \tag{1}$$

Although this system is generally over-constrained, it has a unique exact solution if the conditions of heterogeneous equilibrium are exactly satisfied. The solution is obtained from the Singular Value Decomposition of $\mathbf{T}_{sys}$ (Press et al., 1992)[1]. To clarify the definitions above, consider a simple example: in the system MgO-FeO-SiO_2 (m=3) let us allow the phases olivine, pyroxene, and quartz with the nc=5 phase components Mg_2SiO_4, Fe_2SiO_4, $MgSiO_3$, $FeSiO_3$, and SiO_2. Then (1) for this example reduces to

$$\begin{bmatrix} 2 & 0 & 1 \\ 0 & 2 & 1 \\ 1 & 0 & 1 \\ 0 & 1 & 1 \\ 0 & 0 & 1 \end{bmatrix} \begin{bmatrix} \mu_{MgO} \\ \mu_{FeO} \\ \mu_{SiO_2} \end{bmatrix} = \begin{bmatrix} \mu^{Olivine}_{Mg_2SiO_4} \\ \mu^{Olivine}_{Fe_2SiO_4} \\ \mu^{Pyroxene}_{MgSiO_3} \\ \mu^{Pyroxene}_{FeSiO_3} \\ \mu^{Quartz}_{SiO_2} \end{bmatrix}. \tag{2}$$

If μ_{sys} is further transformed into the chemical potentials of nc liquid components μ_{liq}, a fictive liquid is then sufficiently characterized to use the saturation algorithm of Ghiorso (1994) without further modification. Indeed, this method can be used as presented to detect the saturation of non-ideal liquids with respect to subsolidus assemblages.

---

[1] Several of the algorithms herein use the Singular Value Decomposition (SVD). To briefly review its properties: there exists for any matrix **A**, square or rectangular, a decomposition $\mathbf{A} = \mathbf{U}.\text{diag}[\mathbf{w}].\mathbf{V}^T$, where if **A** is n x m, **U** is n x m and row-orthonormal, **w** is an n-vector containing the singular values and diag[**w**] is a square matrix with **w** on the main diagonal and zero elsewhere, and $\mathbf{V}^T$ is an n x n row- and column-orthonormal matrix. If **A** is square or n >m, any elements of **w** equal to zero indicate that A is singular. If n < m, there will be at least m-n zero elements of **w**; any additional zero elements indicate that **A** is singular. The pseudoinverse of **A**, $\mathbf{A}^+$ (where $\mathbf{A}^+.\ \mathbf{A} = \mathbf{I}_m$) can always be constructed from $\mathbf{A}^+ = \mathbf{V}.\text{diag}[1/\mathbf{w}].\mathbf{U}^T$, where the reciprocal of zero or nearly zero elements of **w** is taken to be zero (!). Solving systems $\mathbf{A}.\mathbf{x} = \mathbf{b}$ by taking $\mathbf{x} = \mathbf{A}^+.\mathbf{b}$ yields the exact solution vector **x** when **A** is square and nonsingular. When the system is overconstrained (n > m) or if **A** is singular and **b** is not in the rangespace of **A**, the vector **x** is that which minimizes $\|\mathbf{Ax} - \mathbf{b}\|_2$. When the system is underconstrained (n < m) or if **A** is singular and **b** is in the rangespace of **A**, the vector **x** is the particular member of the family of solutions such that $\|\mathbf{x}\|_2$ is minimized, and the columns of **V** corresponding to zero singular values form an orthonormal basis for the nullspace, i.e., they can be added to the particular solution **x** in any linear combination to produce a feasible solution vector. For full discussions, see Lawson and Hanson (1974) and Press (1992).

3. Adding and removing phases

In the implementation of Ghiorso and Sack (1995), when a saturated phase is recognized or a phase exsolution is required, a trivial mass of the new phase is added by subtracting from the liquid the needed mass of each liquid component in order to make up the desired solid composition. Similarly, when during the course of potential minimization the mass of a solid drops to a (smaller) trivial level, it is removed by adding the appropriate amount of each component to the liquid to conserve bulk composition. The compositional freedom of the liquid makes this procedure trivial in both cases. When liquid is absent, however, more care is required. Two methods present themselves: allowing negligible changes in the bulk composition, and the procedure described below. If the mass of phases added or dropped is sufficiently small, the change in bulk composition implied by simply adding or removing the components contained in the solid from the bulk may be negligible. When performing calculations near a phase boundary, however, the unpredictability and path-dependence of this procedure may be unacceptable. We prefer to find a method which exactly satisfies the original bulk composition constraints.

The procedure is essentially a general method for assigning a bulk composition to phase components, but as the masses involved represent small perturbations to an assemblage already near (metastable) equilibrium, the lack of petrological insight in the solution is not a disadvantage. We begin by transforming the composition of phase j to be added or dropped, represented by the signed number of moles of its phase components (positive if the phase is being added, negative if it is being dropped) as a vector $\mathbf{m}_j$ of length na_j into the nc system components using the nc x na_j stoichiometry matrix $\mathbf{T}_j$:

$$\delta\mathbf{m}_{sys} = \mathbf{T}_j \cdot \mathbf{m}_j \,. \tag{3}$$

Let us say that the remaining assemblage after phase j is dropped or the preexisting assemblage to which phase j is to be added contains n_{sol} phase components (here we count coexisting phases of the same mineral as independent phase components in order to

minimize the perturbation). We seek a vector $\delta\mathbf{m}_{sol}$ of perturbations to the number of moles of each phase in the assemblage which adds up to the desired change in the system components. If $\mathbf{T}_{sol}$ is the nc x n_{sol} stoichiometry matrix which transforms the system components of the assemblage to the set of phase components to be perturbed ($\mathbf{T}_{sol} = \mathbf{T}_{sys}^{T}$), the problem is expressed by the system

$$\mathbf{T}_{sol} \cdot \delta\mathbf{m}_{sol} = \delta\mathbf{m}_{sys}, \tag{4}$$

which is, in general, underconstrained, i.e., there is an (n_{sol} - nc) dimensional space of solutions all of which satisfy the constraints. Solution of this system by SVD will produce the solution vector $\delta\mathbf{m}_{sol}$ which has the smallest 2-norm (i.e., the member of the solution family with minimum $(\delta\mathbf{m}_{sol}^{T} \cdot \delta\mathbf{m}_{sol})^{1/2}$). It is possible to take advantage of this property to choose instead the solution which least perturbs the assemblage. The smallest relative perturbation to the assemblage is obtained by taking as much mass as possible from the phase components most abundant in the assemblage and as little mass as possible from the least abundant phase components. The SVD can be forced to choose this solution by weighting the rows of $\mathbf{T}_{sol}$ as follows: let $\mathbf{m}_{sol}$ be the vector of total abundances of the n_{sol} phase components in the assemblage to be perturbed, and denote the n_{sol} x n_{sol} diagonal matrix with $\mathbf{m}_{sol}$ on the main diagonal and zeros elsewhere as $\mathbf{M}_{sol}$. Since the matrix is diagonal, its inverse is simply the diagonal matrix with the reciprocal of each element of $\mathbf{m}_{sol}$ along its main diagonal. Then we have

$$[\mathbf{T}_{sol} \cdot \mathbf{M}_{sol}] \cdot [\mathbf{M}_{sol}^{-1} \cdot \delta\mathbf{m}_{sol}] = \delta\mathbf{m}_{sys}, \tag{5}$$

which we solve by obtaining the SVD of $[\mathbf{T}_{sol} \cdot \mathbf{M}_{sol}]$, which yields on backsubstitution the particular solution $[\mathbf{M}_{sol}^{-1} \cdot \delta\mathbf{m}_{sol}]$ with the smallest 2-norm. The least-squares constraint on the particular solution thereby acts most strongly on the elements of this vector which have been weighted to large values by dividing by small elements of $\mathbf{m}_{sol}$. The desired solution is then obtained simply by premultiplying the particular solution by $\mathbf{M}_{sol}$, which recovers the desired solution vector $\delta\mathbf{m}_{sol}$.

Even though this method is intended to make small perturbations to the assemblage, it is possible for it to fail by overstepping the stoichiometry limits on one or more phases. Should this occur, the calculation can always be resumed by returning to the initial guess methods documented above.

4. Measuring and buffering fO_2

The algorithms of Ghiorso and Sack (1995) use the parameterization of Kress and Carmichael (1991) for Fe^{3+}/Fe^{2+} in silicate liquids as a function of composition, temperature, pressure, and fO_2 (i.e., the fugacity of oxygen) to (1) obtain fO_2 and its first and second derivatives with respect to all the intensive parameters in any liquid composition at any P and T, and (2) to constrain the liquid to a fixed fO_2 (i.e., to buffer the assemblage). In the absence of a liquid, a more direct method is required. For particular mineral assemblages, this is straightforward; the challenge is to find a general method that works for any Fe^{3+} and Fe^{2+} bearing mineral assemblage. Let us first consider the case of a spinel, olivine, and pyroxene bearing assemblage. We can then write a balanced redox reaction:

$$6\ Fe_2SiO_4^{ol} + 6\ CaMgSi_2O_6^{px} + O_2 = 2\ Fe_3O_4^{sp} + 6\ CaFeSi_2O_6^{px} + 3\ Mg_2Si_2O_6^{px},$$

which can be expressed

$$\sum_{i=1}^{6} n_i m_i = 0, \tag{6}$$

where i=1 refers to oxygen, n_i are stoichiometric coefficients (negative for reactants, positive for products), and m_i are molar quantities of the reactant and product phase components. The reaction is characterized by the equilibrium constant

$$K = \frac{(a_{Mt}^{sp})^2\,(a_{Hd}^{px})^6\,(a_{En}^{px})^3}{(a_{Fa}^{ol})^6\,(a_{Di}^{px})^6\,fO_2} = \exp(-\Delta G^o/RT), \tag{7}$$

where a is activity, R the gas constant, T the absolute temperature, and ΔG^o the standard-state Gibbs free energy of reaction. Hence at equilibrium,

$$RT\ln fO_2 = \Delta G^o + RT\ln\left(\frac{(a^{sp}_{Mt})^2\,(a^{px}_{Hd})^6\,(a^{px}_{En})^3}{(a^{ol}_{Fa})^6\,(a^{px}_{Di})^6}\right) \tag{8}$$

or more generally

$$RT\ln fO_2 = \sum_{i=1}^{6} n_i\, g^o{}_i + RT\sum_{i=2}^{6} n_i \ln a_i \tag{9}$$

where $g^o{}_i$ is the standard-state molar free energy of phase component i, a_i is the activity of phase component i in the appropriate phase, and the sum over activities excludes oxygen (i=1). All the derivatives of fO_2 with respect to intensive variables can be obtained from this expression. Buffering the system to a prescribed fO_2 simply requires forcing the reaction towards or away from oxygen until the activities of the components change so as to yield the correct fO_2.

Now a technique is required for finding a balanced redox reaction among the m phase components actually present in the assemblage plus O_2; once such a reaction is found, the procedure for calculating fO_2 is identical to that for the spinel-pyroxene-olivine oxybarometer above. We proceed as follows: construct a right-hand-side vector $\delta\mathbf{m}^*_{sys}$ of length $nc+1$ representing the net change in moles of oxygen and system components effected by the desired reaction, and set the values equal to the stoichiometry of the simplest redox reaction possible amongst the system components and oxygen. If the system components are oxides, for example, we use the reaction

$$4\,FeO + O_2 = 2\,Fe_2O_3, \tag{10}$$

resulting in $\delta\mathbf{m}^*{}_{sys}{}^T = \{-1,0,0,0,0,2,-4,0,0,0\}$, for example, for adding O_2 to the system SiO_2-TiO_2-Al_2O_3-Cr_2O_3-Fe_2O_3-FeO-MgO-CaO-Na_2O. Note that the first position in $\delta\mathbf{m}^*_{sys}$ represents the stoichiometric coefficient for O_2; the rest of the vector indexes the system components in their usual order. Next we construct the $(nc+1)$ x $(m+1)$ matrix $\mathbf{T}^*_{sol}$ which converts the system components plus O_2 to all the solid phase components present in the assemblage plus phase O_2(g). Hence if we make O_2 the first phase and the first component

$$\mathbf{T}^*_{sol} = \begin{bmatrix} 1 & 0 & \dots & 0 \\ 0 & & & \\ \vdots & & \mathbf{T}_{sol} & \\ 0 & & & \end{bmatrix}. \qquad (11)$$

Then any solution vector $\mathbf{n}^*_{sol}$ satisfying

$$\mathbf{T}^*_{sol} \cdot \mathbf{n}^*_{sol} = \delta\mathbf{m}^*_{sys} \qquad (12)$$

is a balanced redox reaction which adds one mole of O_2 to the system while converting four moles of Fe^{2+} into Fe^{3+}. This system is underconstrained, but we have some grounds on which to choose amongst the feasible solutions. If, once again, we wish to find the reaction which minimizes the perturbation to the system required to introduce or remove a given quantity of oxygen, then, proceeding as above, we construct the diagonal weighting matrix $\mathbf{M}^*_{sol}$ and assign a large value to the first element, representing $O_2(g)$. Then we compute the SVD of $[\mathbf{T}^*_{sol} \cdot \mathbf{M}^*_{sol}]$, backsubstitute to obtain the weighted particular solution $[\mathbf{M}^{*-1}_{sol} \cdot \mathbf{n}^*_{sol}]$, and then recover the desired reaction stoichiometry $\mathbf{n}^*_{sol}$ by premultiplying by $\mathbf{M}^*_{sol}$. On the other hand, it may be desired for computational reasons to find the simplest reaction among the feasible solutions, e.g., that involving the fewest phase components. This may be obtained by constructing a matrix whose first column is the particular solution to the unweighted SVD problem and whose other columns form an orthonormal basis for the nullspace (e.g., those columns of V returned by the SVD $\mathbf{T}^*_{sol} = \mathbf{U}.\text{diag}[\mathbf{w}].\mathbf{V}^T$ that correspond to zeroes in $\mathbf{w}$), and performing a column-reduction to insert as many zeros as possible into the desired column.

Applications

These methods were developed with the intent of making fractional melting calculations more convenient. To model perfect fractional fusion, a series of steps are performed where an increment of melt is completely removed from the system. In the absence of the capacity to compute liquid-free assemblages, this requires either restarting from a liquid initial guess or leaving a small amount of melt behind. The former is very

time-consuming, since many phases must be added back after every extraction to reach the near-solidus region from liquid initial guesses. The latter is theoretically unsatisfying, since even a small amount of residual melt can influence the results (e.g., trace element fractionations involving highly incompatible elements). It is also dangerous, since from an infinitesimal amount of melt, the minimization algorithm may try to follow a path to the next equilibrium that would eliminate the melt temporarily.

With the four modifications detailed above, however, the MELTS equilibrium engine can be applied to range of solid-state equilibrium problems. Brown (1996), for example, used MELTS with my subsolidus extensions to calculate density and mineral assemblages (and hence, together with mineral physics data, seismic velocity) for tectonic and stable North American mantle lithosphere. Application of this method to a full range of crustal metamorphic problems will depend, however, on progress in models of mineral thermodynamics for a number of highly complex minerals. Phases such as staurolite, amphibole, chlorite, chloritoid, etc., have many end members and highly complex ordering phenomena that have not yet to my knowledge been adequately modeled.

The algorithms developed herein, together with those of Ghiorso (1994) and Ghiorso and Sack (1995), are capable of finding equilibrium at fixed (T, P, fO_2) as well as (S, P, fO_2), (H, P, fO_2), or (T, V, fO_2). This is not, however, the best way to calculate fO_2-buffered isentropic, isenthalpic, or isochoric equilibria. First, it is computationally extremely inefficient. More importantly, though, it is unclear what this calculation represents. Buffering of fO_2 requires adding or removing O_2 from the system at many steps. If we enforce constant S, for example, this implies that the O_2 entering or leaving the system is at absolute zero, since it carries no entropy. This will implicitly cool or heat the system. This is unlikely to correspond to any meaningful physical situation. Instead I recommend a two-stage procedure which alternates between (1) steps toward equilibrium at fixed (*S, P*) in a closed system and (2) buffering steps where O_2 is added or removed at the current temperature of the system and the reference entropy is adjusted accordingly.

A norm for subsolidus initial guesses to MELTS

A wide range of basalts and peridotites can be successfully assigned to a norm which utilizes two-pyroxenes, either olivine or quartz, and at least one aluminous mineral. The following procedure is customized to produce good initial guesses for peridotites in the system SiO2-TiO2-Al2O3±Cr2O3-Fe2O3-FeO±NiO-MgO±MnO± CoO-CaO-Na2O±K2O, using the following phase components:

olivine	fayalite	Fa	Fe_2SiO_4
	forsterite	Fo	Mg_2SiO_4
	monticellite	Mc	$CaMgSiO_4$
	tephroite	Tp	Mn_2SiO_4
	Ni-olivine	NiOl	Ni_2SiO_4
	Co-olivine	CoOl	Co_2SiO_4
clinopyroxene	cpx-diopside	CDi	$CaMgSi_2O_6$
	cpx-enstatite	CEn	$Mg_2Si_2O_6$
	cpx-hedenbergite	CHd	$CaFeSi_2O_6$
	cpx-aluminobuffoonite	CAbf	$CaMg_{0.5}Ti_{0.5}AlSiO_6$
	cpx-buffoonite	CBf	$CaMg_{0.5}Ti_{0.5}Fe^{3+}SiO_6$
	cpx-essenite	CEs	$CaFe^{3+}AlSiO_6$
	cpx-jadeite	CJd	$NaAlSi_2O_6$
orthopyroxene	opx-diopside	ODi	$CaMgSi_2O_6$
	opx-enstatite	OEn	$Mg_2Si_2O_6$
	opx-hedenbergite	OHd	$CaFeSi_2O_6$
	opx-aluminobuffoonite	OAbf	$CaMg_{0.5}Ti_{0.5}AlSiO_6$
	opx-buffoonite	OBf	$CaMg_{0.5}Ti_{0.5}Fe^{3+}SiO_6$
	opx-essenite	OEs	$CaFe^{3+}AlSiO_6$
	opx-jadeite	OJd	$NaAlSi_2O_6$
spinel	hercynite	Hc	$FeAl_2O_4$
	chromite	Cr	$FeCr_2O_4$
	spinel	Sp	$MgAl_2O_4$
	magnetite	Mt	Fe_3O_4
	ulvospinel	Uv	Fe_2TiO_4
garnet	pyrope	Py	$Mg_3Al_2Si_3O_{12}$
	almandine	Alm	$Fe_3Al_2Si_3O_{12}$
	grossular	Gr	$Ca_3Al_2Si_3O_{12}$
feldspar	albite	Ab	$NaAlSi_3O_8$
	anorthite	An	$CaAl_2Si_2O_8$
	sanidine	Sd	$KAlSi_3O_8$

Procedure:

Rule 0. Convert analysis in oxides or other system components to molar abundances of oxides in 100 grams of system; select from one to three aluminous phases (garnet, spinel, feldspar) to include; if Cr_2O_3 is present spinel is mandatory and if K_2O is included feldspar in mandatory. Decide whether olivine is likely to be needed; if MnO, NiO, or CoO is present, olivine is mandatory. Quartz will be added if necessary.

Rule 1 (Cr_2O_3, MnO, NiO, CoO).
Assign all Cr_2O_3 to Cr. Deduct Cr from FeO.
Assign all MnO to Tp (Tp = 0.5 * MnO). Deduct Tp from SiO_2.
Assign all NiO to NiOl (NiOl = 0.5 * NiO). Deduct NiOl from SiO_2.
Assign all CoO to CoOl (CoOl = 0.5 * CoO). Deduct CoOl from SiO_2.

Rule 2 (Na_2O, K_2O). If the system contains K_2O, feldspar must be included.
Assign all K_2O to Sd (Sd = 2*K_2O); deduct 0.5*Sd from Al_2O_3 and 3*Sd from SiO_2.
If feldspar is to be included:
Assign 0.9*Na_2O to Ab, leaving remainder for jadeite (Ab = 1.8*Na_2O); deduct 0.5*Ab from Al_2O_3 and 3*Ab from SiO_2.
Assign 0.66*Na_2O to CJd (CJd = 1.32*Na_2O); deduct 0.5*CJd from Al_2O_3 and 2*CJd from SiO_2.
Assign remaining Na_2O to OJd (OJd = 2.0*Na_2O); deduct 0.5*OJd from Al_2O_3 and 2*OJd from SiO_2.

Rule 3 (TiO_2, Fe_2O_3 in spinel). If spinel is to be included:
Assign 0.25*TiO_2 to Uv; deduct 2*Uv from FeO.
Assign 0.4*Fe_2O_3 to Mt; deduct Mt from FeO.

Rule 4 (Al_2O_3).
If spinel is to be included:
Assign 0.5*Al_2O_3 to Sp; deduct Sp from MgO.
IF (Mt + Cr + 2*Uv - 0.2*Al2O3 > 0) assign -0.2*Al_2O_3 to Hc (i.e. set Hc = -0.2*Al_2O_3, and Al_2O_3 = 1.2*Al_2O_3) and add -Hc to FeO.
ELSE set Hc = (0.001 - Mt - Cr - 2*Uv), add -Hc to Al_2O_3 and FeO.
If feldspar is to be included:
Assign 0.64*Al_2O_3 to An; deduct An from CaO and 2*An from SiO_2.
If garnet is to be included:
Assign 0.6*Al_2O_3 to TotalGt, a temporary variable.
Assign TotalGt*(2.0*FeO/(2.0*FeO+3.0*MgO+0.5*CaO)) to Alm; deduct 2*Alm from FeO.
Assign TotalGt*(3.0*MgO/(2.0*FeO+3.0*MgO+0.5*CaO)) to Py; deduct 2*Py from MgO.
Assign TotalGt*(0.5*CaO/(2.0*FeO+3.0*MgO+0.5*CaO)) to Gr; deduct 2*Gr from CaO.
Deduct TotalGt from Al_2O_3 and 3.0*TotalGt from SiO_2.

Rule 5 (TiO_2, Fe_2O_3, Al_2O_3). Perform all the following steps before deducting anything from TiO_2, Fe_2O_3, or Al_2O_3.

Set OAbf = $0.75*(Al_2O_3 + TiO_2 - Fe_2O_3)$.
Set CAbf = $0.25*(Al_2O_3 + TiO_2 - Fe_2O_3)$.
Set OBf = $0.75*(Fe_2O_3 + TiO_2 - Al_2O_3)$.
Set CBf = $0.25*(Fe_2O_3 + TiO_2 - Al_2O_3)$.
Set OEs = $0.75*(Fe_2O_3 + Al_2O_3 - TiO_2)$.
Set CEs = $0.25*(Fe_2O_3 + Al_2O_3 - TiO_2)$.
Deduct ($Al_2O_3 + TiO_2 + Fe_2O_3$) from CaO and SiO2.
Deduct TiO_2 from MgO.

Set TiO_2, Fe_2O_3, and Al_2O_3 equal to zero.

Rule 6 (CaO). Perform the following steps before modifying CaO:

Set CHd = 0.15*CaO. Deduct CHd from FeO and 2*CHd from SiO_2.
IF olivine is to be (provisionally) included, set OHd = CaO.
ELSE set OHd = FeO.
Set ODi = -1.05*OHd.

Deduct (CHd + OHd + ODi) from CaO.
Deduct ODi from MgO. Deduct OHd from FeO.
Deduct 2*(OHd + ODi) from SiO_2.
*IF olivine is to be (provisionally) included, set CDi = 0.833*CaO.*
ELSE set CDi = CaO.
Deduct CDi from CaO and MgO. Deduct 2*CDi from SiO_2.
IF (CaO < 0) the composition is infeasible. End in failure.
IF olivine is to be included, assign remaining CaO to Mc and deduct Mc from MgO and SiO_2.

Rule 7 (MgO, FeO, SiO_2).

IF olivine is to be included, assign remaining FeO to Fa (Fa = 0.5*FeO); deduct Fa from SiO_2.
IF (MgO > SiO_2) and olivine is to be included, set Fo = (MgO - SiO_2); deduct Fo from SiO_2 and 2*Fo from MgO.
Set OEn = 0.475*MgO; deduct 2*OEn from MgO and SiO_2.
Assign remaining MgO to CEn (CEn = 0.5*MgO). Deduct 2*CEn from SiO_2.
IF (SiO2 > 0), a silica excess exists. Add quartz to the assemblage and assign all remaining SiO_2 to quartz.
IF any oxide is not now equal to zero, the composition is infeasible. End in Defeat.
ELSE return successfully.

Appendix 2. Source code for computer programs

The computer codes in this section are all written in ANSI C and are known to compile and execute using Gnu C under SunOS 4.1.1 and IBM C under AIX 3.2.5. The modules (source code and include files) included in this appendix are listed in Table H-1 along with a brief summary of their purpose. These modules are not free-standing; they are intended to be used with the MELTS code version 3.0.x by Mark S. Ghiorso and Richard Sack. To replicate the calculations described in this thesis, interested persons must obtain the MELTS source code (not the publicly available executable) from Mark S. Ghiorso at the University of Washington. The symbols in Table H-2 are referenced in these codes but defined in MELTS 3.0.4.

Table H-1. Modules and functions included in this appendix

Table H-2. Symbols referenced in this appendix but defined in MELTS code

Symbol Name	Purpose
allocSilminStatePointer()	allocate memory to struct
copySilminStateStructure()	make a duplicate of state of system
checkForCoexistingSolids()	exsolution routine
addOrDropLiquid()	modify solids for change in bulk comp
getAffinityAndComposition()	test saturation of non-ideal solutions
gibbs()	standard-state properties of endmembers
InitComputeDataStruct()	molecular weights, conversion factors...
correctTforChangeInEnthalpy()	enforce isenthalpic constraint in advance
correctTforChangeInEntropy()	enforce isentropic constraint in advance
subsolidusmuO2()	for buffering when liquid is absent
silmin()	core subroutine to do an equilibration

Other functions listed in silmin.h below are called only within the MELTS code.

```
/*
**++
** FACILITY:  adiabat_1Sh: Silicate Melts batch path finder
**
**  MODULE DESCRIPTION:
**
**     Calculates isentropic, isothermal, or isobaric
**       equilibrium paths for according to SILMIN,
**       for fixed bulk composition.
**
**  MODIFICATION HISTORY:
**
**       V1.0-1       Paul D. Asimow  August 2, 1994
**       V1.0-2  Paul D. Asimow  August 15, 1994
**            As documented, with environment variables
**       V1.0-3  Paul D. Asimow  August 29, 1994
**            Begin using adiabat_support.c and adiabat.h
**            Add provision for MINP other than 1.0 atm.
**       V2.0-1  Paul D. Asimow November 11, 1994
**            uses isentropic silmin calculation
**       V3.0-1  Paul D. Asimow March 22, 1995
**            Integrated solid-only or solid+melt calculation
**       V3.1-1  Paul D. Asimow August 7, 1995
**            Added subsolidus fO2 buffering, if isentropic fO2
**            buffering is allowed
**       V4.1-0  Paul D. Asimow December 19, 1995
**            Allow changes in bulk composition and entropy calculated
**            to mimic melt focusing
**       V5.1-0  Paul D. Asimow May 1, 1996
**            Add isograd tracking function
**       V6.1-0  Paul D. Asimow  June 25, 1996
**            changes for Compatibility with Melts3
**--
*/

#include <math.h>
#include <stdio.h>
#include <stdlib.h>
#include <string.h>
#include <malloc.h>

#include "interface.h"
#include "silmin.h"
#include "search_limits.h"
#include "adiabat.h"
#include "recipes.h"
#include "lawson_hanson.h"
#include "nash.h"
```

```
#include "trace.h"

#define ISOBARIC 2
#define ISOTHERMAL 1
#define ISENTROPIC 0

SilminState    *silminState;
SilminState      *liquidState;
SilminInputData silminInputData;
int modeFlag;
double liqAffinity, last_P, *ySol;

int adiabat_1s(double S0, int batch, int argc, char *argv[]);
void printPhases(void);

void main(int argc, char *argv[])
{
 int menu = 1, z = 0, i, j, batch = 0, modetemp;
 char filename[80], searchname[80];
 double r, S0=0.0, ptemp;
 FILE *fp;

 InitComputeDataStruct();       /* needed on start-up */
 silminState = allocSilminStatePointer();
 states = allocSilminStatePointer();

 /* get parameters from environment variables, if set */
 if (getenv("ADIABAT_1_DELTAP") != NULL)
  DELTAP = atof(getenv("ADIABAT_1_DELTAP"));
 else DELTAP = Ddp;
 if (getenv("ADIABAT_1_DELTAT") != NULL)
  DELTAT = atof(getenv("ADIABAT_1_DELTAT"));
 else DELTAT = Ddt;
 if (getenv("ADIABAT_1_STOL") != NULL)
  STOL = atof(getenv("ADIABAT_1_STOL"));
 else STOL = Dst;
 if (getenv("ADIABAT_1_MAXP") != NULL)
  MAX_P = atof(getenv("ADIABAT_1_MAXP"));
 else MAX_P = Dmp;
 if (getenv("ADIABAT_1_MAXT") != NULL)
  MAX_T = atof(getenv("ADIABAT_1_MAXT"));
 else MAX_T = Dmt;
 if (getenv("ADIABAT_1_MINPHI") != NULL)
  MIN_PHI = atof(getenv("ADIABAT_1_MINPHI"));
 else MIN_PHI = Dmphi;
 if (getenv("ADIABAT_1_MINP") != NULL)
  MINP = atof(getenv("ADIABAT_1_MINP"));
 else MINP = 1.0;
 if (getenv("ADIABAT_1_MODE") != NULL) {
```

```
  if (!strcmp(getenv("ADIABAT_1_MODE"), "isothermal")) modeFlag =
ISOTHERMAL;
  if (!strcmp(getenv("ADIABAT_1_MODE"), "isobaric")) modeFlag = ISOBARIC;
 } else modeFlag = ISENTROPIC;

 /* read file of permitted exsolutions */
 exsolve = (int *) calloc((unsigned) npc, sizeof(int));
 search = (int *) calloc((unsigned) npc, sizeof(int));
 (getenv("ADIABAT_SEARCH_FILE") != NULL) ?
  strcpy(searchname,getenv("ADIABAT_SEARCH_FILE")) :
  strcpy(searchname, "adiabat.searches");
 if ((fp = fopen(searchname,"r")) == NULL)
  printf("Couldn't find file with allowed exsolutions; please set manually\n");
 else {
  while (fscanf(fp, "%d %d", &i, &j) != EOF) {
   exsolve[i] = 1; search[i+j] = 1;
  }
  fclose(fp);
 }

 /* turn off phases not yet implemented */
 for (i=0;i<npc;i++) {
  if (solids[i].type == PHASE) (silminState->incSolids)[i] = TRUE;
  if (!strcmp(solids[i].label, "leucite ss")) (silminState->incSolids)[i] = FALSE;
  else if (!strcmp(solids[i].label, "orthopyroxene")) (silminState->incSolids)[i] = FALSE;
  else if (!strcmp(solids[i].label, "ortho oxide")) (silminState->incSolids)[i] = FALSE;
  else if (!strcmp(solids[i].label, "nepheline ss")) (silminState->incSolids)[i] = FALSE;
 }
 silminState->incSolids[npc] = TRUE;  /* liquid included by default */


 if (argc == 1) {       /* interactive mode */
  while(menu != QUIT) {
   printf("*** ADIABAT_1_Sh -- Batch ");
   if (modeFlag == ISENTROPIC) printf("isentrope w/ or w/o liquid ***\n");
   else if (modeFlag == ISOBARIC) printf("isobar w/ or w/o liquid ***\n");
   else if (modeFlag == ISOTHERMAL) printf("isotherm w/ or w/o liquid ***\n");
   printf("Choose:\n");
   printf("0. QUIT\n");
   printf("1. Read input file to set composition of system\n");
   printf("2. Write output file\n");
   printf("3. Execute\n");
   printf("5. Twiddle parameters\n");
   printf("6. Set allowed exsolution searches\n");
   printf("7. Single isobaric, isothermal calculation\n");
   printf("8. Impose initial entropy\n");
   printf("9. Follow mineral isograd\n");
   printf("Your choice:");
   scanf("%d", &menu);
```

```
switch (menu) {
 case 1:
  printf("Filename:");
   scanf("%s", &filename);
   getInputDataFromFile(filename);
   break;
 case 2:
  printf("Filename:");
   scanf("%s", &filename);
  if (extractorFactor == NULL)
   extractorFactor = (double *) calloc((unsigned) z, sizeof(double));
  putMultipleDataToFile(filename, z, 0, states[0].bulkTD.s);
  break;
 case 3:
  switch (z = adiabat_1s(S0, batch, argc, argv)) {
   case 0: printf("1 atm run failed!\n"); break;
   default: printf("Successful return from adiabat_1...\n");
  }
  break;
case 5:
  printf("Starting Temp = %f C; new temperature = ", silminState->T-273.15);
  scanf("%lf", &silminState->T); silminState->T += 273.15;
  printf("Starting Pressure = %f bars; new start pressure = ", silminState->P);
  scanf("%lf", &silminState->P); if (silminState->P < 1.0) silminState->P = 1.0;
  break;
 case 6:
  printf("Phases presently turned on for exsolution check:\n");
  for (i=0;i<npc;i++) if (solids[i].type == PHASE && exsolve[i])
   printf("  %d %s\n", i, solids[i].label);
  printf("Phases allowed to precipitate but not checked:\n");
  for (i=0;i<npc;i++) if (solids[i].type == PHASE &&
   (silminState->incSolids)[i] && !exsolve[i])
   printf("  %d %s\n", i, solids[i].label);
  i=0;
  while (i != -1) {
   printf("Give number of solid to change (-1 when done):");
   scanf("%d", &i);
   exsolve[i] = !exsolve[i];
  }
  for (i=0;i<npc;i++) {
   if (solids[i].type == PHASE && exsolve[i]) {
    printf("Endmembers of %s presently looked towards:\n", solids[i].label);
    for (j=1;j<=solids[i].na;j++) if (search[i+j])
     printf("  %d %s\n", j, solids[i+j].label);
    printf("Endmembers of %s presently ignored:\n", solids[i].label);
    for (j=1;j<=solids[i].na;j++) if (!search[i+j])
     printf("  %d %s\n", j, solids[i+j].label);
    j = 0;
    while (j != -1) {
```

```
        printf("Give number of endmember to change (-1 when done):");
        scanf("%d", &j);
        search[i+j] = !search[i+j];
       }
      }
     }
     if ((fp = fopen(searchname, "w")) == NULL)
      printf("Couldn't write search default file\n");
     else {
      for (i=0;i<npc;i++) if (solids[i].type == PHASE && exsolve[i]) {
       for (j=1;j<=solids[i].na;j++) if (search[i+j])
        fprintf(fp, "%d %d\n", i, j);
       }
      fclose(fp);
     }
     break;
    case 7:
     ptemp = MAX_P;
     MAX_P = silminState->P - 1.0;
     modetemp = modeFlag; modeFlag = ISENTROPIC;
     z = adiabat_1s(S0,batch, argc, argv);
     MAX_P = ptemp;
     modeFlag = modetemp;
     printf("P %.0f, T %.2f, S %.6f\n", silminState->P, silminState->T,
      silminState->bulkTD.s);
     printPhases();
     break;
    case 8:
     printf("What is S0: ");
     scanf("%lf", &S0);
     break;
    case 9:
     z = isograd(S0, batch, argc, argv);
     break;
    default:
     break;
   }
  }
 } else {       /* batch mode */
  batch = 1;
  if (!getInputDataFromFile(argv[1])) {       /* first arg = input filename */
   silminState->T = atof(argv[2]);             /* second arg = starting T   */
   if (*argv[3] == 'C') silminState->T += 273.15; /* third arg = Celsius flag */
   silminState->P = atof(argv[4]);         /* fourth arg = starting P    */
   S0 = atof(argv[5]);                  /* fifth arg = S0 */
   z = adiabat_1s(S0, batch, argc, argv);
   if (extractorFactor == NULL)
    extractorFactor = (double *) calloc((unsigned) z, sizeof(double));
   putMultipleDataToFile(argv[6], z, 0, states[0].bulkTD.s);  /* 6rd arg = output file */
```

```
    }
  }
}

int adiabat_1s(double S0, int batch, int argc, char *argv[])
{
 int i,j,k,l,o,p,z;   /* counting indices */
 char phasename[40];
 int iter;
 int isentropic = (modeFlag == ISENTROPIC);
 int equilibriumGuess;

 /* first, need initial guess assemblage. Two methods are available:
    all liquid starting guess, as in MELTS; and a customized norm calculation,
    pdaNorm, in which case a list of phases must be specified. The list of
    phases must include two pyroxenes. */
 if (!batch) {
  printf("(1) Superliquidus or (0) subsolidus initial guess ?? ");
  scanf("%d", &equilibriumGuess);
 } else equilibriumGuess = (argc == 7);  /* no phases listed on command line */

 if (equilibriumGuess && !silminState->incSolids[npc]) {
  printf("Turning liquid on!\n");
  silminState->incSolids[npc] = TRUE;
 }

 if (!equilibriumGuess) {
  /* ask for list of phases for norm (all solids off by default) */
  z = 7;
  while(strcmp(phasename,"x")) {
   if (!batch) {
    printf("Phase to include (by name, lower case) (x when done): ");
    scanf("%s", &phasename);
   } else {
    if (z < argc) strcpy(phasename, argv[z++]);
    else strcpy(phasename, "x");
   }
   for(i=0;i<npc;i++) {
    if (!strcmp(phasename, solids[i].label)) {
     silminState->nSolidCoexist[i]++;
     if (silminState->nSolidCoexist[i] > 1)
      for (j=0;j<=solids[i].na;j++) {
       silminState->solidComp[i+j] = (double *)
        realloc(silminState->solidComp[i+j], silminState->nSolidCoexist[i]*
        sizeof(double));
       silminState->solidDelta[i+j] = (double *)
        realloc(silminState->solidDelta[i+j], silminState->nSolidCoexist[i]*
        sizeof(double));
      }
```

```
      break;
     }
    }
    if (i==npc && strcmp(phasename, "x")) printf("Phase not recognized!\n");
   }

   if (!pdaNorm()) {
    printf("Error in initial guess routine -- using superliquidus start\n");
    equilibriumGuess = TRUE;
    silminState->incSolids[npc] = 1;
    for (i=0;i<npc;i++) {
     for (j=0;j<silminState->nSolidCoexist[i];j++) {
      silminState->solidComp[i][j] = 0.0;
      if (solids[i].na > 1) {
       for (k=0;k<solids[i].na;k++) silminState->solidComp[i+1+k][j] = 0.0;
      }
     }
     silminState->nSolidCoexist[i] = 0;
    }
   } else { /* set liquid components to zero */
    for (i=0;i<nlc;i++) silminState->liquidComp[i] = 0.0;
    for (i=0;i<nc;i++)  silminState->dspLiquidComp[i] = 0.0;
   }

   printPhases();
  }

  /* First calculation gives reference entropy unless user assigned.
     Then we step in pressure and/or temperature along the desired path... */
  i=0;
  if (modeFlag == ISENTROPIC && S0 != 0.0) {
   silminState->refEntropy = S0; silminState->isentropic = TRUE;
   correctTforChangeInEntropy();
  } else {silminState->refEntropy = 0.0; silminState->isentropic = FALSE;}
  if (!silmin()) {
   printf("Initial calculation failed!\n");
   return 0;
  }
  if (S0 == 0.0 && modeFlag == ISENTROPIC) {
   S0 = silminState->bulkTD.s;
   silminState->refEntropy = S0;
   silminState->isentropic = TRUE;
  }
  while (silminState->P <= MAX_P && silminState->P >= MINP && silminState->T
<=
     MAX_T && silminState->T >= 273.15) {

   /* save history of path in array states[] */
   copyStateInfo(&states[i++], silminState);
```

```
  states = reAllocSilminStatePointer(states,(unsigned) (i+1));

  /* option to calculate parameters in isentropic productivity equation */
  if (getenv("ADIABAT_DO_DTDPATF") != NULL) getdTdPatF();

  /* option to distribute trace elements */
  if (getenv("ADIABAT_DO_TRACE") != NULL)
   (void) doTraceElements(FIRST | SECOND);

  if (getenv("ADIABAT_CRASH_FILE") != NULL)
   putMultipleDataToFile(getenv("ADIABAT_CRASH_FILE"), i, silminState->T,
    states[i].bulkTD.s);

  /* option to simulate melt focusing by adding liquid */
  if (getenv("ADIABAT_FOCUS") != NULL)
   doFocus(atof(getenv("ADIABAT_FOCUS_FACTOR")));

  if (modeFlag != ISOBARIC) silminState->P += DELTAP;
  if (modeFlag == ISOBARIC) silminState->T += DELTAT;
  if (modeFlag != ISENTROPIC) silminState->refEntropy = 0.0;
  else correctTforChangeInEntropy();

  iter = 0;
  if (!silmin())
   {printf("Failure in silmin\n"); return i;}
  if (!batch) printf("Adiabat_1sh_after: P %f, T %f\n", (silminState->P),
      (silminState->T));
  printPhases();
 }
 return i;
}

/* print out phase compositions */
void printPhases(void) {
 int i, j, k;
 double *mm, *r, mass;
 char *formula;

 if (silminState->liquidMass != 0.0) {
  printf("liquid: %.3f g ", silminState->liquidMass);
  for (i=0;i<nc;i++) printf("%.2f ", silminState->dspLiquidComp[i]);
  printf("\n");
 }

 for (i=0;i<npc;i++) {
  for (j=0;j<(silminState->nSolidCoexist)[i];j++) {
   if (solids[i].na == 1)
    printf("%s: %.3f g, composition %s\n", solids[i].label,
     (silminState->solidComp)[i][j]*solids[i].mw, solids[i].formula);
```

```
    else {
      mm = (double *) calloc(solids[i].na, sizeof(double));
      r = (double *) calloc(solids[i].na, sizeof(double));
      for (k=0, mass=0.0; k<solids[i].na; k++) {
        mm[k] = (silminState->solidComp)[i+1+k][j];
        mass += (silminState->solidComp)[i+1+k][j]*solids[i+1+k].mw;
      }
      (*solids[i].convert)(SECOND, THIRD, silminState->T, silminState->P,
        (double *) NULL, mm, r, (double *) NULL, (double **) NULL,
        (double ***) NULL, (double **) NULL, (double ****) NULL);
      (*solids[i].display)(FIRST, silminState->T, silminState->P,
        r, &formula);
      printf("%s: %f g, composition %s\n", solids[i].label, mass, formula);
      if (!(*solids[i].test)(SIXTH, silminState->T, silminState->P, 0, 0, (char **) NULL,
        (char **) NULL, (double *) NULL, mm))
        printf("Phase %s is infeasible\n", solids[i].label);
      free(mm); free(r);
    }
   }
  }
}

/* function to construct phase diagram boundaries by following
   appearance/disappearance of phases.  Can do minerals or liquid,
   including exsolution boundaries as well as saturation boundaries.
   For liquid, can follow constant melt fraction contours too. */
int isograd(double S0, int batch, int argc, char *argv[])
{
 int i,j,k,l,o,p,z;   /* counting indices */
 char phasename[40];
 int iter, phage, tSide, in, nPhage;
 int equilibriumGuess;
 double bracket, fudge, Phi1, Phi2, inT, outT;
 double F, fTarget;

 if (!batch) {
  printf("(1) Superliquidus or (0) subsolidus initial guess ?? ");
  scanf("%d", &equilibriumGuess);
 } else equilibriumGuess = (argc == 7);  /* no phases listed on command line */

 if (equilibriumGuess && !silminState->incSolids[npc]) {
  printf("Turning liquid on!\n");
  silminState->incSolids[npc] = TRUE;
 }

 if (!equilibriumGuess) {

  /* ask for list of phases for initial guess (all solids off by default) */
  z = 7;
```

```
while(strcmp(phasename,"x")) {
 if (!batch) {
  printf("Phase to include (by name, lower case) (x when done): ");
  scanf("%s", &phasename);
 } else {
  if (z < argc) strcpy(phasename, argv[z++]);
  else strcpy(phasename, "x");
 }
 for(i=0;i<npc;i++) {
  if (!strcmp(phasename, solids[i].label)) {
   silminState->nSolidCoexist[i]++;
   if (silminState->nSolidCoexist[i] > 1)
    for (j=0;j<=solids[i].na;j++) {
     silminState->solidComp[i+j] = (double *)
      realloc(silminState->solidComp[i+j], silminState->nSolidCoexist[i]*
      sizeof(double));
     silminState->solidDelta[i+j] = (double *)
      realloc(silminState->solidDelta[i+j], silminState->nSolidCoexist[i]*
      sizeof(double));
    }
   break;
  }
 }
 if (i==npc && strcmp(phasename, "x")) printf("Phase not recognized!\n");
}

if (!pdaNorm()) {
 printf("Error in initial guess routine -- using superliquidus start\n");
 equilibriumGuess = TRUE;
 silminState->incSolids[npc] = 1;
 for (i=0;i<npc;i++) {
  for (j=0;j<silminState->nSolidCoexist[i];j++) {
   silminState->solidComp[i][j] = 0.0;
   if (solids[i].na > 1) {
    for (k=0;k<solids[i].na;k++) silminState->solidComp[i+1+k][j] = 0.0;
   }
  }
  silminState->nSolidCoexist[i] = 0;
 }
} else { /* set liquid components to zero */
 for (i=0;i<nlc;i++)  silminState->liquidComp[i] = 0.0;
 for (i=0;i<nc;i++)  silminState->dspLiquidComp[i] = 0.0;
}

printPhases();
}

while(TRUE) {
 printf("Phase to track boundary of (by name, lower case): ");
```

```
 scanf("%s", &phasename);
 if (!strcmp(phasename, "rhm")) strcpy(phasename, "rhm oxide");
 for(i=0;i<npc;i++) {
  if (!strcmp(phasename, solids[i].label)) {
   if (!strcmp(phasename, "feldspar") ||
     !strcmp(phasename,"pyroxene")) {
     printf("How many coexisting phases to track? ");
     scanf("%d", &nPhage);
   } else nPhage = 1;
   phage = i;
   break;
  }
 }
 if (!strcmp(phasename, "liquid")) {
  phage = npc;
  printf("What F value (default = 0)? ");
  scanf("%lf", &fTarget);
  if (fTarget < 0.0 || fTarget > 1.0) fTarget = 0.0;
  break;
 }
 if (i==npc) printf("Phase not recognized!\n");
 else break;
}
printf("Enter 1 if phase is in on high-temperature side: ");
scanf("%d", &tSide);
if (tSide != 1) tSide = -1;

i=0;
silminState->refEntropy = 0.0;
silminState->isentropic = FALSE;
if (!silmin()) {
 printf("Initial calculation failed!\n");
 return 0;
}
F = silminState->liquidMass/(silminState->liquidMass + silminState->solidMass);
bracket = 2.0; fudge = (nPhage==1?0.01:1); iter = 0;
while (silminState->P <= MAX_P && silminState->P >= MINP && silminState->T
<=
  MAX_T && silminState->T >= 273.15) {
  inT = 0.0; outT = 1.0;
  while(TRUE) {
   if ((phage != npc && silminState->nSolidCoexist[phage] != nPhage-1)
     || (phage == npc && F > fTarget)) {
     outT = silminState->T;
     if (inT != 0.0) silminState->T = (inT + outT)/2.0;
     else silminState->T -= tSide*bracket;
    } else {
     in=1;
     inT = silminState->T;
```

```
    if (outT != 1.0) silminState->T = (inT + outT)/2.0;
    else silminState->T += tSide*bracket;
   }
   silminState->refEntropy = 0.0;
   silmin();
   iter++;
   F = silminState->liquidMass/(silminState->liquidMass + silminState->solidMass);

   /* convergence criteria */
   if (phage==npc) {
    if (fTarget == 0.0 && liqAffinity<.0001 && silminState->liquidMass == 0.0) break;
    if (fTarget != 0.0 && fabs(F - fTarget) < .00001) break;
   } else if (nPhage==1) {
    if (ySol[phage] < .0001 && silminState->nSolidCoexist[phage] == 0)
     break;
   } else if (fabs(inT-outT)<.01) break;
  }

  copyStateInfo(&states[i++], silminState);
  states = reAllocSilminStatePointer(states,(unsigned) (i+1));

  if (getenv("ADIABAT_DO_TRACE") != NULL)
   (void) doTraceElements(FIRST | SECOND);

  if (getenv("ADIABAT_CRASH_FILE") != NULL)
   putMultipleDataToFile(getenv("ADIABAT_CRASH_FILE"), i, silminState->T,
    states[i].bulkTD.s);

  silminState->P += DELTAP;
  iter = 0;
  if (!batch) printf("Adiabat_1sh_after: P %f, T %f\n", (silminState->P),
      (silminState->T));
  printPhases();
  silminState->refEntropy = 0.0;
  silmin();
  F = silminState->liquidMass/(silminState->liquidMass + silminState->solidMass);
  if ((phage != npc && silminState->nSolidCoexist[phage] != nPhage-1)
     || (phage == npc && F > fTarget)) {
   inT = 0.0;
  } else {
   outT = 1.0;
  }
 }
 return i;
}
```

```
/*
**++
** FACILITY:  adiabat_2Sh: fractional or continuous path finder
**
** MODULE DESCRIPTION:
**
**    Calculates isentropic, isobaric, or isothermal fractional
**     or continuous melting paths for according to SILMIN.
**
** MODIFICATION HISTORY:
**
**    V1.0-1  Paul D. Asimow  August 2, 1994
**         batch melting version, adiabat_1
**    V2.0-1  Paul D. Asimow  August 4, 1994
**         fractional melting version, adiabat_2
**    V2.0-2  Paul D. Asimow  August 15, 1994
**         Documented, environment variables added
**    V3.0-1  Paul D. Asimow  November 22, 1994
**         H-minimizing version
**     V4.0-1  Paul D. Asimow March 31, 1995
**          Integrated solid-only or solid+melt calculation
**          New search algorithm using liquid affinity
**     V4.0-2  Paul D. Asimow April 14, 1995
**          Includes accumulated liquid and trace element modules
**          Include adiabat_3 functionality (continuous melting)
**     V4.1-1  Paul D. Asimow August 7, 1995
**          Added subsolidus fO2 buffering, if isentropic fO2
**          buffering is allowed
**--
*/

#include <math.h>
#include <stdio.h>
#include <stdlib.h>
#include <string.h>
#include <malloc.h>

#include "interface.h"
#include "silmin.h"
#include "search_limits.h"
#include "adiabat.h"
#include "recipes.h"
#include "lawson_hanson.h"
#include "nash.h"
#include "tracc.h"

#define ISOBARIC 2
#define ISOTHERMAL 1
#define ISENTROPIC 0
```

```
SilminState    *silminState;
SilminInputData silminInputData;
SilminState *liquidState;
extern SilminState *solidState;
int modeFlag;
double liqAffinity, last_P;

int adiabat_2s(double S0, int batch, int argc, char *argv[]);
double extractMelt(int z);
void printPhases(void);
void AtmLiquidi(void);

void main(int argc, char *argv[])
{
 int menu = 1, z = 1, i, j, batch = 0, modetemp;
 char filename[80], searchname[80];
 double r, S0=0.0, ptemp;
 FILE *fp;

 InitComputeDataStruct();       /* needed on start-up */
 silminState = allocSilminStatePointer();
 states = allocSilminStatePointer();
 liquidState = NULL;

 /* get parameters from environment variables, if set */
 if (getenv("ADIABAT_2_PHITOL") != NULL)
  PHITOL = atof(getenv("ADIABAT_2_PHITOL"));
 else PHITOL = Dphit;
 if (getenv("ADIABAT_2_MAXP") != NULL)
  MAX_P = atof(getenv("ADIABAT_2_MAXP"));
 else MAX_P = Dmp;
 if (getenv("ADIABAT_2_MAXT") != NULL)
  MAX_T = atof(getenv("ADIABAT_2_MAXT"));
 else MAX_T = Dmt;
 if (getenv("ADIABAT_2_DELTAPHI") != NULL)
  DELTAPHI = atof(getenv("ADIABAT_2_DELTAPHI"));
 else DELTAPHI = Ddphi;
 if (getenv("ADIABAT_2_MINP") != NULL)
  MINP = atof(getenv("ADIABAT_2_MINP"));
 else MINP = 1.0;
 if (getenv("ADIABAT_2_CONTINUOUS") != NULL) {
  if (getenv("ADIABAT_2_MINF") != NULL)
   MINf = atof(getenv("ADIABAT_2_MINF"));
  else MINf = Dmf;
 } else MINf = 0.0;
 if (getenv("ADIABAT_2_MODE") != NULL) {
  if (!strcmp(getenv("ADIABAT_2_MODE"), "isothermal")) modeFlag =
ISOTHERMAL;
```

```
 if (!strcmp(getenv("ADIABAT_2_MODE"), "isobaric")) modeFlag = ISOBARIC;
} else modeFlag = ISENTROPIC;

/* read file of permitted exsolutions */
exsolve = (int *) calloc((unsigned) npc, sizeof(int));
search = (int *) calloc((unsigned) npc, sizeof(int));
(getenv("ADIABAT_SEARCH_FILE") != NULL) ?
 strcpy(searchname,getenv("ADIABAT_SEARCH_FILE")) :
 strcpy(searchname, "adiabat.searches");
if ((fp = fopen(searchname,"r")) == NULL)
 printf("Couldn't find file with allowed exsolutions; please set manually\n");
else {
 while (fscanf(fp, "%d %d", &i, &j) != EOF) {
  exsolve[i] = 1; search[i+j] = 1;
 }
 fclose(fp);
}

/* turn off phases not yet implemented */
for (i=0;i<npc;i++) {
 if (solids[i].type == PHASE) (silminState->incSolids)[i] = TRUE;
 if (!strcmp(solids[i].label, "leucite ss")) (silminState->incSolids)[i] = FALSE;
 else if (!strcmp(solids[i].label, "orthopyroxene")) (silminState->incSolids)[i] = FALSE;
 else if (!strcmp(solids[i].label, "ortho oxide")) (silminState->incSolids)[i] = FALSE;
 else if (!strcmp(solids[i].label, "nepheline ss")) (silminState->incSolids)[i] = FALSE;
}
silminState->incSolids[npc] = TRUE;  /* liquid included by default */

if (argc == 1) {       /* interactive mode */
 while(menu != QUIT) {
  printf("*** ADIABAT_2_Sh -- ");
  if (MINf == 0.0) printf("Fractional ");
  else printf("Continuous ");
  if (modeFlag == ISENTROPIC) printf("isentrope by enthalpy min ***\n");
  else if (modeFlag == ISOBARIC) printf("isobar ***\n");
  else if (modeFlag == ISOTHERMAL) printf("isotherm ***\n");
  printf("Choose:\n");
  printf("0. QUIT\n");
  printf("1. Read input file to set composition of system\n");
  printf("2. Write output file\n");
  printf("3. Execute\n");
  printf("5. Twiddle parameters\n");
  printf("6. Set allowed exsolution searches\n");
  printf("7. Impose initial entropy\n");
  printf("8. Compute 1 atm liquidi\n");
  printf("Your choice:");
  scanf("%d", &menu);
  switch (menu) {
   case 1:
```

```
  printf("Filename:");
   scanf("%s", &filename);
   getInputDataFromFile(filename);
   break;
case 2:
  printf("Filename:");
   scanf("%s", &filename);
  putMultipleDataToFile(filename, z, 0, states[z-1].bulkTD.s);
  break;
case 3:
  switch (z = adiabat_2s(S0, batch, argc, argv)) {
   case 0: printf("First run failed!\n"); break;
   default: printf("Successful return from adiabat_1...\n");
  }
  break;
case 5:
  printf("Starting Temp = %f C; new temperature = ", silminState->T-273.15);
  scanf("%lf", &silminState->T); silminState->T += 273.15;
  printf("Starting Pressure = %f bars; new start pressure = ", silminState->P);
  scanf("%lf", &silminState->P); if (silminState->P < 1.0) silminState->P = 1.0;
  break;
case 6:
  printf("Phases presently turned on for exsolution check:\n");
  for (i=0;i<npc;i++) if (solids[i].type == PHASE && exsolve[i])
   printf("  %d %s\n", i, solids[i].label);
  printf("Phases allowed to precipitate but not checked:\n");
  for (i=0;i<npc;i++) if (solids[i].type == PHASE &&
   (silminState->incSolids)[i] && !exsolve[i])
   printf("  %d %s\n", i, solids[i].label);
  i=0;
  while (i != -1) {
   printf("Give number of solid to change (-1 when done):");
   scanf("%d", &i);
   exsolve[i] = !exsolve[i];
  }
  for (i=0;i<npc;i++) {
   if (solids[i].type == PHASE && exsolve[i]) {
    printf("Endmembers of %s presently looked towards:\n", solids[i].label);
    for (j=1;j<=solids[i].na;j++) if (search[i+j])
     printf("  %d %s\n", j, solids[i+j].label);
    printf("Endmembers of %s presently ignored:\n", solids[i].label);
    for (j=1;j<=solids[i].na;j++) if (!search[i+j])
     printf("  %d %s\n", j, solids[i+j].label);
    j = 0;
    while (j != -1) {
     printf("Give number of endmember to change (-1 when done):");
     scanf("%d", &j);
     search[i+j] = !search[i+j];
    }
```

```
        }
       }
       if ((fp = fopen(searchname, "w")) == NULL)
        printf("Couldn't write search default file\n");
       else {
        for (i=0;i<npc;i++) if (solids[i].type == PHASE && exsolve[i]) {
         for (j=1;j<=solids[i].na;j++) if (search[i+j])
          fprintf(fp, "%d %d\n", i, j);
        }
        fclose(fp);
       }
       break;
      case 7:
       printf("What is S0: ");
       scanf("%lf", &S0);
       break;
      case 8:
       AtmLiquidi();
       break;
      default:
       break;
     }
    }
   } else {       /* batch mode */
    batch = 1;
    if (!getInputDataFromFile(argv[1])) {       /* first arg = input filename */
     silminState->T = atof(argv[2]);            /* second arg = starting T   */
     if (argv[3] == "C") silminState->T += 273.15; /* third arg = Celsius flag */
     silminState->P = atof(argv[4]);         /* fourth arg = starting P    */
     S0 = atof(argv[5]);                  /* fifth arg = S0 */
     z = adiabat_2s(S0, batch, argc, argv);
     putMultipleDataToFile(argv[6], z, 0, states[0].bulkTD.s);  /* 6rd arg = output file */
    }
   }
}

int adiabat_2s(double S0, int batch, int argc, char *argv[])
{
 int i=0;       /* number of extractions (return value) */
 int j,k,l,o,p,z;    /* counting indices */
 char phasename[40];
 int iter;
 int isentropic = (modeFlag == ISENTROPIC);
 int equilibriumGuess;
 double Pold, Told, Phi0;     /* saves last P, for refining prod */
 double fudge = 1.0, Phi1, Phi2; /* for quadratic convergence */
 double prod = 50000;  /* initial guess at productivity */

 /* two options for initial guess: all liquid as in MELTS, or a custom
```

```
  norm calculation, for which we specify a list of phases.  The list
  must include two pyroxenes. */
if (!batch) {
 printf("(1) Superliquidus or (0) subsolidus initial guess ?? ");
 scanf("%d", &equilibriumGuess);
} else equilibriumGuess = (argc == 7);  /* no phases listed on command line */

if (equilibriumGuess && !silminState->incSolids[npc]) {
 printf("Turning liquid on!\n");
 silminState->incSolids[npc] = TRUE;
}

if (!equilibriumGuess) {
 /* ask for list of phases for initial guess (all solids off by default) */
 z = 7;
 while(strcmp(phasename,"x")) {
  if (!batch) {
   printf("Phase to include (by name, lower case) (x when done): ");
   scanf("%s", &phasename);
  } else {
   if (z < argc) strcpy(phasename, argv[z++]);
   else strcpy(phasename, "x");
  }
  for(k=0;k<npc;k++) {
   if (!strcmp(phasename, solids[k].label)) {
    silminState->nSolidCoexist[k]++;
    if (silminState->nSolidCoexist[k] > 1)
     for (j=0;j<=solids[k].na;j++) {
      silminState->solidComp[k+j] = (double *)
       realloc(silminState->solidComp[k+j], silminState->nSolidCoexist[k]*
       sizeof(double));
      silminState->solidDelta[k+j] = (double *)
       realloc(silminState->solidDelta[k+j], silminState->nSolidCoexist[k]*
       sizeof(double));
     }
    break;
   }
  }
  if (k==npc && strcmp(phasename, "x")) printf("Phase not recognized!\n");
 }

 if (!pdaNorm()) {
  printf("Error in initial guess routine -- using superliquidus start\n");
  equilibriumGuess = TRUE;
  silminState->incSolids[npc] = 1;
 } else { /* set liquid components to zero */
  for (k=0;k<nlc;k++) silminState->liquidComp[k] = 0.0;
  for (k=0;k<nc;k++)  silminState->dspLiquidComp[k] = 0.0;
 }
```

```
 printPhases();
}

/* First calculation gives reference entropy unless user assigned.
  Then we step along assigned path looking for desired melt fraction... */
i=0;
if (modeFlag == ISENTROPIC)
 {silminState->refEntropy = S0; silminState->isentropic = TRUE;}
else {silminState->refEntropy = 0.0; silminState->isentropic = FALSE;}
if (!silmin()) {
 printf("Initial calculation failed!\n");
 return 0;
}
if (S0 == 0.0 && modeFlag == ISENTROPIC) {
 S0 = silminState->bulkTD.s;
 silminState->refEntropy = S0;
}
iter = 0;
while (iter < MAX_P_ITER) {
 if (fabs(silminState->meltFraction - DELTAPHI) >= PHITOL) {/*melt fraction search
*/
   if (modeFlag != ISOBARIC) {
    if (silminState->meltFraction == 0.0)
     silminState->P -= liqAffinity*5.0;  /* guess at vl-vs in J/bar */
    else if ((silminState->meltFraction - DELTAPHI) > .01)
     silminState->P += .01*prod*fudge;
    else silminState->P += (silminState->meltFraction - DELTAPHI)*prod*fudge;
    if (silminState->P <= MINP) {printf("We made it to 1 bar.\n"); return i;}
    if (silminState->P > MAX_P) {printf("P got too big!\n"); return i;}
   } else {
    if (silminState->meltFraction == 0.0)
     silminState->T += liqAffinity*50.0;  /* guess at sl-ss in J/K */
    else if ((silminState->meltFraction - DELTAPHI) > .01)
     silminState->T -= .01*fudge;
    else silminState->T -= (silminState->meltFraction - DELTAPHI)*fudge;
    if (silminState->T <= 600.0) {printf("T got too low.\n"); return i;}
    if (silminState->T > MAX_T) {printf("T got too big!\n"); return i;}
   }

   if (modeFlag != ISENTROPIC)
     {silminState->refEntropy = 0.0; silminState->isentropic = 0.0;}
   else correctTforChangeInEntropy();
   if (!silmin())
    {printf("Failure in silmin\n"); return i;}

   iter++;
   /* this code refines a fudge factor every 5 iterations to achieve
        nearly quadratic convergence. */
```

```
if (iter == 1 || iter == 6 || iter == 11) Phi1 = silminState->meltFraction;
if (iter == 2 || iter == 7 || iter == 12) {
 Phi2 = silminState->meltFraction;
 if (fabs((DELTAPHI - Phi2)/(DELTAPHI - Phi1)) >= 1.0) {
  printf("We have P divergence; lowering pfudge\n");
  fudge = 1.0;
 }
 if (Phi1 != Phi2 && Phi1 != 0.0 && Phi2 != 0.0)
     fudge *= (Phi1 - DELTAPHI)/(Phi1 - Phi2);
 if (fudge > 30.0) fudge = 30.0;
}
} else {      /* Successful phi search */

/* save history of successful search points in array states[] */
copyStateInfo(&states[i], silminState);
states = reAllocSilminStatePointer(states,(unsigned) (i+2));
if (!batch)
 printf("Phi search good: P %f, T %f, s %f, phi %f,totalS %f,totalH %f,totalM %f\n",
 (silminState->P), (silminState->T), silminState->bulkTD.s,
 silminState->meltFraction, silminState->refEntropy + liquidState->refEntropy +
 solidState->solidTD.s, silminState->bulkTD.h + liquidState->refEnthalpy +
 solidState->solidTD.h, silminState->liquidMass + silminState->solidMass +
 liquidState->liquidMass + liquidState->solidMass + solidState->solidMass);

/* options to compute parameters in isentropic productivity equation and
  to distribute trace elements */
if (getenv("ADIABAT_DO_DTDPATF") != NULL) getdTdPatF();
if (getenv("ADIABAT_DO_TRACE") != NULL)
 doTraceElements(FIRST | SECOND | THIRD);

/* option to track accumulated liquid */
if (getenv("ADIABAT_2_ACCUMLIQ") != NULL) {
 trackAccumulatedLiquid(); /* This now does extraction, too */
 i++;
 if (!batch)
     printf("Accum done: P %f, T %f, s %f, phi %f,totalS %f,totalH %f,totalM %f\n",
   (silminState->P), (silminState->T), silminState->bulkTD.s,
   silminState->meltFraction, silminState->refEntropy + liquidState->refEntropy,
   silminState->bulkTD.h + liquidState->refEnthalpy, silminState->liquidMass +
   silminState->solidMass + liquidState->liquidMass + liquidState->solidMass);
}

/* Take out liquid, recalculate size and composition of system*/
if (getenv("ADIABAT_2_ACCUMLIQ") == NULL) {S0 = extractMelt(i++);
if (!batch)
 printf("Melt extracted: P %f, T %f, s %f, phi %f, totalS %f, totalH %f, totalM %f\n",
 (silminState->P), (silminState->T), silminState->bulkTD.s,
 silminState->meltFraction, silminState->refEntropy + liquidState->refEntropy,
 silminState->bulkTD.h + liquidState->refEnthalpy, silminState->liquidMass +
```

```
    silminState->solidMass + liquidState->liquidMass + liquidState->solidMass);
   }

   if (getenv("ADIABAT_CRASH_FILE") != NULL)
    putMultipleDataToFile(getenv("ADIABAT_CRASH_FILE"), i, silminState->T,S0);
   if (getenv("ADIABAT_RESTART_FILE") != NULL)
    putInputDataToFile(getenv("ADIABAT_RESTART_FILE"));

   if (modeFlag != ISOBARIC) {
    silminState->P -= DELTAPHI*prod;
    if ((silminState->P) < MINP) (silminState->P) = MINP;
   } else {
    silminState->T += DELTAPHI*200;  /* best guess at Tprod */
    if (silminState->T > MAX_T) silminState->T = MAX_T;
   }
   if (modeFlag != ISENTROPIC)
    {silminState->refEntropy = 0.0; silminState->isentropic = 0.0;}
   else correctTforChangeInEntropy();
   if (!silmin()) {printf("Silmin failed!\n"); return i;}
   iter = 0;
  }
 }
 if (iter >= MAX_P_ITER) printf("Pressure search failed\n");
 return i;
}

/* Remove some or all of the melt from the system */
double extractMelt(int z)      /* returns new reference entropy */
{
 int i, j, k;
 double liquidout;

 liquidout = ((silminState->meltFraction - MINf)/silminState->meltFraction);

 for (i=0;i<nc;i++) {  /* get new bulk composition */
  for (j=0;j<nlc;j++) {
   (silminState->bulkComp)[i]-=
    liquidout*(silminState->liquidComp)[j]*(liquid[j].liqToOx)[i];
  }
  if ((silminState->bulkComp)[i] < 1.0E-08) (silminState->bulkComp)[i] = 0.0;
 }

 /* remove melt */
 for (i=0;i<nlc;i++) (silminState->liquidComp)[i]-=liquidout*silminState->liquidComp[i];


 /* -> Calculate liquid end-member properties                    */
 for (j=0; j<nlc; j++) {
  if ((silminState->liquidComp)[j] != 0.0)
```

```
    gibbs(silminState->T, silminState->P, liquid[j].label, &(liquid[j].ref),
      &(liquid[j].liq), &(liquid[j].fus), &(liquid[j].cur));
   else
    multiplyThermoData(&(liquid[j].cur), 0.0);
 }

 /* -> Calculate solid  end-member properties                    */
 for (j=0; j<npc; j++) {
  if (solids[j].type == PHASE) {
   if ((silminState->incSolids)[j]) {
    if(solids[j].na == 1)
     gibbs(silminState->T, silminState->P, solids[j].label,
       &(solids[j].ref), NULL, NULL, &(solids[j].cur));
    else {
     for (k=0; k<solids[j].na; k++) {
      gibbs(silminState->T, silminState->P, solids[j+1+k].label,
        &(solids[j+1+k].ref), NULL, NULL, &(solids[j+1+k].cur));
     }
     j += solids[j].na;
    }
   }
  }
 }

 /* -> Calculate O2 end-member properties if path is buffered          */
 if (silminState->fo2Path != FO2_NONE) gibbs(silminState->T, silminState->P,
   "O2", &(oxygen.ref), NULL, NULL, &(oxygen.cur));

 /* Now recalculate system properties */
 if (liquidout == 1.0) (silminState->liquidMass) = 0.0;
 else silminState->liquidMass = getLiquidProperties(silminState,
     &(silminState->liquidTD),
     &(silminState->liqViscosity), TRUE);
 (silminState->solidMass) = getBulkSolidProperties(silminState,
     &(silminState->solidTD), TRUE);
 getSystemProperties(silminState, &(silminState->bulkTD),
     &(silminState->viscosity), &(silminState->meltFraction),
     TRUE);
 silminState->refEntropy = silminState->bulkTD.s;
 return silminState->bulkTD.s;
}

int localSaturationState(double *rSol, SilminState *liquidState);

/* This code reads in the accumulated liquid compositions from a
   previous run and computes the liquidus temperature of each composition
   at 1 bar.  It is of limited use, but I was curious to see how
   the liquidus varied during progressive melting... */
void AtmLiquidi(void) {
```

```
FILE *fp1, *fp2;
int i, j, k, hasSuperSaturation;
char *line, *saveline;
double *ySol, topT, botT, liquidusT, P;

fp1 = fopen("/home/paul/HMelts/output/accum_liquid.out", "r");
fp2 = fopen("/home/paul/HMelts/output/accum_liquidus.out", "w");

line = (char *) malloc((unsigned) 200*sizeof(char));
saveline = line;
ySol = (double *) malloc((unsigned) (npc+1)*sizeof(double));

silminState->P = 1.0;
if (fgets(line, 200, fp1) == NULL) return; /* header line */
while (fgets(line, 200, fp1) != NULL) {
 sscanf(line, "%lf %*lf %*lf %lf %*lf", &P, &topT);
 for (i=0;i<4;i++) line = (1+strchr(line,' '));
 for (i=0;i<nc;i++) sscanf((line=(1+strchr(line, ' '))),
    "%lf", &silminState->dspLiquidComp[i]);
 line = saveline;
 for (j=0;j<nlc;j++)
  for (k=0,silminState->liquidComp[j] = 0.0;k<nc;k++)
   silminState->liquidComp[j] += (silminState->dspLiquidComp)[k]
      *(bulkSystem[k].oxToLiq)[j]/bulkSystem[k].mw;
 silminState->T = topT;
 hasSuperSaturation = localSaturationState(ySol, silminState);
 /* get top bracket */
 while (hasSuperSaturation) {
  silminState->T += 50.0;
  hasSuperSaturation = localSaturationState(ySol, silminState);
 }
 topT = silminState->T;
 /* get bottom bracket */
 while (!hasSuperSaturation) {
  topT = silminState->T;
  silminState->T -= 50.0;
  hasSuperSaturation = localSaturationState(ySol, silminState);
 }
 botT = silminState->T;
 /* now bisect */
 while (topT - botT > 0.01) {
  silminState->T = (topT + botT) / 2.0;
  hasSuperSaturation = localSaturationState(ySol, silminState);
  if (hasSuperSaturation) botT = silminState->T;
  else topT = silminState->T;
 }
 liquidusT = (topT + botT) / 2.0;
 fprintf(fp2, "%.0f %.2f\n", P, liquidusT);
}
```

```
 fclose(fp1);
 fclose(fp2);
}
```

```
/*
**      Support routines for adiabatic path finders
**
**      Version 5 for compatibility with Melts 3.0.x  May 1996
*/

#include <math.h>
#include <stdio.h>
#include <stdlib.h>
#include <string.h>
#include <malloc.h>

#include "interface.h"
#include "silmin.h"
#include "recipes.h"
#include "search_limits.h"
#include "adiabat.h"

#define REALLOC(x, y) (((x) == NULL) ? malloc(y) : realloc((x), (y)))
#define SQUARE(x) ((x)*(x))

#define SUCCESS 1
#define FAILURE 0

void multiplyThermoData(ThermoData *target, double factor)
{
 target->g *= factor;
 target->h *= factor;
 target->s *= factor;
 target->v *= factor;
 target->cp *= factor;
 target->dcpdt *= factor;
 target->dvdt *= factor;
 target->dvdp *= factor;
 target->d2vdt2 *= factor;
 target->d2vdtdp *= factor;
 target->d2vdp2 *= factor;
}

void putMultipleDataToFile(char *fileName, int z, int t, double S0) {
 int i,j, k, l, n;
 FILE *fp;
 double *r, *m, mass, *olivine, *opx, *cpx1, *cpx2, *spinel, *feldspar;
 double *garnet, *quartz, *rutile;
 double totalMass, *residueComp, **cpxComp;
 char *formula;
 ThermoData solidTD;
 double s;
 int mode = 0;
```

```
double saveT, saveP;

r = (double *) malloc((unsigned) nc*sizeof(double));
m = (double *) malloc((unsigned) nc*sizeof(double));
residueComp = (double *) malloc((unsigned) nc*sizeof(double));
olivine = (double *) calloc((unsigned) z, sizeof(double));
opx = (double *) calloc((unsigned) z, sizeof(double));
cpx1 = (double *) calloc((unsigned) z, sizeof(double));
cpx2 = (double *) calloc((unsigned) z, sizeof(double));
spinel = (double *) calloc((unsigned) z, sizeof(double));
feldspar = (double *) calloc((unsigned) z, sizeof(double));
garnet = (double *) calloc((unsigned) z, sizeof(double));
quartz = (double *) calloc((unsigned) z, sizeof(double));
rutile = (double *) calloc((unsigned) z, sizeof(double));
cpxComp = (double **) dmatrix(0,z,0,nc);

if (z>2) mode = (states[0].P == states[1].P); /* isobaric calculation ? */

if ((fp = fopen(fileName, "w")) == NULL) {
  printf("Output error -- can't open file.\n");
  return;
}

fprintf(fp, "starting entropy %f\n", states[0].refEntropy);
fprintf(fp, "ending entropy %f\n", S0);
fprintf(fp, "P T F phi s h v cp mass fO2");
if (silminState->fo2Path != FO2_NONE) {
  if (silminState->fo2Path == FO2_QFM) fprintf(fp, "(delta QFM)");
  if (silminState->fo2Path == FO2_QFM_P3) fprintf(fp, "(delta QFM_P3)");
  if (silminState->fo2Path == FO2_QFM_P2) fprintf(fp, "(delta QFM_P2)");
  if (silminState->fo2Path == FO2_QFM_P1) fprintf(fp, "(delta QFM_P1)");
  if (silminState->fo2Path == FO2_QFM_M1) fprintf(fp, "(delta QFM_M1)");
  if (silminState->fo2Path == FO2_QFM_M2) fprintf(fp, "(delta QFM_M2)");
  if (silminState->fo2Path == FO2_QFM_M3) fprintf(fp, "(delta QFM_M3)");
  if (silminState->fo2Path == FO2_NNO) fprintf(fp, "(delta NNO)");
  if (silminState->fo2Path == FO2_IW) fprintf(fp, "(delta IW)");
  if (silminState->fo2Path == FO2_HM) fprintf(fp, "(delta HM)");
} else fprintf(fp, "(absolute)");
fprintf(fp, " sl-ss hl-hs\n");
saveT = silminState->T; saveP = silminState->P;
for (j=0;j<z;j++) {
   double fo2 = states[j].fo2;
   double F, QFM, slminusss, hlminushs;
   if (silminState->fo2Path != FO2_NONE)
     fo2 -= getlog10fo2(states[j].T,states[j].P,silminState->fo2Path);
   silminState->T = states[j].T; silminState->P = states[j].P;
   subsolidusmuO2(ELEVENTH, &QFM, (double *) NULL, (double *) NULL,
     (double *) NULL,
     (double **) NULL, (double *) NULL, (double *) NULL,
```

```
    (double *) NULL, (double *) NULL, (double *) NULL);
   QFM /= R * states[j].T * log(10.0);
   if (states[j].liquidMass != 0.0 && states[j].solidMass != 0.0) {
    slminusss = states[j].liquidTD.s/states[j].liquidMass -
            states[j].solidTD.s/states[j].solidMass;
    hlminushs = states[j].liquidTD.h/states[j].liquidMass -
            states[j].solidTD.h/states[j].solidMass;
   } else {slminusss = 0.0; hlminushs = 0.0;}
   F = states[j].liquidMass/(states[j].liquidMass+states[j].solidMass);
   fprintf(fp,
    "%.2f %.2f %.16f %.6f %9.6f %f %.3f %.6f %.6f %.3f %.3f %.6g %.6g\n",
    states[j].P, states[j].T, F, states[j].meltFraction, states[j].bulkTD.s,
    states[j].bulkTD.h, states[j].bulkTD.v, states[j].bulkTD.cp,
    states[j].solidMass+states[j].liquidMass, fo2, QFM, slminusss, hlminushs);
}
silminState->T = saveT; silminState->P = saveP;
fprintf(fp, "\nLiquid Compositions:\n");
if (mode) fprintf(fp, "T ");
else fprintf(fp, "P ");
for (k=0;k<nc;k++) fprintf(fp, "%s ", bulkSystem[k].label);
for (j=0;j<z;j++) if (states[j].liquidMass != 0.0) {
 if (mode) fprintf(fp, "\n%.2f", states[j].T);
 else fprintf(fp, "\n%.0f", states[j].P);
 for (k=0;k<nc;k++) fprintf(fp, " %.6g", (states[j].dspLiquidComp)[k]);
} else {
 if (mode) fprintf(fp, "\n%.2f ---", states[j].T);
 else fprintf(fp, "\n%.0f ---", states[j].P);
}

fprintf(fp, "\n\nSolids\n");
for (i=0;i<z;i++) {
 /* -> Calculate solid  end-member properties                    */
 for (j=0; j<npc; j++) {
  if (solids[j].type == PHASE) {
   if ((states[i].incSolids)[j]) {
    if(solids[j].na == 1)
     gibbs(states[i].T, states[i].P, solids[j].label,
      &(solids[j].ref), NULL, NULL, &(solids[j].cur));
    else {
     for (k=0; k<solids[j].na; k++) {
      gibbs(states[i].T, states[i].P, solids[j+1+k].label,
       &(solids[j+1+k].ref), NULL, NULL, &(solids[j+1+k].cur));
     }
     j += solids[j].na;
    }
   }
  }
 }
```

```
if (mode) fprintf(fp, "Temperature %.2f\n", states[i].T);
else fprintf(fp, "Pressure %.0f\n", states[i].P);
for (j=0;j<npc;j++) {
  for (k=0;k<(states[i].nSolidCoexist)[j];k++) {
    if (solids[j].na == 1) {
      fprintf(fp,"%s %f %s\n", solids[j].label,
        (states[i].solidComp)[j][k]*solids[j].mw, solids[j].formula);
      if (!strcmp(solids[j].label, "quartz"))
        quartz[i] = (states[i].solidComp)[j][k]*solids[j].mw;
      if (!strcmp(solids[j].label, "rutile"))
        rutile[i] = (states[i].solidComp)[j][k]*solids[j].mw;
    } else {
      for (l=0, mass=0.0; l<solids[j].na; l++) {
        m[l] = (states[i].solidComp)[j+1+l][k];
        mass += (states[i].solidComp)[j+1+l][k]*solids[j+1+l].mw;
      }
      (*solids[j].convert)(SECOND, THIRD, states[i].T, states[i].P,
        (double *) NULL, m, r, (double *) NULL, (double **) NULL,
        (double ***) NULL, (double **) NULL, (double ****) NULL);
      (*solids[j].display)(FIRST, states[i].T, states[i].P,
        r, &formula);
      /* (void) getSolidProperties(&states[i], j, k, &solidTD, TRUE); */
      fprintf(fp,"%s %f %s\n", solids[j].label, mass, formula);
      if (!strcmp(solids[j].label,"olivine")) olivine[i] = mass;
      else if (!strcmp(solids[j].label, "pyroxene") && !strncmp("c", formula, 1)) {
        if (cpx1[i] == 0.0) cpx1[i] = mass;
        else cpx2[i] = mass;
        for (n=0; n<nc; n++) {
          for (l=0, cpxComp[i][n] = 0.0; l<solids[j].na; l++)
            cpxComp[i][n] += (states[i].solidComp)[j+1+l][k]*
              (solids[j+1+l].solToOx)[n]*bulkSystem[n].mw;
          cpxComp[i][n] *= 100.0/mass;
        }
      } else if (!strcmp(solids[j].label, "pyroxene") && !strncmp("o", formula, 1))
          opx[i] = mass;
      else if (!strcmp(solids[j].label,"spinel")) spinel[i] = mass;
      else if (!strcmp(solids[j].label, "garnet")) garnet[i] = mass;
      else if (!strcmp(solids[j].label, "feldspar")) feldspar[i] = mass;
    }
  }
 }
}
fprintf(fp, "\nSolidsTable:\n");
if (mode)
 fprintf(fp, "T liquid olivine opx cpx1 cpx2 spinel garnet feldspar quartz rutile\n");
else fprintf(fp, "P liquid olivine opx cpx spinel garnet feldspar quartz\n");
for (i=0;i<z;i++) {
 if (mode) fprintf(fp,"%.2f %.6f %.6f %.6f %.6f %.6f %.6f %.6f %.6f %.6f %.6f\n",
    states[i].T, states[i].liquidMass, olivine[i], opx[i], cpx1[i], cpx2[i], spinel[i],
```

```
    garnet[i], feldspar[i], quartz[i], rutile[i]);
 else fprintf(fp,"%.0f %.6f %.6f %.6f %.6f %.6f %.6f %.6f %.6f %.6f\n", states[i].P,
    states[i].liquidMass, olivine[i], opx[i], cpx1[i], spinel[i],
    garnet[i], feldspar[i], quartz[i], rutile[i]);
}
fprintf(fp, "\nResidual bulk composition table:\n");
if (mode) fprintf(fp, "T ");
else  fprintf(fp, "P ");
for (k=0;k<nc;k++) fprintf(fp, "%s ", bulkSystem[k].label);
for (j=0;j<z;j++) {
 for (k=0,totalMass=0.0;k<nc;k++) {
  residueComp[k] = states[j].bulkComp[k];
  for (i=0;i<nc;i++) residueComp[k] -= states[j].liquidComp[i] * liquid[i].liqToOx[k];
  residueComp[k] *= bulkSystem[k].mw;
  totalMass += residueComp[k];
 }
 for (k=0;k<nc;k++) residueComp[k] *= 100.0/totalMass;
 if (mode) fprintf(fp, "\n%.2f", states[j].T);
 else fprintf(fp, "\n%.0f", states[j].P);
 for (k=0;k<nc;k++) fprintf(fp, " %.6g", residueComp[k]);
}

fprintf(fp, "\nBulk composition table:\n");
if (mode) fprintf(fp, "T ");
else  fprintf(fp, "P ");
for (k=0;k<nc;k++) fprintf(fp, "%s ", bulkSystem[k].label);
for (j=0;j<z;j++) {
 for (k=0,totalMass=0.0;k<nc;k++) {
  residueComp[k] = states[j].bulkComp[k];
  residueComp[k] *= bulkSystem[k].mw;
  totalMass += residueComp[k];
 }
 for (k=0;k<nc;k++) residueComp[k] *= 100.0/totalMass;
 if (mode) fprintf(fp, "\n%.2f", states[j].T);
 else fprintf(fp, "\n%.0f", states[j].P);
 for (k=0;k<nc;k++) fprintf(fp, " %.6g", residueComp[k]);
}

fprintf(fp, "\nCpx composition table:\n");
if (mode) fprintf(fp, "T ");
else  fprintf(fp, "P ");
for (k=0;k<nc;k++) fprintf(fp, "%s ", bulkSystem[k].label);
for (j=0;j<z;j++) {
 if (mode) fprintf(fp, "\n%.2f", states[j].T);
 else fprintf(fp, "\n%.0f", states[j].P);
 for (k=0;k<nc;k++) fprintf(fp, " %.6g", cpxComp[j][k]);
}

free_dmatrix(cpxComp,0,z,0,nc);
```

```
 free(r); free(m); free(olivine); free(opx); free(cpx1); free(spinel);
 free(garnet); free(feldspar); free(quartz); free(rutile); free(cpx2);
 fprintf(fp, "\n\nBulk Composition:\n");
 for (i=0,totalMass=0.0;i<nc;i++)
  totalMass+=(silminState->bulkComp)[i]*bulkSystem[i].mw;
 for (i=0;i<nc;i++) fprintf(fp, "%s %g %f\n", bulkSystem[i].label,
  (silminState->bulkComp)[i],
  (silminState->bulkComp)[i]*bulkSystem[i].mw*100.0/totalMass);
 fclose(fp);
}

void freeSilminStatePointer(SilminState *p)
{
 int i;

 for (i=0;i<npc;i++) {
  free((p->solidDelta)[i]);
  free((p->solidComp)[i]);
 }

 free(p->cylSolids);
 free(p->incSolids);
 free(p->solidDelta);
 free(p->nSolidCoexist);
 free(p->solidComp);
 free(p->liquidDelta);
 free(p->liquidComp);
 free(p->dspLiquidComp);
 free(p->bulkComp);

 free(p);
}

int localSaturationState(double *rSol, SilminState *liquidState);
extern SilminState *liquidState;
SilminState *solidState;
/* function to keep track of accumulated liquid.  It is big and messy
  because there are many cases, determined by environment variables.
  The options are:
  ADIABAT_DO_GRAVITY adds entropy to account for gravity in the infinite
     permeability limit
  ADIABAT_ACCUM_CRYSTALLIZE keeps "accumulated liquid" pot at equilibrium,
     otherwise it is possibly a metastable liquid
  ADIABAT_ACCUM_FRAC_CRYST causes the crystals formed in the "accumulated
     liquid" pot to be removed to a third reservoir representing the walls of the conduit
  ADIABAT_ACCUM_T_EQUIL forces all the reservoirs to the same temperature */
void trackAccumulatedLiquid(void) {
 int i, j, k, ns;
 FILE *fp;
```

```
static double *rLiq, T, *ySol;
static double *outLiquidComp;
double sTotal, cpTotal, mTotal, hTotal;
double residual = 1.0, adiabatT, liquidusT, topT, botT, pTemp;
int hasSuperSaturation, iter = 0;
static int beenHere = 0;
double liquidout, saveMeltFraction, oldResidual;
static SilminState *saveState;
double ol=0.0, opx=0.0, cpx=0.0, plag=0.0, spinel=0.0;
double *mSol = (double *) malloc((unsigned) 10*sizeof(double));
double *rSol = (double *) malloc((unsigned) 10*sizeof(double));
static double oldP;

liquidout = (silminState->meltFraction - MINf)/silminState->meltFraction;

if (liquidState == NULL) {
  liquidState = (SilminState *) allocSilminStatePointer();
  solidState = (SilminState *) allocSilminStatePointer();
  saveState = (SilminState *) allocSilminStatePointer();
  rLiq = (double *) malloc((unsigned) nlc*sizeof(double));
  outLiquidComp = (double *) malloc((unsigned) nlc*sizeof(double));
  ySol = (double *) malloc((unsigned) npc*sizeof(double));
  liquidState->liquidMass = 0.0;
  liquidState->T = silminState->T; liquidState->refEntropy = 0.0;
  liquidState->solidMass = 0.0; liquidState->refEnthalpy = 0.0;
  for (i=0;i<npc;i++) liquidState->incSolids[i] = silminState->incSolids[i];
  for (i=0;i<npc;i++) solidState->incSolids[i] = silminState->incSolids[i];
  solidState->incSolids[npc] = 0; /* disallow liquid */
 }

 /* Optionally, add an entropy source corresponding to the gravitational
  potential energy that is dissipated during one-dimensional steady porous
  flow with infinite permeability.  We do this first since the next step is
  to obtain the temperature of the liquid pot at the new pressure. */
 if (getenv("ADIABAT_DO_GRAVITY") != NULL && liquidState->liquidTD.v !=
0.0) {
   double soldensity, liqdensity, F;
   double totalMass;
   double g = 9.8; /* m s^-2 */
   double dz;

   soldensity = 1000.0*(silminState->liquidMass+silminState->solidMass)/
      silminState->bulkTD.v;
   liqdensity = 1000.0*liquidState->liquidMass/liquidState->liquidTD.v; /* kg m^-3 */
   totalMass = liquidState->liquidMass+solidState->solidMass+
       silminState->liquidMass+silminState->solidMass; /* g */
   F = liquidState->liquidMass/totalMass;
   totalMass /= 1000.0;  /* kg */
   dz = 100000.0*(oldP - silminState->P)/(g*soldensity); /* m */
```

```
 liquidState->refEntropy += dz*F*totalMass*g*(soldensity-liqdensity)/
    (liqdensity*silminState->T);
}
oldP = silminState->P;

/* Move previous accumulated liquid (and solids if any) to new pressure
    isentropically, get T and enthalpy at the new pressure  */
liquidState->P = silminState->P;
if (liquidState->liquidMass != 0.0) {
 if (getenv("ADIABAT_ACCUM_CRYSTALLIZE")==NULL){
  while ((fabs(residual) > 10.0*DBL_EPSILON*fabs(liquidState->refEntropy))
    && (iter < 50)) {
   sTotal  = 0.0;
   cpTotal = 0.0;
   /* accumulated liquid */
   for (i=0, mTotal= 0.0; i<nlc; i++) {
    mTotal += liquidState->liquidComp[i];
    gibbs(liquidState->T, liquidState->P, liquid[i].label, &(liquid[i].ref),
     &(liquid[i].liq), &(liquid[i].fus), &(liquid[i].cur));
    sTotal  += liquidState->liquidComp[i]*(liquid[i].cur).s;
    cpTotal += liquidState->liquidComp[i]*(liquid[i].cur).cp;
   }
   conLiq(SECOND, THIRD, liquidState->T, liquidState->P, (double *) NULL,
    liquidState->liquidComp, rLiq, (double *) NULL, (double **) NULL,
    (double ***) NULL, (double *) NULL);
   smixLiq(FIRST,  liquidState->T, liquidState->P, rLiq, &pTemp,
    (double *) NULL, (double **) NULL);
   sTotal += mTotal*pTemp;
   cpmixLiq(FIRST, liquidState->T, liquidState->P, rLiq, &pTemp,
    (double *) NULL, (double *) NULL);
   cpTotal += mTotal*pTemp;

   residual = sTotal - liquidState->refEntropy;
   if (fabs(residual) > 10.0*DBL_EPSILON*fabs(liquidState->refEntropy))
    liquidState->T -= residual*liquidState->T/cpTotal;
   iter++;
  }
 } else {  /* do this at equilibrium ! */
  copyStateInfo(saveState, silminState);
  copyStateInfo(silminState, liquidState);
  silminState->isentropic = TRUE;
  correctXforChangeInBulkComp();
  correctTforChangeInEntropy();
  silmin();
  silminState->isentropic = FALSE;
  copyStateInfo(liquidState, silminState);
  copyStateInfo(silminState, saveState);
 }
```

```
 /* get new reference enthalpy for accumulated pot */
 /* accumulated liquid */
 for (i=0, mTotal= 0.0, liquidState->liquidTD.h = 0.0; i<nlc; i++) {
  mTotal += liquidState->liquidComp[i];
  gibbs(liquidState->T, liquidState->P, liquid[i].label, &(liquid[i].ref),
       &(liquid[i].liq), &(liquid[i].fus), &(liquid[i].cur));
  liquidState->liquidTD.h  += liquidState->liquidComp[i]*(liquid[i].cur).h;
 }
 conLiq(SECOND, THIRD, liquidState->T, liquidState->P, (double *) NULL,
     liquidState->liquidComp, rLiq, (double *) NULL, (double **) NULL,
     (double ***) NULL, (double *) NULL);
 hmixLiq(FIRST,  liquidState->T, liquidState->P, rLiq, &pTemp);
 liquidState->liquidTD.h += mTotal*pTemp;

 /* add cotravelling solids, if any, to enthalpy */
 if (getenv("ADIABAT_ACCUM_CRYSTALLIZE") != NULL &&
    liquidState->solidMass != 0.0) {
  for (i=0, liquidState->solidTD.h = 0.0; i<npc; i++) {
    for (ns=0; ns<(liquidState->nSolidCoexist)[i]; ns++) {
     mTotal = (liquidState->solidComp)[i][ns];
     if (solids[i].na == 1) {
      gibbs(liquidState->T, liquidState->P, solids[i].label,
           &(solids[i].ref), NULL, NULL, &(solids[i].cur));
      liquidState->solidTD.h  += mTotal*(solids[i].cur).h;
     } else {
      for (j=0; j<solids[i].na; j++) {
       mSol[j] = (liquidState->solidComp)[i+1+j][ns];
       gibbs(liquidState->T, liquidState->P, solids[i+1+j].label,
            &(solids[i+1+j].ref), NULL, NULL, &(solids[i+1+j].cur));
       liquidState->solidTD.h  += mSol[j]*(solids[i+1+j].cur).h;
      }
      (*solids[i].convert)(SECOND, THIRD, liquidState->T, liquidState->P,
           (double *) NULL, mSol, rSol, (double *) NULL, (double **) NULL,
           (double ***) NULL, (double **) NULL, (double ****) NULL);
      (*solids[i].hmix)(FIRST, liquidState->T, liquidState->P, rSol,&pTemp);
      liquidState->solidTD.h += mTotal*pTemp;
     }
    }
   }
 }
 liquidState->refEnthalpy = liquidState->solidTD.h + liquidState->liquidTD.h;
}

/* move conduit walls to new pressure isentropically, get new reference T and H;
   note liquid is disallowed in solidState, so this may be metastable. */
if (solidState->solidMass != 0.0) {
 /* move isentropically */
 solidState->P = silminState->P;
 copyStateInfo(saveState, silminState);
```

```
 copyStateInfo(silminState, solidState);
 silminState->isentropic = TRUE;
 correctXforChangeInBulkComp();
 correctTforChangeInEntropy();
 silminState->isentropic = FALSE;
 copyStateInfo(solidState, silminState);
 copyStateInfo(silminState, saveState);
 for (i=0, solidState->solidTD.h = 0.0; i<npc; i++) {
  for (ns=0; ns<(solidState->nSolidCoexist)[i]; ns++) {
   mTotal = (solidState->solidComp)[i][ns];
   if (solids[i].na == 1) {
    gibbs(solidState->T, solidState->P, solids[i].label,
          &(solids[i].ref), NULL, NULL, &(solids[i].cur));
    solidState->solidTD.h  += mTotal*(solids[i].cur).h;
   } else {
    for (j=0; j<solids[i].na; j++) {
     mSol[j] = (solidState->solidComp)[i+1+j][ns];
     gibbs(solidState->T, solidState->P, solids[i+1+j].label,
           &(solids[i+1+j].ref), NULL, NULL, &(solids[i+1+j].cur));
     solidState->solidTD.h  += mSol[j]*(solids[i+1+j].cur).h;
    }
    (*solids[i].convert)(SECOND, THIRD, solidState->T, solidState->P,
          (double *) NULL, mSol, rSol, (double *) NULL, (double **) NULL,
          (double ***) NULL, (double **) NULL, (double ****) NULL);
    (*solids[i].hmix)(FIRST, solidState->T, solidState->P, rSol,&pTemp);
    solidState->solidTD.h += mTotal*pTemp;
   }
  }
 }
 solidState->refEnthalpy = solidState->solidTD.h;
}


/* Calculate accumulated fractional liquid composition, extract liquid from silminState */
for (i=0;i<nlc;i++) {
 liquidState->liquidComp[i] += liquidout*silminState->liquidComp[i];
 for (j=0;j<nc;j++) liquidState->bulkComp[j] +=
    liquidout * silminState->liquidComp[i] * liquid[i].liqToOx[j];
 for (j=0;j<nc;j++) silminState->bulkComp[j] -=
    liquidout * silminState->liquidComp[i] * liquid[i].liqToOx[j];
 silminState->liquidComp[i] *= (1.0 - liquidout);
}

for (i=0, liquidState->liquidMass = 0.0;i<nc;i++) {
 for (j=0,liquidState->dspLiquidComp[i]=0.0;j<nlc;j++)
  liquidState->dspLiquidComp[i] += liquidState->liquidComp[j]*
   liquid[j].liqToOx[i]*bulkSystem[i].mw;
 liquidState->liquidMass += liquidState->dspLiquidComp[i];
 silminState->dspLiquidComp[i] *= (1.0 - liquidout);
```

```
}
silminState->liquidMass *= (1.0 - liquidout);
for (i=0;i<nc;i++) liquidState->dspLiquidComp[i] *=
 ( liquidState->liquidMass==0.0 ? 0.0 : 100.0/liquidState->liquidMass );

/* Calculate accumulated liquid pot enthalpy and T */
liquidState->liquidTD.h += liquidout*silminState->liquidTD.h;
liquidState->refEnthalpy = liquidState->solidTD.h + liquidState->liquidTD.h;
residual = 1.0;
while ((fabs(residual) > 10.0*DBL_EPSILON*fabs(liquidState->refEnthalpy))
     && (iter < 50)) {
 hTotal  = 0.0;
 cpTotal = 0.0;
 /* accumulated liquid */
 for (i=0, mTotal= 0.0; i<nlc; i++) {
  mTotal += liquidState->liquidComp[i];
  gibbs(liquidState->T, silminState->P, liquid[i].label, &(liquid[i].ref),
   &(liquid[i].liq), &(liquid[i].fus), &(liquid[i].cur));
  hTotal  += liquidState->liquidComp[i]*(liquid[i].cur).h;
  cpTotal += liquidState->liquidComp[i]*(liquid[i].cur).cp;
 }
 conLiq(SECOND, THIRD, liquidState->T, silminState->P, (double *) NULL,
  liquidState->liquidComp, rLiq, (double *) NULL, (double **) NULL,
  (double ***) NULL, (double *) NULL);
 hmixLiq(FIRST,  liquidState->T, silminState->P, rLiq, &pTemp);
 hTotal += mTotal*pTemp;
 cpmixLiq(FIRST, liquidState->T, silminState->P, rLiq, &pTemp,
  (double *) NULL, (double *) NULL);
 cpTotal += mTotal*pTemp;

 /* add cotravelling solids, if any */
 if (getenv("ADIABAT_ACCUM_CRYSTALLIZE") != NULL &&
   liquidState->solidMass != 0.0) {
  for (i=0; i<npc; i++) {
   for (ns=0; ns<(liquidState->nSolidCoexist)[i]; ns++) {
    mTotal = (liquidState->solidComp)[i][ns];
    if (solids[i].na == 1) {
     gibbs(liquidState->T, silminState->P, solids[i].label,
          &(solids[i].ref), NULL, NULL, &(solids[i].cur));
     hTotal  += mTotal*(solids[i].cur).h;
     cpTotal += mTotal*(solids[i].cur).cp;
    } else {
     for (j=0; j<solids[i].na; j++) {
      mSol[j] = (liquidState->solidComp)[i+1+j][ns];
      gibbs(liquidState->T, silminState->P, solids[i+1+j].label,
           &(solids[i+1+j].ref), NULL, NULL, &(solids[i+1+j].cur));
      hTotal  += mSol[j]*(solids[i+1+j].cur).h;
      cpTotal += mSol[j]*(solids[i+1+j].cur).cp;
     }
```

```
        (*solids[i].convert)(SECOND, THIRD, liquidState->T, silminState->P,
              (double *) NULL, mSol, rSol, (double *) NULL, (double **) NULL,
              (double ***) NULL, (double **) NULL, (double ****) NULL);
        (*solids[i].hmix)(FIRST, liquidState->T, silminState->P, rSol,&pTemp);
        hTotal += mTotal*pTemp;
        (*solids[i].cpmix)(FIRST, liquidState->T, silminState->P, rSol,
              &pTemp, (double *) NULL, (double *) NULL);
        cpTotal += mTotal*pTemp;
       }
      }
     }
    }

 residual = hTotal - liquidState->refEnthalpy;
 if (fabs(residual) > 10.0*DBL_EPSILON*fabs(liquidState->liquidTD.h))
  liquidState->T -= residual/cpTotal;
 iter++;
}
adiabatT = liquidState->T;

/* calculate accumulated liquid pot entropy */
for (i=0, mTotal= 0.0, liquidState->liquidTD.s = 0.0; i<nlc; i++) {
 mTotal += liquidState->liquidComp[i];
 liquidState->liquidTD.s  += liquidState->liquidComp[i]*(liquid[i].cur).s;
}
smixLiq(FIRST,  liquidState->T, silminState->P, rLiq, &pTemp,
 (double *) NULL, (double **) NULL);
liquidState->liquidTD.s += mTotal*pTemp;

/* add cotravelling solids, if any */
if (getenv("ADIABAT_ACCUM_CRYSTALLIZE") != NULL &&
    liquidState->solidMass != 0.0) {
 for (i=0,liquidState->solidTD.s = 0.0; i<npc; i++) {
  for (ns=0; ns<(liquidState->nSolidCoexist)[i]; ns++) {
   mTotal = (liquidState->solidComp)[i][ns];
   if (solids[i].na == 1) {
    liquidState->solidTD.s  += mTotal*(solids[i].cur).s;
   } else {
    for (j=0; j<solids[i].na; j++) {
     mSol[j] = (liquidState->solidComp)[i+1+j][ns];
     liquidState->solidTD.s  += mSol[j]*(solids[i+1+j].cur).s;
    }
    (*solids[i].convert)(SECOND, THIRD, liquidState->T, silminState->P,
          (double *) NULL, mSol, rSol, (double *) NULL, (double **) NULL,
          (double ***) NULL, (double **) NULL, (double ****) NULL);
    (*solids[i].smix)(FIRST, liquidState->T, silminState->P, rSol,&pTemp,
        (double *) NULL, (double **) NULL);
    liquidState->solidTD.s += mTotal*pTemp;
   }
```

```
    }
  }
}
liquidState->refEntropy = liquidState->solidTD.s + liquidState->liquidTD.s;

/* find liquidus */
hasSuperSaturation = localSaturationState(ySol, liquidState);
/* get top bracket */
while (hasSuperSaturation) {
 liquidState->T += 50.0;
 hasSuperSaturation = localSaturationState(ySol, liquidState);
}
topT = liquidState->T;
/* get bottom bracket */
while (!hasSuperSaturation) {
 liquidState->T -= 50.0;
 hasSuperSaturation = localSaturationState(ySol, liquidState);
}
botT = liquidState->T;
/* now bisect */
while (topT - botT > 0.01) {
 liquidState->T = (topT + botT) / 2.0;
 hasSuperSaturation = localSaturationState(ySol, liquidState);
 if (hasSuperSaturation) botT = liquidState->T;
 else topT = liquidState->T;
}
liquidusT = (topT + botT) / 2.0;
liquidState->T = adiabatT;

/* If option ADIABAT_ACCUM_CRYSTALLIZE is set and option
   ADIABAT_ACCUM_T_EQUIL is NOT set, do the crystallization here */
/* currently an isenthalpic calculation, resets S and T */
if (getenv("ADIABAT_ACCUM_T_EQUIL") == NULL &&
     getenv("ADIABAT_ACCUM_CRYSTALLIZE") != NULL) {
 copyStateInfo(saveState, silminState);
 copyStateInfo(silminState, liquidState);
 silminState->isenthalpic = TRUE;
 silminState->isentropic = FALSE;
 correctXforChangeInBulkComp();
 correctTforChangeInEnthalpy();
 silmin();
 copyStateInfo(liquidState, silminState);
 copyStateInfo(silminState, saveState);
 adiabatT = liquidState->T;
 liquidState->refEntropy = liquidState->solidTD.s + liquidState->liquidTD.s;

 /* if option ADIABAT_ACCUM_FRAC_CRYST is set, remove crystals to solidState,
    i.e. plate them on the walls of the conduit. */
 if (getenv("ADIABAT_ACCUM_FRAC_CRYST") != NULL
```

```
    && liquidState->solidMass != 0.0) {
  int ns;
  for (i=0;i<npc;i++) {
   if (solidState->nSolidCoexist[i] < liquidState->nSolidCoexist[i]
        && liquidState->nSolidCoexist[i] > 1) {
    for (j=0;j<=solids[i].na;j++) {
     solidState->solidComp[i+j] = REALLOC(solidState->solidComp[i+j],
        liquidState->nSolidCoexist[i]*sizeof(double));
     solidState->solidDelta[i+j] = REALLOC(solidState->solidDelta[i+j],
        liquidState->nSolidCoexist[i]*sizeof(double));
    }
   }
   if (solidState->nSolidCoexist[i] < liquidState->nSolidCoexist[i])
    solidState->nSolidCoexist[i] = liquidState->nSolidCoexist[i];

   for (ns=0;ns<liquidState->nSolidCoexist[i];ns++) {
    if (solids[i].na == 1) {
     solidState->nSolidCoexist[i] = 1;
     solidState->solidComp[i][ns] += liquidState->solidComp[i][ns];
     solidState->solidMass +=  (liquidState->solidComp)[i][ns]*solids[i].mw;
     solidState->solidMass -=  (liquidState->solidComp)[i][ns]*solids[i].mw;
     for (j=0; j<nc; j++) {
      (solidState->bulkComp)[j] +=
           (solids[i].solToOx)[j]*(liquidState->solidComp)[i][ns];
      (liquidState->bulkComp)[j] -=
           (solids[i].solToOx)[j]*(liquidState->solidComp)[i][ns];
     }
     (liquidState->solidComp)[i][ns] = 0.0;
     liquidState->nSolidCoexist[i]--;
    } else {
     (solidState->solidComp)[i][ns] += (liquidState->solidComp)[i][ns];
     for (j=0; j<solids[i].na; j++) {
      (solidState->solidComp)[i+1+j][ns] += (liquidState->solidComp)[i+1+j][ns];
      solidState->solidMass+= (liquidState-
>solidComp)[i+1+j][ns]*solids[i+1+j].mw;
      liquidState->solidMass-= (liquidState-
>solidComp)[i+1+j][ns]*solids[i+1+j].mw;
      for (k=0; k<nc; k++) {
       (solidState->bulkComp)[k] +=
        (solids[i+1+j].solToOx)[k]*(liquidState->solidComp)[i+1+j][ns];
       (liquidState->bulkComp)[k] -=
        (solids[i+1+j].solToOx)[k]*(liquidState->solidComp)[i+1+j][ns];
      }
      (liquidState->solidComp)[i+1+j][ns] = 0.0;
     }
     (liquidState->solidComp)[i][ns] = 0.0;
     liquidState->nSolidCoexist[i]--;
    }
   }
```

```
    }
    liquidState->solidMass = 0.0;
    solidState->refEntropy += liquidState->solidTD.s;
    solidState->refEnthalpy += liquidState->solidTD.h;
    solidState->solidTD.s += liquidState->solidTD.s;
    solidState->solidTD.h += liquidState->solidTD.h;
    liquidState->refEntropy -= liquidState->solidTD.s;
    liquidState->refEnthalpy -= liquidState->solidTD.h;
    liquidState->solidTD.s = 0.0;
    liquidState->solidTD.h = 0.0;
    if (solidState->T == 0.0) solidState->T = liquidState->T;
  } /* end remove crystals to walls */
} /* end crystallization without T_EQUIL */

/* If option ADIABAT_ACCUM_T_EQUIL is set, allow accumulated liquid
   and residual solid to come to thermal equilibrium at constant H --
   replaces silminState->T, silminState->bulkTD.s, and liquidState->bulkTD.s.

   If option ADIABAT_ACCUM_CRYSTALLIZE is set, the accumulated liquid
   is allowed to crystallize during this step, if it is below its
   liquidus. This operation overwrites liquidState->liquidComp and
   liquidState->liquidMass, and puts the accumulated fractionated
   solids in liquidState->solidComp and ->solidMass. The accumulated
   solids DO participate in the thermal equilibration.

   If option ADIABAT_ACCUM_FRAC_CRYST is set, the solids crystallized
   from the accumulated liquid are immediately removed to a third reservoir,
   the "walls" of the conduit. Here they are chemically isolated, but
   continue to participate in the thermal equilbration. */

if (getenv("ADIABAT_ACCUM_T_EQUIL") != NULL) {
  double totalH = liquidState->refEnthalpy + silminState->solidTD.h +
     (1.0 - liquidout)*silminState->liquidTD.h + solidState->refEnthalpy;
  int quad = 0;
  double oldT = 0.0, newT;

  residual = 1.0; iter = 0; oldResidual = 1.0;
  while ((fabs(residual) > /*10.0*DBL_EPSILON*fabs(totalH)*/ 1.0e-05)
      && (iter < 50)) {
    hTotal  = 0.0;
    cpTotal = 0.0;

    /* add up enthalpy; begin with accumulated assemblage */
    if (getenv("ADIABAT_ACCUM_CRYSTALLIZE") != NULL) {
      liquidState->T = silminState->T;
      liquidState->isenthalpic = FALSE;  /* isothermal run */
      liquidState->isentropic = FALSE;
      copyStateInfo(saveState, silminState);
      copyStateInfo(silminState, liquidState);
```

```
correctXforChangeInBulkComp();
silmin();
copyStateInfo(liquidState, silminState);
copyStateInfo(silminState, saveState);
adiabatT = liquidState->T;
liquidState->refEntropy = liquidState->liquidTD.s + liquidState->solidTD.s;

if (getenv("ADIABAT_ACCUM_FRAC_CRYST") != NULL
   && liquidState->solidMass != 0.0) {
 /* move crystals in accumulated liquid to conduit walls */
 double *m = (double *) malloc((unsigned) nc*sizeof(double));
 int ns;
 for (i=0;i<npc;i++) {
  if (solidState->nSolidCoexist[i] < liquidState->nSolidCoexist[i]
     && liquidState->nSolidCoexist[i] > 1) {
    for (j=0;j<=solids[i].na;j++) {
     solidState->solidComp[i+j] = REALLOC(solidState->solidComp[i+j],
      liquidState->nSolidCoexist[i]*sizeof(double));
     solidState->solidDelta[i+j] = REALLOC(solidState->solidDelta[i+j],
      liquidState->nSolidCoexist[i]*sizeof(double));
    }
  }
  if (solidState->nSolidCoexist[i] < liquidState->nSolidCoexist[i])
   solidState->nSolidCoexist[i] = liquidState->nSolidCoexist[i];

  for (ns=0;ns<liquidState->nSolidCoexist[i];ns++) {
   if (solids[i].na == 1) {
    solidState->nSolidCoexist[i] = 1;
    solidState->solidComp[i][ns] += liquidState->solidComp[i][ns];
    solidState->solidMass +=
       (liquidState->solidComp)[i][ns]*solids[i].mw;
    liquidState->solidMass -=
       (liquidState->solidComp)[i][ns]*solids[i].mw;
    for (j=0; j<nc; j++) {
     (solidState->bulkComp)[j] +=
        (solids[i].solToOx)[j]*(liquidState->solidComp)[i][ns];
     (liquidState->bulkComp)[j] -=
        (solids[i].solToOx)[j]*(liquidState->solidComp)[i][ns];
    }
    (liquidState->solidComp)[i][ns] = 0.0;
    liquidState->nSolidCoexist[i]--;
   } else {
    (solidState->solidComp)[i][ns] += (liquidState->solidComp)[i][ns];
    for (j=0; j<solids[i].na; j++) {
     m[j] = (liquidState->solidComp)[i+1+j][ns];
     (solidState->solidComp)[i+1+j][ns] += m[j];
     solidState->solidMass += m[j]*solids[i+1+j].mw;
     liquidState->solidMass -= m[j]*solids[i+1+j].mw;
     for (k=0; k<nc; k++) {
```

```
          (solidState->bulkComp)[k] += (solids[i+1+j].solToOx)[k]*m[j];
          (liquidState->bulkComp)[k] -= (solids[i+1+j].solToOx)[k]*m[j];
         }
         (liquidState->solidComp)[i+1+j][ns] = 0.0;
        }
        (liquidState->solidComp)[i][ns] = 0.0;
        liquidState->nSolidCoexist[i]--;
       }
      }
     }
     liquidState->solidMass = 0.0;
     solidState->refEntropy += liquidState->solidTD.s;
     solidState->refEnthalpy += liquidState->solidTD.h;
     solidState->solidTD.s += liquidState->solidTD.s;
     solidState->solidTD.h += liquidState->solidTD.h;
     liquidState->refEntropy -= liquidState->solidTD.s;
     liquidState->refEnthalpy -= liquidState->solidTD.h;
     liquidState->solidTD.s = 0.0;
     liquidState->solidTD.h = 0.0;
     solidState->T = liquidState->T;
     free(m);
    }  /* end move crystals to conduit walls */


    /* add accumulated solids to enthalpy */
    if (liquidState->solidMass != 0.0) {
     for (i=0; i<npc; i++) {
      for (ns=0; ns<(liquidState->nSolidCoexist)[i]; ns++) {
       mTotal = (liquidState->solidComp)[i][ns];
       if (solids[i].na == 1) {
        gibbs(silminState->T, silminState->P, solids[i].label,
           &(solids[i].ref), NULL, NULL, &(solids[i].cur));
        hTotal  += mTotal*(solids[i].cur).h;
        cpTotal += mTotal*(solids[i].cur).cp;
       } else {
        for (j=0; j<solids[i].na; j++) {
         mSol[j] = (liquidState->solidComp)[i+1+j][ns];
         gibbs(silminState->T, silminState->P, solids[i+1+j].label,
            &(solids[i+1+j].ref), NULL, NULL, &(solids[i+1+j].cur));
         hTotal  += mSol[j]*(solids[i+1+j].cur).h;
         cpTotal += mSol[j]*(solids[i+1+j].cur).cp;
        }
        (*solids[i].convert)(SECOND, THIRD, silminState->T, silminState->P,
           (double *) NULL, mSol, rSol, (double *) NULL, (double **) NULL,
           (double ***) NULL, (double **) NULL, (double ****) NULL);
        (*solids[i].hmix)(FIRST, silminState->T, silminState->P, rSol,
           &pTemp);
        hTotal += mTotal*pTemp;
        (*solids[i].cpmix)(FIRST, silminState->T, silminState->P, rSol,
```

```
            &pTemp, (double *) NULL, (double *) NULL);
          cpTotal += mTotal*pTemp;
         }
        }
       }
      liquidState->solidTD.h = hTotal;
     } else if (solidState->solidMass != 0.0) {  /* add conduit wall solids to enthalpy */
      solidState->T = liquidState->T;
      for (i=0; i<npc; i++) {
       for (ns=0; ns<(solidState->nSolidCoexist)[i]; ns++) {
        mTotal = (solidState->solidComp)[i][ns];
        if (solids[i].na == 1) {
         gibbs(silminState->T, silminState->P, solids[i].label,
            &(solids[i].ref), NULL, NULL, &(solids[i].cur));
         hTotal  += mTotal*(solids[i].cur).h;
         cpTotal += mTotal*(solids[i].cur).cp;
        } else {
         for (j=0; j<solids[i].na; j++) {
          mSol[j] = (solidState->solidComp)[i+1+j][ns];
          gibbs(silminState->T, silminState->P, solids[i+1+j].label,
             &(solids[i+1+j].ref), NULL, NULL, &(solids[i+1+j].cur));
          hTotal  += mSol[j]*(solids[i+1+j].cur).h;
          cpTotal += mSol[j]*(solids[i+1+j].cur).cp;
         }
         (*solids[i].convert)(SECOND, THIRD, silminState->T, silminState->P,
            (double *) NULL, mSol, rSol, (double *) NULL, (double **) NULL,
            (double ***) NULL, (double **) NULL, (double ****) NULL);
         (*solids[i].hmix)(FIRST, silminState->T, silminState->P, rSol,
            &pTemp);
         hTotal += mTotal*pTemp;
         (*solids[i].cpmix)(FIRST, silminState->T, silminState->P, rSol,
            &pTemp, (double *) NULL, (double *) NULL);
         cpTotal += mTotal*pTemp;
        }
       }
      }
      solidState->solidTD.h = hTotal;
      solidState->refEnthalpy = hTotal;
     }
    }

    /* add accumulated liquid */
    for (i=0, mTotal= 0.0; i<nlc; i++) {
     mTotal += liquidState->liquidComp[i];
     gibbs(silminState->T, silminState->P, liquid[i].label, &(liquid[i].ref),
        &(liquid[i].liq), &(liquid[i].fus), &(liquid[i].cur));
     hTotal  += liquidState->liquidComp[i]*(liquid[i].cur).h;
     cpTotal += liquidState->liquidComp[i]*(liquid[i].cur).cp;
    }
```

```
    conLiq(SECOND, THIRD, silminState->T, silminState->P, (double *) NULL,
      liquidState->liquidComp, rLiq, (double *) NULL, (double **) NULL,
      (double ***) NULL, (double *) NULL);
    hmixLiq(FIRST,  silminState->T, silminState->P, rLiq, &pTemp);
    hTotal += mTotal*pTemp;
    cpmixLiq(FIRST, silminState->T, silminState->P, rLiq, &pTemp,
      (double *) NULL, (double *) NULL);
    cpTotal += mTotal*pTemp;
    liquidState->liquidTD.h = hTotal - liquidState->solidTD.h - solidState->solidTD.h;
    liquidState->refEnthalpy = hTotal - solidState->solidTD.h;

    /* add residual liquid if any */
    if (silminState->liquidComp[0] != 0.0) {
     for (i=0, mTotal= 0.0; i<nlc; i++) {
      mTotal  += silminState->liquidComp[i];
      hTotal  += silminState->liquidComp[i]*(liquid[i].cur).h;
      cpTotal += silminState->liquidComp[i]*(liquid[i].cur).cp;
     }
     conLiq(SECOND, THIRD, silminState->T, silminState->P, (double *) NULL,
      silminState->liquidComp, rLiq, (double *) NULL, (double **) NULL,
      (double ***) NULL, (double *) NULL);
     hmixLiq(FIRST,  silminState->T, silminState->P, rLiq, &pTemp);
     hTotal += mTotal*pTemp;
     cpmixLiq(FIRST, silminState->T, silminState->P, rLiq, &pTemp,
      (double *) NULL, (double *) NULL);
     cpTotal += mTotal*pTemp;
     silminState->liquidTD.h = hTotal - liquidState->refEnthalpy -solidState-
>refEnthalpy;
    } else silminState->liquidTD.h = 0.0;

    /* add residual solids */
    for (i=0; i<npc; i++) {
     for (ns=0; ns<(silminState->nSolidCoexist)[i]; ns++) {
      mTotal = (silminState->solidComp)[i][ns];
      if (solids[i].na == 1) {
       gibbs(silminState->T, silminState->P, solids[i].label,
        &(solids[i].ref), NULL, NULL, &(solids[i].cur));
       hTotal  += mTotal*(solids[i].cur).h;
       cpTotal += mTotal*(solids[i].cur).cp;
      } else {
       for (j=0; j<solids[i].na; j++) {
        mSol[j] = (silminState->solidComp)[i+1+j][ns];
        gibbs(silminState->T, silminState->P, solids[i+1+j].label,
         &(solids[i+1+j].ref), NULL, NULL, &(solids[i+1+j].cur));
        hTotal  += mSol[j]*(solids[i+1+j].cur).h;
        cpTotal += mSol[j]*(solids[i+1+j].cur).cp;
       }
       (*solids[i].convert)(SECOND, THIRD, silminState->T, silminState->P,
        (double *) NULL, mSol, rSol, (double *) NULL, (double **) NULL,
```

```
      (double ***) NULL, (double **) NULL, (double ****) NULL);
     (*solids[i].hmix)(FIRST, silminState->T, silminState->P, rSol,&pTemp);
     hTotal += mTotal*pTemp;
     (*solids[i].cpmix)(FIRST, silminState->T, silminState->P, rSol,
      &pTemp, (double *) NULL, (double *) NULL);
     cpTotal += mTotal*pTemp;
    }
   }
  }
  silminState->solidTD.h = hTotal - silminState->liquidTD.h - liquidState->refEnthalpy

   solidState->refEnthalpy;
  silminState->refEnthalpy = silminState->solidTD.h + silminState->liquidTD.h;

  /* compute residual and adjust T accordingly; alternate steps that use Cp
     with steps that simply interpolate */
  residual = hTotal - totalH; newT = silminState->T;
  if (fabs(residual) < 1.0e-05 && fabs(residual) > fabs(oldResidual)) residual = 0.0;
  if (fabs(residual) > 10.0*DBL_EPSILON*fabs(totalH)) {
   int isentr, isenth;

   if (quad) {
    if (residual != oldResidual) {
     silminState->T += (oldT - silminState->T)*residual/(residual-oldResidual);
    } else silminState->T -= residual/cpTotal;
    quad = 0;
   } else {
    silminState->T -= residual/cpTotal; /* twiddle temperature */
    quad = 1;
   }
   isentr = silminState->isentropic;   /* save old constraints */
   isenth = silminState->isenthalpic;
   silminState->isentropic = FALSE;  /* isothermal run */
   silminState->isenthalpic = FALSE;
   correctXforChangeInBulkComp();
   if (!silmin()) {        /* do silmin at new temp */
    if (fabs(residual) > 1.0e-05) silminState->T += 100.0;
   }
   silminState->isentropic = isentr; /* restore prior constraints */
   silminState->isenthalpic = isenth;
  }
  adiabatT = (liquidState->T = silminState->T);
  solidState->T = adiabatT;
  oldResidual = residual; oldT = newT;
  iter++;
 }
}

/* get solid masses for output file */
```

```
if (getenv("ADIABAT_ACCUM_CRYSTALLIZE") != NULL) {
 if (liquidState->nSolidCoexist[0] == 1)
  for (i=0;i<solids[0].na;i++)
    ol += liquidState->solidComp[i+1+0][0]*solids[i+1+0].mw;
 if (liquidState->nSolidCoexist[18] >= 1)
  for (i=0;i<solids[18].na;i++)
     opx+=liquidState->solidComp[i+1+18][0]*solids[i+1+18].mw;
 if (liquidState->nSolidCoexist[18] >= 2)
  for (i=0;i<solids[18].na;i++)
     cpx+=liquidState->solidComp[i+1+18][1]*solids[i+1+18].mw;
 if (liquidState->nSolidCoexist[34] == 1)
  for (i=0;i<solids[34].na;i++)
     plag+=liquidState->solidComp[i+1+34][0]*solids[i+1+34].mw;
 if (liquidState->nSolidCoexist[54] == 1)
  for (i=0;i<solids[54].na;i++) spinel+=
    liquidState->solidComp[i+1+54][0]*solids[i+1+54].mw;

 if (solidState->nSolidCoexist[0] == 1)
  for (i=0;i<solids[0].na;i++)
     ol += solidState->solidComp[i+1+0][0]*solids[i+1+0].mw;
 if (solidState->nSolidCoexist[18] >= 1)
  for (i=0;i<solids[18].na;i++)
     opx += solidState->solidComp[i+1+18][0]*solids[i+1+18].mw;
 if (solidState->nSolidCoexist[18] >= 2)
  for (i=0;i<solids[18].na;i++)
     cpx += solidState->solidComp[i+1+18][1]*solids[i+1+18].mw;
 if (solidState->nSolidCoexist[34] == 1)
  for (i=0;i<solids[34].na;i++)
     plag+=solidState->solidComp[i+1+34][0]*solids[i+1+34].mw;
 if (solidState->nSolidCoexist[54] == 1)
  for (i=0;i<solids[54].na;i++) spinel+=
    solidState->solidComp[i+1+54][0]*solids[i+1+54].mw;
}

/* if not crystallizing, calculate accumulated liquid pot entropy here*/
 if (getenv("ADIABAT_ACCUM_CRYSTALLIZE") == NULL &&
      getenv("ADIABAT_ACCUM_T_EQUIL") != NULL) {
  for (i=0, mTotal= 0.0, liquidState->liquidTD.s = 0.0; i<nlc; i++) {
   mTotal += liquidState->liquidComp[i];
   gibbs(liquidState->T, liquidState->P, liquid[i].label, &(liquid[i].ref),
        &(liquid[i].liq), &(liquid[i].fus), &(liquid[i].cur));
   liquidState->liquidTD.s  += liquidState->liquidComp[i]*(liquid[i].cur).s;
  }
  conLiq(SECOND, THIRD, liquidState->T, liquidState->P, (double *) NULL,
   liquidState->liquidComp, rLiq, (double *) NULL, (double **) NULL,
   (double ***) NULL, (double *) NULL);
  smixLiq(FIRST,  liquidState->T, silminState->P, rLiq, &pTemp,
   (double *) NULL, (double **) NULL);
  liquidState->liquidTD.s += mTotal*pTemp;
```

```
 liquidState->refEntropy = liquidState->liquidTD.s;
}

/* Calculate new refEntropy for melting pot */
/* residual liquid if any */
if (silminState->liquidComp[0] != 0.0) {
  for (i=0, mTotal= 0.0, silminState->liquidTD.s = 0.0; i<nlc; i++) {
    mTotal  += silminState->liquidComp[i];
    gibbs(silminState->T, silminState->P, liquid[i].label, &(liquid[i].ref),
        &(liquid[i].liq), &(liquid[i].fus), &(liquid[i].cur));
    silminState->liquidTD.s += silminState->liquidComp[i]*(liquid[i].cur).s;
  }
  smixLiq(FIRST,  silminState->T, silminState->P, rLiq, &pTemp,
     (double *) NULL, (double **) NULL);
  silminState->liquidTD.s += mTotal*pTemp;
} else silminState->liquidTD.s = 0.0;

/* residual solids */
for (i=0, silminState->solidTD.s = 0.0; i<npc; i++) {
  for (ns=0; ns<(silminState->nSolidCoexist)[i]; ns++) {
    mTotal = (silminState->solidComp)[i][ns];
    if (solids[i].na == 1) {
      gibbs(silminState->T, silminState->P, solids[i].label,
          &(solids[i].ref), NULL, NULL, &(solids[i].cur));
      silminState->solidTD.s += mTotal*(solids[i].cur).s;
    } else {
      for (j=0; j<solids[i].na; j++) {
        mSol[j] = (silminState->solidComp)[i+1+j][ns];
        gibbs(silminState->T, silminState->P, solids[i+1+j].label,
            &(solids[i+1+j].ref), NULL, NULL, &(solids[i+1+j].cur));
        silminState->solidTD.s += mSol[j]*(solids[i+1+j].cur).s;
      }
      (*solids[i].convert)(SECOND, THIRD, silminState->T, silminState->P,
          (double *) NULL, mSol, rSol, (double *) NULL, (double **) NULL,
          (double ***) NULL, (double **) NULL, (double ****) NULL);
      (*solids[i].smix)(FIRST, silminState->T, silminState->P, rSol,&pTemp,
           (double *) NULL, (double **) NULL);
      silminState->solidTD.s += mTotal*pTemp;
    }
  }
}
silminState->refEntropy = silminState->solidTD.s + silminState->liquidTD.s;

/* -> Calculate O2 end-member properties if path is buffered          */
if (silminState->fo2Path != FO2_NONE) gibbs(silminState->T, silminState->P,
  "O2", &(oxygen.ref), NULL, NULL, &(oxygen.cur));

/* Now recalculate system properties just to be sure */
silminState->liquidMass = getLiquidProperties(silminState,
```

```
    &(silminState->liquidTD),
    &(silminState->liqViscosity), TRUE);
(silminState->solidMass) = getBulkSolidProperties(silminState,
    &(silminState->solidTD), TRUE);
getSystemProperties(silminState, &(silminState->bulkTD),
    &(silminState->viscosity), &(silminState->meltFraction),
    TRUE);
liquidState->liquidMass = getLiquidProperties(liquidState,
    &(liquidState->liquidTD),&(liquidState->liqViscosity), TRUE);
liquidState->solidMass = getBulkSolidProperties(liquidState,
    &(liquidState->solidTD), TRUE);
getSystemProperties(liquidState, &(liquidState->bulkTD),
    &(liquidState->viscosity), &(liquidState->meltFraction), TRUE);
solidState->solidMass = getBulkSolidProperties(solidState,
    &(solidState->solidTD), TRUE);

if (getenv("ADIABAT_ACCUM_LIQ_FILE") != NULL) {
 if ((fp = fopen(getenv("ADIABAT_ACCUM_LIQ_FILE"), "a")) == NULL) {
  printf("Accumulated liquid info file open failed.\n"); return;
 }
} else {
 if ((fp = fopen("accum_liquid.out", "a")) == NULL) {
  printf("Accumulated liquid info file open failed.\n"); return;
 }
}
if (!beenHere) {
 fprintf(fp, "\nP adiabat_T mush_T liquidus_T liqSpt liqMass ");
 for (i=0;i<nc;i++) if (silminState->bulkComp[i] != 0.0)
  fprintf(fp, "%s ", bulkSystem[i].label);
 if (getenv("ADIABAT_ACCUM_CRYSTALLIZE") != NULL) {
  fprintf(fp, "SolidMass olivine opx cpx plag spinel");
 }
 fprintf(fp, "\n");
 beenHere = 1;
}
fprintf(fp, "%.0f %.4f %.4f %.4f %.6f %.6f ", silminState->P, adiabatT,
 silminState->T, liquidusT, liquidState->liquidTD.s, liquidState->liquidMass);
for (i=0;i<nc;i++) if (silminState->bulkComp[i] != 0.0)
 fprintf(fp, "%.3f ", liquidState->dspLiquidComp[i]);
if (getenv("ADIABAT_ACCUM_CRYSTALLIZE") != NULL) {
 fprintf(fp, "%.4f %.4f %.4f %.4f %.4f %.4f",
    liquidState->solidMass, ol, opx, cpx, plag, spinel);
}
fprintf(fp, "\n");
fclose(fp);

return;
}
```

```
/* a dumbed-down version of the MELTS routine that looks for mineral
   saturation; used by liquidus finder above */
int localSaturationState(double *rSol, SilminState *liquidState)
{
 static int *zeroX;
 static double *muSol, *xSol, *muLiq, *rLiq;
 int i, j, k, l, hasSupersat;
 double t, p;

 if (muLiq == NULL) {
  muLiq = (double *) malloc((unsigned) nlc*sizeof(double));
  muSol = (double *) malloc((unsigned) nlc*sizeof(double));
  xSol  = (double *) malloc((unsigned) nlc*sizeof(double));
  zeroX = (int *)    malloc((unsigned) nlc*sizeof(int));
  rLiq = (double *)  malloc((unsigned) nlc*sizeof(double));
 }

 t = liquidState->T;
 p = liquidState->P;

 /* obtain solid and liquid endmember properties */
 for (j=0; j<nlc; j++) {
  if ((liquidState->liquidComp)[j] != 0.0)
    gibbs(liquidState->T, liquidState->P, liquid[j].label, &(liquid[j].ref),
      &(liquid[j].liq), &(liquid[j].fus), &(liquid[j].cur));
  else
    multiplyThermoData(&(liquid[j].cur), 0.0);
 }
 for (j=0; j<npc; j++) {
  if (solids[j].type == PHASE) {
   if ((silminState->incSolids)[j]) {
    if(solids[j].na == 1)
      gibbs(liquidState->T, liquidState->P, solids[j].label,
        &(solids[j].ref), NULL, NULL, &(solids[j].cur));
    else {
      for (k=0; k<solids[j].na; k++) {
       gibbs(liquidState->T, liquidState->P, solids[j+1+k].label,
         &(solids[j+1+k].ref), NULL, NULL, &(solids[j+1+k].cur));
      }
      j += solids[j].na;
     }
    }
   }
 }

 /* obtain liquid chemical potentials */
 conLiq(SECOND, THIRD, t, p, (double *) NULL, liquidState->liquidComp, rLiq,
   (double *) NULL, (double **) NULL, (double ***) NULL,  &(liquidState->fo2));
 actLiq(SECOND, t, p, rLiq, (double *) NULL, muLiq, (double **) NULL);
```

```
for (i=0; i<nlc; i++) if ((liquidState->liquidComp)[i] != 0.0)
 muLiq[i] += (liquid[i].cur).g;

hasSupersat = FALSE;

/* obtain solid chemical potentials, affinities and composition estimates  */
for (i=0; i<npc; i++) {
 rSol[i] = 0.0;
 if (solids[i].type == PHASE) {
  if ((silminState->incSolids)[i]) {
   if (solids[i].na == 1) {

    muSol[0] = (solids[i].cur).g;
    for (k=0; k<nlc; k++) {
     if( (solids[i].solToLiq)[k] != 0.0) {
      if (liquidState->liquidComp[k] != 0.0)
       muSol[0] -= (solids[i].solToLiq)[k] * muLiq[k];
      else {
       muSol[0] = 0.0;
       break;
      }
     }
    }
    rSol[i] = muSol[0]; /* Affinity is < 0 if phase is supersaturated */
    hasSupersat |= (rSol[i] < 0.0);

   } else if (solids[i].na > 1) {

    for (k=0; k<solids[i].na; k++) {
     muSol[k] = (solids[i+1+k].cur).g;
     zeroX[k] = FALSE;
     for (l=0; l<nlc; l++) {
      if( (solids[i+1+k].solToLiq)[l] != 0.0) {
       if (liquidState->liquidComp[l] != 0.0) {
        muSol[k] -= (solids[i+1+k].solToLiq)[l] * muLiq[l];
       } else {
        muSol[k] = 0.0;
        zeroX[k] = TRUE;
        break;
       }
      }
     }
    }

    /* Affinity is returned in rSol[i]. It is < 0 if phase is
       supersaturated. The composition in terms of independent
       variables (ie. solids[i].nr of them) is returned in
       rSol[i+1] to rSol[i+1+solids[i].nr]. It may be converted
       subsequently to moles of endmembers if necessary          */
```

```
      if (!getAffinityAndComposition(t, p, i, zeroX, muSol, &rSol[i],
            &rSol[i+1])) {
       if (!strcmp(solids[i].label, "pyroxene")) {
         int tempZeroX[8];
         for (k=0; k<solids[i].na; k++) tempZeroX[k] = zeroX[k];
         muSol[3] = 0.0; tempZeroX[3] = TRUE;  /* Ca(Ti,Mg)(Al,Si)2O6   */
         muSol[4] = 0.0; tempZeroX[4] = TRUE;  /* Ca(Ti,Mg)(Fe3+,Si)2O6 */
         muSol[5] = 0.0; tempZeroX[5] = TRUE;  /* CaFeAlSiO6            */
         muSol[6] = 0.0; tempZeroX[6] = TRUE;  /* NaAlSi2O6             */
         if (getAffinityAndComposition(t, p, i, tempZeroX, muSol, &rSol[i],
            &rSol[i+1])) {
          if (tempZeroX[3] && !zeroX[3]) rSol[i+2] = 0.0001;
          if (tempZeroX[4] && !zeroX[4]) rSol[i+3] = 0.0001;
          if (tempZeroX[5] && !zeroX[5]) rSol[i+4] = 0.0001;
          if (tempZeroX[6] && !zeroX[6]) rSol[i+5] = 0.0001;
         } else for (k=0; k<=solids[i].na; k++) rSol[i+k] = 0.0;
       } else for (k=0; k<=solids[i].na; k++) rSol[i+k] = 0.0;
      }
      hasSupersat |= (rSol[i] < 0.0);
      i += solids[i].na;
     }
    }
   }
  }
  return hasSupersat;
}

/* silmin assumes that the initial guess satisfies the bulk composition
   constraints.  Hence for routines that change the bulk composition or
   monkey with the phases, we need a routine to check that the masses add
   up before we call silmin().  This function considers the bulk comp
   recorded in silminState->bulkComp[] to be gospel and does whatever surgery
   is needed to make the phases add up to it */
int correctXforChangeInBulkComp(void) {
  static int BeenHere=0;
  static double **liqKernel;
  int i, j, k, l;
  double *deltaBulkComp = dvector(0,nc);
  int enoughLiquid;
  int result = SUCCESS;

  if (!BeenHere) {
    double *w, *b, **v, **a;          /* First time through,              */
    int *e;
    w = dvector(1,nc);                /*  obtain LiqToOx, SVD it,        */
    v = dmatrix(1,nlc,1,nlc);         /*  then backsubstitute with unit */
    a = dmatrix(1,nc,1,nlc);          /*  RHS vectors to get liquid      */
    b = dvector(1,nlc);               /*  kernels; store in rows of      */
```

```
 liqKernel = dmatrix(0,nc,0,nlc);       /*  **liqKernel                    */
 e = (int *) malloc(nlc*sizeof(int));
 for (i=1;i<=nlc;i++) e[i] = TRUE;

 for (i=1;i<=nc;i++)
   for (j=1;j<=nlc;j++)
     a[i][j] = (liquid[j-1].liqToOx)[i-1];
 svdcmp(a, nc, nlc, w, v);
 for (i=0;i<nc;i++) {
   for (j=1;j<=nlc;j++) b[j] = (j==(i+1));
   svbksb(a, w, v, nc, nlc, b, e, (liqKernel[i]-1));
 }
 free_dvector(b,1,nlc);
 free_dmatrix(a,1,nc,1,nlc);
 free_dmatrix(v,1,nlc,1,nlc);
 free_dvector(w,1,nc);
 BeenHere = TRUE;
}

/* compute deltaBulkComp, residual between bulk and sum of phases */
for (i=0;i<nc;i++) {
 deltaBulkComp[i] = -silminState->bulkComp[i];
 for (j=0;j<nlc;j++) deltaBulkComp[i] +=
   silminState->liquidComp[j] * (liquid[j].liqToOx)[i];
 for (j=0;j<npc;j++) {
   for (k=0;k<silminState->nSolidCoexist[j];k++) {
     if (solids[j].na == 1) deltaBulkComp[i] +=
       silminState->solidComp[j][k] * (solids[j].solToOx)[i];
     else for (l=0;l<solids[j].na;l++) deltaBulkComp[i] +=
       silminState->solidComp[j+1+l][k] * (solids[j+1+l].solToOx)[i];
   }
 }
}
/* we use the local function if liquid is sufficient else use addOrDropLiquid().
   First criterion is that the change should not reduce any liquid component by
   more than 95%. */
for (i=0,enoughLiquid=TRUE;i<nlc;i++) {
 double dumb;
 for (j=0,dumb=0.0;j<nc;j++) dumb += bulkSystem[j].oxToLiq[i] * deltaBulkComp[j];
 if (dumb > 0.0 &&
     dumb > 0.95*silminState->liquidComp[i]) enoughLiquid = FALSE;
}
if (enoughLiquid) {
 /* If deltaBulkComp[i] != 0.0, use liqKernel to adjust liquidComp */
 for (i=0;i<nc;i++) {
   if (deltaBulkComp[i] != 0.0) {
     for (j=0;j<nlc;j++) silminState->liquidComp[j] -=
       deltaBulkComp[i] * liqKernel[i][j];
   }
```

```
 }
 for (i=0;i<nlc;i++) if (silminState->liquidComp[i] < 100.0*DBL_EPSILON)
  silminState->liquidComp[i] = 0.0;
} else if (!addOrDropLiquid(deltaBulkComp)) {
 /* failed once -- try again with half of the residual assigned to each method */
 printf("Correct X for Bulk Composition FAILED!\n");
 for (i=0;i<nc;i++) deltaBulkComp[i] /= 2.0;
 for (i=0,enoughLiquid=TRUE;i<nlc;i++) {
  double dumb;
  for (j=0,dumb=0.0;j<nc;j++) dumb += bulkSystem[j].oxToLiq[i] * deltaBulkComp[j];
  if (dumb > 0.0 &&
   dumb > 0.95*silminState->liquidComp[i]) enoughLiquid = FALSE;
 }
 if (enoughLiquid && addOrDropLiquid(deltaBulkComp)) {
  /* If deltaBulkComp[i] != 0.0, use liqKernel to adjust liquidComp */
  for (i=0;i<nc;i++) {
   if (deltaBulkComp[i] != 0.0) {
    for (j=0;j<nlc;j++) silminState->liquidComp[j] -=
     deltaBulkComp[i] * liqKernel[i][j];
   }
  }
  for (i=0;i<nlc;i++) if (silminState->liquidComp[i] < DBL_EPSILON)
   silminState->liquidComp[i] = 0.0;
 } else {
  /* failed again -- dump liquid, run pdaNorm for solid initial guess */
  printf("Correct X for Bulk Composition FAILED again - running norm!\n");
  if (!pdaNorm()) {
   int ns;

   /* failed again -- melt system for sure-fire liquid initial guess */
   printf("Correct X for Bulk Composition FAILED three times - melting system!\n");
   for (i=0;i<nlc;i++)
    for (j=0, silminState->liquidComp[i]=0.0; j<nc; j++)
     silminState->liquidComp[i] +=
      bulkSystem[j].oxToLiq[i]*silminState->bulkComp[j];
   for (i=0,silminState->liquidMass=0.0;i<nc;i++)
    silminState->liquidMass += silminState->bulkComp[i]*bulkSystem[i].mw;
   for (i=0;i<npc;i++) {
    for (ns=0;ns<silminState->nSolidCoexist[i];ns++) {
     silminState->solidComp[i][ns] = 0.0;
     if (solids[i].na > 1) for (j=0;j<solids[i].na;j++)
      silminState->solidComp[i+1+j][ns] = 0.0;
    }
    silminState->nSolidCoexist[i] = 0;
   }
   silminState->solidMass = 0.0;
   silminState->solidTD.s = 0.0;
  } else {
   for (i=0;i<nlc;i++) silminState->liquidComp[i] = 0.0;
```

```
      silminState->liquidMass = 0.0;
      silminState->liquidTD.s = 0.0;
     }
    }
   }

  free_dvector(deltaBulkComp,0,nc);
  return result;
}

/* This function multiplies the liquid by the specified focusFactor; it
   is part of a calculation that studies the effect of increasing the liquid
   flux to simulate melt focusing */
void doFocus(double focusFactor) {
  int i, j;
  static double integratedFocus = 1;

  silminState->liquidMass *= focusFactor;
  for (i=0;i<nlc;i++) {
    for (j=0;j<nc;j++) silminState->bulkComp[j] +=
      (focusFactor - 1.0)*silminState->liquidComp[i]*liquid[i].liqToOx[j];
    silminState->liquidComp[i] *= focusFactor;
  }
  silminState->refEntropy += silminState->liquidTD.s*(focusFactor - 1.0);
  silminState->liquidTD.s *= focusFactor;

  integratedFocus *= focusFactor;
  printf("Focus factor now up to %f\n", integratedFocus);

  if (getenv("ADIABAT_DO_TRACE") != NULL) doTraceElements(FIFTH);
}

/* This function adds an entropy source corresponding to the gravitational
   potential energy that is dissipated during one-dimensional steady porous
   flow with infinite permeability, when this process is being calculated as
   an equivalent batch melting calculation by a1Sh. This is the infinite
   permeability limit. For finite permeability, we would have to know phi */
void addGravitySource(void) {
  double soldensity, liqdensity, F;
  double g = 9.8;

  soldensity = silminState->solidMass/silminState->solidTD.v;
  liqdensity = silminState->liquidMass/silminState->liquidTD.v;
  F = silminState->liquidMass/(silminState->liquidMass+silminState->solidMass);

  silminState->refEntropy += F*g*(liqdensity-soldensity)/(liqdensity*silminState->T);
  correctTforChangeInEntropy();
  return;
}
```

```
int mod(int i, int base);
/* This function calculates several of the parameters in the isentropic
   productivity equation.  It is used to illustrate the importance of the
   various factors in determining productivity. */
void getdTdPatF(void) {
 static SilminState *saveState;
 static int beenhere = 0, i, j, k, l;
 double residual = 1;
 double fudge = 500.0;
 double T1, T2, F1, F2, F0;
 double dtdpatf, dfdtatp, newSsol, dSdF, dCp, dVa, dFdPnew, dFdPold, SlminusSs;
 double totalMass, mTotal, newSliq, pTemp;
 static double *dnldfatp, **dnsdfatp, *dnldpatf, **dnsdpatf, *mwLiq, *mSol, *rSol;
 double oldSsol, extraterm, dn, dFdPfinite;
 static double *sli, **ssij, *residueComp, *rLiq;
 int iter=0;
 static int *skip;
 FILE *fp;

 if (!beenhere) {
  saveState = allocSilminStatePointer();
  residueComp = dvector(0, nc);
  rLiq = dvector(0, nlc);
  mSol = dvector(0, 7);
  rSol = dvector(0, 6);
  dnldfatp = dvector(0, nlc);
  dnldpatf = dvector(0, nlc);
  dnsdfatp = dmatrix(0, npc-1, 0, 2);
  dnsdpatf = dmatrix(0, npc-1, 0, 2);
  skip = ivector(0, npc);
  sli = dvector(0,nlc);
  ssij = dmatrix(0, npc-1, 0, 2);
  mwLiq = dvector(0, nlc);
  for (i=0;i<nlc;i++)
    for (j=0,mwLiq[i]=0.0;j<nc;j++)
      mwLiq[i] += liquid[i].liqToOx[j] * bulkSystem[j].mw;
  fp = fopen("dtdpatf.out", "a");
  fprintf(fp, "P T dtapatf dfdtatp dCp dVa oldNum extraterm denomFirst Sl Ss");
  fprintf(fp, " SlminusSs dSdF dFdPnew dFdPold dFdPfinite\n");
  fclose(fp);
  beenhere = 1;
 }

 copyStateInfo(saveState, silminState);
 F0 = saveState->liquidMass/(saveState->liquidMass+saveState->solidMass);

 /* get dtdpatf by finite difference in P and search for same F */
 silminState->P -= .0001;
```

```
while (fabs(residual) > 1.0e-12) {
 silminState->refEntropy = 0.0; silminState->isentropic = 0.0;
 silmin();
 iter++;
 residual=silminState->liquidMass/
   (silminState->liquidMass+silminState->solidMass) - F0;

 if (mod(iter,5)==1) {
   T1 = silminState->T;
   F1 = silminState->liquidMass/(silminState->liquidMass+silminState->solidMass);
 } else if (mod(iter,5)==2) {
   T2 = silminState->T;
   F2 = silminState->liquidMass/(silminState->liquidMass+silminState->solidMass);
   if (fabs((F2-F0)/(F1-F0)) > 1.0) fudge /= 2.0;
   if (F1 != F2 && F1 != 0.0 && F2 != 0.0)
     fudge *= (F1-F0)/(F1-F2);
 }

 silminState->T -= fudge*residual;
}
dtdpatf = (saveState->T - silminState->T)/(saveState->P - silminState->P);

/* Record compositional changes due to dP at constant F.
  Fill dndpatf arrays - n is a mass fraction of a component */
for (i=0;i<nlc;i++) {
 dnldpatf[i] = (silminState->liquidComp[i]/silminState->liquidMass -
            saveState->liquidComp[i]/saveState->liquidMass)*mwLiq[i]/
           (silminState->P - saveState->P);
}
/* we also need change in mode -- save change in mass fraction of each phase
  in the mode in dndspatf[i][j]; assumes no one-component phases !!!! */
for (i=0;i<npc;i++) {
 for (j=0;j<silminState->nSolidCoexist[i];j++) {
   if (solids[i].na > 1) {
     for (k=0,totalMass=0.0,mTotal=0.0;k<solids[i].na;k++) {
       totalMass += silminState->solidComp[i+1+k][j]*solids[i+1+k].mw;
       mTotal += saveState->solidComp[i+1+k][j]*solids[i+1+k].mw;
     }
     for (k=0;k<solids[i].na;k++) {
       dnsdpatf[i+1+k][j] = (silminState->solidComp[i+1+k][j]/totalMass -
                   saveState->solidComp[i+1+k][j]/mTotal)*
                     solids[i+1+k].mw/(silminState->P - saveState->P);
     }
     dnsdpatf[i][j] = (totalMass/silminState->solidMass - mTotal/saveState->solidMass)/
          (silminState->P - saveState->P);
   }
  }
 }
 copyStateInfo(silminState, saveState);
```

```
/* Now get (dF/dT)P and change in compositions accompanying dT at constant P */
silminState->T += .0001; silminState->refEntropy = 0.0;
silmin();
F1 = silminState->liquidMass/(silminState->liquidMass+silminState->solidMass);
dfdtatp = 10000.0*(F1 - F0);
for (i=0;i<nlc;i++) {
 dnldfatp[i] = (silminState->liquidComp[i]/silminState->liquidMass -
          saveState->liquidComp[i]/saveState->liquidMass)*mwLiq[i]/(F1 - F0);
}
for (i=0;i<npc;i++) {
 for (j=0;j<silminState->nSolidCoexist[i];j++) {
  if (solids[i].na > 1) {
   for (k=0,totalMass=0.0,mTotal=0.0;k<solids[i].na;k++) {
    totalMass += silminState->solidComp[i+1+k][j]*solids[i+1+k].mw;
    mTotal += saveState->solidComp[i+1+k][j]*solids[i+1+k].mw;
   }
   for (k=0;k<solids[i].na;k++) {
    dnsdfatp[i+1+k][j] = (silminState->solidComp[i+1+k][j]/totalMass -
                saveState->solidComp[i+1+k][j]/mTotal)*
                  solids[i+1+k].mw/(F1 - F0);
   }
   dnsdfatp[i][j] = (totalMass/silminState->solidMass -
    mTotal/saveState->solidMass)/(F1-F0);
  }
 }
}
/* new 12/4/96 calculate (dS/dF)|T,P according to partial specific entropy
  formulation; also add extra term to numerator with partial specfic quantities */
/* 1. partial specific entropy of liquid components*/
dn = 1.0e-08;  /* a mass increment */
for (i=0;i<nlc;i++) {
 copyStateInfo(silminState, saveState);
 silminState->liquidComp[i] += dn/mwLiq[i]; /* add to component of interest */
 conLiq(SECOND, THIRD, silminState->T, silminState->P, (double *) NULL,
  silminState->liquidComp,rLiq,(double *) NULL,(double **) NULL,
  (double ***) NULL, (double *) NULL);
 for (j=0, mTotal= 0.0, newSliq = 0.0; j<nlc; j++) {
  mTotal  += silminState->liquidComp[j];
  gibbs(silminState->T, silminState->P, liquid[j].label, &(liquid[j].ref),
      &(liquid[j].liq), &(liquid[j].fus), &(liquid[j].cur));
  newSliq += silminState->liquidComp[j]*(liquid[j].cur).s;
 }
 smixLiq(FIRST,  silminState->T, silminState->P, rLiq, &pTemp,
    (double *) NULL, (double **) NULL);
 newSliq += mTotal*pTemp;
 sli[i] = (newSliq - saveState->liquidTD.s) / dn;
}
/* 2. partial specific entropy of solid phase components; store specific
```

```
    entropy of the phase in ssij[i][j]; assumes no one-component phases !!!! */
for (i=0;i<npc;i++) {
 for (j=0;j<silminState->nSolidCoexist[i];j++) {
  if (solids[i].na > 1) {
   copyStateInfo(silminState, saveState);
   mTotal = silminState->solidComp[i][j];
   for (l=0,oldSsol=0.0,totalMass=0.0; l<solids[i].na; l++) {
    mSol[l] = (silminState->solidComp)[i+1+l][j];
    totalMass += mSol[l]*solids[i+1+l].mw;
    gibbs(silminState->T, silminState->P, solids[i+1+l].label,
        &(solids[i+1+l].ref), NULL, NULL, &(solids[i+1+l].cur));
    oldSsol += mSol[l]*(solids[i+1+l].cur).s;
   }
   (*solids[i].convert)(SECOND, THIRD, silminState->T, silminState->P,
      (double *) NULL, mSol, rSol, (double *) NULL, (double **) NULL,
      (double ***) NULL, (double **) NULL, (double ****) NULL);
   (*solids[i].smix)(FIRST, silminState->T, silminState->P, rSol,&pTemp,
       (double *) NULL, (double **) NULL);
   oldSsol += mTotal*pTemp;
   ssij[i][j] = oldSsol/totalMass;

   for (k=0;k<solids[i].na;k++) {
    if (silminState->solidComp[i+1+k][j] != 0.0) {
     skip[i] = k; break;
    }
   }
   for (k=0;k<solids[i].na;k++) {
    if (silminState->solidComp[i+1+k][j] != 0.0) {
     for (l=0,newSsol=0.0,mTotal=0.0; l<solids[i].na; l++) {
      mSol[l] = (silminState->solidComp)[i+1+l][j];
      if (l==k)       mSol[l] += dn/solids[i+1+l].mw;
      mTotal += mSol[l];
      newSsol += mSol[l]*(solids[i+1+l].cur).s;
     }
     (*solids[i].convert)(SECOND, THIRD, silminState->T, silminState->P,
      (double *) NULL, mSol, rSol, (double *) NULL, (double **) NULL,
      (double ***) NULL, (double **) NULL, (double ****) NULL);
     (*solids[i].smix)(FIRST, silminState->T, silminState->P, rSol,&pTemp,
       (double *) NULL, (double **) NULL);
     newSsol += mTotal*pTemp;
     ssij[i+1+k][j] = (newSsol - oldSsol)/dn;
    }
   }
  }
 }
}
copyStateInfo(silminState, saveState);
dSdF = silminState->liquidTD.s/silminState->liquidMass -
     silminState->solidTD.s/silminState->solidMass;
```

```
  extraterm = 0.0;
  for (i=1;i<nlc;i++) {
   if (silminState->liquidComp[i] != 0.0) {
    dSdF += F0 * (sli[i] - sli[0]) * dnldfatp[i];
    extraterm += F0 * (sli[i] - sli[0]) * dnldpatf[i];
   }
  }
  for (i=0;i<npc;i++) {
   for (j=0;j<silminState->nSolidCoexist[i];j++) {
    if (solids[i].na > 1) {
     for (k=0,totalMass=0.0;k<solids[i].na;k++)
      totalMass += silminState->solidComp[i+1+k][j]*solids[i+1+k].mw;
     for (k=0;k<solids[i].na;k++) {
      if (k != skip[i] && silminState->solidComp[i+1+k][j] != 0.0) {
       dSdF += (1.0 - F0) * (totalMass / silminState->solidMass) *
              (ssij[i+1+k][j] - ssij[i+1+skip[i]][j]) * dnsdfatp[i+1+k][j];
       extraterm += (1.0 - F0) * (totalMass / silminState->solidMass) *
              (ssij[i+1+k][j] - ssij[i+1+skip[i]][j]) * dnsdpatf[i+1+k][j];
      }
     }
     /* here we add the term for change in mode */
     dSdF += (1.0 - F0) * ssij[i][j] * dnsdfatp[i][j];
     extraterm += (1.0 - F0) * ssij[i][j] * dnsdpatf[i][j];
    }
   }
  }
  SlminusSs = silminState->liquidTD.s/silminState->liquidMass -
      silminState->solidTD.s/silminState->solidMass;
  /* now calculate model dF/dP; assume batch melting.  See Royal Society Paper */
  dCp = F0*silminState->liquidTD.cp/silminState->liquidMass +
        (1-F0)*silminState->solidTD.cp/silminState->solidMass;
  dVa = F0*silminState->liquidTD.dvdt/silminState->liquidMass +
        (1-F0)*silminState->solidTD.dvdt/silminState->solidMass;
  dFdPnew = ((dCp/silminState->T)*dtdpatf - dVa + extraterm)/
         (dCp/(silminState->T * dfdtatp) + dSdF);
  dFdPold = ((dCp/silminState->T)*dtdpatf - dVa)/
         (dCp/(silminState->T * dfdtatp) + SlminusSs);

  /* get dF/dP by finite difference */
  silminState->P -= .0001;
  silmin();
  dFdPfinite = (silminState->liquidMass/(silminState->solidMass+silminState-
>liquidMass)
           - F0)/(silminState->P - saveState->P);
  copyStateInfo(silminState, saveState);
  fp = fopen("dtdpatf.out", "a");
  fprintf(fp, "%.0f %.9g %.9g %.9g %.9g %.9g %.9g %.9g %.9g %.9g %.9g \
       %.9g %.9g %.9g %.9g\n",
      saveState->P, saveState->T, dtdpatf, dfdtatp, dCp, dVa,
```

```
      (dCp/silminState->T)*dtdpatf - dVa, extraterm, dCp/(silminState->T * dfdtatp),
      silminState->liquidTD.s/silminState->liquidMass,
       silminState->solidTD.s/silminState->solidMass,SlminusSs,dSdF,dFdPnew,dFdPold,
      dFdPfinite);
 fclose(fp);
}

int mod(int i, int base) {
 int j=i;
 if (base <= 0) return i;
 while (j > base) j -= base;
 return j;
}
void copyStateInfo(SilminState *target, SilminState *source)
{
  target = copySilminStateStructure(source, target);
}
#undef REALLOC
```

```
/* Module initial_guess.c contains pdaNorm, a method for obtaining an
  initial guess in the subsolidus
**      V1.0-1      Paul D. Asimow  March 22, 1995
**            extracted from solid_support.c
*/


#include <math.h>
#include <stdio.h>
#include <stdlib.h>
#include <string.h>

#include "interface.h"
#include "silmin.h"
#include "adiabat.h"
#include "recipes.h"

int pdaNorm(void) {
  double SiO2,TiO2,Al2O3,Fe2O3,Cr2O3,FeO,MgO,CaO;
  double Na2O,MnO,CoO,NiO,K2O,H2O;
  int garnet, spinel, plag, olivine, quartz;
  int spindex,gtindex,plindex,olindex,qindex,pxindex;
  int i, j, k;

  /* find the oxides and store their indices; this avoids the assumption
     that their order hasn't changed. */
  for (i=0;i<nc;i++) {
    if (!strcmp(bulkSystem[i].label, "SiO2")) SiO2 = silminState->bulkComp[i];
    else if (!strcmp(bulkSystem[i].label, "TiO2")) TiO2 = silminState->bulkComp[i];
    else if (!strcmp(bulkSystem[i].label, "Al2O3")) Al2O3 = silminState->bulkComp[i];
    else if (!strcmp(bulkSystem[i].label, "Fe2O3")) Fe2O3 = silminState->bulkComp[i];
    else if (!strcmp(bulkSystem[i].label, "Cr2O3")) Cr2O3 = silminState->bulkComp[i];
    else if (!strcmp(bulkSystem[i].label, "FeO")) FeO = silminState->bulkComp[i];
    else if (!strcmp(bulkSystem[i].label, "MgO")) MgO = silminState->bulkComp[i];
    else if (!strcmp(bulkSystem[i].label, "NiO")) NiO = silminState->bulkComp[i];
    else if (!strcmp(bulkSystem[i].label, "MnO")) MnO = silminState->bulkComp[i];
    else if (!strcmp(bulkSystem[i].label, "CoO")) CoO = silminState->bulkComp[i];
    else if (!strcmp(bulkSystem[i].label, "CaO")) CaO = silminState->bulkComp[i];
    else if (!strcmp(bulkSystem[i].label, "Na2O")) Na2O = silminState->bulkComp[i];
    else if (!strcmp(bulkSystem[i].label, "K2O")) K2O = silminState->bulkComp[i];
    else if (!strcmp(bulkSystem[i].label, "H2O")) H2O = silminState->bulkComp[i];
   }
   /* find the phases and store their indices.  This avoid the assumption
     that the list of phases hasn't changed. */
   for (i=0;i<npc;i++) {
    if (!strcmp(solids[i].label, "olivine")) olindex = i;
    else if (!strcmp(solids[i].label, "garnet")) gtindex = i;
    else if (!strcmp(solids[i].label, "pyroxene")) pxindex = i;
    else if (!strcmp(solids[i].label, "spinel") && solids[i].type == PHASE) spindex = i;
```

```
 else if (!strcmp(solids[i].label, "feldspar")) plindex = i;
 else if (!strcmp(solids[i].label, "quartz")) qindex = i;
}
spinel = silminState->nSolidCoexist[spindex];
plag = silminState->nSolidCoexist[plindex];
garnet = silminState->nSolidCoexist[gtindex];
olivine = silminState->nSolidCoexist[olindex];
quartz = silminState->nSolidCoexist[qindex];

/* Rule 0 olivine or quartz ? How many pyroxenes? Transition metals OK ? */
if (!quartz && !olivine)
 {printf("Don't know how to solve w/o quartz or olivine.\n"); return 0; }
if (silminState->nSolidCoexist[pxindex] != 2)
 {printf("Can only handle 2 pyroxenes!\n"); return 0;}
if ((MnO != 0.0 || NiO != 0.0 || CoO != 0.0) && (!olivine || solids[olindex].na != 6)) {
 printf("Transition metals included without an allowed site!\n"); return 0;
}

/* Rule 1 Cr2O3 */
if (!spinel && Cr2O3 != 0.0) {printf("Cr2O3 w/o spinel!\n"); return 0;}
else {
 for (i=1;i<=solids[spindex].na;i++)
  if (!strcmp(solids[spindex+i].label, "chromite")) break;
 silminState->solidComp[spindex+i][0] = Cr2O3;     /* chromite */
 Cr2O3 -= silminState->solidComp[spindex+i][0];
 FeO -= silminState->solidComp[spindex+i][0];
}

/* Rule 2 Na2O, K2O */
if (plag) {
 for (i=1;i<=solids[plindex].na;i++)
  if (!strcmp(solids[plindex+i].label, "albite")) break;
 silminState->solidComp[plindex+i][0] = 1.8*Na2O;  /* albite */
 Na2O -= 0.5*silminState->solidComp[plindex+i][0];
 Al2O3 -= 0.5*silminState->solidComp[plindex+i][0];
 SiO2 -= 3.0*silminState->solidComp[plindex+i][0];
 for (i=1;i<=solids[plindex].na;i++)
  if (!strcmp(solids[plindex+i].label, "sanidine")) break;
 silminState->solidComp[plindex+i][0] = K2O;/* sanidine */
 Na2O -= 0.5*silminState->solidComp[plindex+i][0];
 Al2O3 -= 0.5*silminState->solidComp[plindex+i][0];
 SiO2 -= 3.0*silminState->solidComp[plindex+i][0];
}
for (i=1;i<=solids[pxindex].na;i++) if (!strcmp(solids[pxindex+i].label, "jadeite")) break;
silminState->solidComp[pxindex+i][1] = 1.32*Na2O;   /* cpx jadeite */
Al2O3 -= 0.5*silminState->solidComp[pxindex+i][1];
Na2O -= 0.5*silminState->solidComp[pxindex+i][1];
SiO2 -= 2.0*silminState->solidComp[pxindex+i][1];
silminState->solidComp[pxindex+i][0] = 2.0*Na2O;          /* opx jadeite */
```

```
Na2O -= 0.5*silminState->solidComp[pxindex+i][0];
Al2O3 -= 0.5*silminState->solidComp[pxindex+i][0];
SiO2 -= 2.0*silminState->solidComp[pxindex+i][0];

/* Rule 3 TiO2 and Fe2O3 in spinel */
if (spinel) {
  for (i=1;i<=solids[spindex].na;i++)
    if (!strcmp(solids[spindex+i].label, "ulvospinel")) break;
  silminState->solidComp[spindex+i][0] = 0.25*TiO2;  /* ulvospinel */
  TiO2 -= silminState->solidComp[spindex+i][0];
  FeO -= 2.0*silminState->solidComp[spindex+i][0];
  for (i=1;i<=solids[spindex].na;i++)
    if (!strcmp(solids[spindex+i].label, "magnetite")) break;
  silminState->solidComp[spindex+i][0] = 0.4*Fe2O3; /* magnetite */
  Fe2O3 -= silminState->solidComp[spindex+i][0];
  FeO -= silminState->solidComp[spindex+i][0];
}

/* Rule 4 Al2O3 */
if (spinel) {
  int spinelcomp, hercynite, magnetite, chromite, ulvospinel;

  for (i=1;i<=solids[spindex].na;i++){
    if (!strcmp(solids[spindex+i].label, "spinel")) spinelcomp = i;
    else if (!strcmp(solids[spindex+i].label, "hercynite")) hercynite = i;
    else if (!strcmp(solids[spindex+i].label, "magnetite")) magnetite = i;
    else if (!strcmp(solids[spindex+i].label, "chromite")) chromite = i;
    else if (!strcmp(solids[spindex+i].label, "ulvospinel")) ulvospinel = i;
  }
  silminState->solidComp[spindex+spinelcomp][0] =
      0.5*Al2O3/(spinel+plag+garnet); /* spinel */
  silminState->solidComp[spindex+hercynite][0] =
      -0.2*Al2O3/(spinel+plag+garnet); /* hercynite */
  if (silminState->solidComp[spindex+hercynite][0] +
      silminState->solidComp[spindex+magnetite][0] +
      silminState->solidComp[spindex+chromite][0] +
      silminState->solidComp[spindex+ulvospinel][0]*2.0 < 0.0)
      silminState->solidComp[spindex+hercynite][0] = 0.001 -
    silminState->solidComp[spindex+magnetite][0] +
    silminState->solidComp[spindex+chromite][0] +
    silminState->solidComp[spindex+ulvospinel][0]*2.0; /* enforce composition limit */
  MgO -= silminState->solidComp[spindex+spinelcomp][0];
  FeO -= silminState->solidComp[spindex+hercynite][0];
  Al2O3 -= (silminState->solidComp[spindex+hercynite][0] +
      silminState->solidComp[spindex+spinelcomp][0]);
}
if (plag) {
  for (i=1;i<=solids[plindex].na;i++)
    if (!strcmp(solids[plindex+i].label, "anorthite")) break;
```

```
 silminState->solidComp[plindex+i][0] = 0.64*Al2O3; /* anorthite */
 CaO -= silminState->solidComp[plindex+i][0];
 Al2O3 -= silminState->solidComp[plindex+i][0];
 SiO2 -= 2.0*silminState->solidComp[plindex+i][0];
}
if (garnet) {
 for (i=1;i<=solids[gtindex].na;i++)
   if (!strcmp(solids[gtindex+i].label, "almandine")) break;
 silminState->solidComp[gtindex+i][0] =
   0.6*Al2O3*(2.0*FeO/(2.0*FeO+3.0*MgO+0.5*CaO));  /* almandine */
 FeO -= 3.0*silminState->solidComp[gtindex+i][0];
 for (i=1;i<=solids[gtindex].na;i++)
  if (!strcmp(solids[gtindex+i].label, "grossular")) break;
 silminState->solidComp[gtindex+i][0] =
   0.6*Al2O3*(0.5*CaO/(2.0*FeO+3.0*MgO+0.5*CaO));  /* grossular */
 CaO -= 3.0*silminState->solidComp[gtindex+i][0];
 for (i=1;i<=solids[gtindex].na;i++)
  if (!strcmp(solids[gtindex+i].label, "pyrope")) break;
 silminState->solidComp[gtindex+i][0] =
  0.6*Al2O3*(3.0*MgO/(2.0*FeO+3.0*MgO+0.5*CaO));      /* pyrope */
 MgO -= 3.0*silminState->solidComp[gtindex+i][0];
 SiO2 -= 3.0*0.6*Al2O3;
 Al2O3 -= 0.6*Al2O3;
}

/* Rule 5 TiO2, Fe2O3, Al2O3 */
for (i=1;i<=solids[pxindex].na;i++)
 if (!strcmp(solids[pxindex+i].label, "alumino-buffonite")) break;
silminState->solidComp[pxindex+i][0] =
 0.75*(Al2O3 + TiO2 - Fe2O3);  /* opx aluminobuffonite */
silminState->solidComp[pxindex+i][1] =
 0.25*(Al2O3 + TiO2 - Fe2O3);  /* cpx aluminobuffonite */
for (i=1;i<=solids[pxindex].na;i++)
 if (!strcmp(solids[pxindex+i].label, "buffonite")) break;
silminState->solidComp[pxindex+i][0] =
  0.75*(-Al2O3 + TiO2 + Fe2O3); /* opx buffonite */
silminState->solidComp[pxindex+i][1] =
  0.25*(-Al2O3 + TiO2 + Fe2O3); /* cpx buffonite */
for (i=1;i<=solids[pxindex].na;i++)
 if (!strcmp(solids[pxindex+i].label, "essenite")) break;
silminState->solidComp[pxindex+i][0] =
  0.75*(Al2O3 - TiO2 + Fe2O3);  /* opx essenite */
silminState->solidComp[pxindex+i][1] =
  0.25*(Al2O3 - TiO2 + Fe2O3);  /* cpx essenite */
CaO -= (Al2O3+TiO2+Fe2O3);
MgO -= TiO2;  SiO2 -= (Al2O3+TiO2+Fe2O3);
Al2O3 -= Al2O3; TiO2 -= TiO2; Fe2O3 -= Fe2O3;

/* Rule 6 CaO */
```

```
{
 int hd, di;
 for (i=1;i<=solids[pxindex].na;i++) {
  if (!strcmp(solids[pxindex+i].label, "hedenbergite")) hd = i;
  else if (!strcmp(solids[pxindex+i].label, "diopside")) di = i;
 }
 silminState->solidComp[pxindex+hd][1] = 0.15*CaO;          /* cpx hedenbergite */
 FeO -= 0.15*CaO; SiO2 -= 0.30*CaO;
 silminState->solidComp[pxindex+hd][0] = (olivine?CaO:FeO);  /* opx hedenbergite */
 silminState->solidComp[pxindex+di][0] =
  -1.05*silminState->solidComp[pxindex+hd][0];              /* opx diopside */
 CaO -= silminState->solidComp[pxindex+hd][0] +
    silminState->solidComp[pxindex+di][0] +
    silminState->solidComp[pxindex+hd][1];
 MgO -= silminState->solidComp[pxindex+di][0];
 SiO2 -= 2.0*(silminState->solidComp[pxindex+hd][0] +
   silminState->solidComp[pxindex+di][0]);
 FeO -= silminState->solidComp[pxindex+hd][0];
 silminState->solidComp[pxindex+di][1] = (olivine?0.833*CaO:CaO); /* cpx diopside
*/
 SiO2 -= 2.0*silminState->solidComp[pxindex+di][1];
 MgO -= silminState->solidComp[pxindex+di][1];
 CaO -= silminState->solidComp[pxindex+di][1];
 for (i=1;i<=solids[olindex].na;i++)
    if (!strcmp(solids[olindex+i].label, "monticellite")) break;
 silminState->solidComp[olindex+i][0] =
  ((CaO>0.0 && olivine)?CaO:0.0);       /*monticellite*/
 CaO -= silminState->solidComp[olindex+i][0];
 MgO -= silminState->solidComp[olindex+i][0];
 SiO2 -= silminState->solidComp[olindex+i][0];
}

/* Rule 7 MnO, NiO, CoO */
if (olivine && solids[olindex].na >= 6) {
 for (i=1;i<=solids[olindex].na;i++)
    if (!strcmp(solids[olindex+i].label, "tephroite")) break;
 silminState->solidComp[olindex+i][0] = MnO/2.0;
 SiO2 -= MnO/2.0; MnO -= MnO;
 for (i=1;i<=solids[olindex].na;i++)
  if (!strcmp(solids[olindex+i].label, "Co-olivine")) break;
 silminState->solidComp[olindex+i][0] = CoO/2.0;
 SiO2 -= CoO/2.0; CoO -= CoO;
 for (i=1;i<=solids[olindex].na;i++)
  if (!strcmp(solids[olindex+i].label, "Ni-olivine")) break;
 silminState->solidComp[olindex+i][0] = NiO/2.0;
 SiO2 -= NiO/2.0; NiO -= NiO;
}

/* Rule 8 FeO, MgO, SiO2 */
```

```
for (i=1;i<=solids[olindex].na;i++) if (!strcmp(solids[olindex+i].label, "fayalite")) break;
silminState->solidComp[olindex+i][0] = (olivine?FeO/2.0:0.0); /* fayalite */
FeO -= 2.0*silminState->solidComp[olindex+i][0];
SiO2 -= silminState->solidComp[olindex+i][0];
for (i=1;i<=solids[olindex].na;i++)
  if (!strcmp(solids[olindex+i].label, "forsterite")) break;
silminState->solidComp[olindex+i][0] =
  (((MgO-SiO2)>0 && olivine)?(MgO-SiO2):0.0);    /* forsterite */
MgO -= 2.0*silminState->solidComp[olindex+i][0];
SiO2 -= silminState->solidComp[olindex+i][0];
for (i=1;i<=solids[pxindex].na;i++)
  if (!strcmp(solids[pxindex+i].label, "clinoenstatite")) break;
silminState->solidComp[pxindex+i][0] = 0.5*0.95*MgO; /* opx enstatite */
silminState->solidComp[pxindex+i][1] = 0.5*0.05*MgO; /* cpx enstatite */
SiO2 -= MgO;
MgO -= MgO;
if (SiO2 > 0.0) {
  if (!silminState->incSolids[qindex]) {
     printf("Need quartz but it's not included!\n");
     return -1;
  }
  silminState->solidComp[qindex][0] = SiO2;
  silminState->nSolidCoexist[qindex] = 1;
  SiO2 -= SiO2;
}

/* Rule 9 H2O */
if (H2O != 0.0) {
  printf("Adding water to initial guess assemblage\n");
  for (i=0;i<npc;i++) if (!strcmp(solids[i].label, "water")) break;
  silminState->incSolids[i] = 1;
  silminState->nSolidCoexist[i] = 1;
  silminState->solidComp[i][0] = H2O;
  H2O -= H2O;
}

/* Total minerals */
for (i=0,silminState->solidComp[olindex][0]=0.0;i<solids[olindex].na;i++)
  silminState->solidComp[olindex][0] += silminState->solidComp[olindex+i+1][0];
for (i=0,silminState->solidComp[gtindex][0]=0.0;i<solids[gtindex].na;i++)
  silminState->solidComp[gtindex][0] += silminState->solidComp[gtindex+i+1][0];
for (i=0,silminState->solidComp[pxindex][0]=0.0,
     silminState->solidComp[pxindex][1]=0.0;i<solids[pxindex].na;i++) {
  silminState->solidComp[pxindex][0] += silminState->solidComp[pxindex+i+1][0];
  silminState->solidComp[pxindex][1] += silminState->solidComp[pxindex+i+1][1];
}
for (i=0,silminState->solidComp[plindex][0]=0.0;i<solids[plindex].na;i++)
  silminState->solidComp[plindex][0] += silminState->solidComp[plindex+i+1][0];
for (i=0,silminState->solidComp[spindex][0]=0.0;i<solids[spindex].na;i++)
```

```
 silminState->solidComp[spindex][0] += silminState->solidComp[spindex+i+1][0];

/* Check sums */
if (SiO2 != 0.0) {printf("Silica error of %f\n", SiO2); return 0;}
if (MgO != 0.0) {printf("Magnesia error of %f\n", MgO); return 0;}

/* check minerals */
for (i=0;i<npc;i++) {
 for (j=0;j<silminState->nSolidCoexist[i];j++) {
  if (solids[i].na == 1) {
   if (silminState->solidComp[i][j] < 0.0) return 0;
  } else {
   double *mSol = dvector(0, solids[i].na);
   for (k=0;k<solids[i].na;k++)
    mSol[k] = silminState->solidComp[i+1+k][j];
   if (silminState->solidComp[i][j] < 0.0) {
    free_dvector(mSol, 0, solids[i].na);
    return 0;
   }
   if (!(*solids[i].test)(SIXTH, 1000.0, 1.0, (int) NULL, (int) NULL,
    (char **) NULL, (char **) NULL, (double *) NULL, mSol)) {
    free_dvector(mSol, 0, nc);
    return 0;
   }
   free_dvector(mSol, 0, nc);
  }
 }
}
silminState->liquidMass = 0.0; /* no liquid allowed */
return 1;
}
```

```
/*
**++
**  FACILITY:  subthermo_calc.c
**
**  MODULE DESCRIPTION:
**
**     routines to return thermodynamic properties (descended from
**       create_managed.c in Melts package)
**
**  MODIFICATION HISTORY:
**
**        V4.0-1        Paul D. Asimow  July 24, 1994
**             deleted all X11 dependencies, create_managed(), etc.
**             keep only useful init routines for non-X11 subroutine version
**        V4.0-2  Paul D. Asimow  July 27, 1994
**             add getSystemProperties(), getBulkSolidProperties(),
**             and addThermoData().  Modify all to pass ThermoData structures.
**        V5.0-1  Paul D. Asimow  November 11, 1994
**             Modify calls to *vmix and *cpmix for isentropic derivatives.
**             Gibbs now returns S(P,T)
**        V6.0-1  Paul D. Asimow  June 3, 1996
**             Compatible with Melts 3
**--
*/

#include <ctype.h>
#include <math.h>
#include <string.h>
#include <stdio.h>
#include <stdlib.h>

#include "interface.h"
#include "silmin.h"

/* Initialize global SILMIN structures */

#include "sol_struct_data.h"
#include "liq_struct_data.h"
#include "param_struct_data.h"

double getLiquidProperties(SilminState *state, ThermoData *value,
      double *viscosity, int derivatives)
{
  double *m, mass = 0.0, moles, *r;
  int i, j, na, nr;

  na = nc;
  nr = nc - 1;
```

```
m = (double *) malloc((unsigned) na*sizeof(double));
r = (double *) malloc((unsigned) nr*sizeof(double));

for (i=0, moles=0.0; i<nc; i++) {
  m[i]  = (state->liquidComp)[i]; moles += m[i];
}
for (i=0;i<nc;i++) {
  (state->dspLiquidComp)[i] = 0.0;
  for (j=0;j<nc;j++) (state->dspLiquidComp)[i] +=
     m[j]*(liquid[j].liqToOx)[i]*bulkSystem[i].mw;
  mass += (state->dspLiquidComp)[i];
}
for (i=0;i<nc;i++) (state->dspLiquidComp)[i] *= (100.0/mass);

(*conLiq)(SECOND, THIRD, state->T, state->P, (double *) NULL,
  m, r, (double *) NULL, (double **) NULL, (double ***) NULL,
  (double *) NULL);

/* The Gibbs energy of the phase (J)    */
(*gmixLiq)(FIRST, state->T, state->P, r, &(value->g),
  (double *) NULL, (double **) NULL);
for (i=0, value->g *= moles; i<na; i++) value->g += m[i]*liquid[i].cur.g;

/* The Enthalpy of the phase (J)        */
(*hmixLiq)(FIRST, state->T, state->P, r, &(value >h));
for (i=0, value->h *= moles; i<na; i++) value->h += m[i]*liquid[i].cur.h;

/* The Entropy of the phase (J/K) at P,T    */
(*smixLiq)(FIRST, state->T, state->P, r, &(value->s),
  (double *) NULL, (double **) NULL);
for (i=0, value->s *= moles; i<na; i++) value->s += m[i]*liquid[i].cur.s;

/* The Volume of the phase (cc)         */
(*vmixLiq)(FIRST, state->T, state->P, r, &(value->v),
  (double *) NULL, (double **) NULL, (double *) NULL, (double *) NULL,
  (double *) NULL, (double *) NULL, (double *) NULL, (double *) NULL,
  (double *) NULL);
for (i=0, value->v *= moles; i<na; i++) value->v += m[i]*liquid[i].cur.v;
value->v *= 10.0; /* joules/bar -> cc */

/* The Heat Capacity of the phase (J/K) */
(*cpmixLiq)(FIRST, state->T, state->P, r, &(value->cp),
  (double *) NULL, (double *) NULL);
for (i=0, value->cp *= moles; i<na; i++) value->cp += m[i]*liquid[i].cur.cp;

/* Various Derivatives */
if (derivatives) {
  value->dcpdt = 0.0;
  for (i=0;i<na;i++) value->dcpdt += m[i]*liquid[i].cur.dcpdt; /* dcpdt */
```

```
  value->dvdt = 0.0;
  for (i=0;i<na;i++) value->dvdt += m[i]*liquid[i].cur.dvdt;   /* dvdt  */
  value->dvdp = 0.0;
  for (i=0;i<na;i++) value->dvdp += m[i]*liquid[i].cur.dvdp;   /* dvdp  */
  value->d2vdt2 = 0.0;
  for (i=0;i<na;i++) value->d2vdt2 += m[i]*liquid[i].cur.d2vdt2;   /* d2vdt2  */
  value->d2vdp2 = 0.0;
  for (i=0;i<na;i++) value->d2vdp2 += m[i]*liquid[i].cur.d2vdp2;   /* d2vdp2  */
  value->d2vdtdp = 0.0;
  for (i=0;i<na;i++) value->d2vdtdp += m[i]*liquid[i].cur.d2vdtdp; /* d2vdtdp */
 }

 /* The Viscosity of the phase (log poise)   */
 (*visLiq)(FIRST, state->T, state->P, r, viscosity);

 free(m); if (na > 1) free(r);
 return mass;
}


double getSolidProperties(SilminState *state, int index, int ns, ThermoData *value,
      int derivatives)
{
 double *m, mass, moles, *r;
 int i, na, nr;

 na = solids[index].na;
 nr = solids[index].nr;

 m = (double *) malloc((unsigned) na*sizeof(double));
 if (na == 1) {
  m[0]  = (state->solidComp)[index][ns];
  mass  = m[0]*solids[index].mw;
  moles = m[0];
 } else {
  for (i=0, mass=0.0, moles=0.0; i<na; i++) {
   m[i]  = (state->solidComp)[index+1+i][ns];
   mass  += m[i]*solids[index+1+i].mw;
   moles += m[i];
  }
  r = (double *) malloc((unsigned) nr*sizeof(double));
  (*solids[index].convert)(SECOND, THIRD, state->T, state->P,
   (double *) NULL, m, r, (double *) NULL, (double **) NULL,
   (double ***) NULL, (double **) NULL, (double ****) NULL);
 }

 /* The Gibbs energy of the phase (J)    */
 if (na == 1) value->g = m[0]*solids[index].cur.g;
 else {
```

```
 (*solids[index].gmix)(FIRST, state->T, state->P, r, &(value->g),
 (double *) NULL, (double **) NULL, (double ***) NULL);
 value->g *= moles;
 for (i=0; i<na; i++) value->g += m[i]*solids[index+1+i].cur.g;
}

/* The Enthalpy of the phase (J)       */
if (na == 1) value->h = m[0]*solids[index].cur.h;
else {
 (*solids[index].hmix)(FIRST, state->T, state->P, r, &(value->h));
 value->h *= moles;
 for (i=0; i<na; i++) value->h += m[i]*solids[index+1+i].cur.h;
}

/* The Entropy of the phase (J/K) at P,T     */
if (na == 1) value->s = m[0]*solids[index].cur.s;
else {
 (*solids[index].smix)(FIRST, state->T, state->P, r, &(value->s),
  (double *) NULL, (double **) NULL);
 value->s *= moles;
 for (i=0; i<na; i++) value->s += m[i]*solids[index+1+i].cur.s;
}

/* The Volume of the phase (cc)        */
if (na == 1) value->v = m[0]*solids[index].cur.v;
else {
 (*solids[index].vmix)(FIRST, state->T, state->P, r, &(value->v),
  (double *) NULL, (double **) NULL, (double *) NULL, (double *) NULL,
  (double *) NULL, (double *) NULL, (double *) NULL, (double *) NULL,
  (double *) NULL);
 value->v *= moles;
 for (i=0; i<na; i++) value->v += m[i]*solids[index+1+i].cur.v;
}
value->v *= 10.0; /* joules/bar -> cc */

/* The Heat Capacity of the phase (J/K) */
if (na == 1) value->cp = m[0]*solids[index].cur.cp;
else {
 (*solids[index].cpmix)(FIRST, state->T, state->P, r, &(value->cp),
  (double *) NULL, (double *) NULL);
 value->cp *= moles;
 for (i=0; i<na; i++) value->cp += m[i]*solids[index+1+i].cur.cp;
}

/* Various Derivatives */
if (derivatives) {
 if (na == 1) {
    value->dcpdt = m[0]*solids[index].cur.dcpdt;
    value->dvdt = m[0]*solids[index].cur.dvdt;
```

```
      value->dvdp = m[0]*solids[index].cur.dvdp;
      value->d2vdt2 = m[0]*solids[index].cur.d2vdt2;
      value->d2vdp2 = m[0]*solids[index].cur.d2vdp2;
      value->d2vdtdp = m[0]*solids[index].cur.d2vdtdp;
    } else {
     (*solids[index].cpmix)(SECOND, state->T, state->P, r,(double *) NULL,
      &(value->dcpdt), (double *) NULL);
     value->dcpdt *= moles;
     for (i=0; i<na; i++) value->dcpdt += m[i]*solids[index+1+i].cur.dcpdt;
     (*solids[index].vmix)(FOURTH | FIFTH | SIXTH | SEVENTH | EIGHTH,
      state->T, state->P, r, (double *) NULL, (double *) NULL, (double **)
      NULL, &(value->dvdt), &(value->dvdp), &(value->d2vdt2), &(value->d2vdtdp),
      &(value->d2vdp2), (double *) NULL, (double *) NULL);
     value->dvdt *= moles;
     for (i=0; i<na; i++) value->dvdt += m[i]*solids[index+1+i].cur.dvdt;
     value->dvdp *= moles;
     for (i=0; i<na; i++) value->dvdp += m[i]*solids[index+1+i].cur.dvdp;
     value->d2vdt2 *= moles;
     for (i=0; i<na; i++) value->d2vdt2 += m[i]*solids[index+1+i].cur.d2vdt2;
     value->d2vdp2 *= moles;
     for (i=0; i<na; i++) value->d2vdp2 += m[i]*solids[index+1+i].cur.d2vdp2;
     value->d2vdtdp *= moles;
     for (i=0; i<na; i++) value->d2vdtdp += m[i]*solids[index+1+i].cur.d2vdtdp;
    }
  }

  free(m); if (na > 1) free(r);
  return mass;
}

void addThermoData(ThermoData *value, ThermoData temp);

double getSystemProperties(SilminState *state, ThermoData *value,
 double *viscosity, double *phi, int derivatives)
{
  double mass, volSol, Lviscosity;
  int i,j;
  ThermoData temp;
  double *moles;

  moles = (double *) malloc(nc*sizeof(double));

  if (silminState->liquidMass != 0.0)
    mass = getLiquidProperties(state, value, &Lviscosity,
        derivatives);
  else {mass = 0.0; multiplyThermoData(value, 0.0);}
  volSol = 0.0;
  for (i=0; i<npc; i++)
    for (j=0; j<(state->nSolidCoexist)[i]; j++) {
```

```
    mass += getSolidProperties(state, i, j, &temp,
      derivatives);
    addThermoData(value, temp);
    volSol += temp.v;
   }
 /* The Viscosity of the system (log poise)   A == 0.5 */
 *viscosity = (volSol < 0.5*valuc->v) ?
          Lviscosity - 2.0*log10(1.0 - 2.0*volSol/value->v) : 0.0;
 /* Melt Fraction */
 *phi = (value->v == 0.0) ? 0.0 : (1.0 - volSol/value->v);

 /* fO2 */
 if (silminState->liquidMass != 0.0) {
  for (i=0;i<nc;i++)  /* oxides */
    for (j=0,moles[i]=0.0;j<nc;j++) /* liquid components */
      moles[i] += (state->liquidComp)[j]*(liquid[j].liqToOx)[i];

   conLiq(FIRST, SEVENTH, state->T, state->P, moles, (double *) NULL,
       (double *) NULL, (double *) NULL, (double **) NULL, (double ***) NULL,
      &(state->fo2));
 }
 free(moles);
 return mass;
}

double getBulkSolidProperties(SilminState *state, ThermoData *value,
      int derivatives)
{
 double mass;
 int i, j, k;
 ThermoData temp;

 mass = 0.0;
 value->g = 0.0; value->h = 0.0; value->s = 0.0; value->v = 0.0; value->cp = 0.0;
 if (derivatives) {
  value->dcpdt = 0.0; value->dvdt = 0.0; value->dvdp = 0.0;
  value->d2vdt2 = 0.0; value->d2vdp2 = 0.0; value->d2vdtdp = 0.0;
 }
 for (i=0; i<npc; i++) {
  if (solids[i].type == PHASE) {
   for (j=0; j<(state->nSolidCoexist)[i]; j++) {
     mass += getSolidProperties(state, i, j, &temp,
        derivatives);
     addThermoData(value, temp);
    }
   }
  }

  return mass;
```

```
}

void addThermoData(ThermoData *value, ThermoData temp)
{
 value->g += temp.g;
 value->h += temp.h;
 value->s += temp.s;
 value->v += temp.v;
 value->cp += temp.cp;
 value->dcpdt += temp.dcpdt;
 value->dvdt += temp.dvdt;
 value->dvdp += temp.dvdp;
 value->d2vdt2 += temp.d2vdt2;
 value->d2vdp2 += temp.d2vdp2;
 value->d2vdtdp += temp.d2vdtdp;
}
```

```
/* Routine to compute trace element distributions as an adjunct to MELTS.
   Uses constant mineral D's to obtain bulk D based on mode.  Mineral D's
   reside in trace_data.h, which also initializes the array of structs
   traceElements[] and the integer nTraceElements. */

#include <math.h>
#include <stdio.h>
#include <stdlib.h>
#include <string.h>
#include <malloc.h>

#include "silmin.h"
#include "adiabat.h"
#include "trace_data.h"

#define REALLOC(x, y) (((x) == NULL) ? malloc(y) : realloc((x), (y)))

extern double last_P;

void doTraceElements(int mode) {
  int i, j, k, l, ns;
  double mass, liquidout;
  FILE *fp;
  char clino[5];

  if (traceElements[0].solidComp == NULL) {
    for (i=0;i<nTraceElements;i++) {
      traceElements[i].solidComp=(double **) malloc((unsigned) (npc+1)*sizeof(double
*));
      for (j=0;j<=npc;j++) traceElements[i].solidComp[j] =
        (double *) calloc((unsigned) 1, sizeof(double));
    }
  }

  if (mode & FIRST) {
    /* get bulk D's */
    for (i=0;i<nTraceElements;i++) traceElements[i].bulkPartition = 0.0;
    for (j=0;j<npc;j++) {
      if (solids[j].type == PHASE && silminState->incSolids[j]) {
        for (k=0;k<silminState->nSolidCoexist[j];k++) {
          if (solids[j].na == 1) {
            for (i=0;i<nTraceElements;i++)
              traceElements[i].bulkPartition += traceElements[i].Partition[j] *
                 silminState->solidComp[j][k] * solids[j].mw;
          } else {
            double *m = (double *) calloc((unsigned) solids[j].na, sizeof(double));
            double *r = (double *) calloc((unsigned) solids[j].nr, sizeof(double));
            char *formula;
```

```
      for (l=0,mass=0.0;l<solids[j].na;l++)
        mass +=  (m[l] = silminState->solidComp[j+1+l][k]) * solids[j+1+l].mw;
      if (strcmp(solids[j].label,"pyroxene"))
        for (i=0;i<nTraceElements;i++)
          traceElements[i].bulkPartition += traceElements[i].Partition[j] * mass;
      else {
        (*solids[j].convert)(SECOND, THIRD, silminState->T, silminState->P,
          (double *) NULL, m, r, (double *) NULL, (double **) NULL,
          (double ***) NULL, (double **) NULL, (double ****) NULL);
        (*solids[j].display)(FIRST, silminState->T, silminState->P, r, &formula);
        if (!strncmp("o", formula, 1)) {       /* orthopyroxene */
          for (i=0;i<nTraceElements;i++)
            traceElements[i].bulkPartition += traceElements[i].Partition[j+2] * mass;
          clino[k] = 'o';
        } else {
          for (i=0;i<nTraceElements;i++)       /* clinopyroxene */
            traceElements[i].bulkPartition += traceElements[i].Partition[j+1] * mass;
          clino[k] = 'c';
        }
      }
      free(m); free(r);
    }
   }
  }
 }
for (i=0;i<nTraceElements;i++)
  traceElements[i].bulkPartition /= silminState->solidMass;

/* Compute liquid concentrations */
for (i=0;i<nTraceElements;i++) traceElements[i].liquidComp =
  traceElements[i].bulkComp * (silminState->liquidMass + silminState->solidMass) /
  (silminState->liquidMass + traceElements[i].bulkPartition * silminState->solidMass);

/* Compute mineral concentrations */
for (j=0;j<npc;j++) {
  if (solids[j].type == PHASE && silminState->incSolids[j]) {
    if ((ns = silminState->nSolidCoexist[j]) > 1)
      for (i=0;i<nTraceElements;i++) traceElements[i].solidComp[j] =
        (double *) REALLOC(traceElements[i].solidComp[j], ns*sizeof(double));
    for (k=0;k<ns;k++) {
      if (strcmp(solids[j].label, "pyroxene"))
        for (i=0;i<nTraceElements;i++) traceElements[i].solidComp[j][k] =
          traceElements[i].liquidComp * traceElements[i].Partition[j];
      else if (clino[k] == 'o')
        for (i=0;i<nTraceElements;i++) traceElements[i].solidComp[j][k] =
          traceElements[i].liquidComp * traceElements[i].Partition[j+2];
      else if (clino[k] == 'c')
        for (i=0;i<nTraceElements;i++) traceElements[i].solidComp[j][k] =
          traceElements[i].liquidComp * traceElements[i].Partition[j+1];
```

```
    }
   }
  }

  /* Compute bulk solid concentration */
  for (i=0;i<nTraceElements;i++) traceElements[i].solidComp[npc][0] =
   traceElements[i].liquidComp * traceElements[i].bulkPartition;
}

if (mode & SECOND) {
  if (getenv("ADIABAT_TRACE_FILE") != NULL) {
   if ((fp = fopen(getenv("ADIABAT_TRACE_FILE"), "a")) == NULL) return;
  } else if ((fp = fopen("trace.out", "a")) == NULL) return;

  fprintf(fp, "%.0f %.2f ", silminState->P, silminState->T);
  for (i=0;i<nTraceElements;i++) fprintf(fp, "%s ", traceElements[i].label);
  fprintf(fp, "\nD  ");
  for (i=0;i<nTraceElements;i++) fprintf(fp, "%.6g ", traceElements[i].bulkPartition);
  fprintf(fp, "\nBulk  ");
  for (i=0;i<nTraceElements;i++) fprintf(fp, "%.6g ", traceElements[i].bulkComp);
  fprintf(fp, "\nLiquid  ");
  for (i=0;i<nTraceElements;i++) fprintf(fp, "%.6g ", traceElements[i].liquidComp);
  fprintf(fp, "\nBulk Solid  ");
  for (i=0;i<nTraceElements;i++) fprintf(fp,"%.6g",traceElements[i].solidComp[npc][0]);
  for (j=0;j<npc;j++) {
   if (solids[j].type == PHASE && silminState->incSolids[j]) {
    for (k=0;k<silminState->nSolidCoexist[j];k++) {
     if (!strcmp(solids[j].label, "pyroxene"))
      fprintf(fp, "\n%s%s  ", (clino[k]=='c' ? "clino" : "ortho"), solids[j].label);
     else fprintf(fp, "\n%s  ", solids[j].label);
     for (i=0;i<nTraceElements;i++)
      fprintf(fp, "%.6g ", traceElements[i].solidComp[j][k]);
    }
   }
  }
  fprintf(fp, "\n");
  fclose(fp);
}

if (mode & THIRD) {       /* Fractionation: Call this before extracting melt */
  liquidout = (silminState->meltFraction - MINf)/silminState->meltFraction;
  for (i=0;i<nTraceElements;i++) {
   traceElements[i].bulkComp -= traceElements[i].liquidComp * liquidout *
    silminState->liquidMass / (silminState->liquidMass + silminState->solidMass);
  }
 }

 if (getenv("ADIABAT_2_ACCUMLIQ") != NULL) {/*add liquid to accumulated
liquid*/
```

```
  for (i=0;i<nTraceElements;i++) {
   traceElements[i].accumLiq = (accumLiqMass*traceElements[i].accumLiq +
    silminState->liquidMass*traceElements[i].liquidComp)/(accumLiqMass+
    silminState->liquidMass);
  }
  accumLiqMass += silminState->liquidMass;
  for (i=0;i<nTraceElements;i++) {
   traceElements[i].pointDepthLiq =
(pointDepthDenom*traceElements[i].pointDepthLiq+
    accumLiqMass*traceElements[i].accumLiq)/(pointDepthDenom+accumLiqMass);
  }
  pointDepthDenom += silminState->liquidMass*(silminState->P-last_P);

  if (getenv("ADIABAT_TRACE_ACCUM_FILE") != NULL) {
   if ((fp = fopen(getenv("ADIABAT_TRACE_ACCUM_FILE"),"a")) != NULL) {
    fprintf(fp,"\n%.0f %.2f %.6g %.6g ",silminState->P,silminState->T,accumLiqMass,
        pointDepthDenom);
    for (i=0;i<nTraceElements;i++) fprintf(fp, "%.6g ", traceElements[i].accumLiq);
    for (i=0;i<nTraceElements;i++) fprintf(fp, "%.6g ", traceElements[i].pointDepthLiq);
    fclose(fp);
   }
  }
 }

 if (mode & FIFTH) {      /* for Focusing calculations */
  double focusFactor;
  focusFactor = atof(getenv("ADIABAT_FOCUS_FACTOR"));

  for (i=0;i<nTraceElements;i++) {
   traceElements[i].bulkComp += traceElements[i].liquidComp * (focusFactor-1) *
    silminState->liquidMass / (silminState->liquidMass + silminState->solidMass);
  }
 }
}

#undef REALLOC
```

```
/*
**      function prototypes for adiabatic path finding routines
*/

#ifndef _ADIABAT_H
#define _ADIABAT_H

void displayStates(int z);
SilminState *reAllocSilminStatePointer(SilminState *q, unsigned z);
void copyStateInfo(SilminState *target, SilminState *source);
void copyThermoData(ThermoData *target, ThermoData *source);
void multiplyThermoData(ThermoData *target, double factor);
void putMultipleDataToFile(char *fileName, int z, int t, double S0);
double extractMelt(int z);
void displaySilminState(void);
void freeSilminStatePointer(SilminState *p);
void printThermoData(SilminState *state);
void trackAccumulatedLiquid(void);
void doFocus(double focusFactor);
void getdTdPatF(void);

SilminState *states;   /* array of SilminState structs to hold data */
double *extractorFactor; /* saves renormalization constants */

/* parameters modifiable by environment and passed to support routines */
#define QUIT 0
#define MAX_S_ITER 30  /* maximum number of tries at given P to find right T */
#define MAX_P_ITER 20  /* maximum tries to find right P for melting increment */
#define Dst 1.0E-06    /* tolerance on wandering of system entropy */
#define Dphit 1.0E-04  /* tolerance on melting increment */
#define Dmp 50000    /* bars */
#define Ddphi 0.01     /* melting increment */
#define Dmf .005;      /* fraction left behind during continuous melting */
#define Ddp 1000       /* bars */
#define Dminp 3000   /* bars; not used by adiabat_1, where Dminp is 1.0 */
#define DdZ0 100000    /* cm */
#define DdT 3.0E+11          /* seconds = 10^4 years */
#define Dk0 1.0E-05  /* cm^2, incorporates grainsize */
#define Dpexp 3              /* exponent in porosity-permeability relation */
#define Dmphi .002   /* effective solidus for adiabat_1 */
#define Dmt 2000       /* maximum temperature for isobars */
#define Ddt 10               /* default T step for isobars */

/* global variables */
double STOL, PHITOL, MAX_P, DELTAPHI, MINf, DELTAP, MINP, DZ0;
double DF, DT, K0, MIN_PHI, DELTAT, MAX_T;
int PERM_EXP;

#endif
```

```
/*
**      Declarations for vectors which tell checkForCoexistingSolids
**      whether to look at given phases and in given component directions
*/

int *exsolve;
int *search;



#ifndef __Trace_h
#define __Trace_h

/* Include file for cheap trace element modeling as an attachment to
  MELTS or adiabat routines

  V1.0  4/5/95  Coefficients from Hirschmann et al, debug version */

void doTraceElements(int mode);

typedef struct _traceElements {
 char *label;            /* element name */
 double bulkComp;    /* total element content in system (ppm) */
 double liquidComp;  /* liquid element content (ppm) */
 double accumLiq;    /* accumulated liquid composition (ppm) */
 double pointDepthLiq; /* point-and-depth average liquid (ppm) */
 double **solidComp;   /* solid element content (ppm) */
 double bulkPartition; /* D */
 double Partition[73];          /* liquid/solid coefficient for each phase */
} TraceElements;

double accumLiqMass;
double pointDepthDenom;
#endif
```

```
#ifndef _Silmin_h
#define _Silmin_h

/*
**++
**  FACILITY:  Asimow's subroutine version of MELTS algorithms
**
**  MODULE DESCRIPTION:
**
**     SILMIN include file (file: SILMIN.H)
**
**  MODIFICATION HISTORY:
**
**       V5.0-1  Paul D. Asimow  May 6, 1996
**                port Melts3.0.x version to subsolidus
**--
*/

#include <ctype.h>
#include <float.h>
#include <limits.h>
#include <math.h>
#include <stdio.h>
#include <stdlib.h>
#include <string.h>
#include <time.h>

/*
 *=========================================================
 * Numerical constants
 */
#define TAU   DBL_EPSILON  /* machine precision            */
#define BIG   DBL_MAX      /* maximum double precision number */
#ifndef TRUE
#define TRUE  1
#endif
#ifndef FALSE
#define FALSE 0
#endif

/*
 *=========================================================
 * Macros
 */
#ifdef ABS
#undef ABS
#endif
#define ABS(x)   ((x) < 0 ? -(x) : (x))
#ifdef MAX
```

```
#undef MAX
#endif
#define MAX(a,b) ((a) > (b) ? (a) : (b))
#ifdef MIN
#undef MIN
#endif
#define MIN(a,b) ((a) < (b) ? (a) : (b))

/*
 *=============================================================
 * Public liquid solution functions:
 */

void conLiq  (int inpMask, int outMask, double t, double p, double *o,
          double *m, double *r, double *x, double **dm, double ***dm2,
          double *logfo2);
int testLiq (int mask, double t, double p, int na, int nr, char **names,
         char **formulas, double *r, double *m);
void dispLiq (int mask, double t, double p, double *x, char **formula);
void actLiq  (int mask, double t, double p, double *x, double *a,
          double *mu, double **dx);
void gmixLiq (int mask, double t, double P, double *x, double *gmix,
          double *dx, double **dx2);
void hmixLiq (int mask, double t, double P, double *x, double *hmix);
void smixLiq (int mask, double t, double P, double *x, double *smix,
          double *dx, double **dx2);
void cpmixLiq(int mask, double t, double P, double *x, double *cpmix,
          double *dt, double *dx);
void vmixLiq (int mask, double t, double P, double *x, double *vmix,
          double *dx, double **dx2, double *dt, double *dp, double *dt2,
          double *dtdp, double *dp2, double *dxdt, double *dxdp);
void muO2Liq(int mask, double t, double p, double *m, double *muO2, double *dm,
          double *dt, double *dp, double **d2m, double *d2mt, double *d2mp,
          double *d2t2, double *d2tp, double *d2p2);
void visLiq  (int mask, double t, double P, double *x, double *viscosity);

/*
 *=============================================================
 * Argument BITMASKs for public solid solution functions:
 */
#define FIRST      000001 /* octal for binary 0000000000001 */
#define SECOND     000002 /* octal for binary 0000000000010 */
#define THIRD      000004 /* octal for binary 0000000000100 */
#define FOURTH     000010 /* octal for binary 0000000001000 */
#define FIFTH      000020 /* octal for binary 0000000010000 */
#define SIXTH      000040 /* octal for binary 0000000100000 */
#define SEVENTH    000100 /* octal for binary 0000001000000 */
#define EIGHTH     000200 /* octal for binary 0000010000000 */
#define NINTH      000400 /* octal for binary 0000100000000 */
```

```
#define TENTH      001000 /* octal for binary 0001000000000 */
#define ELEVENTH   002000 /* octal for binary 0010000000000 */
#define TWELFTH    004000 /* octal for binary 0100000000000 */
#define THIRTEENTH 010000 /* octal for binary 1000000000000 */

/*
 *============================================================
 * Algorithmic constants
 */
#define MASSIN  1.0e-5  /* initial mass of included phases        */
#define MASSOUT 1.0e-7  /* minimal mass of included phases        */
#define SCALET  1000.0  /* scaling factor for T in isenthalpic calcs */
#define SCALEP  1000.0  /* scaling factor for P in isochoric calcs  */
#define ITERMX  100     /* maximum number of quadratic interations  */

#define R       8.3143  /* gas constant (J/K)                     */
#define TR      298.15  /* reference temperature (K)              */
#define PR      1.0     /* reference pressure (bars)              */

/*
 *============================================================
 * Thermodynamic data structures
 *  (1) These are type definitions, and are incorporated into actual
 *      data structures which characterize each phase
 */
typedef struct _thermoRef {
 double h, s, v;       /* enthalpy (J), entropy (J/K), volume (J/bar) */
 double k0, k1, k2, k3; /* Berman and Brown (1985) Cp parameters      */
 double v1, v2, v3, v4; /* Berman (1988) volume functions             */
 double Tt, deltah;    /* Transition temperature (K) and enthalpy (J) */
 double l1, l2;        /* lambda Cp funcs (J/K)**1/2                 */
} ThermoRef;

typedef struct _thermoLiq {
 double v, dvdt, dvdp; /* volume of liquid (0 K), and T,P derivatives  */
 double d2vdtp, d2vdp2; /* second derivatives of volume of liquid      */
 double tfus, sfus, cp; /* T fusion (K), S fusion (J/K), liquid Cp (J/K) */
 double tglass;        /* T glass transition (K)                     */
} ThermoLiq;

typedef struct _thermoData {
 double g, h, s, v, cp; /* gibbs energy (J), enthalpy (J), entropy (J/K) */
                /* volume (J/bar) and heat capacity (J/K)      */
 double dcpdt, dvdt, dvdp;      /* various T, P derivatives */
 double d2vdt2, d2vdp2, d2vdtdp;
} ThermoData;

typedef struct _modelParameters {
 char   *label;  /* label for the model parameter                 */
```

```
 double  enthalpy; /* value of the model parameter (J)              */
 double  entropy;  /* value of the model parameter (J/K)            */
 double  volume;   /* value of the model parameter (J/bar)          */
 int     activeH;  /* active enthalpy parameter (TRUE), inactive (FALSE) */
 int     activeS;  /* active entropy  parameter (TRUE), inactive (FALSE) */
 int     activeV;  /* active volume   parameter (TRUE), inactive (FALSE) */
} ModelParameters;

extern
ModelParameters modelParameters[]; /* data structure
                          containing nc*(nc-1) entries */
/*
 *============================================================
 * Bulk System, Liquid, and Solids data
 */
#define FEO   1
#define FE2O3 2
#define OTHER 0

typedef struct _bulkSystem {
 char     *label;  /* label for oxide compositional variables      */
 int      type;    /* FEO, FE2O3, OTHER oxide                      */
 double   coeff;   /* coefficient if OTHER, for ferrous/ferric calc */
 double   mw;      /* molecular weights of oxides                  */
 double   *oxToLiq; /* pointer to an array of length [nc] which converts
                       moles of oxides to moles of liquid components */
 int      *oxToElm; /* pointer to an array of length [106] which converts
                       moles of oxides to moles of elements        */
} BulkSystem;
extern BulkSystem bulkSystem[];
extern int nc;

typedef struct _liquid {
 char     *label;  /* label for the liquid component               */
 double   *liqToOx; /* pointer to an array of length [nc] which converts
                       component moles to moles of oxides          */
 ThermoRef  ref;    /* reference properties (solid) at TR, PR       */
 ThermoLiq  liq;    /* reference properties (liquid)                */
 ThermoData fus;    /* reference properties (liquid) at T fusion, PR */
 ThermoData cur;    /* current thermodynamic data at T, P           */
} Liquid;
extern Liquid liquid[];
extern int nlc;
extern int nls;

#define PHASE     1
#define COMPONENT 0

typedef struct _solids {
```

```
char     *label;  /* label for solid phase or solid phase components  */
int      type;    /* PHASE or COMPONENT                               */
char     *formula; /* character string formula                        */
double   *solToOx; /* pointer to an array of length [nc] which converts
                      COMPONENT moles to moles of oxides             */
double   *solToLiq;/* pointer to an array of length [nc] which converts
                      COMPONENT moles to moles of liquid components  */
double   mw;      /* molecular weight pure phase or component        */
/* Defined if type is COMPONENT, else empty                          */
ThermoRef  ref;   /* ref thermodynamic data, constants at TR, PR     */
ThermoData cur;   /* current thermodynamic data                      */
int      na;      /* if type == PHASE; number of endmember components */
int      nr;      /* if type == PHASE; number of independent variables */
/* Defined if type is PHASE, else pointers to void. common arguments:
  mask - bitwise mask for selecting input/output
  t    - Temperature (K)
  p    - Pressure (bars)
  *x   - (pointer to x[]) Array of independent compositional variables
*/
/* returns TRUE if values are correct/within bounds, else returns FALSE  */
int (*test) (int mask, double t, double p,
  int   na,     /* # of components in solution    BINARY MASK: 000001 */
  int   nr,     /* # of indep compos variables    BINARY MASK: 000010 */
  char **names,   /* names compon, expected order  BINARY MASK: 000100 */
  char **formulas, /* form of compon, expected order BINARY MASK: 001000 */
  double *r,    /* indep compositional variables  BINARY MASK: 010000 */
  double *m     /* moles of endmember components  BINARY MASK: 100000 */
);      /* r[] and m[] are tested for bound constraints              */
void (*convert) (int inpMask, int outMask, double t, double p,
  double *e,    /* moles of elements             BINARY MASK: 00000001 */
  double *m,    /* moles of endmember components  BINARY MASK: 00000010 */
  double *r,    /* indep compositional variables  BINARY MASK: 00000100 */
  double *x,    /* mole fractions of endmember cmp BINARY MASK: 00001000 */
  double **dm,  /* matrix[i][j]: dr[i]/dm[j]      BINARY MASK: 00010000 */
  double ***d2m, /* cube[i][j][k]: d2r[i]/dm[j]dm[k]BINARY MASK: 00100000 */
  double **dr,  /* matrix[i][j]: dx[i]/dr[j]      BINARY MASK: 01000000 */
  double ****d3m /* 4d[i][j][k][l]: d3r[i]/dm[j]dm[k]dm[l] MASK: 10000000 */
);
void (*activity) (int mask, double t, double p, double *x,
  double *a,  /* (pointer to a[]) activities        BINARY MASK: 0001 */
  double *mu, /* (pointer to mu[]) chemical potentials BINARY MASK: 0010 */
  double **dx /* (pointer to dx[][]) d(a[])/d(x[])    BINARY MASK: 0100 */
);      /* exclusion applied to activities if:    BINARY MASK: 1000 */
void (*gmix) (int mask, double t, double p, double *x,
  double *gmix, /* Gibbs energy of mixing           BINARY MASK: 0001 */
  double *dx,   /* (pointer to dx[]) d(g)/d(x[])     BINARY MASK: 0010 */
  double **dx2, /* (pointer to dx2[][]) d2(g)/d(x[])2 BINARY MASK: 0100 */
  double ***dx3 /* (pointer to dx3[][][]) d3(g)/d(x[])3BINARY MASK: 1000 */
);
```

```
 void (*hmix) (int mask, double t, double p, double *x,
   double *hmix  /* Enthalpy of mixing                    BINARY MASK: 1 */
 );
 void (*smix) (int mask, double t, double p, double *x,
   double *smix,  /* Entropy of mixing                   BINARY MASK: 001 */
   double *dx,    /* (pointer to dx[]) d(s)/d(x[])       BINARY MASK: 010 */
   double **dx2   /* (pointer to dx2[][]) d2(s)/d(x[])2   BINARY MASK: 100 */
 );
 void (*cpmix) (int mask, double t, double p, double *x,
   double *cpmix, /* Heat capacity of mixing             BINARY MASK: 001 */
   double *dt,    /* d(cp)/d(t)                        BINARY MASK: 010 */
   double *dx     /* d(cp)/d(x[])                       BINARY MASK: 100 */
 );
 void (*vmix) (int mask, double t, double p, double *x,
   double *vmix, /* Volume of mixing                  BINARY MASK: 0000000001 */
   double *dx,   /* (pointer to dx[]) d(v)/d(x[])  BINARY MASK: 0000000010 */
   double **dx2, /* (point dx2[][]) d(v)/d(x[])2   BINARY MASK: 0000000100 */
   double *dt,   /* d(v)/d(t)                      BINARY MASK: 0000001000 */
   double *dp,   /* d(v)/d(p)                       BINARY MASK: 0000010000 */
   double *dt2,  /* d2(v)/d(t)2                     BINARY MASK: 0000100000 */
   double *dtdp, /* d2(v)/d(t)d(p)                  BINARY MASK: 0001000000 */
   double *dp2,  /* d2(v)/d(p)2                     BINARY MASK: 0010000000 */
   double *dxdt, /* d2(v)/d(x[])d(t)                BINARY MASK: 0100000000 */
   double *dxdp  /* d2(v)/d(x[])d(p)                BINARY MASK: 1000000000 */
 );
 void (*display) (int mask, double t, double p, double *x,
   char **formula /* Mineral formula for interface display  BINARY MASK: 1 */
 );
} Solids;
extern Solids solids[];
extern int npc;

typedef struct _oxygen {
 double    *liqToOx; /* pointer to an array of length [nc] which converts
                        moles of liquid components to moles of oxygen      */
 double    *solToOx; /* pointer to an array of length [npc] which converts
                        moles of solid phase/components to moles of oxygen */
 ThermoRef  ref;     /* reference thermodynamic data, constants at TR, PR  */
 ThermoData cur;     /* current thermodynamic data                         */
} Oxygen;
extern Oxygen oxygen;

/*
 *============================================================
 * Status of calculation and intensive and extensive variables for the system
 */

#define FO2_NONE   0
#define FO2_HM     1
```

```
#define FO2_NNO    2
#define FO2_QFM    3
#define FO2_IW     4
#define FO2_QFM_P3  5
#define FO2_QFM_P2  6
#define FO2_QFM_P1  7
#define FO2_QFM_M1  8
#define FO2_QFM_M2  9
#define FO2_QFM_M3 10

/* This is the only struct significantly modified from standard MELTS */
typedef struct _silminState {
 double *bulkComp;     /* current bulk composition (moles of oxides)     */
 double *dspLiquidComp;  /* displayed bulk composition (grams of oxides)   */
 ThermoData bulkTD;     /* current thermodynamic properties of the system  */
 double meltFraction;  /* Volume fraction liquid */
 double viscosity;       /* viscosity of system (log 10 poise) */
 double liqViscosity;  /* viscosity of liquid (log 10 poise) */

 double *liquidComp;   /* current liquid composition (moles of liq comp)  */
 double *liquidDelta;  /* correction to liquidComp[] from quadratic min   */
 double liquidMass;    /* current mass of liquids (grams)                 */
 ThermoData liquidTD;  /* current thermodynamic properties of the liquids */
 int    multipleLiqs;  /* current value of toggle mode (TRUE/FALSE)       */

 double **solidComp;   /* current solid composition (moles of endmembers) */
 int    *nSolidCoexist; /* number of coexisting solids (cols of solidComp) */
 double **solidDelta;  /* correction to solidComp[] from quadratic min    */
 double solidMass;     /* current mass of solids (grams)                  */
 int    *incSolids;    /* current solid phases to be allowed to precip    */
 int    *cylSolids;    /* current solid phases suppressed due to cycling  */
 ThermoData solidTD;   /* current thermodynamic properties of the solids  */

 double T;           /* current temperature (K)                          */
 double P;           /* current pressure (bars)                          */

 double fo2;          /* current value of fo2 (numeric, base 10 log)     */
 int    fo2Path;      /* current value of fo2 path (i.e. FO2_NONE, etc   */
 double oxygen;       /* reference value of O2 content in the system     */

 int    isenthalpic;  /* current value of isenthalpic mode (TRUE/FALSE)  */
 double refEnthalpy;  /* reference enthalpy of the system                */
 int    isentropic;   /* current value of isentropic mode (TRUE/FALSE)   */
 double refEntropy;   /* reference entropy of the system                 */
 double tDelta;       /* correction to temperature from quadratic min    */

 int    isochoric;    /* current value of isochoric mode (TRUE/FALSE)    */
 double refVolume;    /* reference volume of the system                  */
 double pDelta;       /* correction to pressure from quadratic min       */
```

```
} SilminState;

extern SilminState *silminState;

typedef struct _silminInputData {
 char *name;      /* name of file which contains current input parameters */
 char *title;     /* title information                                    */
} SilminInputData;

extern SilminInputData silminInputData;

typedef struct _silminHistory *SilminHistoryPtr;
typedef struct _silminHistory {
 SilminState     *state;              /* current state of the system */
 SilminHistoryPtr next;
} SilminHistory;

extern SilminHistory *silminHistory;

typedef struct _constraints {
 double *lambda;     /* Array of length nc+3 of Lagrange multipliers     */
 double lambdaO2;    /* Lagrange multiplier for f O2 constraint          */
 double lambdaH;     /* Lagrange multiplier for isenthalpic constraint   */
 double lambdaS;     /* Lagrange multiplier for isentropic constraint    */
 double lambdaV;     /* Lagrange multiplier for isochoric constraint     */
 double *liquidDelta; /* Correction vector of liquid moles to maintain feas */
 double **solidDelta; /* Correction vector of solid moles to maintain feasi */
 double T;           /* Consistent Temperature of the system             */
 double P;           /* Consistent Pressure of the system                */
 double fo2;         /* Constraint log 10 fO2 of the system              */
} Constraints;

extern Constraints *constraints;

/*
 *=============================================================
 * Externally defined support functions:
 */
SilminState *allocSilminStatePointer(void);
SilminState *copySilminStateStructure(SilminState *pOld, SilminState *pNew);
int addOrDropLiquid(double *deltaBulkComp);
int checkForCoexistingSolids(void);
int checkForCoexistingLiquids(void);
int spinodeTest(void);
int checkStateAgainstInterface(void);
int evaluateSaturationState(double *rSol, double *rLiq);
int getAffinityAndComposition(double t, double p, int index, int *zeroX,
    double *muMinusMu0, double *affinity, double *indepVar);
void getEqualityConstraints(int *conRows, int *conCols, double ***cMatrixPt,
```

```
    double **hVectorPt, double **dVectorPt, double **yVectorPt);
double getLiquidProperties(SilminState *state, ThermoData *value,
    double *viscosity, int derivatives);
double getSolidProperties(SilminState *state, int index, int ns, ThermoData *value,
    int derivatives);
double getSystemProperties(SilminState *state, ThermoData *value,
    double *viscosity, double *phi, int derivatives);
double getBulkSolidProperties(SilminState *state, ThermoData *value,
        int derivatives);
double getlog10fo2(double t, double p, int buffer);
double getdlog10fo2dt(double t, double p, int buffer);
double getdlog10fo2dp(double t, double p, int buffer);
double getd2log10fo2dt2(double t, double p, int buffer);
double getd2log10fo2dp2(double t, double p, int buffer);
void getProjGradientAndHessian(int conRows, int conCols, double ***eMatrixPt,
    double ***bMatrixPt, double **cMatrix, double *hVector, double *dVector,
    double *yVector);
void gibbs(double t, double p, char *name, ThermoRef *phase,
    ThermoLiq *liquid, ThermoData *fusion, ThermoData *result);
void InitComputeDataStruct(void);
void intenToExtenGradient(double pMix, double *dpMix, int nr,  double *dp,
    int na, double mTotal, double **drdm);
void intenToExtenHessian(double pMix, double *dpMix, double **d2pMix,
    int nr, double **d2p, int na, double mTotal, double **drdm,
    double ***d2rdm2);
double linearSearch(double lambda, int *notcomp);
void correctTforChangeInEnthalpy(void);
void correctTforChangeInEntropy(void);
void correctPforChangeInVolume(void);
int correctXforChangeInBulkComp(void);

int subsolidusmuO2(int mask, double *muO2, double *dm, double *dt, double *dp,
  double **d2m, double *d2mt, double *d2mp, double *d2t2, double *d2tp,
  double *d2p2);

#endif /* _Silmin_h */
```

```
#include "trace.h"

#ifndef __Trace_data_h
#define __Trace_data_h

/* Include file for cheap trace element modeling as an attachment to
  MELTS or adiabat routines

  V2.0  5/24/95 Coefficients and souce from McKenzie and O'Nions */

int nTraceElements = 14;        /* number of trace elements used */

TraceElements traceElements[] = {
 {"La", 0.206, 0.0, 0.0, 0.0, NULL, 0.0,
    {0.0004, /*ol*/ 0.0,0.0,0.0,0.0,0.0,0.0, 0.0 /* sphene */,
       0.01 /* garnet */, 0.0,0.0,0.0, 0.0 /* melilite */, 0.0,0.0, 0.0 /* opx */, 0.0,0.0,
       0.0 /* pyroxene */, 0.054,0.002,0.0,0.0,0.0,0.0,0.0, 0.0 /* aenigmatite */,
       0.17 /* cummingtonite */, 0.0,0.0, 0.0 /* biotite */, 0.0,0.0, 0.0 /* musc */,
       0.27 /* feldspar */, 0.0,0.0,0.0,
       0.0 /* quartz */, 0.0 /* tridymite */, 0.0 /* cristobalite */,
       0.0 /* neph ss */, 0.0,0.0,0.0,0.0,
       0.0 /* nepheline */, 0.0 /* kalsilite */, 0.0 /* leucite ss */, 0.0,0.0,
       0.0 /* leucite */, 0.0 /* corundum */, 0.0 /* rutile */, 0.0 /* perovskite */,
       0.01 /* spinel */, 0.0,0.0,0.0,0.0,0.0,0.0,
       0.0 /* rhm oxide */, 0.0,0.0,0.0,0.0,0.0, 0.0 /* ortho oxide */, 0.0,0.0,0.0,0.0,
       0.0 /* whitlockite */, 0.0 /* apatite */, 0.0 /* water */} },
 {"Ce", 0.722, 0.0, 0.0, 0.0, NULL, 0.0,
    {0.0005, /*ol*/ 0.0,0.0,0.0,0.0,0.0,0.0,0.0, 0.0 /* sphene */,
       0.021 /* garnet */, 0.0,0.0,0.0,0.0, 0.0 /* melilite */, 0.0,0.0, 0.0 /* opx */, 0.0,0.0,
       0.0 /* pyroxene */, 0.098,0.003,0.0,0.0,0.0,0.0,0.0,0.0, 0.0 /* aenigmatite */,
       0.26 /* cummingtonite */, 0.0,0.0, 0.0 /* biotite */, 0.0,0.0, 0.0 /* musc */,
       0.2 /* feldspar */, 0.0,0.0,0.0,0.0,
       0.0 /* quartz */, 0.0 /* tridymite */, 0.0 /* cristobalite */,
       0.0 /* neph ss */, 0.0,0.0,0.0,0.0,0.0,
       0.0 /* nepheline */, 0.0 /* kalsilite */, 0.0 /* leucite ss */, 0.0,0.0,
       0.0 /* leucite */, 0.0 /* corundum */, 0.0 /* rutile */, 0.0 /* perovskite */,
       0.01 /* spinel */, 0.0,0.0,0.0,0.0,0.0,0.0,0.0,
       0.0 /* rhm oxide */, 0.0,0.0,0.0,0.0,0.0,0.0, 0.0 /* ortho oxide */, 0.0,0.0,0.0,0.0,
       0.0 /* whitlockite */, 0.0 /* apatite */, 0.0 /* water */} },
 {"Pr", 0.143, 0.0, 0.0, 0.0, NULL, 0.0,
    {0.0008, /*ol*/ 0.0,0.0,0.0,0.0,0.0,0.0,0.0,0.0, 0.0 /* sphene */,
       0.054 /* garnet */, 0.0,0.0,0.0,0.0, 0.0 /* melilite */, 0.0,0.0, 0.0 /* opx */, 0.0,0.0,
       0.0 /* pyroxene */, 0.15,0.0048,0.0,0.0,0.0,0.0,0.0,0.0, 0.0 /* aenigmatite */,
       0.35 /* cummingtonite */, 0.0,0.0, 0.0 /* biotite */, 0.0,0.0, 0.0 /* musc */,
       0.17 /* feldspar */, 0.0,0.0,0.0,0.0,
       0.0 /* quartz */, 0.0 /* tridymite */, 0.0 /* cristobalite */,
       0.0 /* neph ss */, 0.0,0.0,0.0,0.0,0.0,
       0.0 /* nepheline */, 0.0 /* kalsilite */, 0.0 /* leucite ss */, 0.0,0.0,
```

```
      0.0 /* leucite */, 0.0 /* corundum */, 0.0 /* rutile */, 0.0 /* perovskite */,
      0.01 /* spinel */, 0.0,0.0,0.0,0.0,0.0,
      0.0 /* rhm oxide */, 0.0,0.0,0.0,0.0,0.0, 0.0 /* ortho oxide */, 0.0,0.0,0.0,
      0.0 /* whitlockite */, 0.0 /* apatite */, 0.0 /* water */} },
{"Nd", 0.815, 0.0, 0.0, 0.0, NULL, 0.0,
   {0.001, /*ol*/ 0.0,0.0,0.0,0.0,0.0,0.0, 0.0 /* sphene */,
      0.087 /* garnet */, 0.0,0.0,0.0, 0.0 /* melilite */, 0.0,0.0, 0.0 /* opx */, 0.0,0.0,
      0.0 /* pyroxene */, 0.21,0.0068,0.0,0.0,0.0,0.0,0.0,0.0, 0.0 /* aenigmatite */,
      0.44 /* cummingtonite */, 0.0,0.0, 0.0 /* biotite */, 0.0,0.0, 0.0 /* musc */,
      0.14 /* feldspar */, 0.0,0.0,0.0,
      0.0 /* quartz */, 0.0 /* tridymite */, 0.0 /* cristobalite */,
      0.0 /* neph ss */, 0.0,0.0,0.0,0.0,
      0.0 /* nepheline */, 0.0 /* kalsilite */, 0.0 /* leucite ss */, 0.0,0.0,
      0.0 /* leucite */, 0.0 /* corundum */, 0.0 /* rutile */, 0.0 /* perovskite */,
      0.01 /* spinel */, 0.0,0.0,0.0,0.0,0.0,0.0,
      0.0 /* rhm oxide */, 0.0,0.0,0.0,0.0,0.0, 0.0 /* ortho oxide */, 0.0,0.0,0.0,0.0,
      0.0 /* whitlockite */, 0.0 /* apatite */, 0.0 /* water */} },
{"Sm", 0.299, 0.0, 0.0, 0.0, NULL, 0.0,
   {0.0013, /*ol*/ 0.0,0.0,0.0,0.0,0.0,0.0,0.0, 0.0 /* sphene */,
      0.217 /* garnet */, 0.0,0.0,0.0,0.0, 0.0 /* melilite */, 0.0,0.0, 0.0 /* opx */, 0.0,0.0,
      0.0 /* pyroxene */, 0.26,0.01,0.0,0.0,0.0,0.0,0.0,0.0, 0.0 /* aenigmatite */,
      0.76 /* cummingtonite */, 0.0,0.0, 0.0 /* biotite */, 0.0,0.0, 0.0 /* musc */,
      0.11 /* feldspar */, 0.0,0.0,0.0,
      0.0 /* quartz */, 0.0 /* tridymite */, 0.0 /* cristobalite */,
      0.0 /* neph ss */, 0.0,0.0,0.0,0.0,
      0.0 /* nepheline */, 0.0 /* kalsilite */, 0.0 /* leucite ss */, 0.0,0.0,
      0.0 /* leucite */, 0.0 /* corundum */, 0.0 /* rutile */, 0.0 /* perovskite */,
      0.01 /* spinel */, 0.0,0.0,0.0,0.0,0.0,0.0,
      0.0 /* rhm oxide */, 0.0,0.0,0.0,0.0,0.0, 0.0 /* ortho oxide */, 0.0,0.0,0.0,0.0,
      0.0 /* whitlockite */, 0.0 /* apatite */, 0.0 /* water */} },
{"Eu", 0.115, 0.0, 0.0, 0.0, NULL, 0.0,
   {0.0016, /*ol*/ 0.0,0.0,0.0,0.0,0.0,0.0,0.0, 0.0 /* sphene */,
      0.032 /* garnet */, 0.0,0.0,0.0,0.0, 0.0 /* melilite */, 0.0,0.0, 0.0 /* opx */, 0.0,0.0,
      0.0 /* pyroxene */, 0.31,0.013,0.0,0.0,0.0,0.0,0.0,0.0, 0.0 /* aenigmatite */,
      0.88 /* cummingtonite */, 0.0,0.0, 0.0 /* biotite */, 0.0,0.0, 0.0 /* musc */,
      0.73 /* feldspar */, 0.0,0.0,0.0,
      0.0 /* quartz */, 0.0 /* tridymite */, 0.0 /* cristobalite */,
      0.0 /* neph ss */, 0.0,0.0,0.0,0.0,
      0.0 /* nepheline */, 0.0 /* kalsilite */, 0.0 /* leucite ss */, 0.0,0.0,
      0.0 /* leucite */, 0.0 /* corundum */, 0.0 /* rutile */, 0.0 /* perovskite */,
      0.01 /* spinel */, 0.0,0.0,0.0,0.0,0.0,0.0,0.0,
      0.0 /* rhm oxide */, 0.0,0.0,0.0,0.0,0.0, 0.0 /* ortho oxide */, 0.0,0.0,0.0,0.0,
      0.0 /* whitlockite */, 0.0 /* apatite */, 0.0 /* water */} },
{"Gd", 0.419, 0.0, 0.0, 0.0, NULL, 0.0,
   {0.0015, /*ol*/ 0.0,0.0,0.0,0.0,0.0,0.0,0.0, 0.0 /* sphene */,
      0.498 /* garnet */, 0.0,0.0,0.0,0.0, 0.0 /* melilite */, 0.0,0.0, 0.0 /* opx */, 0.0,0.0,
      0.0 /* pyroxene */, 0.3,0.016,0.0,0.0,0.0,0.0,0.0,0.0, 0.0 /* aenigmatite */,
      0.86 /* cummingtonite */, 0.0,0.0, 0.0 /* biotite */, 0.0,0.0, 0.0 /* musc */,
      0.066 /* feldspar */, 0.0,0.0,0.0,
```

```
      0.0 /* quartz */, 0.0 /* tridymite */, 0.0 /* cristobalite */,
      0.0 /* neph ss */, 0.0,0.0,0.0,0.0,
      0.0 /* nepheline */, 0.0 /* kalsilite */, 0.0 /* leucite ss */, 0.0,0.0,
      0.0 /* leucite */, 0.0 /* corundum */, 0.0 /* rutile */, 0.0 /* perovskite */,
      0.01 /* spinel */, 0.0,0.0,0.0,0.0,0.0,
      0.0 /* rhm oxide */, 0.0,0.0,0.0,0.0,0.0, 0.0 /* ortho oxide */, 0.0,0.0,0.0,0.0,
      0.0 /* whitlockite */, 0.0 /* apatite */, 0.0 /* water */} },
{"Tb", 0.077, 0.0, 0.0, 0.0, NULL, 0.0,
  {0.0015, /*ol*/ 0.0,0.0,0.0,0.0,0.0,0.0, 0.0 /* sphene */,
      0.75 /* garnet */, 0.0,0.0,0.0,0.0, 0.0 /* melilite */, 0.0,0.0,0.0, 0.0 /* opx */, 0.0,0.0,
      0.0 /* pyroxene */, 0.31,0.019,0.0,0.0,0.0,0.0,0.0,0.0, 0.0 /* aenigmatite */,
      0.83 /* cummingtonite */, 0.0,0.0,0.0, 0.0 /* biotite */, 0.0,0.0,0.0, 0.0 /* musc */,
      0.06 /* feldspar */, 0.0,0.0,0.0,0.0,
      0.0 /* quartz */, 0.0 /* tridymite */, 0.0 /* cristobalite */,
      0.0 /* neph ss */, 0.0,0.0,0.0,0.0,0.0,
      0.0 /* nepheline */, 0.0 /* kalsilite */, 0.0 /* leucite ss */, 0.0,0.0,
      0.0 /* leucite */, 0.0 /* corundum */, 0.0 /* rutile */, 0.0 /* perovskite */,
      0.01 /* spinel */, 0.0,0.0,0.0,0.0,0.0,0.0,
      0.0 /* rhm oxide */, 0.0,0.0,0.0,0.0,0.0, 0.0 /* ortho oxide */, 0.0,0.0,0.0,0.0,
      0.0 /* whitlockite */, 0.0 /* apatite */, 0.0 /* water */} },
{"Dy", 0.525, 0.0, 0.0, 0.0, NULL, 0.0,
  {0.0017, /*ol*/ 0.0,0.0,0.0,0.0,0.0,0.0, 0.0 /* sphene */,
      1.06 /* garnet */, 0.0,0.0,0.0,0.0, 0.0 /* melilite */, 0.0,0.0,0.0, 0.0 /* opx */, 0.0,0.0,
      0.0 /* pyroxene */, 0.33,0.022,0.0,0.0,0.0,0.0,0.0,0.0, 0.0 /* aenigmatite */,
      0.78 /* cummingtonite */, 0.0,0.0,0.0, 0.0 /* biotite */, 0.0,0.0,0.0, 0.0 /* musc */,
      0.055 /* feldspar */, 0.0,0.0,0.0,0.0,
      0.0 /* quartz */, 0.0 /* tridymite */, 0.0 /* cristobalite */,
      0.0 /* neph ss */, 0.0,0.0,0.0,0.0,0.0,
      0.0 /* nepheline */, 0.0 /* kalsilite */, 0.0 /* leucite ss */, 0.0,0.0,
      0.0 /* leucite */, 0.0 /* corundum */, 0.0 /* rutile */, 0.0 /* perovskite */,
      0.01 /* spinel */, 0.0,0.0,0.0,0.0,0.0,0.0,
      0.0 /* rhm oxide */, 0.0,0.0,0.0,0.0,0.0, 0.0 /* ortho oxide */, 0.0,0.0,0.0,0.0,
      0.0 /* whitlockite */, 0.0 /* apatite */, 0.0 /* water */} },
{"Ho", 0.120, 0.0, 0.0, 0.0, NULL, 0.0,
  {0.0016, /*ol*/ 0.0,0.0,0.0,0.0,0.0,0.0, 0.0 /* sphene */,
      1.53 /* garnet */, 0.0,0.0,0.0,0.0, 0.0 /* melilite */, 0.0,0.0,0.0, 0.0 /* opx */, 0.0,0.0,
      0.0 /* pyroxene */, 0.31,0.026,0.0,0.0,0.0,0.0,0.0,0.0, 0.0 /* aenigmatite */,
      0.73 /* cummingtonite */, 0.0,0.0,0.0, 0.0 /* biotite */, 0.0,0.0,0.0, 0.0 /* musc */,
      0.048 /* feldspar */, 0.0,0.0,0.0,0.0,
      0.0 /* quartz */, 0.0 /* tridymite */, 0.0 /* cristobalite */,
      0.0 /* neph ss */, 0.0,0.0,0.0,0.0,0.0,
      0.0 /* nepheline */, 0.0 /* kalsilite */, 0.0 /* leucite ss */, 0.0,0.0,0.0,
      0.0 /* leucite */, 0.0 /* corundum */, 0.0 /* rutile */, 0.0 /* perovskite */,
      0.01 /* spinel */, 0.0,0.0,0.0,0.0,0.0,0.0,0.0,0.0,
      0.0 /* rhm oxide */, 0.0,0.0,0.0,0.0,0.0,0.0, 0.0 /* ortho oxide */, 0.0,0.0,0.0,0.0,
      0.0 /* whitlockite */, 0.0 /* apatite */, 0.0 /* water */} },
{"Er", 0.347, 0.0, 0.0, 0.0, NULL, 0.0,
  {0.0015, /*ol*/ 0.0,0.0,0.0,0.0,0.0,0.0,0.0,0.0, 0.0 /* sphene */,
      2.00 /* garnet */, 0.0,0.0,0.0,0.0, 0.0 /* melilite */, 0.0,0.0,0.0, 0.0 /* opx */, 0.0,0.0,
```

```
        0.0 /* pyroxene */, 0.3,0.03,0.0,0.0,0.0,0.0,0.0,0.0, 0.0 /* aenigmatite */,
        0.68 /* cummingtonite */, 0.0,0.0, 0.0 /* biotite */, 0.0,0.0, 0.0 /* musc */,
        0.041 /* feldspar */, 0.0,0.0,0.0,
        0.0 /* quartz */, 0.0 /* tridymite */, 0.0 /* cristobalite */,
        0.0 /* neph ss */, 0.0,0.0,0.0,0.0,
        0.0 /* nepheline */, 0.0 /* kalsilite */, 0.0 /* leucite ss */, 0.0,0.0,
        0.0 /* leucite */, 0.0 /* corundum */, 0.0 /* rutile */, 0.0 /* perovskite */,
        0.01 /* spinel */, 0.0,0.0,0.0,0.0,0.0,0.0,
        0.0 /* rhm oxide */, 0.0,0.0,0.0,0.0,0.0, 0.0 /* ortho oxide */, 0.0,0.0,0.0,
        0.0 /* whitlockite */, 0.0 /* apatite */, 0.0 /* water */} },
{"Tm", 0.054, 0.0, 0.0, 0.0, NULL, 0.0,
    {0.0015, /*ol*/ 0.0,0.0,0.0,0.0,0.0,0.0, 0.0 /* sphene */,
        3.00 /* garnet */, 0.0,0.0,0.0, 0.0 /* melilite */, 0.0,0.0, 0.0 /* opx */, 0.0,0.0,
        0.0 /* pyroxene */, 0.29,0.04,0.0,0.0,0.0,0.0,0.0,0.0, 0.0 /* aenigmatite */,
        0.64 /* cummingtonite */, 0.0,0.0, 0.0 /* biotite */, 0.0,0.0, 0.0 /* musc */,
        0.036 /* feldspar */, 0.0,0.0,0.0,
        0.0 /* quartz */, 0.0 /* tridymite */, 0.0 /* cristobalite */,
        0.0 /* neph ss */, 0.0,0.0,0.0,0.0,
        0.0 /* nepheline */, 0.0 /* kalsilite */, 0.0 /* leucite ss */, 0.0,0.0,
        0.0 /* leucite */, 0.0 /* corundum */, 0.0 /* rutile */, 0.0 /* perovskite */,
        0.01 /* spinel */, 0.0,0.0,0.0,0.0,0.0,0.0,
        0.0 /* rhm oxide */, 0.0,0.0,0.0,0.0,0.0, 0.0 /* ortho oxide */, 0.0,0.0,0.0,
        0.0 /* whitlockite */, 0.0 /* apatite */, 0.0 /* water */} },
{"Yb", 0.347, 0.0, 0.0, 0.0, NULL, 0.0,
    {0.0015, /*ol*/ 0.0,0.0,0.0,0.0,0.0,0.0, 0.0 /* sphene */,
        4.03 /* garnet */, 0.0,0.0,0.0, 0.0 /* melilite */, 0.0,0.0, 0.0 /* opx */, 0.0,0.0,
        0.0 /* pyroxene */, 0.28,0.049,0.0,0.0,0.0,0.0,0.0,0.0, 0.0 /* aenigmatite */,
        0.59 /* cummingtonite */, 0.0,0.0, 0.0 /* biotite */, 0.0,0.0, 0.0 /* musc */,
        0.031 /* feldspar */, 0.0,0.0,0.0,
        0.0 /* quartz */, 0.0 /* tridymite */, 0.0 /* cristobalite */,
        0.0 /* neph ss */, 0.0,0.0,0.0,0.0,
        0.0 /* nepheline */, 0.0 /* kalsilite */, 0.0 /* leucite ss */, 0.0,0.0,
        0.0 /* leucite */, 0.0 /* corundum */, 0.0 /* rutile */, 0.0 /* perovskite */,
        0.01 /* spinel */, 0.0,0.0,0.0,0.0,0.0,0.0,
        0.0 /* rhm oxide */, 0.0,0.0,0.0,0.0,0.0, 0.0 /* ortho oxide */, 0.0,0.0,0.0,
        0.0 /* whitlockite */, 0.0 /* apatite */, 0.0 /* water */} },
{"Lu", 0.057, 0.0, 0.0, 0.0, NULL, 0.0,
    {0.0015, /*ol*/ 0.0,0.0,0.0,0.0,0.0,0.0, 0.0 /* sphene */,
        5.5 /* garnet */, 0.0,0.0,0.0, 0.0 /* melilite */, 0.0,0.0, 0.0 /* opx */, 0.0,0.0,
        0.0 /* pyroxene */, 0.28,0.06,0.0,0.0,0.0,0.0,0.0,0.0, 0.0 /* aenigmatite */,
        0.51 /* cummingtonite */, 0.0,0.0, 0.0 /* biotite */, 0.0,0.0, 0.0 /* musc */,
        0.025 /* feldspar */, 0.0,0.0,0.0,
        0.0 /* quartz */, 0.0 /* tridymite */, 0.0 /* cristobalite */,
        0.0 /* neph ss */, 0.0,0.0,0.0,0.0,
        0.0 /* nepheline */, 0.0 /* kalsilite */, 0.0 /* leucite ss */, 0.0,0.0,
        0.0 /* leucite */, 0.0 /* corundum */, 0.0 /* rutile */, 0.0 /* perovskite */,
        0.01 /* spinel */, 0.0,0.0,0.0,0.0,0.0,0.0,
        0.0 /* rhm oxide */, 0.0,0.0,0.0,0.0,0.0, 0.0 /* ortho oxide */, 0.0,0.0,0.0,
        0.0 /* whitlockite */, 0.0 /* apatite */, 0.0 /* water */} }
```

```
};

#endif
```